Work Hardening and Mechanical Anisotropy of Aluminium Sheets and Profiles

by

Øyvind Ryen

A thesis submitted to

The Norwegian University of Science and Technology (NTNU)

in partial fulfilment of the requirements for the degree of

Doktor Ingeniør

Trondheim

November 2003

Preface

This research was carried out as part of the EC Fifth Framework project VIRFORM, Contract No. G1RD-CT-1999-00155. Funding by the European Community and by the industrial partners is gratefully acknowledged. My supervisors, Professor Erik Nes and Professor Hans Jørgen Roven, are greatly acknowledged for their contagious scientific enthusiasm, for stimulating me to speak at conferences and meetings and for motivating me during this work. Dr. Bjørn Holmedal also deserves lots of credit for taking time to long and clarifying discussions and helping me with the modelling results. Thanks also to my co-workers, Dr. Knut Sjølstad, Mr. Randulf Valle, Mr. Stian Tangen and all the rest of the people at the Department of Materials Technology. Some of the results presented have been provided by the diploma works of Mr. Hans Ivar Laukli and Mr. Eirik Berntsen at the department.

The project has given me the opportunity to get in contact with industry and universities around Europe. I would like to thank Dr. Trond Furu at Hydro Aluminium Sunndalsøra, professor Paul Van Houtte and Dr. Say-Yi Li at Katholieke Universiteit Leuven and Professor Olaf Engler at Hydro Aluminium Deutschland for many interesting discussion and exchange of results and information. A very special thanks goes to professor John Humphreys, Dr. Edwin Eardley and Dr. Andrew Clarke at the University of Manchester (UMIST) for introducing me to the English culture and for bringing me deeper into the fields of high-resolution EBSD.

Finally, my best thanks go to Marianne, who has been extremely patient with me during the most busy periods of this work.

Abstract

The processing of aluminium alloys from casting to end product is associated with a large number of metallurgical phenomena. In order to further improve and optimise process routes and alloys, a thorough understanding of the thermomechanical treatments by experimental observations and physically based modelling is necessary .

In part A of this thesis the work hardening behaviour of non-heat treatable alloys is followed up to large strains. The evolution in strength, microstructure and texture during cold rolling is analysed in commercially pure aluminium, AlMg alloys and AlMn alloys, covering both solid solution strengthening, particle strengthening, grain size effects and effects of impurities. A recently developed model for work hardening is applied to these alloys and discussed in relation to the experimental observations. The model successfully predicts the effects of Mg in solid solution, and is used to explain the effects of non-shearable particles and grain size on the strength and work hardening in stage II-III. Mn, Fe and Si in solid solution are suggested to create solute clusters that increase the strength significantly. At higher strains, stage IV, an unexpectedly low work hardening rate of high-Mg alloys is ascribed to a different storage pattern of dislocation and an increased amount of shear bands. High-resolution EBSD in FE-SEM is demonstrated to be a promising tool for substructure characterisation of cold rolled alloys.

In part B the mechanical anisotropy of flat extruded profiles of heat-treatable alloys is investigated. Two recrystallised alloys, AA6063 and 7030, and two non-recrystallised alloys, AA6082 and 7108, are tested in uniaxial tension in the solution heat treated condition, exhibiting strong directionality of yield stress, work hardening rate, elongation and r-value. The initial textures are very strong, and the anisotropy is analysed in terms of the Taylor model. The texture is found to be responsible for most of the strength anisotropy in the non-recrystallised alloys, while other sources of anisotropy must be present in the recrystallised alloys. Variations in the deformation structure development, indicating different slip activity in different directions, are believed to be partly responsible. The Taylor RC model predicts the r-values very well in all alloys, and a number of active slip systems in each position between two and three is assumed to be realistic for all alloys and directions.

Table of contents

1. Introduction

The weight of today's cars is continuously increasing as a result of growing demands for security, comfort and engine power. However, requirements to reduce the fuel consumption and air pollution force the car industry to apply low-weight materials to a greater extent than today. More sophisticated material solutions, for example by replacing steel with lighter materials, is an obvious method to try to reduce car weight. Aluminium is such a material, with a specific weight of only 35% of steel.

Aluminium alloys are, after iron and steel, the second most widely used material group in the automotive industry, and the number of applications is increasing. Products based on rolled sheets and extruded profiles include bumpers, outer panels and space frames (fig. 1.1). Forged and cast components are used as well.

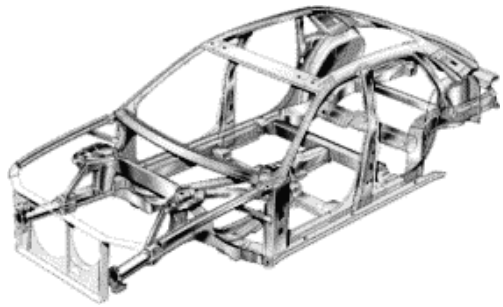

Figure 1.1: Space frame, an assembly of various rolled, extruded and high-pressure die cast components.

Aluminium has both good and bad properties as compared to steel and other materials. Besides the low weight, some of the great advantages of aluminium alloys are the high strength-to-weight ratio, good corrosion resistance, high energy absorption capacity and crash-worthiness, and its ability to be processed into complex geometrical shapes. Additionally, because of the relatively low melting point of aluminium, the energy consumption during recycling or remelting is low.

Some of the disadvantages of aluminium alloys as compared to steel are the lower strength, the limited formability of sheets and not least the high raw material and manufacturing costs. Another challenge for the producers of aluminium products is the extreme demands on shape tolerances, troubled by the high elastic springback of sheets and profiles. All these factors are problems that need to be overcome if aluminium alloys shall have any chance of replacing steel components in cars.

Whether this will happen is a question for the future. In the meantime, however, a further development of our knowledge concerning aluminium alloys will increase the possibility of gaining weight-reductions in the automotive industry, and may also force the steel industry to come up with new products and properties. For further discussions of aluminium as an automotive material, see Carle and Blount (1999), Miller et al. (2000) and Haenle et al. (2001).

Processing of aluminium sheets and profiles

An industrial processing schedule for aluminium sheets may look like the one in fig. 1.2. The material is direct-chill (DC) cast, homogenised, break-down rolled, multi-stand tandem hot rolled, cold rolled and annealed. In addition, the sheet will have to be formed into the final product, such as a bonnet or a car door. At all steps of the production line metallurgical phenomena occur, depending on temperature, deformation, time and alloy composition. In order to keep control of the final material properties it is essential to understand what is happening during such a complex sequence of thermomechanical treatments. During cold rolling the strength of aluminium alloys increases due to work hardening resulting from the development of a deformation structure. The cold rolled product is therefore a thin sheet with a high strength. The final annealing stabilises the material and provides a compromise between strength and ductility. Part A of this thesis deals with alloys subjected to cold rolling, i.e. at the downstream end of the production line. Commercially pure aluminium (AA1xxx), aluminium-magnesium alloys (AA5xxx) and aluminium-manganese alloys (AA3xxx) are investigated.

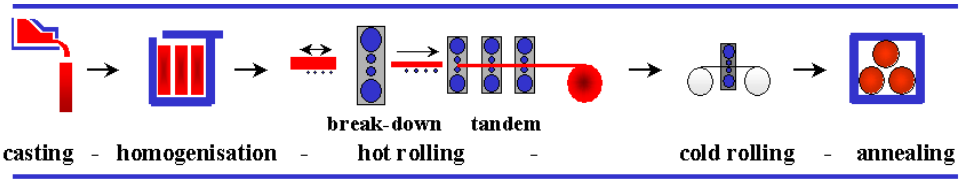

Figure 1.2: Industrial processing schedule for aluminium sheet.

The processing of extrusions is slightly different, as the homogenised metal is directly extruded into profiles of the desired shapes, fig. 1.3. These profiles are then given additional forming operations, for instance into bumpers or space frame beams. The extrusion process gives products with a strong directionality of their properties, which is a great challenge for the forming industry. Part B of this work is dedicated to such problems in heat-treatable aluminium alloys with magnesium and silicon (AA6xxx) and

with magnesium and zinc (AA7xxx). Industrial forming operations of such alloys are often carried out in the low-strength solution heat-treated condition, known as the W-temper, which requires a relatively low force. The desired strength is achieved through later ageing treatments.

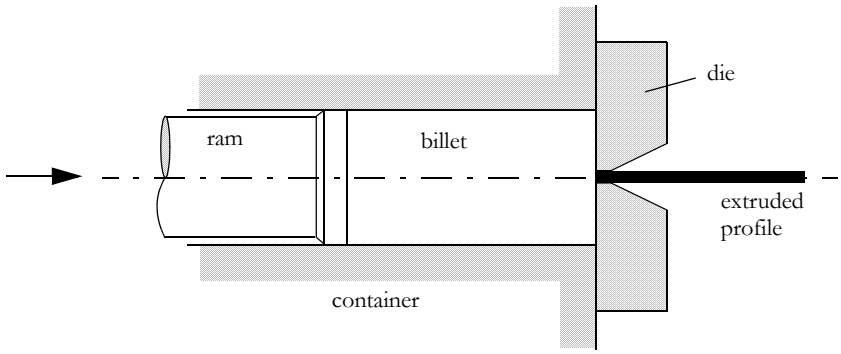

Figure 1.3: Sketch of the extrusion process, where a ram presses the billet through a die of a desired shape.

As mentioned above, the material behaviour is strongly dependent on the preceding treatment, and hence it is necessary to see the process as a whole. This work is a contribution to a project which focuses on the whole process chain from casting to end product. The project, denoted VIR[*], is divided into three sub-projects; Virtual Casting, Virtual Fabrication and Virtual Forming. The present PhD-thesis belongs to the latter project (VIRFORM), which aims to develop an integrated model for formability, work hardening and texture development of aluminium sheets and profiles.

Modelling in material science

The main scope of the VIR[*]-project is to develop a *through process model* for industrial production of aluminium products. In this context, such a model is a mathematical formulation that links the final properties of the alloy to the alloy chemistry and process history. It relies on a fundamental theoretical understanding of the microstructure of the materials, and can be used to calculate, verify or predict their properties and behaviour. Models dealt with in this project are physically based, in contrast to the simpler empirical models that traditionally have been used in materials engineering.

Physically based microstructure modelling provides a tool for predicting and understanding material properties and microstructure evolution (Raabe 1998). A better insight into the underlying physics and chemistry may be gained, which can serve as a

guide for new experiments or an optimization of processes or alloys. As computers are ever-increasing their performance, more and more complex models may be applied. Improving analytical methods, e.g. FE-SEM and EBSD, also enable a more accurate characterisation of the microstructure that provides input parameters for testing and verifying the model. By linking several sub-models, as illustrated in fig. 1.4, a through process model may be developed for the process sketched in fig. 1.2. In this case, a homogenisation model provides parameters regarding the alloy chemistry, such as solute content and particle structure, which are of importance for the modelling of work hardening and substructure. By using an FEM model, the deformation history in terms of strain, strain rate and temperature for a forming operation (hot rolling, cold rolling, extrusion) can be calculated. These input parameters are then used in models for deformation texture and work hardening. The resulting texture and substructure are used in a model for recovery and recrystallisation during subsequent annealing to calculate grain size and texture. A model for microchemistry is also in progress.

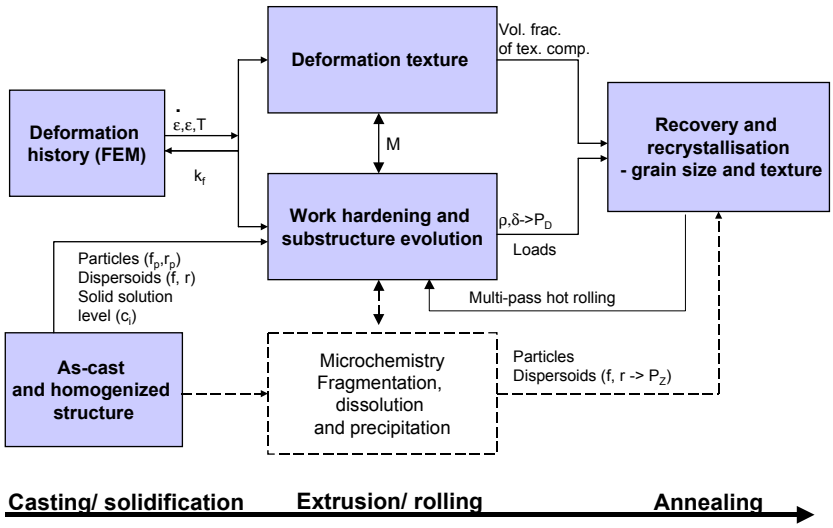

Figure 1.4: Integrated modelling of an industrial process chain linking several sub-models. Input/ output parameters are given.

An essential part of the present thesis is the use of a model for work hardening and substructure evolution of fcc-metals developed by Nes, Marthinsen and co-workers (Nes 1998, Nes and Marthinsen 2002). The model gives the flow stress and substructural parameters as a function of the applied deformation history. It has proved to be in good accordance with experimental observations, covering a wide range of temperatures,

strain rates and alloys. Some problems have come to light during large strain deformation at room temperature (cold rolling), and the goal of part A of this thesis is to explore the effects of solid solutions, particles and grain size in terms of the model.

The formability of a sheet or profile is often simply described using phenomenological models or crystal plasticity models. In a recent approach an attempt is made to combine several metallurgical and mechanical aspects of the forming process into a constitutive model, see fig. 1.5 (Hopperstad et al. 2003, Lademo et al. 2002). The outcome is a relationship between the stress tensor and the strain tensor. One of the parts of the model is the texture of the material, and in part B of this work the classical crystal plasticity model by Taylor (1938) is used to study the anisotropy of mechanical properties in extruded profiles.

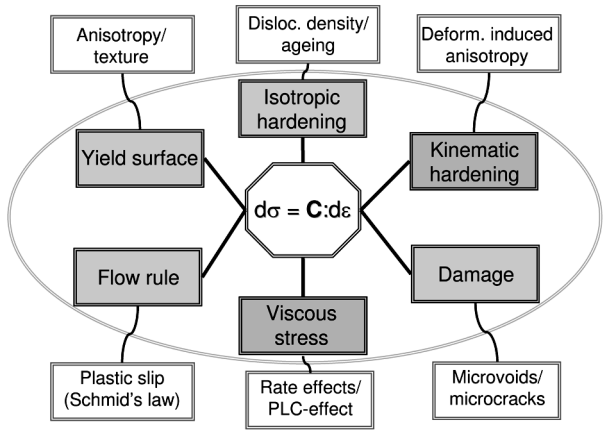

Figure 1.5: Constitutive modelling of formability (Hopperstad et al. 2003).

2. Theoretical background

In this chapter an overview is given on some basic concepts regarding aluminium alloys and their microstructure and mechanical properties. The development of a deformation structure and texture during cold deformation is presented in section 2.2. Pure metals, solid solution alloys and particle containing alloys are covered here. Thereafter, solution hardening (section 2.3) and particle hardening (section 2.4) are reviewed. In section 2.5 the concept of work hardening is described. Here, a more in-depth presentation of this phenomenon is given with a model for work hardening. Finally, mechanical anisotropy with respect to the formability is treated in section 2.6.

2.1 Aluminium alloys

2.1.1 Non-heat treatable aluminium alloys

Non-heat treatable aluminium alloys constitute a class of alloys that owe their strength mainly to elements in solid solution, but also to some types of particles. A heat-treatment of such an alloy will generally not produce any strengthening precipitates as in the heat-treatable alloys (an exception is the dispersoids formed in AlMn alloys). The strength may in fact decrease during heat treatment due to the removal of solute atoms. The alloy systems belonging to this class are the AA1xxx system (commercially pure with small amounts of mainly Fe and Si), the AA3xxx system (as AA1xxx with manganese and magnesium additions), the AA5xxx system (as AA1xxx with magnesium addition) and the AA8xxx system (as AA1xxx, but with higher alloy additions).

The strength of these alloys depends strongly on the content of alloying elements. In fig. 2.1 the ultimate tensile strength of a number of commercial non-heat treatable alloys are shown as a function of the amount of alloying elements. An interesting observation is that the tensile strength is approximately linearly dependent on the total alloying addition in wt%, irrespective of element type, and follows the simple equation given in fig. 2.1. It is here distinguished between the O-temper, i.e. annealed condition, and the H18/H38 condition, i.e. cold rolled or cold rolled and stabilised, of the same alloys, which shows the large work hardening potential in these alloys. The dotted and the full lines indicate the difference between the alloys where solution hardening is most important (AA5xxx) and where the particle hardening dominates (AA1xxx, AA8xxx). In the AA3xxx alloys the strength results from both Mn and Mg in solid solution and particles/dispersoids.

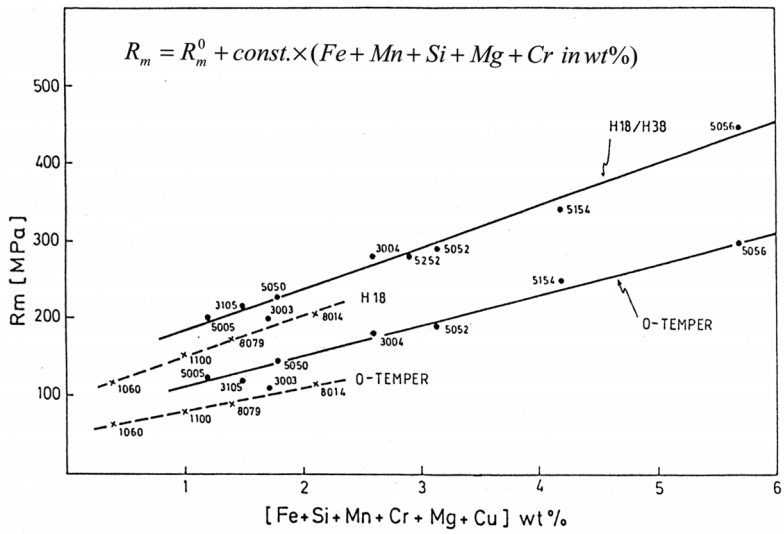

Figure 2.1: The ultimate tensile strength as a function of alloying additions for a wide range of commercial non-heat treatable aluminium alloys. Both O-temper and cold rolled conditions of the same alloys are plotted. (Aluminium Standards and Data 1986)

Solid solution hardening is treated in more detail in section 2.3, and particle hardening in section 2.4.

2.1.2 Heat-treatable aluminium alloys

The heat-treatable aluminium alloys get their strength mainly from precipitate particles, and belong to the AA2xxx, AA6xxx and AA7xxx alloy systems. These alloys are first solution heat-treated, i.e. heated to the single-phase area of the phase diagram where all alloying elements are dissolved into solid solution. A rapid quench freezes the atoms in a supersaturated solid solution (ssss) from where the precipitation sequence starts:

AA6xxx: ssss → GP zones → β'' → $\beta'(Mg_2Si)$ → $\beta(Mg_2Si)$

AA7xxx: ssss → GP zones → η' → $\eta(MgZn_2)$

The precipitation often occurs at room temperature (natural ageing), but an artificial ageing treatment is normally used in order to achieve a stabilised material with as high a strength as possible. Following the sequence from the left to the right, the size of the precipitate increases, and the coherency between the matrix and the precipitate is gradually lost. The maximum strength generally occurs when there is a mixture of coherent and semi-coherent precipitates. An overageing produces stable incoherent

particles, giving a lower strengthening effect. In this work, the alloys are investigated only in the solution heat-treated condition, often referred to as the W-condition.

2.2 Deformation structure and texture

The large plastic deformation that a piece of aluminium is exposed to during rolling or extrusion has great impacts on the microstructure and the crystallographic texture of the material. These changes will influence its mechanical properties, in terms of e.g. strength and anisotropy, and its behaviour during subsequent annealing. In this section a brief overview is given on the current knowledge of deformation structure and texture. It is important to notice, however, that because of the large number of different microstructural features developing during deformation, a unified and complete description of deformation structures has appeared to be difficult to obtain. In many cases the characterisation is a question of definition by the experimentalist.

2.2.1 Dislocation slip and stored energy

The generation and migration of dislocation loops, and the subsequent interaction, storage and recovery of the dislocations are the fundamentals of the evolution of the deformation structure (see e.g. Dieter 1988, Humphreys and Hatherly 1996). Aluminium has a high stacking-fault energy (γ_{sfe}) which makes the dissociation into partial dislocations difficult. Hence cross-slip, and consequently also dynamic recovery, are promoted. In cold forming of aluminium alloys it is a common assumption that all slip occur on the {111}<110> slip systems and that dislocation climb is limited. At higher temperatures however, the existence of non-octahedral slip on the {100}, {110} and {112}-planes is observed (Maurice and Driver 1997). As the slip systems intersect, the mobile dislocations will interact with each other, as well as with obstacles like solute atoms and particles. When the dislocations are stored in the material, they will lead to an increase in the total stored energy:

$$E = \rho\Gamma \tag{2.1}$$

where ρ is the dislocation density and Γ is the line tension of dislocations which is estimated to

$$\Gamma \approx \frac{Gb^2}{2} \tag{2.2}$$

But the system will, as any other system, try to minimise its energy. For the case of aluminium this can be achieved either by organising the dislocations into low-energy configurations, or through dynamic recovery processes where dislocations annihilate each other.

An important aspect is that cold deformation of metals normally is considered to be limited to the temperature regime of $<0.3T_m$, which for aluminium is below 6°C. For most practical applications, cold rolling is performed at room temperature, and due to the plastic work the temperature in the material will rise. So what is generally referred to as cold rolling therefore involves temperatures well above $0.3T_m$. Thus cold rolling of aluminium is associated with thermally activated processes, and a considerable amount of dynamic recovery involving both cross-slip and climb of dislocations is expected. This is particularly true for commercial cold rolling, where the temperature of the sheet may reach 100-150°C due to the strain rates being of the order 50-100.

2.2.2 Grain subdivision

During most deformation processes the original grains in a material will be extensively subdivided. New boundaries are introduced separating volume elements by a misorientation between their lattice orientations. A range of misorientations arises and the spacing of the boundaries are continuously decreased as deformation proceeds.

An extensive study of the boundary spacing was provided by Gil Sevillano et al. (1980). They collected cell size data from a range of materials, normalised them to the cell size

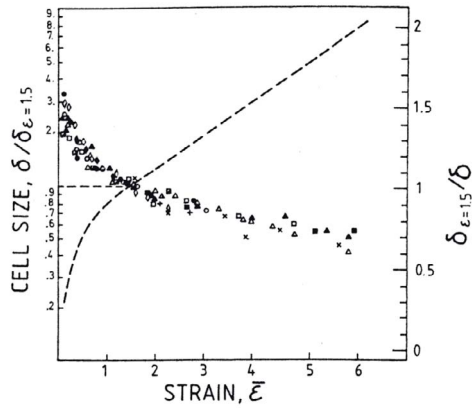

Figure 2.2: Cell size normalised to ε=1.5 for a range of materials. Broken line shows $1/\delta$ vs strain. (Gil Sevillano et al. 1980)

at ε=1.5 and plotted them against the strain. Fig. 2.2 shows that the evolution in cell size with strain is similar for all the investigated alloys, and that the size decreases continuously up to very large strains. Also plotted in the diagram is the inverse of the cell size, which shows a linear dependence on strain above ε=1.

Also the boundary misorientation changes significantly during deformation, and various authors have reported a range of misorientation results. A collection of reported misorientations are given in fig. 2.3, and suggests something between a saturation at about 2-3° and a continuous development (Furu et al. 1995, Furu et al. 1996, Sæter 1997, Nes et al. 1982, Schuh and von Heimendahl 1987, Forbord 1999).

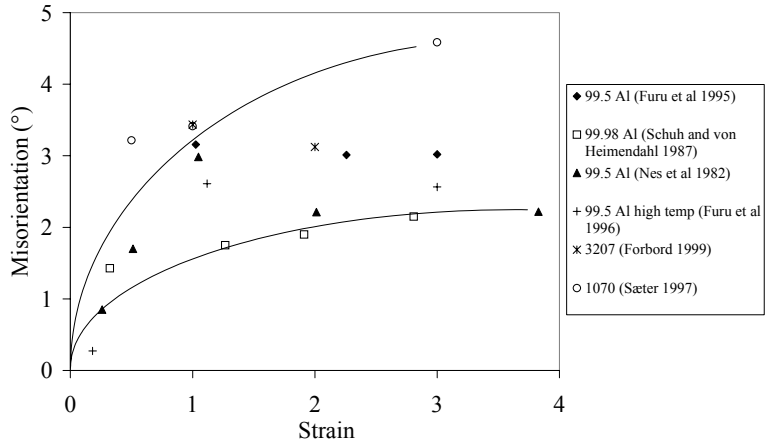

Figure 2.3: Evolution in subgrain misorientation with strain reported by several authors.

Recently, a group at Risø National Laboratory has given a very detailed description of deformation structures, e.g. Hansen (1990), Bay et al. (1992a), Bay et al. (1992b), Liu et al. (1998) and Hughes and Hansen (2000). These works are dealing with cold rolled pure aluminium and nickel (which in this context is very similar to aluminium in terms of crystal structure and stacking fault energy, and hence also deformation structure). An overview of some of their observations and considerations is given in the following.

Their description starts with the assumption that within one grain the combination and number of simultaneously active slip systems vary from place to place. The number of active slip systems at each location is generally lower than the five predicted by the Taylor theory (see section 2.6.2), as this is energetically favourable. Thereby, the grain starts to subdivide into volume elements. Within one element the slip pattern is different from

the neighbouring elements, but collectively they fulfil the Taylor requirement for strain accommodation.

The volume elements correspond to an experimentally observed feature denoted *cell block* (CB) which, as the name indicates, consists of a number of adjacent cells. The boundaries between neighbouring CBs arise out of geometrical necessity, as the selection of slip systems is different on either side of them. Hence, they are termed *geometrically necessary boundaries* (GNBs). Several types of GNBs are described, e.g. *dense dislocation walls* (DDWs), observed at small to moderate strains, and *laminar boundaries* (LBs), separating flat elongated CBs at large strains. *Microbands* (MBs) are plate-like zones bounded by dislocation sheets which tend to develop from the DDWs, and thereby separate CBs. Within the CBs there are *cells* separated by cell boundaries. These boundaries are formed through mutual trapping of mobile and stored dislocations, and thereby they are termed *incidental dislocation boundaries* (IDBs). A schematical illustration of the cells, cell blocks, GNBs and MBs at a moderate strain level is given in fig. 2.4.

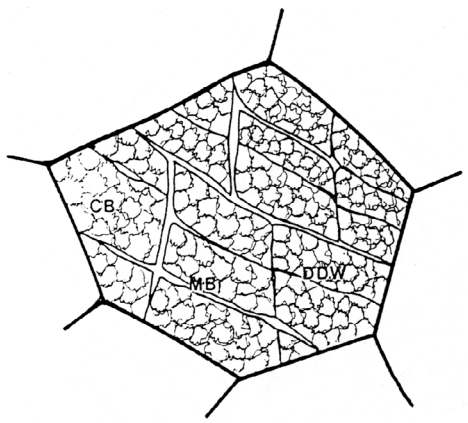

Figure 2.4: Schematical drawing of the early deformation structure in a cell-forming metal. (Hughes 1993)

The grain subdivision starts during the early stages of deformation, and already after 10% cold rolling a well-developed cell block structure has evolved in favourably oriented grains (Liu et al. 1998). At small to moderate strains (up to ε=0.7) most of the GNBs are DDWs and MBs. The majority of them are inclined to the rolling direction by an angle of approximately 40°. A schematical presentation of the substructure at 30% and 50% rolling reduction is shown in fig. 2.5 (a, b).

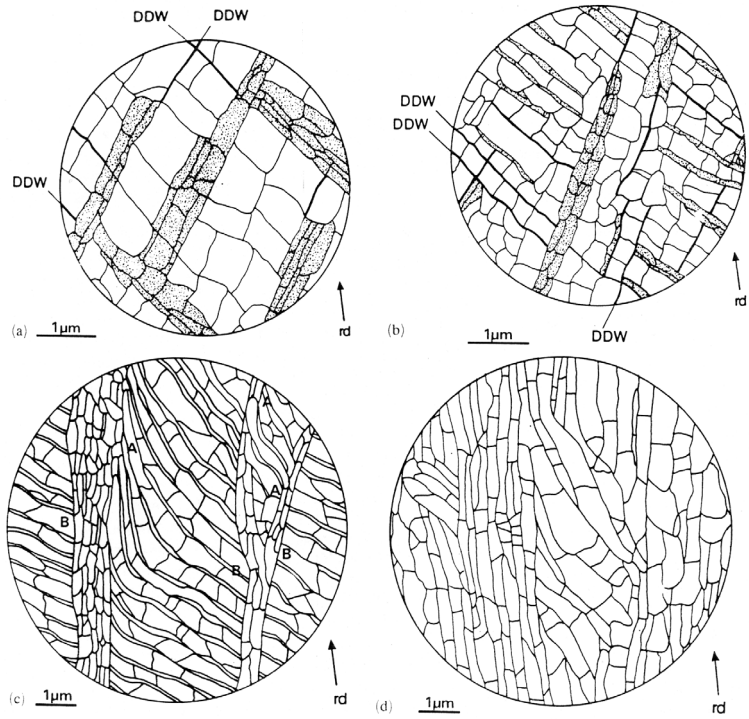

Figure 2.5: Schematical illustration of the changes in substructure during cold rolling. (a) 30% cr (ε=0.36) (b) 50% cr (ε=0.69) (c) 70% cr (ε=1.2) (d) 90% cr (ε=2.3). In (a) and (b) the DDWs are drawn as thick lines and the MBs are dotted. (Bay et al. 1992b)

At higher rolling reductions (ε>0.7) layers of elongated cells or subgrains are formed. The subgrains are grouped in bands of a lamellar structure nearly parallel to the rolling direction. A lamella is essentially a cell block with only one subgrain between its boundaries. The GNBs of this structure therefore appear as lamellar boundaries (LBs), see fig. 2.5 (c, d).

The spacing of both GNBs and IDBs decrease with increasing deformation. Obviously the GNB spacing is larger than the IDB spacing, but the difference diminishes at large strains as the cell blocks finally contain only one cell across its width. This is shown in fig. 2.6 for small to moderate strains in aluminium, and in fig. 2.7 for a wide strain range in nickel. Also the variation in the misorientation across GNBs and IDBs with strain is shown in fig. 2.7. The GNB misorientation is higher and increases more rapidly with strain as compared to the IDBs. While the IDB misorientation increases slowly to about 3° at large strains, the GNB misorientation increases up to 15-20°. Eventually, the GNBs

turn into high-angle boundaries (>15°), and no saturation in the misorientation is observed for these boundaries.

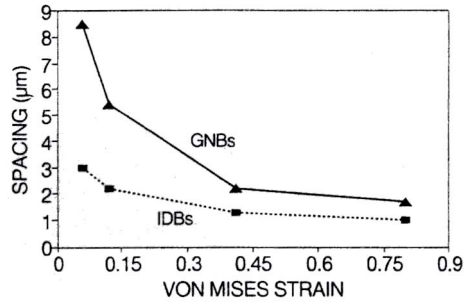

Figure 2.6: Spacing of GNBs and IDBs as a function of strain in pure aluminium. (Liu et al. 1998)

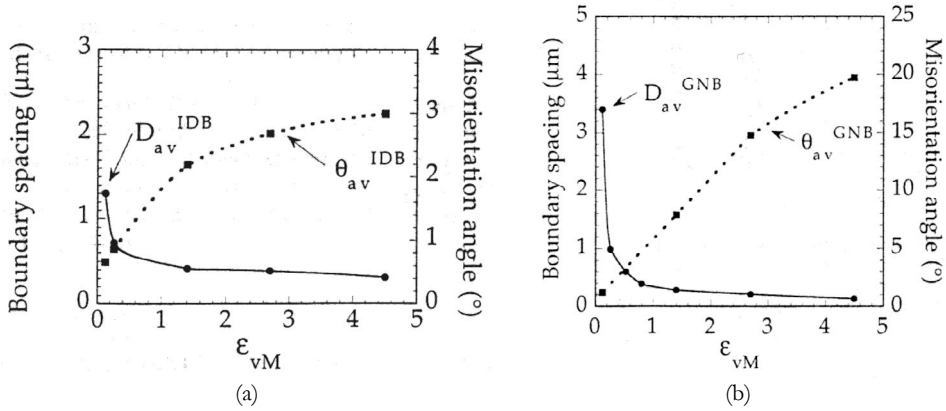

Figure 2.7: Boundary spacing (D) and misorientation (θ) as a function of strain in pure nickel. (a) Geometrically necessary boundaries, (b) incidental dislocation boundaries. (Hughes and Hansen 2000)

2.2.3 Alloying effects on subdivision

Solute atoms

Not all materials build up a well-defined cell structure as described in section 2.2.2. By introducing a considerable amount of solute atoms to an alloy, the friction stress is increased and the dislocation mobility reduced due to solute-dislocation interactions (see section 2.3). This causes large constraints on the dislocation rearrangement, which is essential in the creation of cell boundaries. Instead, a different dislocation structure evolves, known as a Taylor lattice (e.g. Hughes 1993). A Taylor lattice consists of uniform arrays of edge dislocations along the primary slip planes. It is characterised by a

nearly uniform distribution of dislocations, multiple Burgers vectors of dislocations within the array and the organisation of dislocations along {111}-planes. So instead of clustering the dislocations to minimise their energy such as in cell walls, they organise into arrays of alternating sign, a process that also lowers their energy.

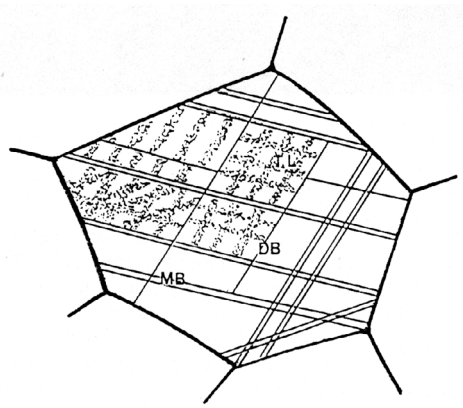

Figure 2.8: Illustration of the grain subdivision in a non-cell forming alloy. TL: Taylor lattice, DB: domain boundary, MB: microband. (Hughes 1993)

The Taylor lattice is an incidental dislocation structure, i.e. the dislocations are trapped incidentally, or statistically. On a larger scale, geometrically necessary boundaries are created in order to account for the variations in selection of slip system between neighbouring volumes. This is analogous to the DDWs appearing in cell-forming metals described in the previous section. However, in non-cell forming alloys they appear as domain boundaries (DBs). The difference between DBs and DDWs is that DBs are parallel to the {111} slip planes. Microbands also appear frequently in non-cell forming alloys (Korbel et al. 1986). These microstructural features are illustrated schematically in fig. 2.8. Note the difference between this subdivision pattern and the one in cell-forming metals in fig. 2.4.

Non-deformable particles

When a matrix containing hard second phase particles is deformed, strain incompatibilities arise around the particles. In order to account for this geometrical effect, an arrangement of geometrically necessary dislocations have to be introduced (Ashby 1971). This results in the occurrence of deformation zones around the particles, as illustrated by fig. 2.9 (a). The deformation zones consist of small subgrains that build up an orientation gradient between the particle surface and the matrix, see fig. 2.9 (b). It

is found that the misorientation increases with both strain and particle radius (Humphreys and Hatherly 1996). Additionally, the presence of second phase particles is observed to increase the overall dislocation density and to reduce the average subgrain size.

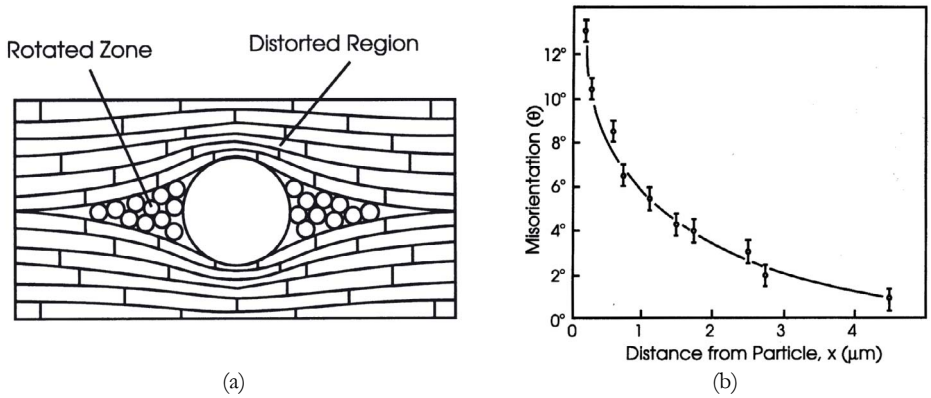

Figure 2.9: (a) Sketch of a deformation zone around a particle in a rolled polycrystal. (b) Lattice misorientation as a function of distance from the particle. (Humphreys and Hatherly 1996)

2.2.4 Dislocation density in the subgrain interior

As mentioned earlier, dislocation loops are generated and expanded during deformation. A large number of these dislocations are used to build up sub-boundaries, but some of them will be stored as a 3-D network in the subgrain interior instead. Even an annealed metal will contain a considerable amount of dislocations, typically 10^{10}-10^{12} m^{-2} (Dieter 1988), but the density increases rapidly, and a severely cold worked material may have an overall dislocation density of up to 10^{16} m^{-2}. It was observed by Nord-Varhaug et al. (2000) that the density of dislocations inside the subgrains saturated in the early stage of deformation. Fig. 2.10 shows a constant dislocation density of around 10^{14} m^{-2} in the strain range of ε=0.03-2 for two commercial aluminium alloys. The density was somewhat higher in the AA3207 alloy, containing 0.4 wt% Mn, than in the more pure AA1050.

This is consistent with the observations in the classical work of Langford and Cohen (1969), where iron was wire-drawn to very large strain. They concluded that most of the dislocations were confined to cell walls and that the density within the cells was comparatively low.

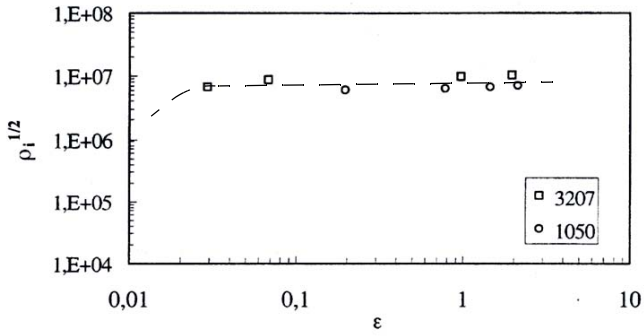

Figure 2.10: Density of dislocations inside the cells/ subgrains of the commercial alloys AA1050 and AA3207, covering a wide strain range (Nord-Varhaug et al. 2000)

2.2.5 Shear banding

Shear bands are narrow regions of intense shear and are a kind of plastic instability. They appear in materials subjected to heavy deformation, such as cold rolling. The bands are non-crystallographic, and in a rolled sheet they are normally aligned about ±35° to the rolling direction and parallel to the transverse direction. Often they intersect several grains and may cross a whole plate leading to failure.

Shear bands have been observed in high-purity aluminium rolled at room temperature. But it is upon the addition of magnesium that shear banding really becomes frequent. The mechanisms involved in shear banding are not fully understood, but Dillamore et al. (1979) analysed the phenomenon in terms of a plastic instability. In plane strain compression, or rolling, the condition for this instability is written as:

$$\frac{1}{\sigma}\cdot\frac{d\sigma}{d\varepsilon} = \frac{n}{\varepsilon} + \frac{m}{\dot{\varepsilon}} + \frac{1+n+m}{M}\cdot\frac{dM}{d\varepsilon} - \frac{m}{\rho}\cdot\frac{d\rho}{d\varepsilon} < 0 \qquad (2.3)$$

where n and m are the strain hardening and strain rate exponents, ρ is the dislocation density and M is the Taylor factor. It follows that instability is favoured by a negative strain rate sensitivity (m), which is the case in AlMg alloys, and a negative $dM/d\varepsilon$. The latter term corresponds to geometric softening, i.e. that instability is favoured if it causes a lattice rotation into a softer orientation.

A more recent contribution to the knowledge of shear banding has been provided by Inagaki and Kohara (1997). They studied the shear banding in polycrystalline binary AlMg alloys with 0.5-5% Mg, given cold rolling reductions up to 95%. The shear band

density increased with both Mg-content and strain, and a critical concentration between 2 and 3% Mg was experienced, above which shear bands formed readily.

The suggested mechanism is that stress concentrations and misfit strains arise at the grain boundaries, and thereby lead to the formation of offsets on the boundaries, see fig. 2.11 (a). It was observed that shear bands grew out of these offsets, and hence the grain boundaries served as nucleation sites for the bands (fig. 2.11 (b)). This effect is enhanced by the presence of Mg-atoms, as they suppress the dislocation movement and give an even more inhomogeneous deformation. However, the orientation difference between the grains on each side of the boundary influences the misfit strain and plays an important role in the formation of offsets. Therefore, not all boundaries are able to nucleate shear bands.

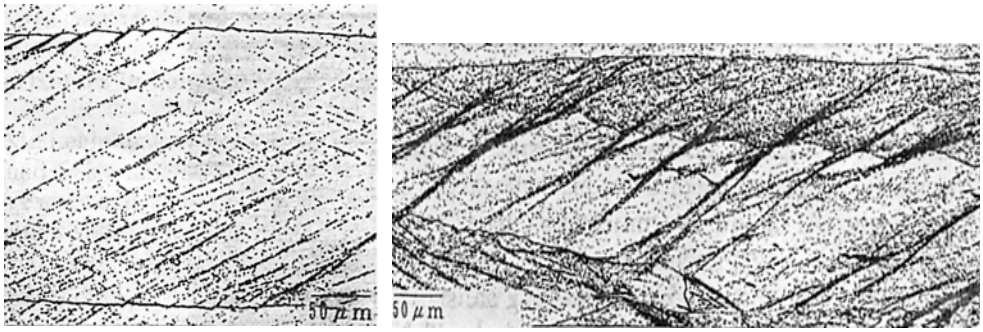

(a) (b)

Figure 2.11: (a) Formation of offsets on a grain boundary in AlMg5, c.r. 50%. (b) Shear bands crossing a grain boundary after c.r. 70%. (Inagaki and Kohara 1997)

The mechanism described above applies only to alloys with more than 2.5% Mg. The low-Mg alloys, on the other hand, did not form any offsets on the grain boundaries. Instead, shear bands were formed by necking of elongated grains. After large rolling reductions the internal stress state varies considerably along the length of a grain, leading to subdivision of the grain and diffuse and localised necking. This mechanism depends on the thickness of the grains, with necking occurring easily in thin grains.

It is suggested by Inagaki et al. (2002) that shear banding may be one of the methods to accommodate strain in hard oriented grains. Material softening has also been related to shear banding (Harren et al. 1988). Geometrical softening, caused by non-uniform lattice

reorientation, influences the localisation process, as channels of softened material and concentrated strain are formed.

The shear banding is also associated with a negative strain rate sensitivity, caused by solute-dislocation interactions which hinder the dislocation mobility (see section 2.3.3). Lloyd (1986) observed a lesser extent of shear banding at low temperatures (77K) and high temperatures (473K) than at room temperature in an AlMg4.5 alloy. Only in the ambient temperature regime, corresponding to the dynamic strain ageing regime, shear banding was extensive.

2.2.6 Rolling type texture

Cold rolling of medium to high-SFE fcc metals, like aluminium alloys, generally leads to an assembly of orientations along two fibres, see fig. 2.12:

- The α-fibre, running from the Goss orientation G={011}<100> to the Brass orientation B={011}<211>. This fibre exists mainly at low degrees of rolling.
- The β-fibre, running from the Copper orientation C={112}<111> through the S-orientation S={123}<634> to the Brass orientation B={011}<211>

The rolling texture can thus be presented by plotting the maximum orientation density, $f(g)$, against the φ_2 angle along the β-fibre. Fig. 2.13 (a) shows such a plot for a quenched alloy cold rolled to various deformation levels. The orientation densities are seen to increase with strain, as a larger and larger fraction of the material rotates into these stable texture components. This rolling-type texture in aluminium is in the literature often referred to as the pure metal or Copper type texture. Rolling and extrusion at elevated temperatures result in a somewhat different texture, known as the Brass-type texture. This is, as the name indicates, characterised by a dominant Brass component (Hirsch 1990, Humphreys and Hatherly 1996).

Alloying elements will affect the rolling texture to some extent, and for this reason a variety of aluminium alloys were investigated and classified by Lücke and Engler (1990). Some of their conclusions were:

- Pure metals: The deformation is homogeneous and mainly C and S texture is created.
- Solid solutions:
  (i) Low deformation: Similar to pure metals.

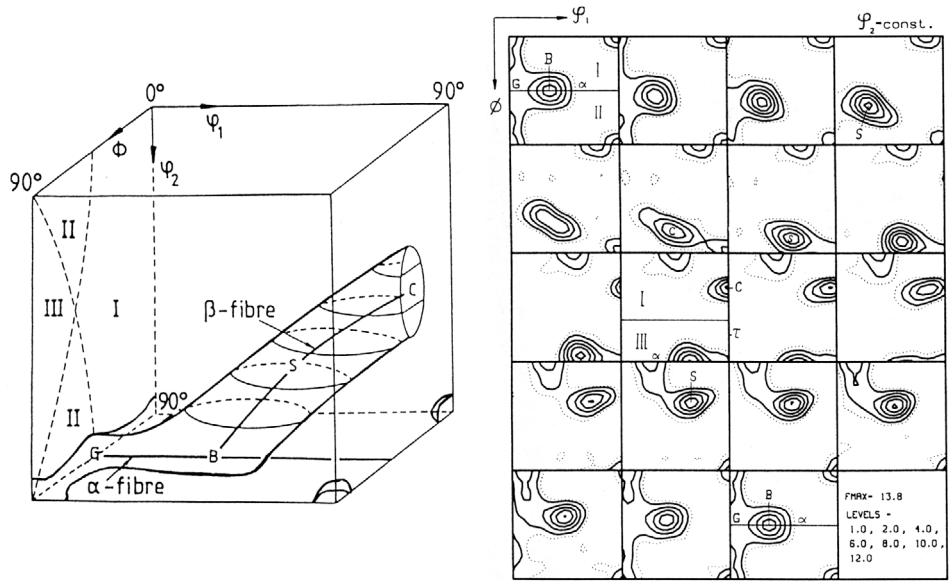

(a) (b)

Figure 2.12: (a) Schematic representation of one branch of the fcc rolling texture in three-dimensional Euler space (ODF). (b) The Euler space represented in sections of constant φ_2. The ideal positions of the texture components (G, B, C and S) are given. (Hirsch 1990)

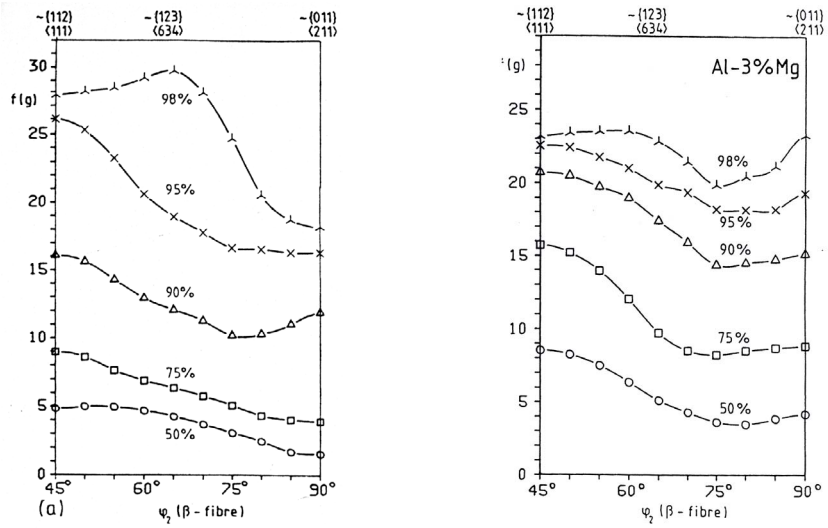

(a) (b)

Figure 2.13: β-fibre density plots after different amounts of cold rolling. (a) A quenched AlCu1.8 alloy (supersaturated solid solution). (b) An AlMg3 alloy that forms shear bands at the largest rolling reductions. (Lücke and Engler 1990)

(ii) High deformation: Shear banding occurs, and an increase in G and B texture is observed (see fig. 2.13 (b)).

- Non-shearable, medium sized particles (0.1-5 μm): The deformation is homogeneous and an enhanced texture development with preferred C texture is observed.

The last observation is, according to the authors, rather surprising, as the deformation zones around the particles would be expected to "randomise" the texture. In alloys with a high amount of larger particles (>5 μm) the deformation zones occupy a large part of the total volume, and in these alloys the texture is weakened. In alloys with only medium sized particles, on the other hand, the volume of the zones is rather small. The effect of this kind of particles is that they cause a reduction in the slip length of the dislocations. This leads to a more homogeneous deformation and an enhanced texture development.

The influence of such particles is similar to that of reducing the grain size. The grain subdivision is less pronounced in fine grained materials, and slip is therefore more homogeneous than in a coarse grained material. Hence, the development of a rolling texture is more rapid in a fine grained material, see fig. 2.14.

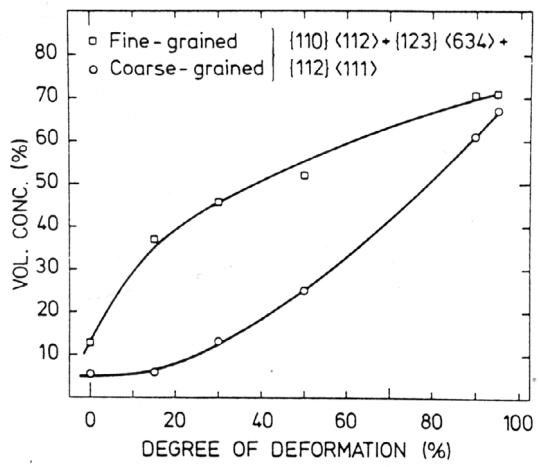

Figure 2.14: Development of rolling texture (sum of C, S and B density) in fine-grained and coarse-grained pure aluminium (50 and 300 μm, respectively). (Hansen 1990)

Concerning the influence of solid solution alloying, the effect of Mg-additions is explored systematically by Koizumi et al. (2000). They measured the texture after 95% cold rolling of binary AlMg alloys, ranging from 0% to 9% Mg. The orientation density

of the three rolling texture components C, S and B were plotted as a function of the Mg concentration, see fig. 2.15. An overall trend is that the texture is weakened by additions of Mg. Especially the S-orientation seems unstable upon alloying, and this was attributed to an orientation dependence of solution hardening. Below 3% Mg no shear banding was observed, and hence most of the texture changes in region 1 are caused by anisotropic solution hardening. The density of the Brass-orientation, however, increases considerably from 3 to 5% Mg (region 2) at the expense of the Copper and S-orientations. With such Mg-concentrations the materials exhibit frequent shear banding, and it is evident that the shear banding enhances the development of the Brass component.

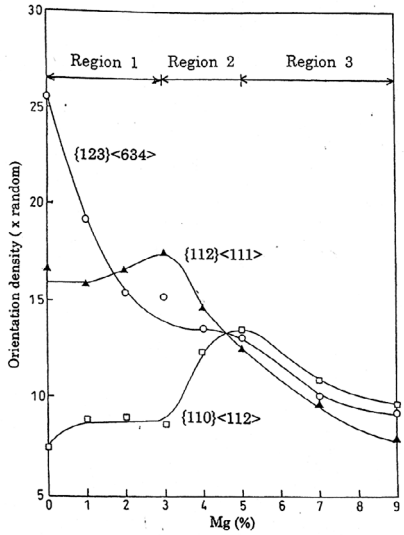

Figure 2.15: Effect of Mg content on the orientation density of rolling texture components after 95% c.r. {112}<111>=C, {123}<634>=S and {110}<112>=B. (Koizumi et al. 2000)

The mechanism is suggested to be as follows (Koizumi et al. 2000): Shear bands are formed only in grains having orientations between C and S, and since the volumes of the bands are rotated away from the parent orientation, the density of C and S-grains will decrease. Furthermore, the material within the shear bands in Copper oriented grains tend to rotate into the metastable Goss orientation, and finally into the Brass orientation. Frequent shear banding thus results in a decrease of C and S, and an increase in B. If the density of shear bands becomes so high that a large volume fraction of the material is occupied by intersecting bands, then the development of a normal rolling texture

becomes difficult. This corresponds to region 3 in fig. 2.15, where the texture is randomised with increasing Mg concentration. The β-fibre is quite uniform in region 3, with *f(g)* being almost equal for the C, S and B.

2.3 Solid solution strengthening and related phenomena

2.3.1 Yield stress and work hardening rate

The introduction of foreign atoms into a crystal lattice invariably increases the strength of the material. Some examples are carbon in iron (steel), zinc in copper (brass), and magnesium in aluminium. This was clearly seen in fig. 2.1 where the strength of aluminium alloys increased upon the addition of magnesium and manganese as alloying elements. Most solute elements in aluminium are present as substitutional atoms, i.e. they occupy the position of an aluminium atom in the lattice. Substitutional alloying requires that the atomic size of the alloying element is roughly similar to the atomic size of aluminium. Sherby et al. (1951) explored the effects of several such alloying elements on the properties of binary aluminium alloys. Magnesium was one of them, and the flow curves of five different alloys, ranging from 0 to 3.2 at% Mg, tested at room temperature and at -195°C, are seen in fig. 2.16. Both the initial yield stress and the rate of work hardening increased with increasing magnesium additions. The great effect of temperature on the properties is also apparent from these results.

Direct solid solution effects

The solid solution strengthening is a result of the interaction between mobile dislocations and the solute atoms. The isolated atoms are centres of elastic distortion, and the atoms and dislocations will therefore interact elastically and exert forces on each other, fig. 2.17 (a). These direct interactions can be subdivided into two groups (Haasen 1996):

- Dislocation friction: Stationary solute atoms act on mobile dislocations.
- Dislocation locking: Solute atoms collect at dislocations at rest.

The friction due to solute atoms increases the already existing friction stress in a pure crystal (the Peierls-Nabarro stress). The effect is a shift of the whole stress-strain curve to higher stresses. A number of locking mechanisms have been suggested (see e.g. Dieter 1988, Haasen 1996). However, the most relevant mechanisms for substitutional alloying

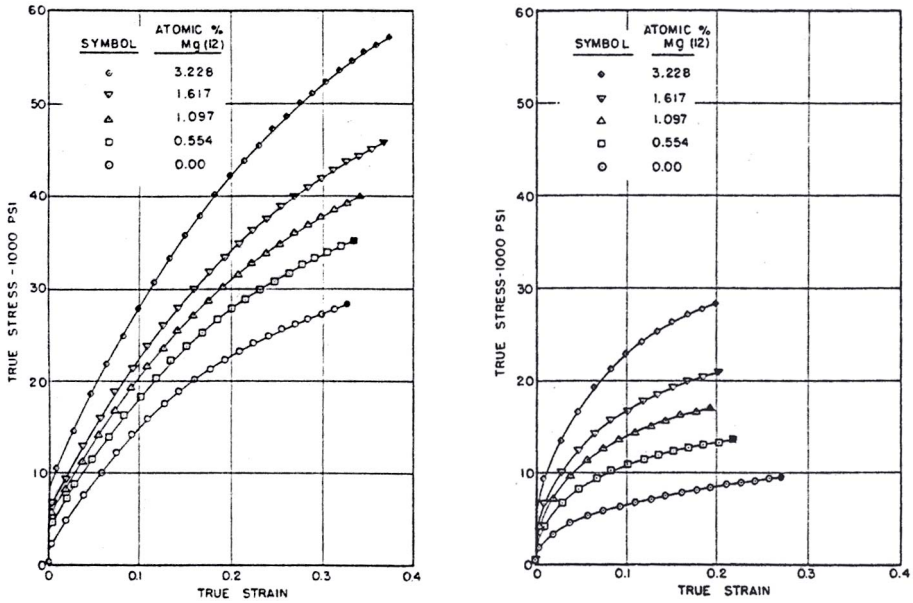

Figure 2.16: Effect of magnesium on the stress-strain behaviour of aluminium at (a) -195°C and (b) 20°C. (Sherby et al. 1951)

of aluminium are the elastic interactions due to the size misfit and modulus misfit between solute atoms and solvent atoms.

(i) Size misfit: When the size of a solute atom differs from the size of the matrix atoms, a strain field is created around the atom, see fig. 2.17. An edge dislocation has a hydrostatic strain field around its core, and when the dislocation passes close to the solute atom, an interaction energy arises between the two strain fields. A size misfit parameter, or the rate of lattice expansion, is given by:

$$\varepsilon_b = \frac{1}{a} \cdot \frac{da}{dc} \tag{2.4}$$

where a is the lattice constant of an alloy with concentration c. The maximum force by this interaction is given by (Mitchell 2001):

$$F_b \approx Gb^2 \varepsilon_b \tag{2.5}$$

(ii) Modulus misfit: The difference in the elastic modulus between the solute atoms and the matrix atoms results in a different bonding around the solute. This creates a hard or

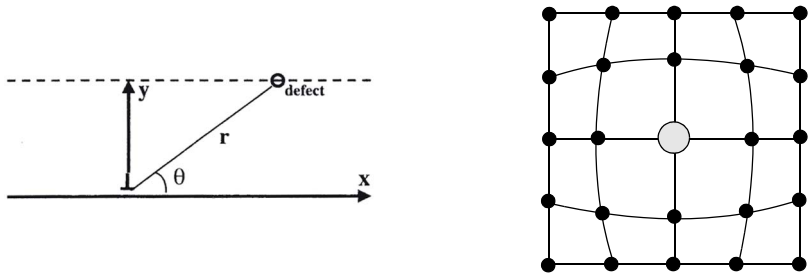

(a) (b)

Figure 2.17: (a) A dislocation passing an atomic-size defect, e.g. a solute atom. (Mitchell 2001) (b) Schematic illustration of the strain field around a solute atom larger than the matrix atoms.

soft "spot" of volume b^3 in the matrix which leads to an elastic interaction with mobile dislocations. Both edge and screw dislocations feel this misfit, given by the modulus misfit parameter:

$$\varepsilon_G = \frac{1}{G} \cdot \frac{dG}{dc} \tag{2.6}$$

The maximum force by this interaction mechanism is given by (Mitchell 2001):

$$F_G \approx \frac{Gb^2}{60} \varepsilon_G \tag{2.7}$$

In a statistical treatment of these interaction mechanisms, where the alloy was considered as a concentrated solution of weak obstacles, they were shown to add up to an effective interaction force (Haasen 1996):

$$F_{eff} = Gb^2 \sqrt{\varepsilon_b{}^2 + \alpha^2 \varepsilon_G{}^2} \tag{2.8}$$

where α is a constant. In this lies that the solute atoms may act on the dislocations with both repulsive and attractive forces. One assumption that is made is that only the atoms adjacent to the slip plane are of importance.

Several authors have reported correlations between the flow stress and the alloy concentration. There seems to be a general agreement that single crystals of fcc substitutional solid solution follow a $c^{2/3}$ dependence (Mitchell 2001), i.e.:

$$\tau = \tau_0 + k \cdot c^{2/3} \tag{2.9}$$

Indirect solid solution effects

The friction and locking described above relate to the interactions between solutes and dislocations. Additionally, the presence of solute atoms leads to a higher net storage rate of dislocations since the recovery rate is low due to the limitations on cross-slip. The result is a higher dislocation density and a different dislocation structure (see section 2.2.3 on the formation of Taylor lattices), giving an increased substructure strengthening, see section 2.5.2. This can be regarded as an indirect solid solution hardening effect.

2.3.2 Yield point phenomenon

A number of metals exhibit a localised, inhomogeneous yield point as illustrated in fig. 2.18 (a). The phenomenon is a result of the formation of Lüders bands at the onset of plastic flow, i.e. at the upper yield point. The load then drops, and as the bands propagate along the specimen, an elongation of the yield point occurs. When the entire gauge length is covered by the bands, the load increases again as normal.

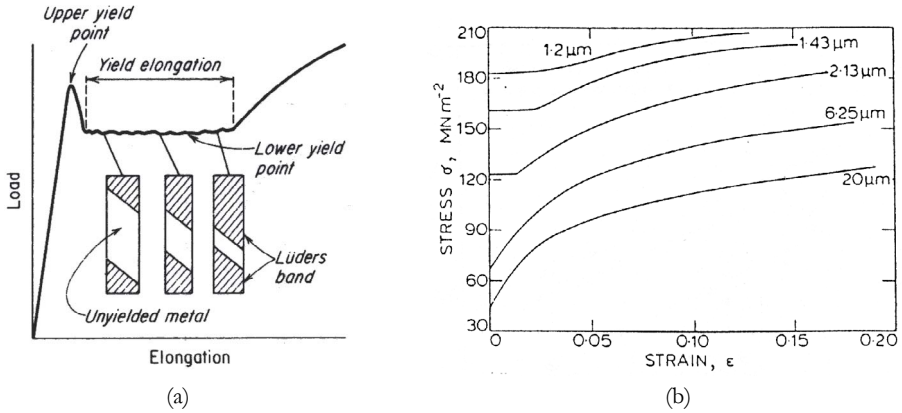

Figure 2.18: (a) Yield point phenomenon and Lüders band. (Dieter 1988) (b) Stress-strain curves for various grain sizes of AlNi6 showing yield point phenomena. (Lloyd 1980a)

Lüders banding is associated with a restriction on the generation and mobility of dislocations. At the yield point, plastic deformation normally starts with dislocation slip. However, if the dislocations are locked in some way, the stress will continue to increase even though the elastic limit of the material is passed. The presence of solute atoms are known to cause this effect as they pin the dislocations at rest (Dieter 1988, Lloyd 1980b). The yield point occurs by unlocking the dislocations at a high stress, or by creating new

dislocations at points of stress concentration. When the dislocations eventually start moving, they move fast and result in a yield drop.

In addition to the solute effect, a reduction in grain size will also give inhomogeneous yielding, see fig. 2.18 (b), where an AlNi6 alloy processed to a wide range of grain sizes were tensile tested (Lloyd 1980a). The effect was attributed to the shortage of mobile dislocations caused by an absence of easily operated dislocation sources. Observations of the ultra fine-grained aluminium alloys showed that the dislocations during deformation tended to concentrate around grain boundaries, indicating inhomogeneous flow.

2.3.3 Strain ageing and serrated yielding

A deformation behaviour often observed in alloys exhibiting yield point phenomena, is the Portevin-LeChatelier effect. It appears as serrations on the stress-strain curve and is caused by dynamic strain ageing. The solute atoms are able to diffuse faster than the velocity of the dislocations. The dislocations are pinned by the solutes in a "catch-and-lock" mechanism, and in order to be released, the load must increase. When they are torn away from the solute atoms due to the stress increase, a sudden load drop occurs. As this happens many times during deformation, the stress-strain curve becomes serrated (Dieter 1988).

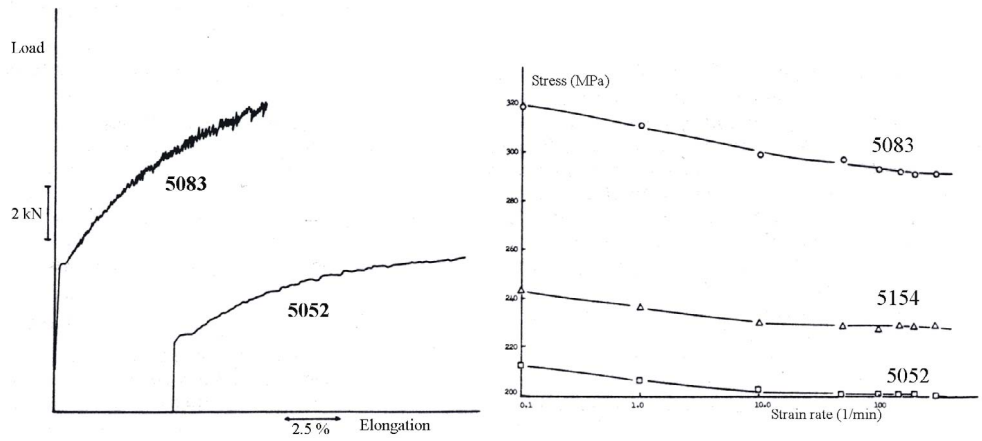

Figure 2.19: (a) Stress-strain behaviour of two AlMg alloys with Lüdering and DSA. (b) Effect of strain rate on the ultimate tensile strength. 5052: 2.34% Mg, D=9 μm. 5154: 3.31% Mg, D=30 μm, 5083: 4.46% Mg, D=12 μm. (Lloyd 1980b)

Dynamic strain ageing (DSA) depends on the temperature and the strain rate, and is associated with a negative strain rate sensitivity. A high strain rate will make it difficult for the atoms to catch the dislocations in time. Hence, the strength will be reduced as the strain rate increases, and a negative strain rate sensitivity is the result, see fig. 2.19 (b). A high temperature will give faster diffusion of solute atoms. On the other hand, if the temperature is too low the diffusivity will be so slow that no flux to the dislocations will occur. Thus, the strain rate sensitivity is negative and DSA occurs only in a limited temperature regime. Serrations are observed in AlMg alloys deformed at room temperature, fig. 2.19 (a). This indicates that the diffusivity of Mg is sufficient at room temperature. The amplitudes of the serrations rank with the amount of Mg in the alloys.

2.4 Particle strengthening

The different types of particles that are present in aluminium alloys can roughly be divided into three groups:

- Primary or constituent particles are formed during solidification or homogenisation. Their radius ranges from about 1 μm and up. The chemical composition depends on the alloy composition and the solidification rate. The particles are hard and not shearable by dislocations.
- Dispersoids are formed, but may also dissolve, during homogenisation. They can also be precipitated during subsequent thermo-mechanical processing. Elements like Mn and Zr precipitate as intermetallic compounds with size 5-200 nm. The dispersoids impose a Zener drag on grain boundaries and prohibit recrystallisation and grain growth. They are hard and not shearable.
- Precipitates: Formed by solution heat-treatment followed by ageing, see section 2.1.2. Except for the overaged incoherent phases, precipitates are small (from a few Å to some hundred nm) and are shearable by dislocations.

For the alloys in part A of this work, only non-shearable particles are of interest. Their contribution to the mechanical properties can be analysed in terms of the Orowan mechanism, sketched in fig. 2.20. A dislocation passing two particles of separation λ will bow out. At stage 3 it has reached its critical curvature, and when the segments meet on the other side they have opposite sign and leave a loop around the particle (4). The dislocation is then free to move on. For each dislocation passing a particle, a loop is added, causing a rapid substructure strengthening of the matrix. Such loops are,

however, only observed at very small strains (<2%). At larger strains, deformation zones with higher dislocation densities and smaller subgrains are formed (section 2.2.3).

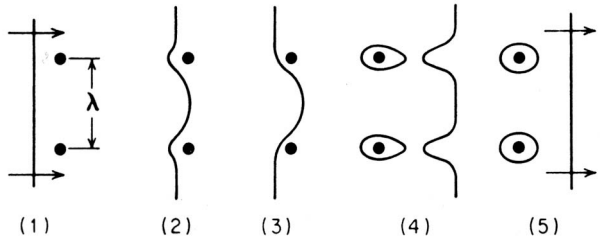

Figure 2.20: Sketch of a dislocation passing two hard particles, based on the Orowan mechanism. (Dieter 1988)

The strengthening produced by second-phase particles is usually additive to the solution strengthening. Suni et al. (1994) discovered these two effect together in an AA3004 alloy over a wide strain range, fig. 2.21. The strength of the alloy was decomposed into a solute component and a second phase component. The second phase contributed substantially to the overall strength, and in the early stage of deformation a rapid increase in this component was observed. After that the second phase contributed by a nearly constant value. The solute component were found to increase with strain because of the strong effect on work hardening.

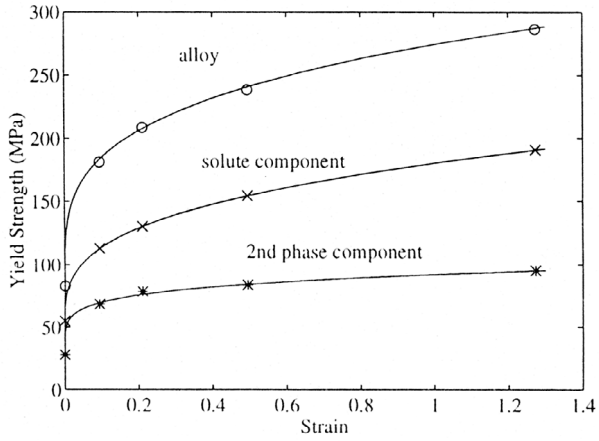

Figure 2.21: Diagram showing the total strength of an alloy (AA3004) decomposed into a solute component and a second phase component. (Suni et al 1994)

2.5 Work hardening

Work hardening, also known as strain hardening or deformation hardening, is a phenomenon where the strength of a material increases during plastic deformation. In this section, first a description of the impacts of work hardening on the material response is given (section 2.5.1). Work hardening is strongly related to the interactions between individual dislocations and between dislocations and barriers in the material. Hence, the work hardening behaviour will depend on the current microstructure, and section 2.5.2 is dedicated to the substructure strengthening. In section 2.5.3 a recently developed model for work hardening is presented.

2.5.1 General description

Stages of work hardening

The work hardening behaviour of a material is most often displayed through its stress-strain curve from which the various stages of work hardening can be identified. Let us first consider a single crystal that is strained in a direction that activates only one slip system, crystal D in fig. 2.22. In the beginning, the deformation occurs by so-called easy glide, represented by stage I in the stress-strain curve. Since the dislocations slip on only one slip system, there are no barriers to dislocation motion other than the internal friction between the atomic planes and any possible pre-existing obstacles. After some deformation, slip will begin to occur on other slip systems as well (multislip), and as the dislocations on intersecting slip planes start to interact with each other, their mobility will be limited and the strength of the material will increase. This stage II of work hardening that we now enter is linear, and it is characterised by a steep rate of order $G/200$. The transition from stage I to II, and the slope of stage II, are strongly dependent on the crystal orientation. If the crystal is oriented so that several slip systems are active from the start, stage I may not even appear, as in crystals A, B and C in fig. 2.22.

During stage II of deformation the dislocation density will increase rapidly. But as the distance between the dislocations becomes sufficiently small, they will start to annihilate each other, or recover. The dynamic recovery phenomenon will reduce the storage rate of dislocations, and the hardening rate decreases. This is pictured by the non-linear region of the stress-strain curve, stage III, in fig. 2.22. Beyond stage III follows a linear stage IV of low hardening rate, fig. 2.23 (a), and in some cases, e.g. in super purity aluminium at room temperature and commercial purity aluminium above around 100°C,

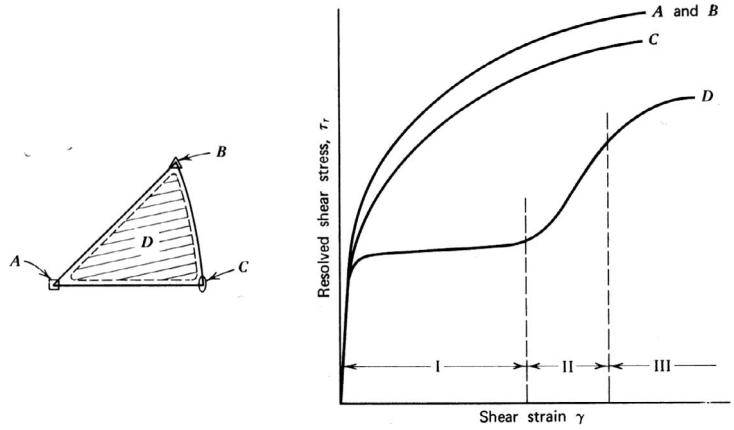

Figure 2.22: Stress-strain curves for single crystals of various orientations. Crystal D, having one active slip system, shows work hardening stages I, II and III. In the multislip orientations A-C, the material goes directly into stage II. (Verhoeven 1975)

a stress saturation (hardening rate=0) is reached. The work hardening behaviour is sometimes presented by the work hardening rate (θ) as a function of stress. Fig. 2.23 (b) shows such a diagram for polycrystals of copper tested in torsion at various temperatures. It is well established that the hardening rate of fcc-metals and alloys increases with decreasing temperature (for a review see Gil Sevillano 1993). θ_{IV} scales with the transition stress τ_{IV} between stage III and IV, i.e.

$$\theta_{IV} = a \cdot \tau_{IV} \tag{2.10}$$

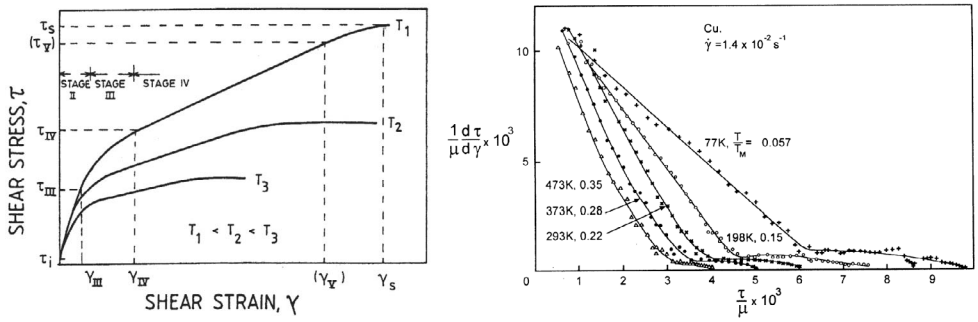

(a) (b)

Figure 2.23: (a) Schematic stress-strain curve at large deformations, showing the work hardening stages II, III and IV, as well as the stress saturation level. (Nes 1998) (b) Work hardening rate as a function of shear stress for Cu polycrystals tested in torsion at various temperatures. (Alberdi 1984, quoted by Kocks and Mecking 2003)

where the scaling parameter a is typically of size 0.1 for fcc-metals.

Polycrystals

In a polycrystal the grains have different orientations and multislip will inevitably occur from the very beginning of plastic deformation. As a consequence of this, stage I is absent in the stress-strain curve of a polycrystal. Another commonly observed difference from the description of single crystals is the non-linearity of stage II. Slip restrictions from grain boundaries and particles will result in a parabolic stress-strain curve:

$$\sigma \propto \sqrt{\varepsilon} \tag{2.11}$$

2.5.2 Substructure strengthening

The substructure of an aluminium alloy may be defined as a mixture of single dislocations and dislocation arrangements (section 2.2). During deformation, interactions with the stored substructure will reduce the mobility of the mobile dislocations. Hence the slip length, i.e. the distance the dislocations travel before they are stored in the material, will be limited by these reactions. As the mobile dislocations are stored, they increase the total dislocation density. The new substructure that is built up will act as barriers to slip, and the slip length is further reduced.

Even an annealed single crystal will contain a large number of dislocations present as a dislocation forest or three-dimensional network. Consider the simple case of a mobile screw dislocation passing through a forest of stored screw dislocations on its slip plane, fig. 2.24. The reaction between the dislocations leaves short edge dislocation segments, or jogs, of length b. If the whole mobile dislocation shall continue to move, these jogs must climb. Climbing requires a generation of vacancies behind the moving jogs, a thermally activated reaction that is difficult at low temperatures. Therefore, the glide of screw dislocations through a dislocation forest is regarded as the speed limiting reaction in cold deformation of aluminium.

It has been known for quite some time that a polycrystal has a higher strength than a single crystal. Furthermore, a fine-grained material is both stronger and more ductile than a coarse-grained material. This is due to the contribution from grain boundaries, which is not only a strengthening effect, but also an effect of distributing slip on different slip systems in neighbouring grains. The simple Hall-Petch relationship (Hall 1951, Petch

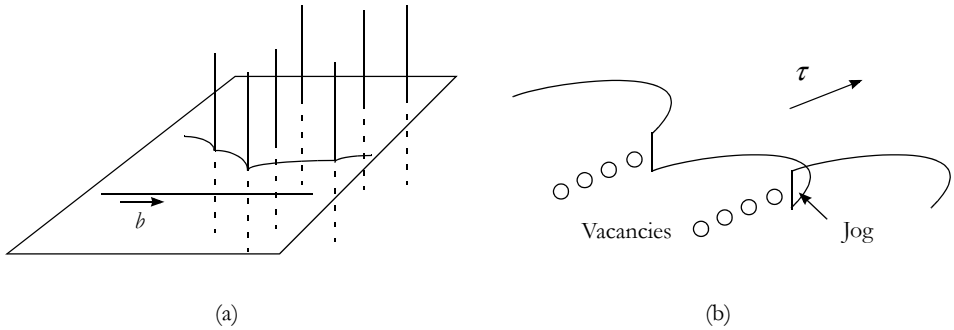

Figure 2.24: (a) A mobile screw dislocation cutting through a forest of stored screw dislocations on a slip plane. (b) After cutting the climbing jogs leave vacancies behind.

1953) is a frequently used expression for the effect of grain size (D) on the yield stress (σ_0):

$$\sigma_0 = \sigma_i + k \cdot \frac{1}{\sqrt{D}} \tag{2.12}$$

σ_i is the lattice friction stress and k is a constant of typical value 0.065-0.07 MPa $\cdot m^{1/2}$ in pure aluminium (Embury 1971, Thompson and Baskes 1973). Alloying elements increase the k-value, and Lloyd (1980a) found k=0.14 MPa $\cdot m^{1/2}$ in an AlNi6 alloy. One physical interpretation of k is that it is a result of slip length restrictions. Grain size effects are further treated in the next subsection.

It has been reported that low-angle boundaries have a similar influence on the yield stress. However, a relation between the flow stress and the subgrain size of the type

$$\sigma \propto \frac{1}{\delta} \tag{2.13}$$

is generally more accepted. Castro-Fernandez et al. (1990), for instance, observed such a relation in a hot worked AlMnMg alloy, and Langford and Cohen (1969) reported the same behaviour in wire-drawn iron, fig. 2.25. In these figures the flow stress of materials subjected to large strains is seen to be proportional to the inverse subgrain size. At such strain levels, stage IV or stress saturation, the dislocation density within the subgrains is constant, see section 2.2.4, and the subgrain size is the only microstructural parameter that varies.

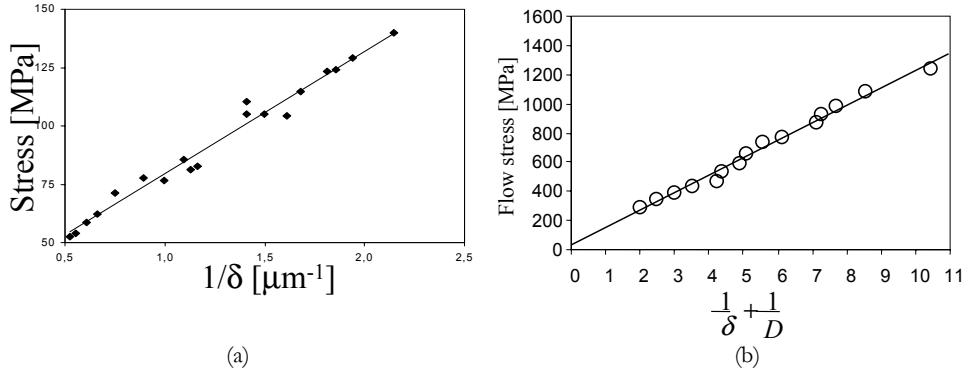

Figure 2.25: Linear relationship between the flow stress and the inverse subgrain size. (a) Hot worked AA3104 (Castro-Fernandez et al. 1990), (b) wire-drawn iron (Langford and Cohen 1969).

2.5.3 Modelling of work hardening

Work hardening is a complex problem, and the establishing of a physically based model and how to solve the problems are still matters of controversy. A common approach is to divide the problem into two. The first problem then relates to how to calculate the critical resolved flow stress for a given microstructure. The second problem is to explain how the deformation history produces this given microstructure. Different schools have approached these problems in different ways, where one major difference pertains to how to describe and characterise the microstructure. A classical approach is to rely on a one-parameter microstructural description. By one-parameter it is meant that during plastic deformation the flow stress is controlled by the average dislocation density (ρ) in the material:

$$\tau = \alpha G b \sqrt{\rho} \tag{2.14}$$

where α is a temperature dependent parameter. A one-parameter model for dislocation storage and dynamic recovery was introduced by Kocks (1976) and further refined by Mecking and Kocks (1981) and Estrin and Mecking (1984). For an extensive recent review, see Kocks and Mecking (2003). The way the dislocations are spatially organised, e.g. in cell structures, is not included in a direct way in such a description. A problem with the model is that it predicts stress saturation at the end of stage III, and therefore a modification, known as the debris model, is suggested (Rollett et al. 1987, Rollett and Kocks 1994). The basic idea of this is that a certain fraction of the dipole collapse events produce dislocation debris, which is left non-recovered in the substructure. The total

dislocation density is separated into two parameters: ρ_{disl}, dislocations in the Frank network, and ρ_{deb}, dislocation debris. The accumulated dislocation debris gives a stage IV of work hardening.

A more sophisticated approach to the problem of work hardening, as compared to the Kocks-Mecking model, is the model developed by Gottstein and co-workers (see e.g. Roters et al. 2000). It is based on a more realistic microstructure description with three internal state variables constituting a cell structure, namely a dislocation density in the cell interior, a dislocation density in the cell walls and a density of mobile dislocations. Their description is similar to that introduced by Mughrabi (1987), and they use his composite model for the flow stress:

$$\tau = \tau_t + \tau_p + (1-f)\alpha G b\sqrt{\rho_i} + f\alpha G b\sqrt{\rho_w} \tag{2.15}$$

where f is the volume fraction of cell boundaries.

Recently, Nes and co-workers have introduced a model for work hardening with similarities to both the models mentioned above (Nes 1998, Marthinsen and Nes 2001, Nes and Marthinsen 2002). It relies on a multi parameter description of the microstructure evolution, fig. 2.26. This is of course a simplified description of the microstructure, compared to the detailed characterisation presented in section 2.2. At small strains the stored dislocations are arranged in a cell structure characterised by a cell size δ, cell walls of thickness h, a wall dislocation density ρ_w, and a dislocation density within the cells ρ_i. At large strains the cell walls have collapsed into sharp sub-boundaries of a well-defined misorientation, φ. A total dislocation density in the material may then be derived:

$$\rho = \rho_i + \frac{\kappa_0 \varphi}{b\delta} \tag{2.16}$$

κ_0 is a geometrical factor of order 3. The last term denotes the dislocations stored in the boundaries, which can be imagined to reflect the dislocation debris in the Rollett-Kocks model above. By using a fictitious misorientation at low strains:

$$\varphi = \frac{\alpha_2}{\alpha_1}\left(\frac{\alpha_2}{\alpha_1 q_c} + 2\right) \cdot \frac{b}{\kappa_0}\sqrt{\rho_i} \tag{2.17}$$

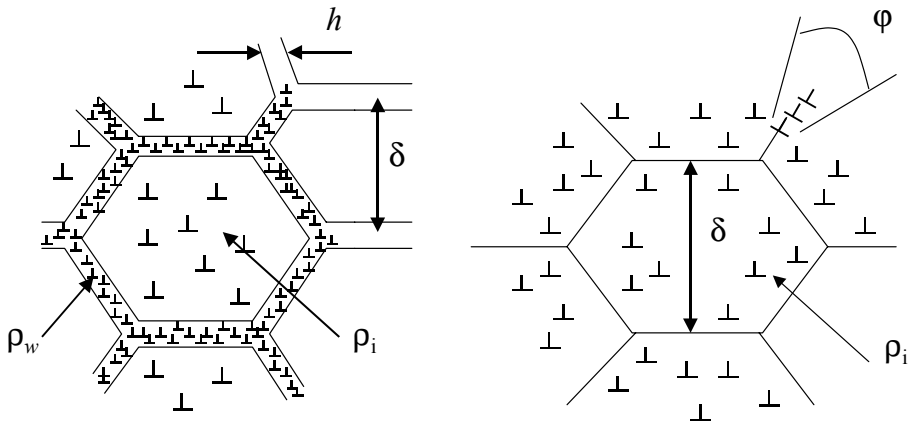

Figure 2.26: Schematic representation of the microstructural parameters used in the work hardening model. (a) Small strains (stage II), (b) large strains (stage IV).

eq. (2.16) may be applied to all strains. The evolution of these parameters with deformation and their influence on the flow stress will be presented in the following subsections. Some aspects of the analysis are not unique for this model, but are used by several models.

Flow stress

At a constant microstructure the flow stress is defined in terms of a thermal component, τ_t, and an athermal component, $\hat{\tau}_a$:

$$\tau = \tau_t + \hat{\tau}_a \tag{2.18}$$

Thermal component: The thermal component is due to short-range interactions between mobile and stored dislocations (cutting of "trees"), dragging of jogs and elements in solid solution. The stress is defined by the Orowan equation:

$$\dot{\gamma} = \rho_m b v \tag{2.19}$$

where $\dot{\gamma}$ is the shear strain rate, ρ_m the density of the mobile dislocations and v the average speed of the mobile dislocations. The density of mobile dislocations is expected to scale with the total dislocation density, i.e. that a fraction of all dislocations present in

the material at any time are mobile. An estimate of $\rho_m \sim 0.1 \cdot \rho$ is used in the model. Eq. (2.19) is written in the following form:

$$2\sinh\frac{\tau_t V_t}{kT} = \frac{\dot{\gamma}}{b^2 \rho_m B_t \nu_D} \cdot \exp\left(\frac{U_t}{kT}\right) \tag{2.20}$$

where V_t is the activation volume, U_t is an activation energy, T is the temperature, k is the Boltzmann's constant, ν_D is the Debye frequency and B_t is a constant. In the case of a pure metal the activation energy is expected to be that required for dragging of jogs on screw dislocations, i.e. $U_t \propto U_{SD}$, the activation energy for self diffusion. The activation volume depends on the spacing of forest dislocations as $V_t = \omega_\rho b^2 \rho^{-1/2}$. In solid solution alloys, the activation energy is that required for separating the solute atoms from the climbing jogs, which depends on the activation energy for solute diffusion and the solute-dislocation interaction energy: $U_t = U_s + \Delta U_s$. The activation volume scales with the spacing of solute atoms along the dislocation core, given by $V_t = \omega_t b^3 c^{-e}$.ω_ρ and ω_t is a scaling factor which needs to be determined experimentally. More details may be found in the work by Nes and Marthinsen (2002). At room temperature, eq. (2.20) essentially gives a relationship between the strain rate, the density of mobile dislocations and the thermal component:

$$\exp(\tau_t) \propto \frac{\dot{\gamma}}{\rho_m} \tag{2.21}$$

Athermal component: The athermal component in eq. (2.18) characterises the rate and temperature independent interaction of dislocations with long-range barriers. These barriers are particles, sub-boundaries, grain boundaries and stored dislocation networks, and hence eq. (2.18) can be written as:

$$\tau = \tau_t + \tau_p + \alpha_1 Gb\sqrt{\rho_i} + \alpha_2 Gb\left(\frac{1}{\delta} + \frac{1}{D}\right) \tag{2.22}$$

Here α_1 and α_2 are constants of the order 0.3 and 2, respectively, $(1/\delta + 1/D)$ represents the average spacing of all boundaries, and τ_p is the contribution from non-deformable particles, given as the Orowan bypass stress according to Ashby (1979):

$$\tau_p = \frac{AGb}{1.24 \cdot 2\pi}\left[\frac{1}{\lambda}\ln\left(\frac{\lambda}{b}\right)\right] \tag{2.23}$$

A is a constant expected to be approximately one. λ is the particle spacing in the slip plane, given by the volume fraction, f_r, and radius, r, of the particles (Brown and Ham 1971):

$$\lambda = 0.8 \cdot r \cdot \left(\sqrt{\frac{\pi}{f_r}} - 2 \right) \tag{2.24}$$

It follows from eq. (2.22) that the dislocation substructure contributes both to the thermal and the athermal components. In the next sub-section the evolution of the microstructure is treated.

Microstructural evolution

The development of a microstructure during deformation is a result of two concurrent processes: athermal storage and dynamic recovery of dislocations. The evolution equation for each of the microstructural parameters are thus given by two terms: Net evolution = storage + recovery.

$$\frac{d\rho_i}{d\gamma} = \frac{d\rho_i^+}{d\gamma} + \frac{d\rho_i^-}{d\gamma} \tag{2.25}$$

$$\frac{d\delta}{d\gamma} = \frac{d\delta^-}{d\gamma} + \frac{d\delta^+}{d\gamma} \tag{2.26}$$

$$\frac{d\varphi}{d\gamma} = \frac{d\varphi^+}{d\gamma} + \frac{d\varphi^-}{d\gamma} \tag{2.27}$$

While physically based expressions are deduced for the internal dislocation density and the subgrain size, no such theory has so far been developed that accounts for the misorientation evolution. The sub-boundary misorientation, φ, is expected to reach a constant level of around 3-4° at the III-IV transition (cf. fig. 2.3 and section 2.2.2). This observation is included as an empirical element in the model.

Athermal storage

The dislocations are stored in the material in three principal ways, see fig. 2.27:

- in the cell interior $\left(\frac{d\rho_i^+}{d\gamma}\right)$
- by forming new cell-boundaries $\left(\frac{d\delta^-}{d\gamma}\right)$
- in old cell-boundaries $\left(\frac{d\varphi^+}{d\gamma}\right)$

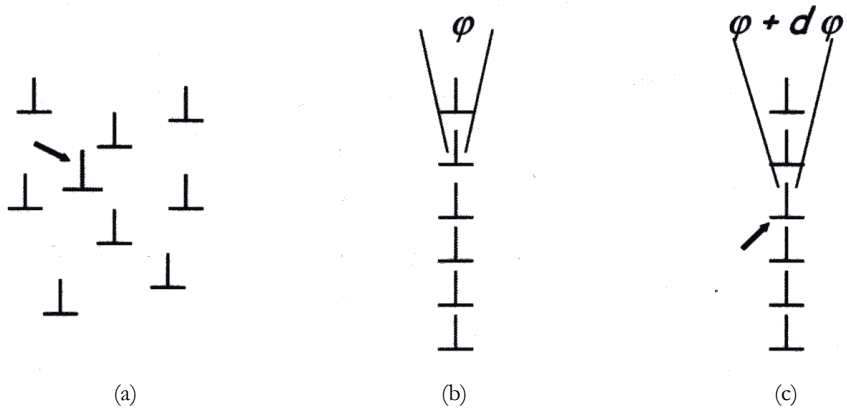

Figure 2.27: Three possibilities of dislocation storage. (a) In a Frank network in the subgrain interior, (b) in new cell boundaries, (c) in old cell boundaries.

A simple analysis of the storage problem gives an expression of a one-parameter type:

$$\frac{d\rho^{+}}{d\gamma} = \frac{2}{bL} \tag{2.28}$$

where L is the slip length. In a pure single crystal the slip is limited only by the interactions between mobile and forest dislocations, see fig. 2.28 (a), and the slip length is given by:

$$L = \frac{C}{\sqrt{\rho}} \tag{2.29}$$

C is a constant proportional to $1/\theta_{II}$, where θ_{II} is the stage II work hardening rate. In a polycrystalline alloy, also other barriers in the material will limit the slip length and affect the athermal storage rate, fig. 2.28 (b). An effective slip length, L_{eff}, is introduced, including both stored dislocations, particles and grain boundaries:

$$\left(\frac{1}{L_{eff}}\right)^2 = \left(\frac{1}{C/\sqrt{\rho}}\right)^2 + \left(\frac{1}{L_G}\right)^2 \tag{2.30}$$

where the L_G term covers the "alloy barriers":

$$\left(\frac{1}{L_G}\right)^2 = \left(\frac{1}{D}\right)^2 + \left(\frac{2f_r}{r}\right)^2 \tag{2.31}$$

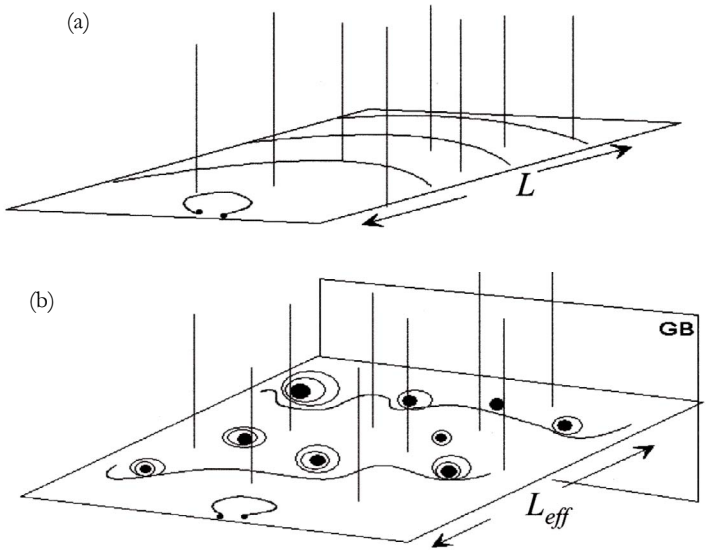

Figure 2.28: Difference in slip length restrictions between (a) a pure metal and (b) an alloy containing particles and grain boundaries.

Because the storage pattern is more complex than eq. (2.28) indicates, a statistical analysis is developed which regulates the athermal storage through the following differential equation (Nes 1998):

$$\frac{d\rho_{nb}^{+}}{d\gamma} = \frac{2S(1-f)L\rho_i}{b} \tag{2.32}$$

where ρ_{nb} represents the dislocations stored in new boundaries, S is a cell/sub-boundary storage parameter and f is the volume fraction of cell boundaries. During stage II this dislocation storage pattern is consistent with the principle of scaling, or similitude - a principle that implies that the microstructural elements scale with each other through three scaling constants:

$$q_c = \delta\sqrt{\rho_i},\ q_h = h/\delta,\ q_b = \sqrt{\rho_b/\rho_i} \tag{2.33}$$

and the storage parameter becomes

$$S = S_{sc} = \frac{fq_b^2}{2C^2(1-f)} \tag{2.34}$$

The resulting storage rate in the cell interior in stage II turns into a modification of eq. (2.28):

$$\frac{d\rho_i^+}{d\gamma} = \frac{1}{1 + f(q_b^2 - 1)} \cdot \frac{2}{bL_{eff}} \tag{2.35}$$

At a constant strain rate and temperature the transition from stage II to III is associated with a saturation of ρ_i (Nord-Varhaug et al. 2000), i.e. a balance is reached between the athermal storage and dynamic recovery of dislocations in the cell interior. This means that eq. (2.25) equals zero, from which it follows that further hardening during stage III and IV requires continued storage of sub-boundaries. This follows from eq. (2.32) in the form:

$$\frac{d\delta^-}{d\gamma} = -\frac{2SC^2\delta^2}{\kappa_0 \varphi L_{eff}} \tag{2.36}$$

where the storage parameter S now becomes a fitting parameter.

Dynamic recovery

By analysing the stability of the cell interior dislocations and the sub-boundary structure, two dynamic recovery processes are incorporated in the model:

- annihilation of dipole segments in the Frank network $\left(\frac{d\rho_i^-}{d\gamma}\right)$
- subgrain growth $\left(\frac{d\delta^+}{d\gamma}\right)$

In the pure metal case these stability problems are analysed in terms of thermally activated cross-slip and climb (Nes 1998, Marthinsen and Nes 2001). Dynamic recovery associated with a 3-D dislocation network will necessarily require both these reactions. In solute containing alloys the rate controlling reaction in cross-slip is assumed to be thermally activated glide of heavily jogged screw dislocations, rather than cross-slip. Recovery of cell-interior dislocation relies on the assumption that network growth is controlled by the collapse of dipoles of separation l_g. The dipoles are formed when mobile dislocations pass through the stored network, and l_g is expected to be much smaller than the average separation of stored dislocations. The collapse rate of dipoles will result in a recovery rate given by:

$$\frac{d\rho_i^-}{dt} = -v_g \rho_i \tag{2.37}$$

where ν_g is the dipole collapse frequency. The derived expression gives:

$$\frac{d\rho_i}{d\gamma} = -\rho_i^{1+x} b^y l_a \xi_\rho B_\rho \frac{\nu_D}{\dot{\gamma}} \left(\exp -\frac{U^*}{kT} \right) 2\sinh\left(\frac{V_\rho G b \sqrt{\rho_i}}{zkT} \right) \tag{2.38}$$

This equation covers three different cases, in which x, y and z, l_a, the activation volume V_ρ and the activation energy U^*, take different values:

(i) In pure metals $x = 1, y = 1, z = 1/2$, $l_a \approx b$ $V_\rho = \xi_\rho b^3$ and $U^* = U_{SD} + \Delta U$.

(ii) In solid solution alloys with thermally activated glide, $x = 1/2, y = 0, z = 2\pi$, $l_a \approx b$, $V_\rho \propto \xi_\rho^s b^3 c^{-e}$ and $U^* = U_s + \Delta U_s$.

(iii) In solid solution alloys with climb, $x = 1, y = 1, z = 1/2$, $l_a = b/c$, $V_\rho \propto \xi_\rho b^3$ and $U^* = U_s + \Delta U_s$.

The average subgrain size in a dynamic situation will increase at a rate

$$\frac{d\delta^+}{d\gamma} = \frac{1}{\dot{\gamma}} \nu_D B_\delta b \exp\left(-\frac{U^*}{kT} \right) 2\sinh\left(\frac{PV_\delta}{kT} \right) \tag{2.39}$$

Here, the activation volume is $V_\delta \propto b^3$ in pure metals and $V_\delta \propto \xi_\delta b^3 c^{-e}$ in solid solution alloys. P is the driving pressure given by $P = 4\gamma_{sb}/\delta$, where γ_{sb} is the sub-boundary energy. ξ_ρ, ξ_δ, B_ρ and B_δ are constants that need to be determined experimentally (see Marthinsen and Nes 2001).

Application

The storage and recovery terms in eq. (2.25) and eq. (2.26) are now available, and together with the particle contribution in eq. (2.23) and the thermal component in eq. (2.20) it is possible to calculate the resolved shear stress, τ. In fig. 2.29 an example of the evolution of ρ_i, δ, φ and τ is given through stage II, III and IV into stress saturation at a constant strain rate and temperature. It shows that ρ_i increases rapidly in stage II, but remains constant during further deformation. The misorientation increases in stage II and III to a constant level in stage IV. The subgrain size decreases gradually all the way until stress saturation is reached. These evolution patterns are reflected in the resulting flow stress.

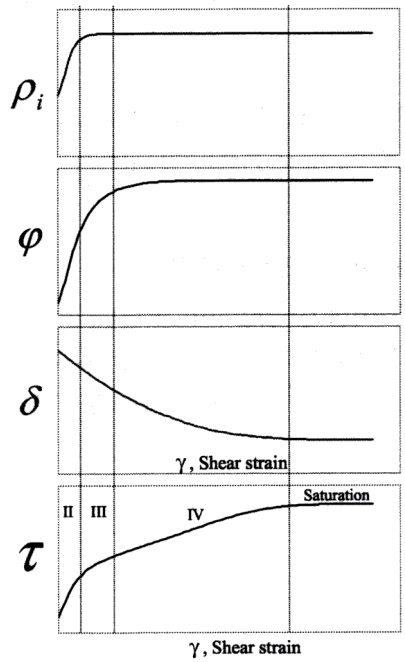

Figure 2.29: Schematical illustration of how the microstructural parameters and the resolved shear stress may vary with strain at room temperature.

To demonstrate the effect of various parameters in the model, some generic stress-strain curves are given in fig. 2.30. Effects of elements in solid solution, grain size and subgrain misorientation are illustrated. In fig. 2.30 (a) solute contents of 0.5, 1 and 2 at% Mg are seen to increase the yield strength and the work hardening rate. The model predicts that the work hardening rate in stage IV (θ_{IV}) scales with the flow stress at the beginning of stage IV (σ_{IV}), which is consistent with eq. (2.10). Reducing the grain size affects the curves by a restriction on the slip length and a direct contribution from the boundaries, fig. 2.30 (b). Non-shearable particles have essentially the same effect as reducing the grain size. The Hall-Petch relationship in fig. 2.30 (c) shows the yield strength as a function of grain size according to eq. (2.12) with a k-value of 0.1, which is close to values found in the literature (e.g. Thompson and Baskes 1973).

If the subgrain size in the material is represented by an average value the model will predict a linear work hardening rate in stage II and a sudden change of gradient when entering stage III. Experimental stress-strain curves are normally curved in both stage II and III and the transition between them is gradual. In the curves in fig. 2.30 (b) the

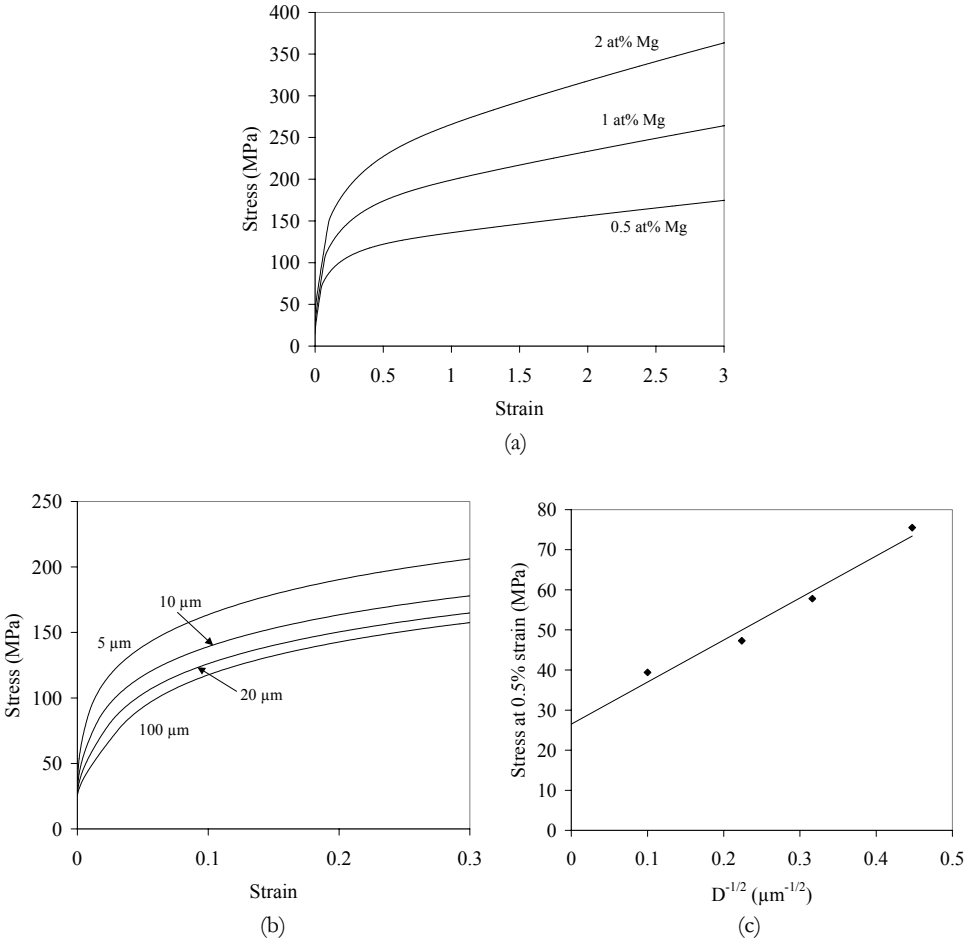

Figure 2.30: Generic stress-strain curves simulating various effects by the work hardening model: (a) Effect of solute content, (b) effect of grain size in an AlMg1 alloy, (c) Hall-Petch plot extracted from (b).

subgrain size δ is not represented by an average value but a Γ-type distribution in order to account for a statistical spread of δ (work in progress, Holmedal and Nes 2003). This distribution is in accordance with experimental observations and a similar development of the model, giving a smooth transition from stage II to III is presented by Marthinsen and Nes (2001).

As a final comment to the work hardening model, it is worth noting that the model at this stage provides the critical resolved shear stress after a given deformation history. For practical purposes we are generally interested in the nominal flow stress of a polycrystal. Then, grain orientation and texture becomes important, and these factors will again

influence the work hardening. For more realistic modelling a combination with a crystal plasticity model is necessary. A very simple method might be to multiply the resolved shear stress with the Taylor factor for the strain path considered (section 2.6.2). At present a more sophisticated approach that integrates the Taylor model and the work hardening model is in progress (Holmedal et al. 2002a).

2.6 Anisotropy and formability

The *formability* of a material defines its ability to withstand plastic deformation without failure. The ability to be formed into various geometrical shapes is one of the most important properties of metals and alloys, but the formability will be strongly dependent on the orientation of the sheet or profile in the forming process. Hence, a good understanding of the directionality of properties may be used to improve and optimise forming operations.

A material that is isotropic has equal mechanical properties in all directions. Most metals used for practical applications, however, exhibit different properties in different spatial directions. For example, in rolled or extruded sheets the tensile properties (yield strength, ductility, r-value etc.) in the sheet plane may vary with the direction of deformation relative to the rolling direction or extrusion direction. This phenomenon is called mechanical *anisotropy*, and is treated in more detail in the following.

2.6.1 Mechanical anisotropy

Several factors are responsible for the anisotropy of mechanical properties. Texture, or crystallographic anisotropy, is probably the most important one, but also the grain shape, precipitates and dislocation structures may influence the properties.

While a single crystal is highly anisotropic, an aggregate of completely differently oriented grains might be almost isotropic. This relates to the variation in strength of different orientations, which for a tensile test is given by the Schmid factor (m) for each grain. In textured polycrystals a large number of the grains have approximately the same orientation, causing anisotropy.

Some of the properties of interest for the manufacturers are the yield strength, the ultimate tensile strength, limit strains and the plastic strain ratio. The strength terms are

closely connected to the Taylor and Schmid factors. The plastic strain ratio is normally given as the r-value and for a tensile test defined as:

$$r = \frac{\varepsilon_w}{\varepsilon_t} \tag{2.40}$$

where ε_w is the width strain and ε_t is the thickness strain. Hence, the r-value gives a relationship between the contractions in the transverse and normal directions of the sheet plane. In the case where r=1, the contractions are equal and the sheet formability is good. If the r-value is small, the thickness contraction is large and the material has a high susceptibility for failure. This happens because the material rapidly goes into a state of plane strain and instability occurs (Marciniak and Duncan 1992). In other forming operations, for instance bending of quadratic tubes, a low r-value is beneficial in the direction of bending because of reduced buckling.

A classical example of anisotropy and formability is the deep-drawing operation of a cup from a textured sheet. Firstly, as the strength varies with direction, a variation in the resistance towards flow will result in an orientation dependence of the elongation. This appears as "ears" on the top of the cup, since a weak direction will have a low flow resistance with an ear as the result. Secondly, a variation in r-value around the cup circle will give different thinning of the cup. Normally, these are undesired effects, as they limit the formability, give varying properties and produce scrap (the ears must be cut off). In smart design operations the mechanical anisotropy can be utilised e.g. by placing the strong directions at critical positions in the final product.

2.6.2 Polycrystal plasticity

Several models for anisotropic behaviour are suggested in the literature, and the classical Sachs and Taylor models are presented below. They are both related to the simple analysis by Schmid (1924) in which a critical resolved shear stress was deduced. Consider fig. 2.31, where a single crystal with cross-section area A is loaded in tension. A {111}-plane with <110>-directions are shown, and the angles between the tensile axis and the considered <110>-direction and a chosen {111}-plane normal are denoted λ and ϕ, respectively. The resolved shear stress on this particular slip system is then given by

$$\tau_c = \frac{F}{A}(\cos\lambda \cdot \cos\phi) \tag{2.41}$$

F/A is the same as the applied stress on the crystal, σ, and $\cos\lambda\cos\phi$ is referred to as the Schmid factor, m, for the considered slip system:

$$\tau_c = m\sigma \tag{2.42}$$

There are twelve different independent slip system in fcc-metals. The Schmid factor will vary with the orientation of the slip system relative to the loading direction, and each slip system will have a value of m<0.5.

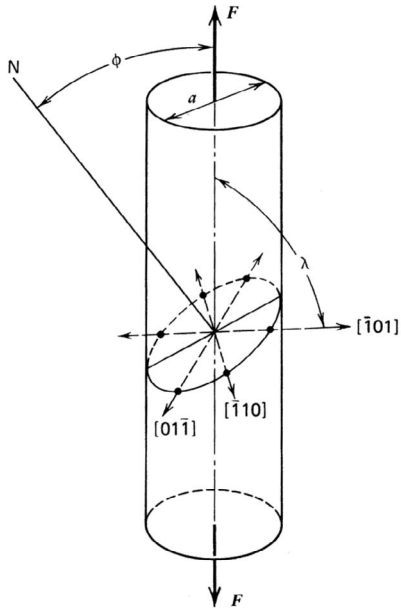

Figure 2.31: Single crystal in tension with slip plane and slip directions. (Verhoeven 1975)

The Sachs model

In the Sachs model it is assumed that each grain deforms independently of its neighbours, and on the slip system that has the highest resolved shear stress (Sachs 1928). For a tensile test this corresponds to a maximum m, eq. (2.42). The Sachs model also says that the stress state is the same in all the grains, i.e. the same as the macroscopic stress. For a tensile test the Sachs model uses Schmid's law, eq. (2.41), to determine the active slip systems, in fcc-metals between one and eight slip systems. However, this simple deformation model does not require compatibility of the strain field between the grains, and is therefore not very realistic, except for very small deformations and for single crystals. The theory is known as the lower bound model and is observed to

underestimate the stress. Modified Sachs models have also been proposed, giving more successful descriptions of polycrystal plasticity (e.g. Leffers 1968).

The Taylor model

Unlike the Sachs model, where the *stress* equilibrium is required, the Taylor model requires *strain* compatibility (Taylor 1938). It rests on some assumptions, where a kinematical equation and an energetic assumption are essential elements:

(i) All grains in a polycrystalline aggregate experience the same strain, equal to the global strain. The macroscopic velocity gradient tensor is equal to the microscopic velocity gradient:

$$L_{ij} = l_{ij} \tag{2.43}$$

which for a tension test is given by:

$$L_{ij} = \begin{bmatrix} 1 & 0 & 0 \\ 0 & -\frac{r}{1+r} & 0 \\ 0 & 0 & -\frac{1}{1+r} \end{bmatrix} \cdot \dot{\varepsilon} \tag{2.44}$$

where $\dot{\varepsilon}$ is the strain rate. A kinematical equation is deduced for the velocity gradient tensor, where the lattice rotation is separated:

$$l_{ij} = \dot{\Omega}_{ij}^{L} + \sum_{s=1}^{12} b_i^s n_j^s \dot{\gamma}^s \tag{2.45}$$

where $\dot{\Omega}^{L}_{ij}$ is the rate of rotation of the crystal lattice, $\dot{\gamma}^s$ is the slip rate on slip system s, and *b* and *n* are the unit vectors of slip direction and slip plane normal, respectively. The kinematical equation says that the combination of all slip processes active at that moment determines what happens to the crystallite. The symmetric part of l_{ij} becomes the strain rate tensor:

$$d_{ij} = \frac{1}{2} \sum_{s=1}^{12} (b_i^s n_j^s + b_j^s n_i^s) \dot{\gamma}^s \tag{2.46}$$

where Taylor's assumption is that $d_{ij}=D_{ij}$, i.e. the strain rate at the microscopic level equals the strain rate prescribed at the macroscopic level. $\frac{1}{2}(b_i^s n_j^s + b_j^s n_i^s)$ is the generalised

Schmid factor, which in uniaxial tension reduces to $\cos\lambda\cos\phi$. Eq. (2.46) gives a set of five independent equations, but twelve unknown $\dot{\gamma}^s$. Therefore additional requirements are needed in order to solve the equations.

(ii) The energetic assumption of Taylor suggests that the slip systems are chosen so that the internally dissipated frictional work is minimised:

$$\dot{W} = \sum_{s=1}^{12} \tau_c^s \cdot \left|\dot{\gamma}^s\right| = \min. \tag{2.47}$$

where τ_c^s is the critical resolved shear stress on slip system s.

Slip occurs on the active slip systems, for which the shear stress, τ^s, reaches τ_c^s. This requirement gives a stress relation when considering the active slip systems only:

$$\frac{1}{2}\sum (b_i^s n_j^s + b_j^s n_i^s)\sigma'_{ij} = \tau_c^s \tag{2.48}$$

from which σ'_{ij}, the deviatoric stress tensor in each grain, may be obtained.

(iii) If the critical resolved shear stress is assumed to be identical in all slip systems, which is a commonly used approximation, no unique solution is obtained for the stress. This will give several sets of (five) non-zero $\dot{\gamma}^s$-values which make $\dot{W}$ minimal. Consequently an ambiguity, referred to as the Taylor ambiguity, arises about which set of slip systems shall be active. Solving the ambiguity can in the simplest case be done by picking one of the solutions by random.

The Taylor factor, *M*, may be defined as the ratio between the shear strain increments on the slip systems and the global strain increment on the crystal:

$$M = \frac{\sum_s \left|\dot{\gamma}^s\right|}{\dot{\varepsilon}} = \frac{\sigma}{\tau_c} \tag{2.49}$$

where it is assumed that all τ_c^s are equal and σ is the equivalent stress. By comparing eq. (2.42) and eq. (2.49) we see that the Taylor factor, *M*, is analogous to the inverse Schmid factor, $1/m$. As they rely on different assumptions regarding the crystal deformation, they will obtain different values. The average Taylor factor for a polycrystalline aggregate is normally larger than the average $1/m$, and the Taylor factor is often referred to as an

upper bound model. In a tensile test of a polycrystal with randomly oriented grains, the average Taylor factor is calculated to be M=3.06.

In a modified Taylor model, known as the relaxed constraints model (RC), some of the strain compatibility restrictions between the grains are relaxed in favour of better stress homogeneity. This results in fewer slip systems involved; in the so-called "pancake" model the number of active slip systems in each grain is reduced from five to three. This can be justified by the shape of a flat, elongated grain. The interface area between two grains on the thin side is so small that no big errors are introduced if the requirement of strain compatibility is relaxed here. For comparison, the Sachs model may be considered as a zero constraints model. A more comprehensive review of the Taylor model may be found e.g. in Van Houtte (1988) and Raabe (1998).

PART A: SHEET MATERIALS

3. Materials and experiments

3.1 Materials

The materials investigated in this part are listed in table 3.1. They are denoted "sheet materials" as they are used in the condition of rolled sheets. Four industrial alloys (AA1050, 3103, 5005 and 5182) were investigated in addition to three commercial grades of AlMg alloys. All the materials were DC-cast by the suppliers listed, and the homogenisation treatments are given in section 3.2. The AA5xxx alloys were further break-down hot rolled and then cold rolled from the transfer gauge.

Table 3.1: Chemical composition of the sheet materials (in wt%).

Alloy	Mg	Mn	Fe	Si	Al	Supplied by
AA1050	0.002	0.003	0.27	0.09	bal. (99.6)	Hydro
AA3103	0.015	1.0	0.57	0.12	bal.	Hydro
AA5005	0.8	-	0.3	0.1	bal.	Corus
AA5182	4.55	0.27	0.21	0.11	bal.	Pechiney
AlMg0.5	0.48	0.008	0.18	0.04	bal.	Hydro
AlMg1	1.01	0.008	0.19	0.04	bal.	Hydro
AlMg3	2.93	0.01	0.2	0.06	bal.	Hydro

- AA1050 is a commercially pure alloy ($Al_{99.6}$), with only small additions of Fe and Si that mainly create coarse particles.
- AA3103 is an alloy with a significant addition of Mn which is present in solid solution and in second phase particles.
- AA5005 has a moderate addition of Mg, which is present in solid solution. Second phase particles.
- AA5182 is an alloy containing a significant addition of Mg, and also some Mn. This gives a high level of Mg in solid solution, and second phase particles are formed as well.
- The three AlMgX alloys, where X refers to wt% Mg, are alloys based on AA1050 with controlled additions of Mg.

3.2 Homogenisation

AA1050 and AlMgX

These alloys were heated at a constant rate of 100°C/h to 550°C, then held at 550°C for 6 hours, and slowly cooled at a rate of 6°C/h to a temperature of 350°C before quenching, see fig. 3.1.

AA3103

AA3103 had a nominal composition of 1.0 wt% Mn, which, using eq. (3.1), where X refers to the atom weight of the elements, corresponds to 0.49 at%. After casting, the amount of Mn in solid solution was measured to be 0.81 wt%, while the rest was present in intermetallic phases. The alloy was given various homogenisation heat treatments in order to produce alloys with different concentrations of Mn in solid solution (Sjølstad 2003), see table 3.2 and fig. 3.1.

$$\text{at\% Mn} = \frac{\frac{100 \cdot \text{wt\%Mn}}{X_{Mn}}}{\frac{\text{wt\%Mn}}{X_{Mn}} + \frac{100 - \text{wt\%Mn}}{X_{Al}}} \tag{3.1}$$

Table 3.2: Homogenisation treatments and the resulting concentrations of Mn in solid solution.

Code	Homogenisation treatment	at% Mn(ss)
AC	(As cast)	0.40
A	Heated at a constant rate of 100°C/h to 610°C, then held at 610°C for 14 hours and finally quenched.	0.24
B	Heated at a constant rate of 100°C/h to 610°C, held at 610°C for 14 hours. Slowly cooled at a rate of 20°C/h to a temperature of 550°C where it was held for 16 hours before quenching.	0.20
C	Heated at a constant rate of 100°C/h to 610°C, held at 610°C for 14 hours. Slowly cooled at a rate of 20°C/h to a temperature of 550°C where it was held for 16 hours. Slowly cooled at a rate of 20°C/h to a temperature of 500°C where it was held for 24 hours. Slowly cooled at a rate of 20°C/h to a temperature of 450°C where it was held for 32 hours before quenching.	0.15

AA5xxx

The AA5xxx alloys were industrially homogenised before break-down hot rolling. The exact procedures are not available.

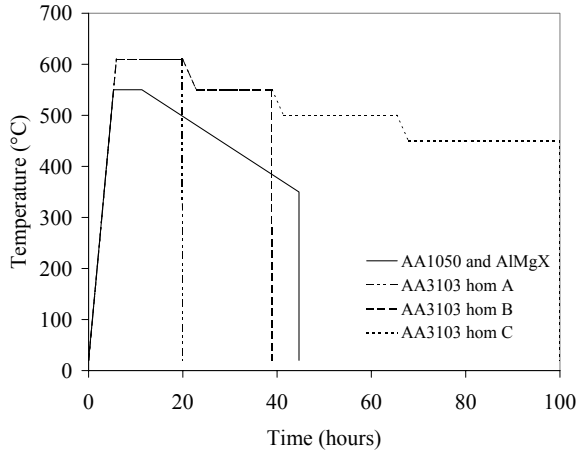

Figure 3.1: Homogenisation treatment of AA1050, AlMgX and AA3103.

3.3 Cold rolling

The alloys AA1050, AA3103 and AlMgX were cold rolled directly from as-cast and homogenised condition in a laboratory mill at NTNU with a relatively low strain rate, probably less than 1. Lubricated rolls were used at maximum speed. The AA5xxx-alloys were first break-down rolled to transfer slab gauges of 24-25 mm thickness. These gauges were then cold rolled by Hydro Aluminium Deutschland. A sketch of the cold rolling process with sample directions is shown in fig. 3.2. The cold rolling strains applied to each alloy are listed in table 3.3. For details about the fine-grained alloys, see section 3.4. In table 3.3 is also given the relation between logarithmic strain (ε), von Mises strain (ε_{vM}) and percentage reduction. These strain measurements are defined by:

$$\varepsilon = \ln\frac{t_0}{t} \tag{3.2}$$

$$\varepsilon_{vM} = \frac{2}{\sqrt{3}} \cdot \varepsilon \tag{3.3}$$

$$\%\ \text{reduction} = \frac{t_0 - t}{t_0} \cdot 100 \tag{3.4}$$

where t_0 and t are given in fig. 3.2.

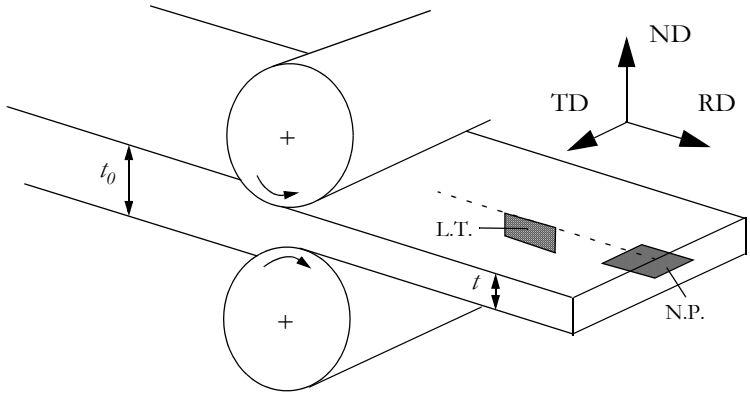

Figure 3.2: Sketch of the cold rolling process. Initial and final thickness, sample directions, the longitudinal transverse section (L.T.) for microscopy and normal plane (N.P.) for global texture measurements are shown.

Table 3.3: Relation between logarithmic strain, von Mises strain and percentage reduction. Rolling strains applied to each alloy are listed.

			Coarse grained				Fine grained
ε	ε_{vM}	% red.	**AA1050**	**AA3103**	**AlMgX**	**AA5xxx**	**AlMg0.5, AlMg3, AA3103**
0.5	0.58	39	x	x	x	x	x
1	1.15	63	x	x	x	x	x
1.5	1.73	78		x			x
2	2.3	87	x	x	x	x	x
2.5	2.89	92		x			
3	3.45	95	x	x	x	x	
4	4.6	98				x	

3.4 Recrystallisation

Some of the cold rolled materials were recrystallised in order to produce variants with smaller grain sizes. Samples of AlMg0.5, AlMg3 and AA3103-B were cold rolled to ε=2 and subsequently recrystallised at 400°C in salt bath. The AlMgX-alloys were annealed for 25 seconds, while the AA3103 alloy was annealed for 45 seconds at 400°C. Because of the possibility for concurrent precipitation of Mn-dispersoids at 400°C in the AA3103

alloy, and thereby undesired changes in mechanical properties, the electrical conductivity was measured before and after recrystallisation (Sjølstad 2003). The change in conductivity was insignificant, and it was concluded that no precipitation had occurred during this heat treatment. In addition, AA1050 and the AlMgX model alloys were cold rolled to various strains and recrystallised. This gave a wider range of grain sizes.

3.5 Tensile testing

AA1050, AA3103 and AlMgX

Tensile specimens were taken from:

- cast + homogenised materials: coarse-grained O-temper
- cold rolled materials: coarse-grained cold rolled
- cold rolled + recrystallised materials: fine-grained O-temper
- recrystallised + cold rolled materials: fine-grained cold rolled (AA3103-B, AlMg0.5 and AlMg3)

Various sample dimensions were used, see table A-1 in the appendix. All the tensile specimens were taken parallel to the rolling direction. The tests were performed in an MTS 880 servo-hydraulic testing machine at a constant ramp rate with a longitudinal extensiometer for strain measurements. The corresponding initial strain rates were in the range 7.7×10^{-4} - 5×10^{-3} s^{-1}.

AA5xxx

The 5xxx alloys were tensile tested in the rolling direction by Hydro Aluminium Deutschland as a part of the VIRFORM project. The transfer gauge and the cold rolled sheet were tested at a strain rate of approximately 6×10^{-3} s^{-1}. Additional tests were performed in the transverse direction of the sheet cold rolled to ε=3.

3.6 Global texture measurements

The global texture of the materials were measured using a Siemens D5000 X-ray diffractometer. The specimens were mechanically ground to the desired position (see fig. 3.2) with SiC-paper of mesh 1200 and etched for 10 minutes in a solution of 15 % NaOH with a teaspoon of sugar pr litre of liquid. To stop the etching reaction the specimens were finally held in 25 % HNO_3 for 20 seconds.

Also EBSD was used to measure the global texture. For this purpose, a relatively large step size, 10-20 μm, was used on a scanning area of about 2-5 mm^2. See section 3.7.2 for more details about EBSD.

X-ray diffraction

In a diffractometer, incoming X-rays are diffracted by the crystal lattice of the specimen according to Bragg's law:

$$2d \cdot \sin\theta = n\lambda \tag{3.5}$$

λ is the wave length of the incoming beam, inclined to the diffracting plane in the sample by an angle θ. d is the spacing of the atom planes, given by

$$d = \frac{a}{\sqrt{h^2 + k^2 + l^2}} \tag{3.6}$$

where a is the lattice constant and $\{hkl\}$ is the Miller indices of the atom plane. As λ and a are constant during an experiment, there will be a unique relationship between the angle of the incoming beam, θ, and the diffracting $\{hkl\}$-plane. A pole figure for a given plane $\{hkl\}$ is measured by selecting the angle θ in accordance with Bragg's law and keeping this constant during the measurement. The pole figure is then measured by rotating and tilting the specimen, during which the distribution of the normal of the $\{hkl\}$-planes are recorded. The four incomplete pole figures {111}, {200}, {220} and {311} were measured and an ODF was determined using the series expansion method (l_{max}=22). See also Bunge (1982) and Randle and Engler (2000) for a further treatment of the theory.

3.7 Microscopy

The microstructure of the cold rolled materials were investigated in the longitudinal transverse section, i.e. the plane containing the rolling direction and normal direction, see fig. 3.2.

3.7.1 Light optical microscopy

Optical microscopy was used to obtain qualitative information on the microstructure of the materials. Macroscopic grain deformation and shear bands were studied by the optical microscope. Magnifications in the range 50x-1000x were applied.

The samples were mechanically ground and polished to 1 μm or OPS, followed by anodising in a 5 % HBF_4 solution for 90 seconds at 20 V. This revealed information on the crystallographic orientation in the specimens when using polarised light.

3.7.2 Scanning electron microscopy

Scanning electron microscopy (SEM) was used to obtain qualitative and quantitative information on grain and subgrain structures as well as microtexture. A Hitachi S-4300SE instrument with a field emission gun (FE-SEM) was used for investigations that required high resolution, while a JEOL JSM-840 instrument with a tungsten filament (W-SEM) was used for low-resolution metallography. 20 kV and 20-25 mm were typical settings for the accelerating voltage and the working distance, respectively.

The SEMs were equipped with a NORDIF digital EBSD detector and an HKL Channel5 EBSD acquisition system for orientation imaging mapping. Orientation maps were constructed with various step sizes. In the W-SEM, 0.2 μm was considered as the smallest reasonable step size, whereas the FE-SEM could handle step sizes down to 0.05 μm. For studies of subgrain structures, a step size of 0.05 μm was used. For the mapping of grain structures, a step size of 0.5-5 μm was used, depending on the grain size.

The post-processing of the EBSD data were performed by means of two software packages with different benefits:

- HKL Channel5, developed by HKL Technology (Ref. HKL). This software was most preferably used due to its user friendliness and flexibility.
- VMAP v8, developed at UMIST, Manchester (Humphreys 2002). The strength of this software was its suitability to process high resolution EBSD maps. It contained a Kuwahara filter for image processing which made it possible to perform orientation averaging in order to filter out orientation noise and thereby obtain statistical data on misorientations down to 0.5° (Humphreys 2001).

Two different specimen preparation techniques were used for the EBSD analyses:

- Specimens were ground to mesh 2400 and electropolished for 20 seconds at 20 V. The electrolyte was the so-called A2: 70% ethanol, 12% distilled water, 10% butylglycol and 8% percloric acid, and held a temperature of 18°C .

- Specimens were mechanically ground and polished to OPS and electropolished for 90 seconds at 12 V. The electrolyte was a 30% nitric acid in methanol solution and the temperature lied between -30 and -40°C.

For successful use of the EBSD technique, the crystal structure of the investigated material has to be ordered or nearly perfect. Otherwise, there will be no diffraction from the crystal, and hence no diffraction patterns are created. This is the reason why electropolishing is needed to remove the deformed layer induced by mechanical polishing. With this preparation, most annealed materials with an ordered crystal structure produce good EBSD patterns. Cold deformed materials, however, have a distorted crystal structure due to the high density of dislocations and subgrain boundaries. With additions of alloying elements the situation becomes even worse, since solute atoms will pin the dislocations and give a higher dislocation density.

Electron Back-Scattering Diffraction

The electron back-scattering diffraction pattern technique (EBSD or EBSP) has over the last ten years become a popular and standardised experimental procedure. It provides a fast and simple method to obtain statistical information on e.g. grain structure, subgrains, texture, phase identification and boundary characterisation. With the increasing speed and capacity of computers, it is now possible to process huge amounts of data acquired by EBSD. A brief presentation of the most important principles is given here, but for an in-depth description of EBSD please refer to a recent book by Randle and Engler (2000).

The physics behind the EBSD is illustrated in fig. 3.3 (a). The specimen is mounted with a 70° tilt in the SEM. The electron beam penetrates into the surface of the specimen, and upon back-scattering the electrons are Bragg diffracted, eq. (3.5), by the lattice planes in a small material volume. The diffracted signal contains Kikuchi-bands, bands of higher intensity than the background scattering. When these bands are projected onto a phosphor screen, they produce a pattern of bright lines, a diffraction pattern, fig. 3.3 (b). As the width and position of the bands correspond directly to the lattice orientation and lattice plane spacing in the specimen, a diffraction pattern contains information that is unique for a given crystal structure and orientation. By capturing the pattern with a camera and applying image analysis on the acquired pattern, a computer software code may be able to identify the pattern and compare it to theoretical values. Now, information in terms of crystallographic orientation, phase, pattern quality etc. is obtained from one *point* in the sample.

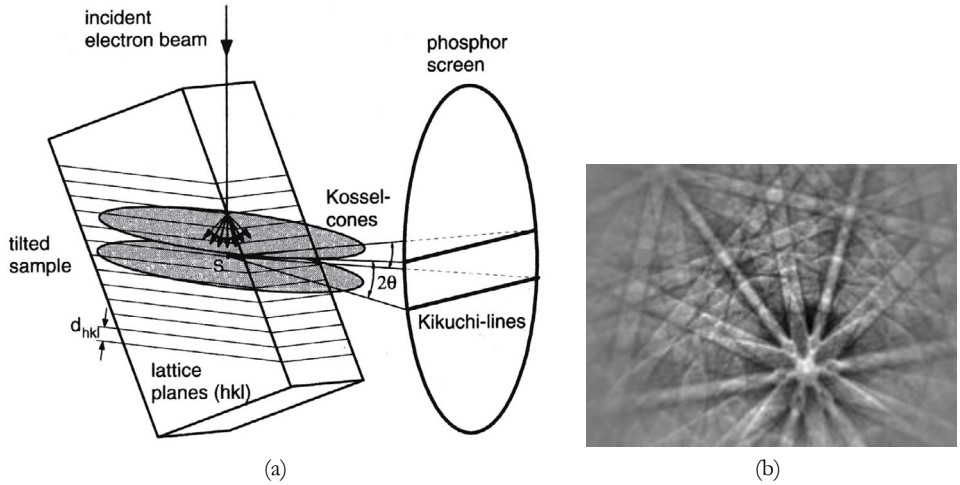

Figure 3.3: (a) Illustration of the main components of EBSD analyses (Randle and Engler 2000). (b) Kikuchi diffraction pattern.

When acquiring an EBSD *map*, the computer controls the electron beam so that it scans a grid on the specimen surface. Information from each pixel in this grid is stored and subsequently put together in a pixel map. A grain or subgrain will then appear as an assembly of equally oriented pixels, and the misorientation between the pixels will constitute boundaries between grains and subgrains. Quantitative measurements, such as (sub)grain size distributions, area fractions and misorientation profiles are possible to extract from the data.

The EBSD results are strongly dependent on the step size. A rule of thumb is that a grain or subgrain shall have at least 5-10 pixels across its width in order to be truly detected (Humphreys 2001). However, if the EBSD data shall be used for texture representation, the step size must be of the order of the grain size.

3.7.3 Transmission electron microscopy

TEM was used to study the deformation structures on a more detailed level than what was possible with the SEM. Measurements of subgrain size, subgrain misorientation and local texture, as well as estimates of dislocation densities, were performed with TEM. The TEM provided pictures of subgrains and dislocations in cold rolled materials, and could be used to verify observations in SEM.

Specimens were prepared by cutting thin slices of about 100 μm that were ground on both sides with SiC-paper to a thin foil. The foils were jet electrolytically thinned in a 30% HNO_3 in methanol solution holding -30°C.

The instrument used here was a JEOL JEM-2010 with a LaB_6 filament operating at 200 kV. For orientation measurements, CBED and indexing of Kikuchi diffraction patterns were used, see below. The TEM was equipped with a wide-angle camera above the viewing screen which captured the diffraction patterns and transferred them through an image processing unit to a computer for semi-automatic indexing. The HKL Channel software was used for this purpose and for the post-processing of data.

Convergent beam electron diffraction

The principles behind the CBED-technique are analogous to the EBSD-technique. Instead of a back-scattering of the electrons from the surface as in EBSD, the electrons now penetrate through the specimen, fig. 3.4. A convergent beam is used in order to focus the beam on a very small region of the material. The incoming electrons then occupy a range of angles relative to the specimen. On their way through the material, the electrons with the correct angle to the {*hkl*}-planes are Bragg diffracted, eq. (3.5), and a Kikuchi pattern is formed below the specimen. The geometry of the pattern then provides information on the orientation of the small material volume the electrons have travelled through (Williams and Carter 1996).

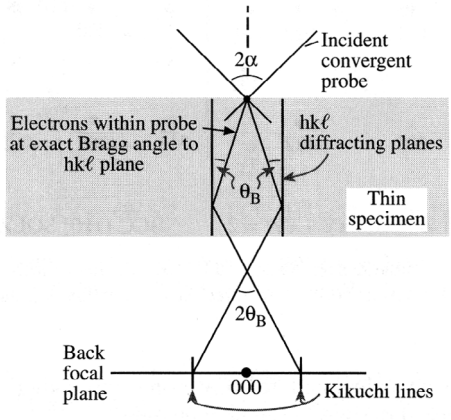

Figure 3.4: Schematical illustration of CBED (Williams and Carter 1996).

One problem with this technique was the strong intensity of the direct beam, which complicated the pattern indexing, see fig. 3.5 (a). This was partly avoided by using an image processing unit that subtracted the bright spot and made it easier to index the patterns, fig. 3.5 (b).

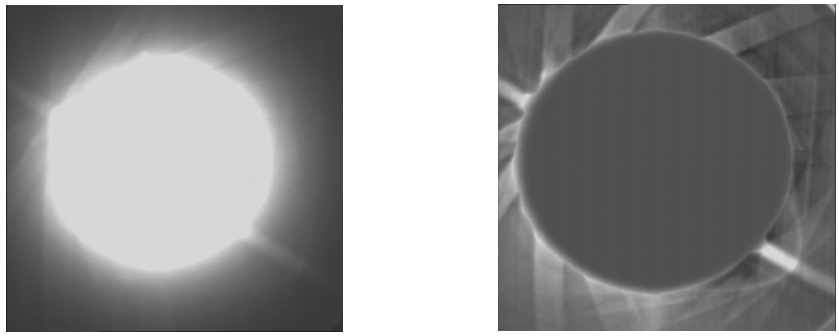

(a) (b)

Figure 3.5: Kikuchi pattern from TEM before (a) and after (b) image processing.

4. Experimental results

In this chapter the experimental results are presented. First, a characterisation of the as-received materials is given in terms of grain structure and texture. In the following sections an examination of the cold rolled materials are presented: Texture development (section 4.2), macroscopic grain deformation (section 4.3) and substructure evolution (section 4.4). Finally the mechanical properties and work hardening behaviour of the materials are presented (section 4.5).

For the case of completion, some results obtained by other laboratories participating in the VIRFORM project and the REAP project are included as well. This basically concerns the characterisation of the as-received materials, texture measurements and mechanical testing, and will be referred to on the way.

4.1 Characterisation of as-received materials

An overview of the grain sizes and textures of the as-received materials is given in table 4.1, with further details in the following sections. The alloys are seen to be rather coarse-grained, and except for AA1050 and AA5005, the grain sizes and textures of the alloys are fairly similar (50-90 μm). In order to investigate the effect of grain size on properties and microstructure, some fine-grained variants were processed to produce finer grain sizes. These are given in table 4.2. Only the materials that were further cold rolled were examined for texture.

4.1.1 Grain structure

The grains were detected using EBSD with a step size much smaller than the grain size. The as-cast alloys and the transfer gauge materials all have equiaxed, homogeneous grain structures. Optical micrographs of the as-cast AA1050 and AlMgX alloys are shown in fig. 4.1, where the variation in grain size is evident. An EBSD map of AA3103-B is given in fig. 4.3 (a). The grain structure of the fine-grained alloys is equiaxed but less uniform. Fine-grained variants of AlMg0.5 and AlMg3 are shown in fig. 4.2 (a, b) and fine-grained AA3103-B in fig. 4.3 (b). The grain structures of the AA5xxx transfer gauges are not shown here, but are similar to the alloys presented above (CORUS 2001, Pechiney 2001).

Table 4.1: Overview of grain sizes and textures in as cast + homogenised materials and transfer gauge materials.

Alloy	Grain size (μm)	Texture
AA1050 as cast + hom	117	Random
AlMg0.5 as cast + hom	86	Random
AlMg1 as cast + hom	79	Random
AlMg3 as cast + hom	68	Random
AA5005 transfer gauge	175[a]	Strong cube texture + minor Bs comp.[b]
AA5182 transfer gauge	50[c]	Weak cube texture[b]
AA3103 as cast, hom A, B and C	65	Random

a. CORUS (2001)
b. Li and Van Houtte (2002a)
c. Pechiney (2001)

Table 4.2: Overview of grain sizes and textures in the materials with refined grain sizes.

Alloy	Grain size (μm)	Texture
AA1050	36	not measured
AA1050	11	not measured
AlMg0.5	40	not measured
AlMg0.5	15	not measured
AlMg0.5	10	Weak cube texture
AlMg1	29	not measured
AlMg1	10	not measured
AlMg3	17	not measured
AlMg3	8	Weak cube texture
AA3103 hom B	6	Weak cube texture

4.1.2 Texture

ODFs of the fine-grained AlMg0.5 and AlMg3, as well as the AA3103-B alloy, both coarse-grained and fine-grained, are shown in fig. A-1 in the appendix. The texture in these alloys is generally weak, and the as-cast alloys have more or less random grain

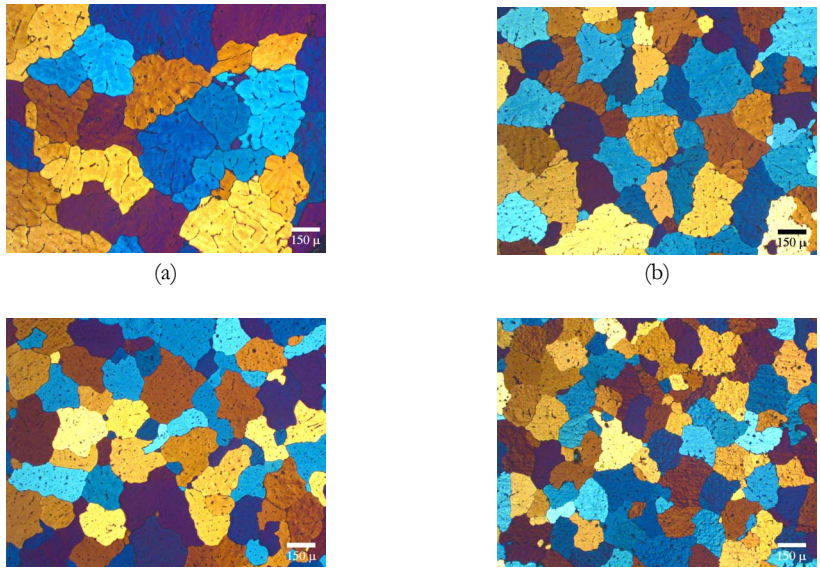

(a) (b)

(c) (d)

Figure 4.1: Optical micrographs of (a) AA1050, (b) AlMg0.5, (c) AlMg1 and (d) AlMg3.

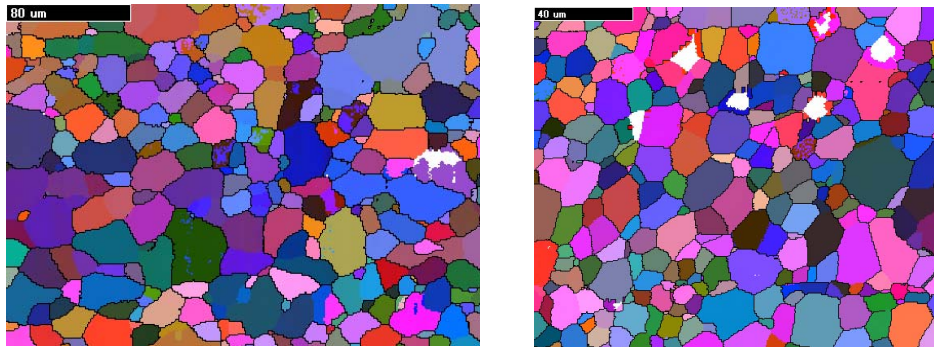

(a) (b)

Figure 4.2: EBSD maps of fine-grained (a) AlMg0.5 (step size 1 µm) and (b) AlMg3 (step size 0.5 µm).

orientations. The fine-grained variants, which are exposed to large deformation and subsequent annealing, tend to have a weak cube texture. Also the transfer gauge of AA5182 has a weak cube texture, see fig. 4.4 (b), while the AA5005, fig. 4.4 (a), has a strong cube texture (36x random) along with a minor brass component (Li and Van Houtte 2002a).

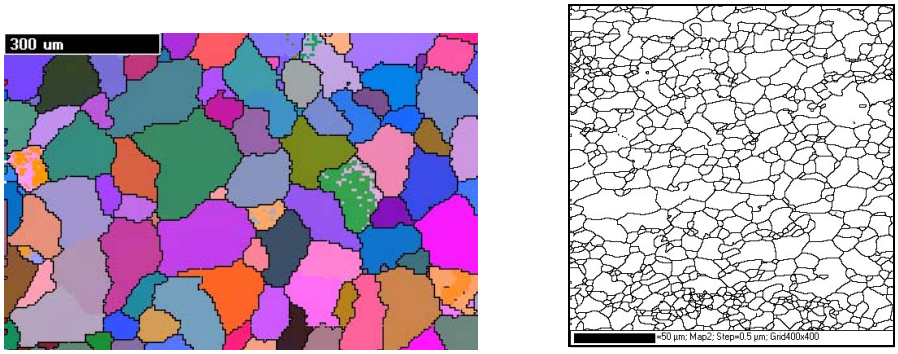

(a) (b)

Figure 4.3: EBSD maps of AA3103. (a) As cast+homogenisation B (step size 5 µm). (b) Fine-grained (step size 0.5 µm).

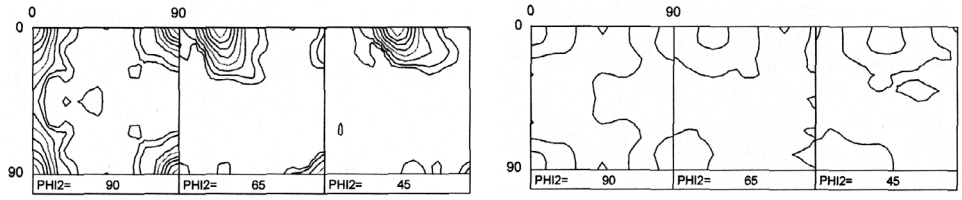

Levels: 1-2-4-7-11-16-22-29

(a) (b)

Figure 4.4: ODF sections from the transfer gauges of (a) AA5005 and (b) AA5182. (From Li and Van Houtte 2002a).

4.2 Global texture development during cold rolling

4.2.1 AA1050 and AlMgX alloys

The development of a rolling texture in AA1050 is shown by the ODFs in fig. 4.5, obtained by X-ray diffraction. At the lowest deformations an α-fibre, including the B-component, and a weak β-fibre have developed. At ε=0.5 the rolling texture is very weak, indicating a slow texture development. With increasing deformation the β-fibre is sharpened with the highest density in the C-orientation. The density plots of the β-fibre are shown in fig. 4.6 (a) where it is seen that most of the rolling texture has developed at a strain of ε=2, whereafter the texture change is relatively small. This texture evolution is characteristic also for the AlMgX alloys. However, the β-fibre density plot of AlMg3, fig. 4.6 (b), shows a slightly different evolution with a higher density of the B-orientation at large strains.

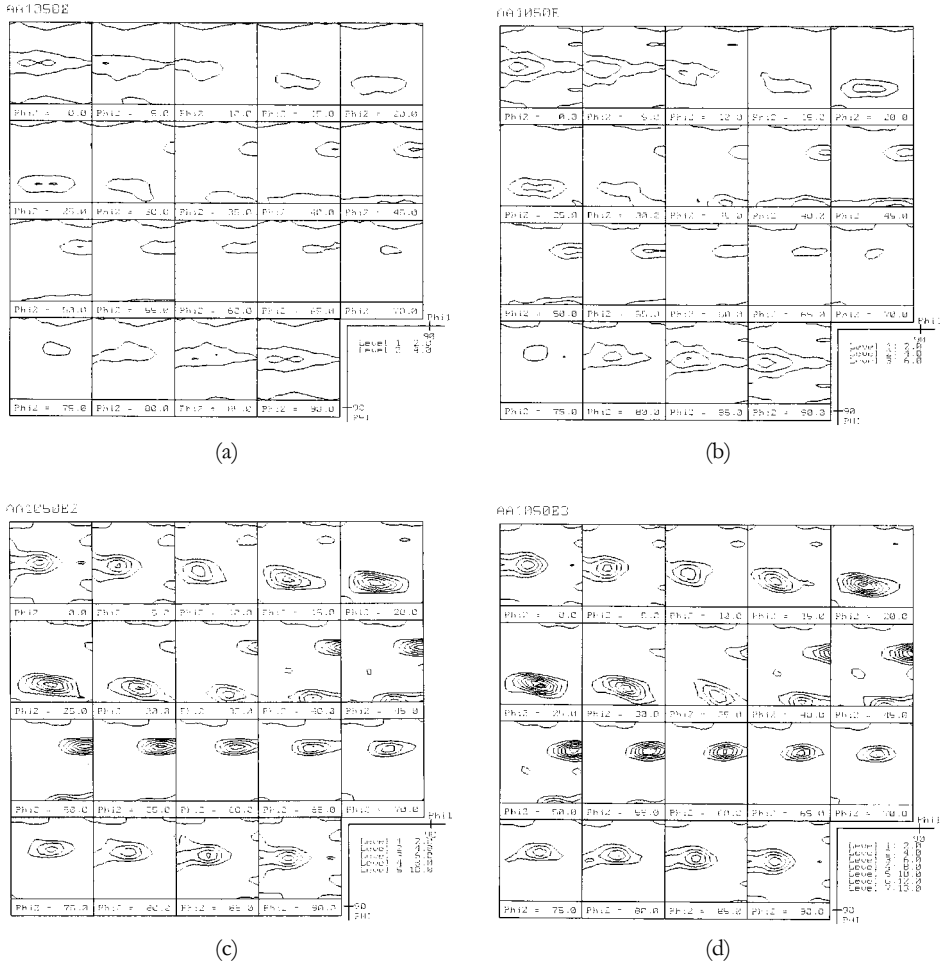

Figure 4.5: ODFs from X-ray diffraction of the AA1050 alloy after cold rolling to (a) ε=0.5, (b) ε=1, (c) ε=2, (d) ε=3.

The effect of the initial grain size on the rolling texture is shown in fig. 4.7. Here, the texture is measured using EBSD on coarse-grained (86 μm) and fine-grained (15 μm) AlMg0.5 cold rolled to ε=0.5 and ε=0.6, respectively. It is mentioned above that the development of a rolling texture is too slow for any strong β-fibre to be formed at these small strains. The fine-grained material, however, exhibits a relatively strong rolling texture with preference at the copper-S orientation already after a rolling strain of ε=0.6.

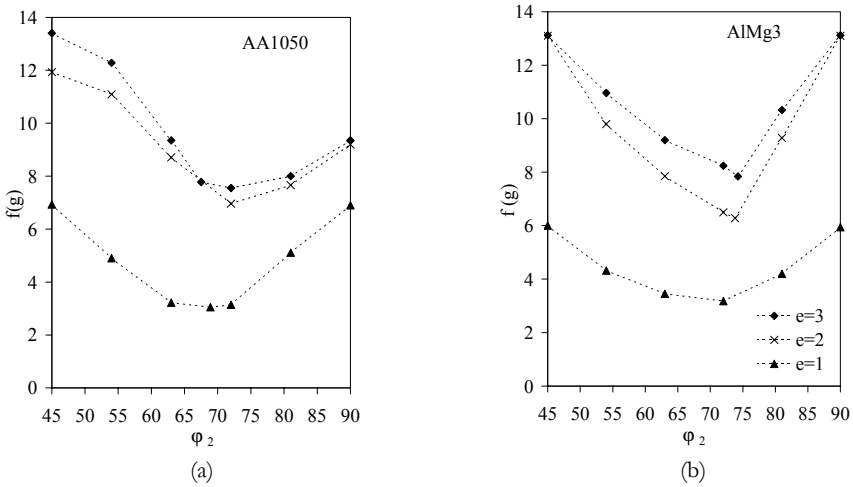

Figure 4.6: β-fibre density plots from X-ray diffraction of (a) AA1050 and (b) AlMg3.

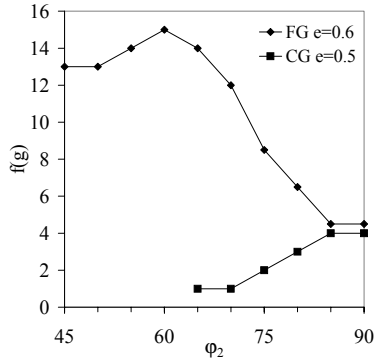

Figure 4.7: β-fibre density plots of a coarse-grained (CG) and a fine-grained (FG) variant of AlMg0.5 cold rolled to ε=0.5 and ε=0.6, respectively. Data obtained by EBSD measurements.

4.2.2 AA5xxx

The global texture development in the AA5xxx alloys is measured by Li and Van Houtte (2002a). The development of the rolling texture is shown by the β-fibre density plots in fig. 4.8. In AA5005 the β-fibre components are in fact absent after rolling up to ε=0.5 and 1. At higher deformations, ε=2-4, the rolling texture becomes well developed, with preference at the B-S side. The low density of the C-orientation in AA5005, and the fact that the texture evolution continues beyond ε=2, are in contrast to what was observed in AA1050 and AlMg3 (fig. 4.6). Most likely, this relates to a different initial texture.

In AA5182 the rolling texture starts developing at the beginning of deformation, and already after a rolling strain of ε=0.5 a well-defined β-fibre is created. Its intensity increases steadily with cold rolling. The orientation density along this fibre is quite uniform and relatively weak as compared to AA5005, AA1050 and the AlMgX alloys.

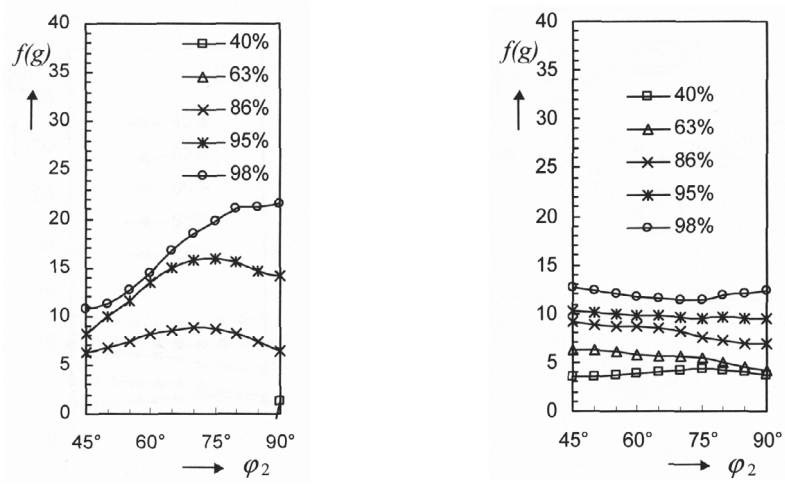

Figure 4.8: β-fibre density plots after cold rolling of (a) AA5005 and (b) AA5182. (From Li and Van Houtte 2002a).

4.3 Macroscopic grain deformation

In this section an overview is given on the microstructural evolution during cold rolling, seen from a macroscopic point of view. With respect to the grain deformation, all the investigated alloys behave more or less in the same way, but there are some differences caused by variations in initial grain size and Mg-content. The AA5005 and AA5182 alloys are used as illustrating examples, as they cover a wide range of cold rolling strain (ε=0.5-4) and Mg-content (0.8-4.55 wt%). Optical micrographs from the longitudinal section are shown in fig. 4.9, all on the same scale.

Basically, the grain deformation corresponds to the global deformation of the sheet. The grains are gradually elongated and flattened out into pancake-shaped grains. Additionally, some break-up of the grains occur. The heterogeneous nature of the grain deformation is also apparent, with large thickness variations of the grains. Some grains tend to deform more strongly than other, and this is especially clear at the lower strain levels where the original grain boundaries are still visible.

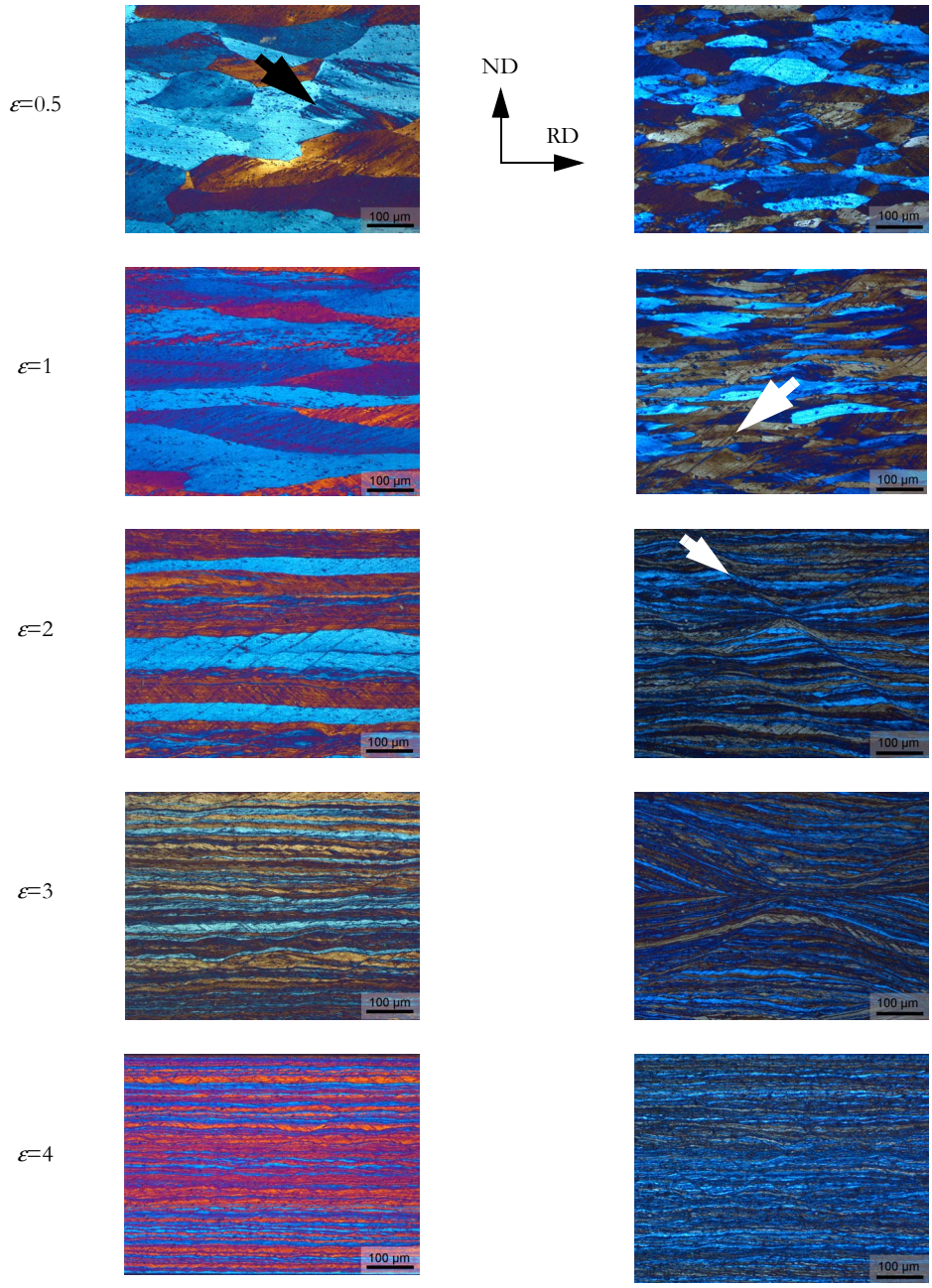

Figure 4.9: Optical micrographs illustrating the grain deformation during cold rolling from ε=0.5 to ε=4. (a) AA5005: 0.8%Mg, D=175 µm. (b) AA5182: 4.55%Mg, D=50 µm. Arrows show in-grain bands and macroscopic shear bands.

In all samples investigated, some linear features or bands, are present in the microstructure. They are inclined to the rolling direction by an angle of 30-45° and in many cases they are confined to a single grain, see for instance AA5005, ε=0.5 in fig. 4.9 (a). In other cases, shear bands crossing several grain boundaries are present, see AA5182, ε=2-3. These features are treated in more detail in the next section.

4.3.1 Shear banding

From fig. 4.9 it is seen that the formation of macroscopic shear bands is much more frequent in the high-Mg alloy AA5182 than in AA5005. This is also illustrated in fig. 4.10, where AA1050 and the AlMgX alloys, all cold rolled to ε=3, are shown. The increase in Mg-level leads to an increased tendency for a formation of offsets on the grain boundaries, in-grain bands and heavy shear.

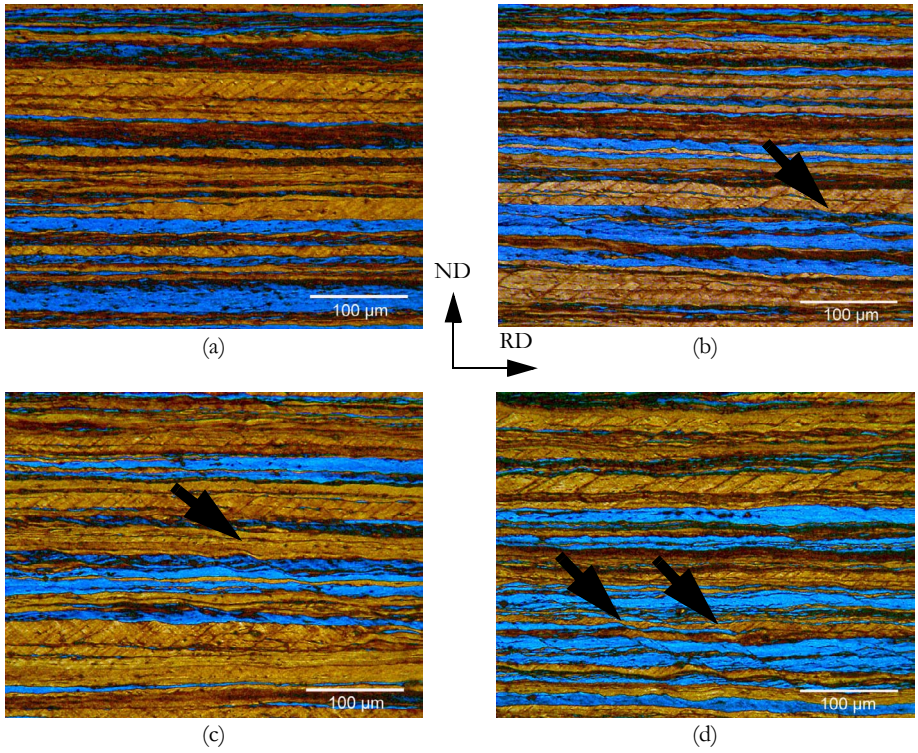

Figure 4.10: Optical micrographs of materials cold rolled to ε=3. (a) AA1050, (b) AlMg0.5, (c) AlMg1, (d) AlMg3. Macroscopic shear bands indicated by arrows.

In this analysis a distinction is made between two types of bands: (i) In-grain shear bands appear in all the alloys at all stages of rolling, see for instance AA5005 cold rolled to ε=0.5

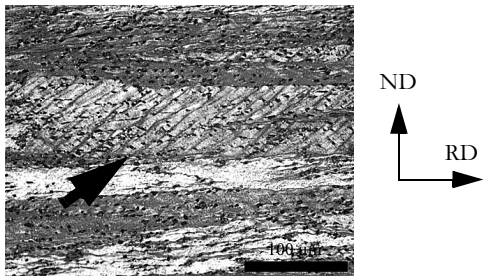

Figure 4.11: Optical micrograph of AA3103-B cold rolled to ε=1.5. In-grain shear bands indicated by arrow.

(fig. 4.9 (a)) and AA3103-B cold rolled to ε=1.5 (fig. 4.11). Offsets are formed on the grain boundaries, but these features are not necessarily associated with heavy shear across the boundaries. (ii) Macroscopic shear bands intersect several grain boundaries with massive shear. These observations are restricted to the high-Mg alloys and/or the highest rolling reductions (see arrows in fig. 4.10). The alloys without Mg, i.e. AA1050 and AA3103, do not form any macroscopic shear bands at the investigated strains, although the in-grain bands are numerous. The observations are summarised in fig. 4.12 and in table A-1 in the appendix. A critical strain for the formation of macroscopic shear bands as a function of Mg-content may be estimated from fig. 4.12. The broken line illustrate that this critical strain decreases with increasing concentration of Mg. Shear bands in AA5182, as they appear in the TEM are shown in fig. 4.13, where bundles of elongated subgrains seem to collapse into regions of intense shear.

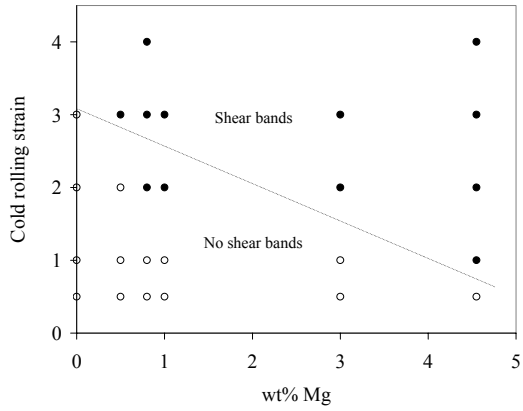

Figure 4.12: The formation of macroscopic shear bands as a function of cold rolling strain and wt% Mg in the alloy. Full circles and open circles represent shear band formation and non-shear band formation, respectively.

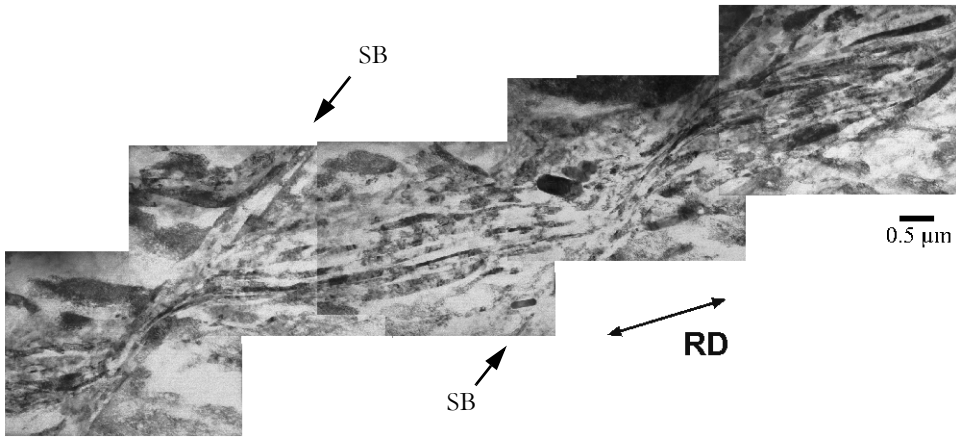

Figure 4.13: TEM micrograph of two shear bands in AA5182 cold rolled to ε=2.

4.3.2 HAGB spacing

It was seen by the optical micrographs above that the grains break up into smaller volumes during cold deformation. A more detailed analysis of this phenomenon is performed using EBSD. The EBSD maps in fig. 4.14 show the evolution in grain structure with increasing cold rolling, a pattern that is in agreement with the optical micrographs in fig. 4.9. A number of newly introduced HAGBs are seen to be unevenly distributed in the material, and in some cases the HAGBs are fragmented. In order to quantify the grain break-up phenomenon, the distance between HAGBs is measured along the normal direction on EBSD maps. The variation in HAGB spacing with cold rolling for the AA1050 and AlMgX alloys is plotted in fig. 4.15. Both coarse-grained and fine-grained AlMg0.5 are shown. Even though the initial HAGB spacing varies due to different grain sizes, it approaches the same value during cold rolling. The decrease of the spacing is seen to be most rapid in the coarsest grained materials.

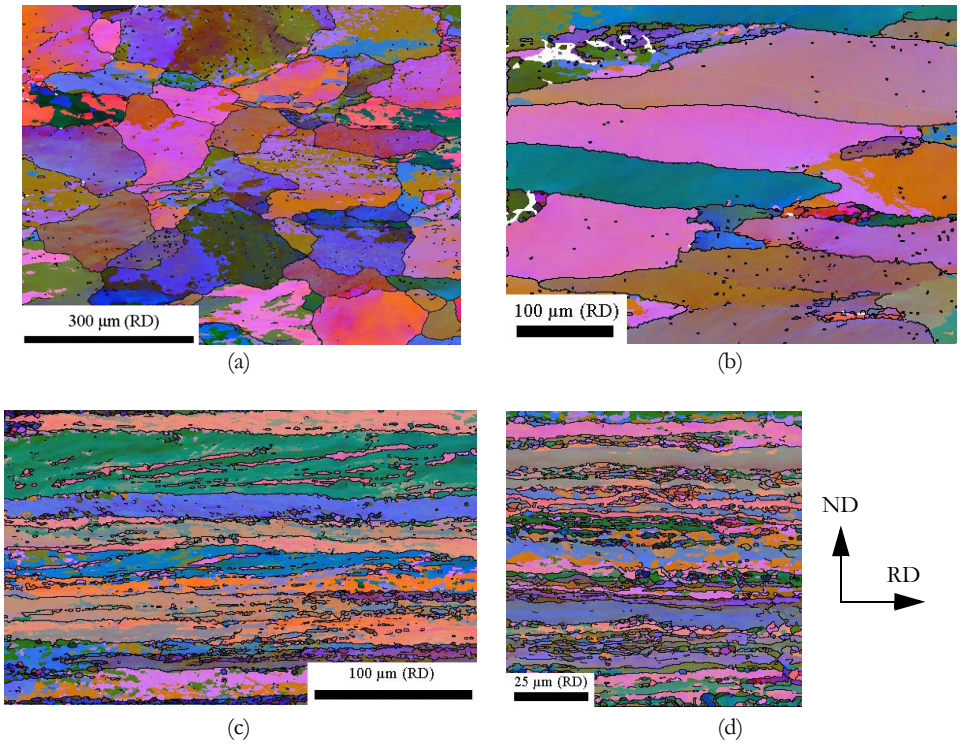

Figure 4.14: EBSD-maps showing the evolution in deformation structure during cold rolling. (a) AlMg0.5 ε=0.5, (b) AlMg0.5 ε=1, (c) AA1050 ε=2, (d) AA1050 ε=3. High-angle boundaries are shown. Note the difference in magnification.

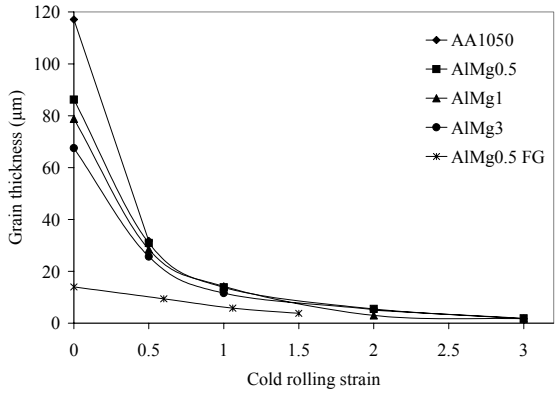

Figure 4.15: HAGB spacing as a function of cold rolling strain in various alloys. Both coarse-grained and fine-grained AlMg0.5 are shown.

4.4 Substructure evolution

In this section results from high resolution EBSD (FE-SEM) and TEM are presented. First, a qualitative description of the observed substructure is given, showing strong similarities with the deformation structure reported in the literature (section 2.2.2). Then, a quantitative description in terms of subgrain size and misorientation is presented. EBSD maps of the cold rolled structure were acquired by a step size of 0.05 μm, mainly from the alloys AA1050, AlMg1 and AlMg3. The combination of high solute levels and high strains made the indexing of EBSD patterns difficult, illustrated by the average indexing fractions for each alloy and strain shown in table A-2 in the appendix. In the results presented here, no less than 70% indexing is accepted.

4.4.1 A qualitative description

Evolution with cold rolling strain

In fig. 4.16 and fig. 4.17 the evolution in deformation structure is shown on a finer scale than in the previous section (fig. 4.14). The EBSD maps of the cold rolled structure illustrate, in a qualitative manner, the formation of boundaries and the alignment of them. The maps are built up by Euler colours, i.e. colours composed from the crystal orientation, and boundaries indicating misorientation between neighbouring volumes. All the maps have been post-processed using VMAP with five runs of the Kuwahara-9 filter in order to filter out the orientation noise. Some extrapolation of non-indexed areas is also performed.

In general, the microstructure is seen to be refined with increasing strain. The inhomogeneous evolution of the deformation structure is also apparent at all stages. A change in the character of the structure occurs between ε=1 and ε=2. At the moderate strain levels, i.e. ε=0.5-1 in fig. 4.16, extended dislocation boundaries and microbands separate volumes (cell blocks) of rather diffuse internal structures. The boundaries are inclined to the rolling direction by a range of angles between 0 and 45°, and in some cases they are seen to intersect each other, as in fig. 4.16 (b).

At higher strains, ε=2-3 in fig. 4.17, a majority of the extended boundaries have become almost parallel to the rolling direction, i.e. they may be defined as lamellar boundaries (LBs). At ε=3 some shear bands are visible as well. At this point a subgrain structure has developed, in contrast to the more diffuse structure seen at lower strains.

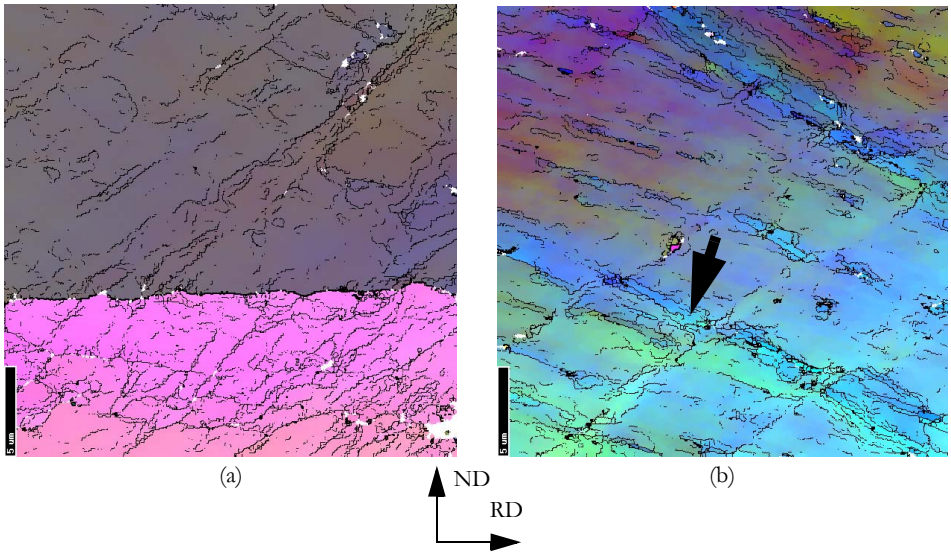

Figure 4.16: EBSD maps showing the substructure after moderate cold rolling of AlMg3. Misorientations >1° are displayed, illustrating the alignment of dislocation boundaries. (a) ε=0.5, showing two grains (Euler colours). (b) ε=1, showing one grain with intersecting microbands (relative Euler colours). The scale bar is 5 µm long.

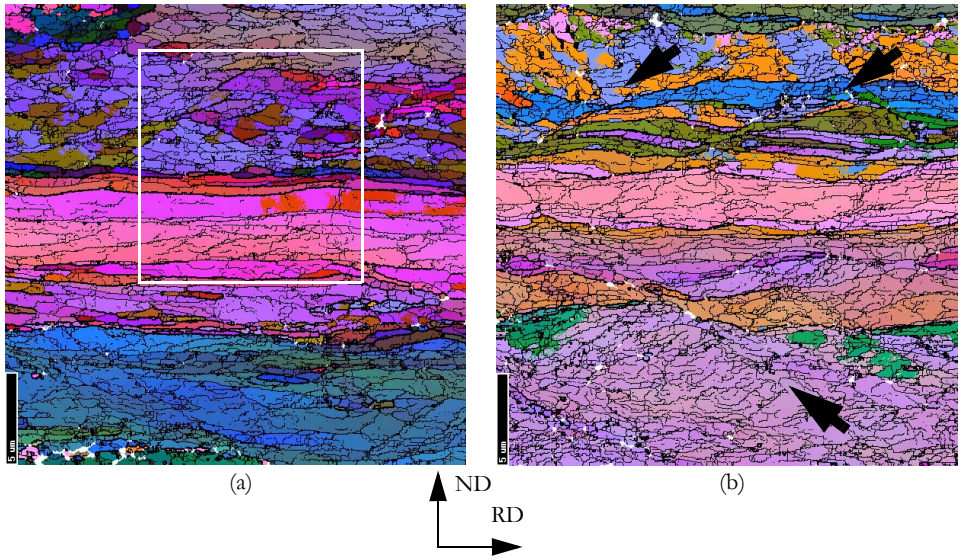

Figure 4.17: EBSD maps showing the substructure after large strain cold rolling of AlMg1. Euler colours and misorientations >1° (thin lines) and >15° (bold lines) are displayed, illustrating the alignment of grain boundaries and sub-boundaries. (a) ε=2. Section within the frame is enlarged in fig. 4.18. (b) ε=3, with shear bands indicated by arrows. The scale bar is 5 µm long.

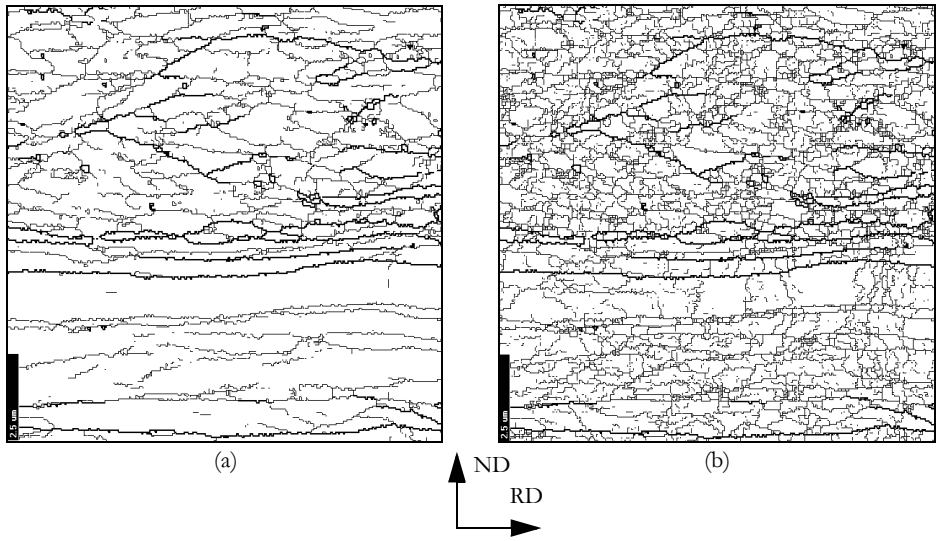

Figure 4.18: EBSD misorientation maps of AlMg1 ε=2 (from the centre of fig. 4.17 (a)) showing the difference in subdivision in two regions: a lamellar structure in the lower part of the map and a "parallelogram structure" in the upper part. (a) Boundaries: 2 and 15°, (b) boundaries: 0.5 and 15°. The scale bar is 2.5 μm long.

A closer study of the map of the ε=2 material in fig. 4.17 (a) reveals a difference in character of the subdivision between two grains. Fig. 4.18 is an enlarged section of fig. 4.17 (a) with different boundary misorientations shown. In (a) the minimum misorientation is set to 2°, while in (b) the minimum misorientation is set to 0.5° on the same area, in order to distinguish between different types of boundaries. In the lower part of the map, a grain has broken up into elongated cell blocks separated by boundaries of 2-25° misorientation. When the boundaries of misorientation less than 2° are added to the map in (b), it is apparent that the cell blocks are further subdivided into cells. In the upper part of the map a parallelogram shaped structure has developed with misorientations ranging from 3° to 30°. Also these domains are further subdivided.

TEM micrographs of the AlMg1 alloy cold rolled to ε=0.5 are shown in fig. 4.19. The dislocation structure is seen to be non-uniform, with both elongated subgrains (a) and more equiaxed diffuse cells (b). In (b) the cell walls are seen to have a considerable thickness. Since the variations in the substructure within one sample are large, these pictures serve only as examples. After cold rolling to higher strains, clusters of narrow elongated bands, or lamellae, appear frequently. Fig. 4.20 is a mapped area of AlMg1, cold rolled to ε=2, where such a laminar subgrain structure is seen.

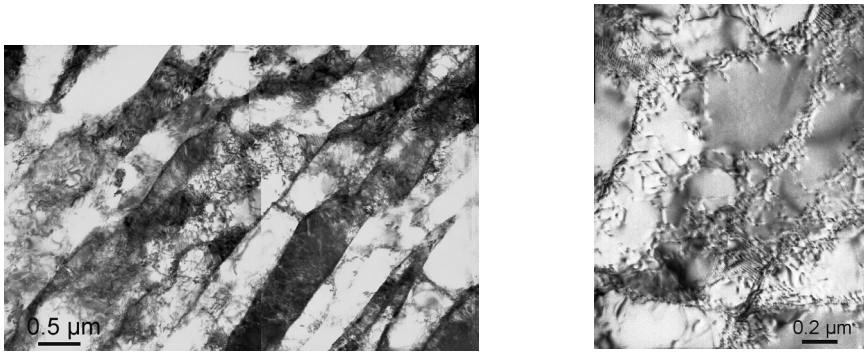

(a) (b)

Figure 4.19: TEM micrographs showing variations in the substructure in AlMg1 cold rolled to ε=0.5. (a) Elongated subgrains with sharp boundaries and (b) more equiaxed cells with diffuse boundaries.

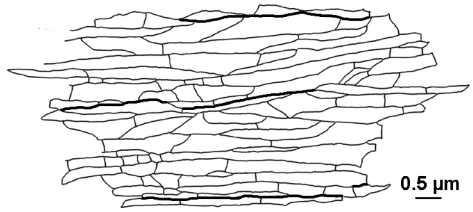

Figure 4.20: TEM-mapping of subgrains in AlMg1, ε=2. HAGBs given by bold lines.

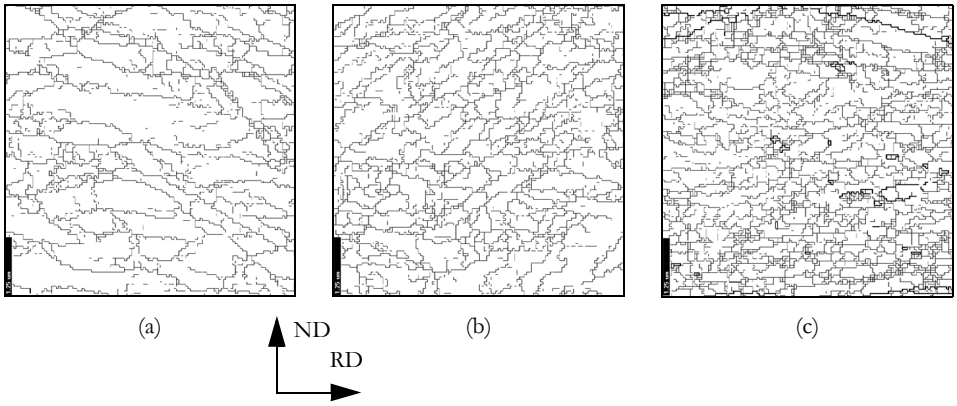

Figure 4.21: EBSD maps of similar magnification illustrating the influence of Mg-addition on the subgrain structure. Here, grains of copper orientation after cold rolling to ε=2 are shown. (a) AA1050, (b) AlMg1, (c) AlMg3. Boundaries of >0.5° misorientation are plotted. The scale bar is 1.25 µm long.

Effect of Mg-addition

One effect of the Mg-addition on the substructure can be seen in fig. 4.21. These EBSD maps show the subgrain boundaries within copper oriented grains in AA1050, AlMg1 and AlMg3 cold rolled to ε=2. Obviously, the structure becomes more refined as the Mg concentration is increased.

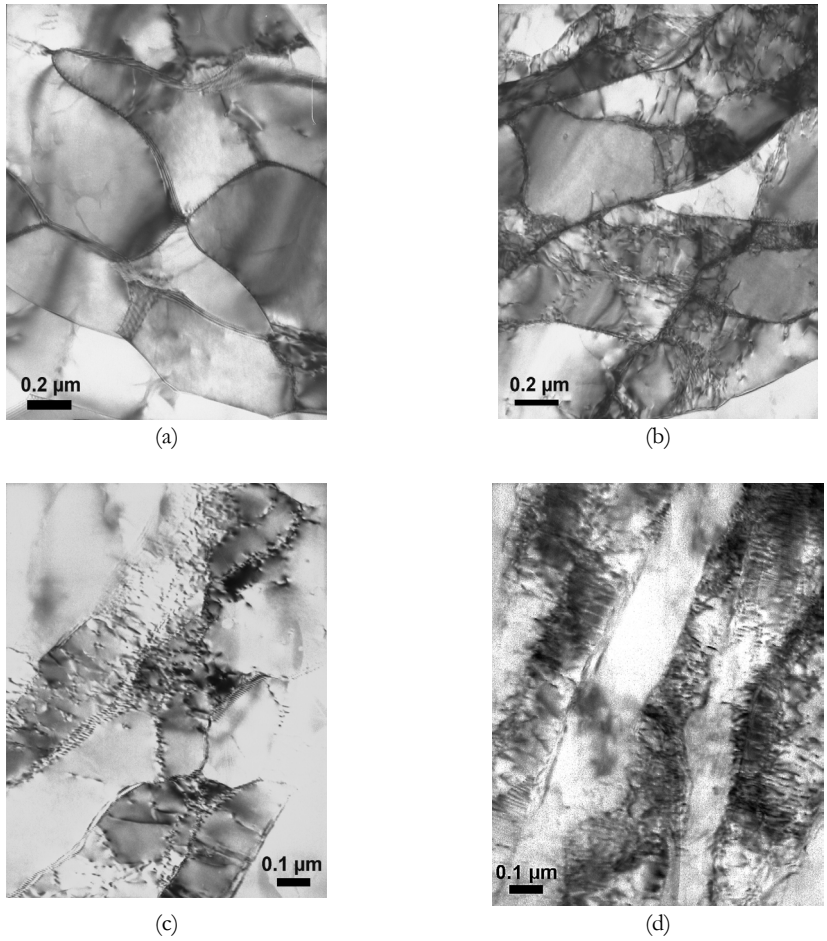

Figure 4.22: TEM micrographs of subgrains in (a) AA1050, (b) AlMg0.5, (c) AlMg1 and (d) AlMg3, all cold rolled to ε=2.

Another effect of the Mg-addition is the observed difference in dislocation density inside the subgrains. Fig. 4.22 shows TEM micrographs of subgrains in AA1050 and the AlMgX alloys after cold rolling to ε=2. In AA1050(a), sharp subgrain boundaries surround almost dislocation-free regions in the material. With Mg present in the material

the dislocation density is seen to increase, and in the AlMg3 alloy the dislocation structure is very diffuse. There is also a tendency towards thinner and more elongated subgrains in the AlMg alloys

4.4.2 Subgrain size

The subgrain size was measured by the linear intercept method along the normal direction on EBSD maps. Several maps were acquired from each specimen since the degree of grain subdivision varied from grain to grain. Several thousand measurements were obtained from each specimen. In order to be able to compare the results as good as possible, a constant step size of 0.05 μm was used in all the substructure analyses. Subgrains are in this context defined as all material volumes surrounded by either low-angle boundaries (<15°) or high-angle boundaries (>15°). No distinction is made between different types of boundaries, as GNBs or IDBs. An intercept length of 0.15 μm (three steps in the EBSD map) and a misorientation of 0.5° are used as lower cut-off values. The VMAP software is used in these analyses, and an average subgrain size is calculated for each map.

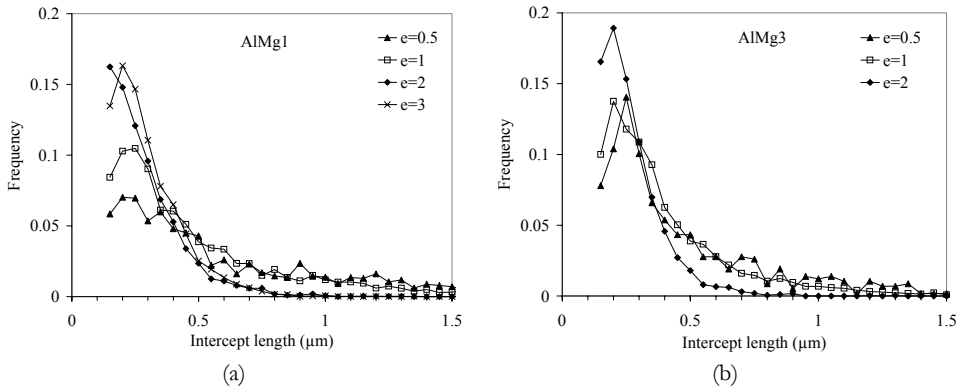

Figure 4.23: Frequency distribution of intercept lengths along ND in (a) AlMg1 and (b) AlMg3 after various cold rolling reductions. 0.15 μm (three steps in the EBSD map) is set as the lowest accepted value.

The evolution in subgrain size with cold rolling strain is plotted as frequency distributions in fig. 4.23 for AlMg1 and AlMg3. Here, it is seen that the number of small subgrains (<0.4 μm) increases with strain. At ε=0.5 intercept lengths up to 10 μm, or even more, are detected, while at the highest strains almost no subgrains are larger than 0.75 μm. Average values are shown in fig. 4.24 for AA1050, AlMg1 and AlMg3. As expected, the subgrain size decreases with increased thickness reduction of the sheet.

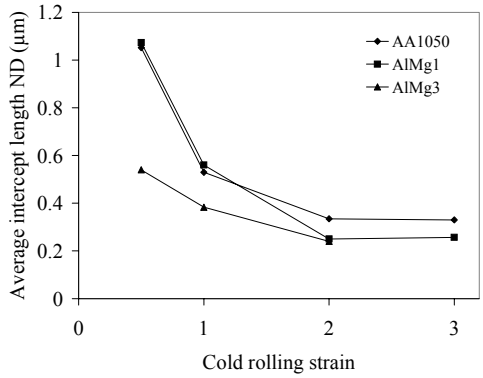

Figure 4.24: Average intercept length, or subgrain size, in the normal direction measured on EBSD maps of AA1050, AlMg1 and AlMg3.

The addition of Mg in the alloys also results in a smaller subgrain size, in accordance with the observed trend in fig. 4.21. Especially the AlMg3 alloy, which has an average subgrain size of 0.55 µm already at ε=0.5, shows a more rapid refinement of the substructure than AlMg1 and AA1050.

4.4.3 Subgrain misorientation

SEM results

The same procedure as used for subgrain size measurements in the previous subsection was used to find the misorientation between subgrains. Only boundaries between 0.5° and 15° are included in this analysis. Frequency distributions for each of the strain levels are plotted in fig. 4.25 (a, b) for AlMg1 and AlMg3. With increasing strain the number of boundaries <1.5° is reduced while the number of boundaries >1.5° is increased. Average values are shown in fig. 4.25 (c), where the misorientation increases with strain. No clear variations with the Mg-content are observed.

TEM results

Orientation measurements were also performed in TEM, both on TEM-maps, along line scans and from randomly chosen subgrains. This investigation resulted in misorientation distributions as in fig. 4.26 (a), where the misorientation in AlMg1 after cold rolling to ε=0.5 and ε=2 is shown. It is seen that the peak is shifted towards higher angles as the strain increases. The average misorientation of LAGBs (0-15°) is calculated and the evolution of this parameter with strain is plotted in fig. 4.26 (b), showing a continuous

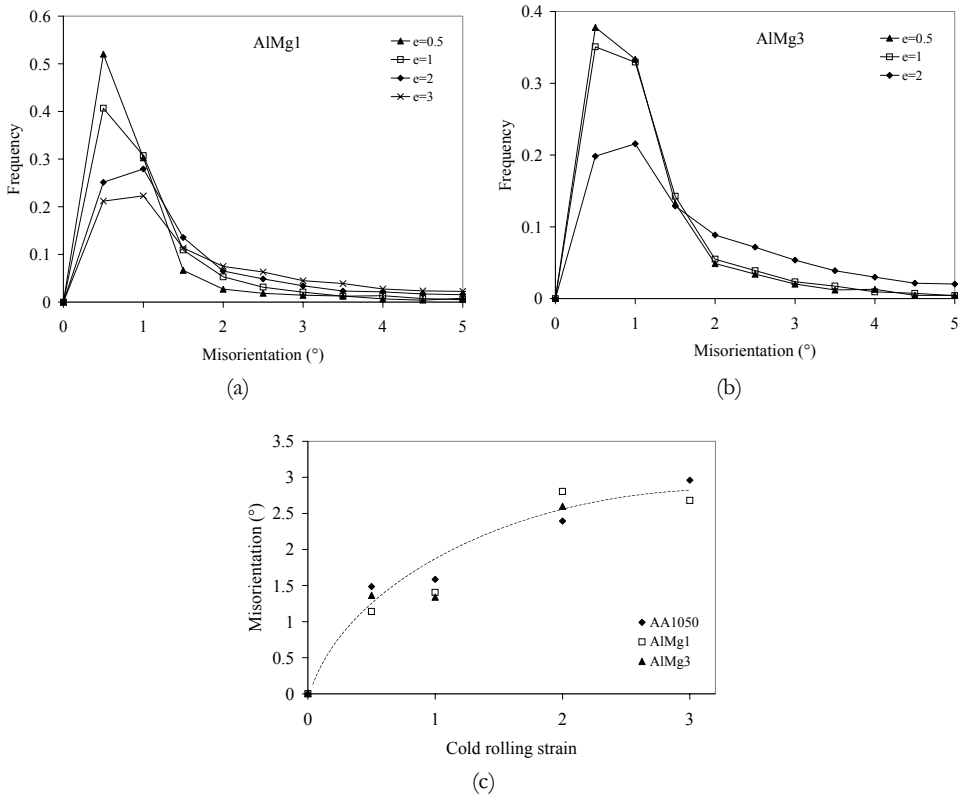

Figure 4.25: (a,b) Frequency distributions of misorientations in AlMg1 and AlMg3. (c) Average subgrain misorientation measured on EBSD maps of AA1050, AlMg1 and AlMg3.

increase with strain, except for AlMg0.5. It should be noted that a relatively small number of boundaries were measured using this technique, see table A-3 in the appendix.

The above results from EBSD and TEM show that the subgrain misorientation in these alloys increases with deformation in the investigated strain range. The largest part of the increase occurs in the early stage of deformation, i.e. during the building-up of a subgrain structure. The TEM-results, fig. 4.26 (b) may also indicate that a higher Mg-content makes the misorientation increases at the highest strains. This trend is, however, not observed in EBSD. It is also interesting to note that the EBSD-results are considerably smaller than the TEM-results, about one half. This discrepancy is caused by the different measuring techniques and will be further discussed in the following subsection.

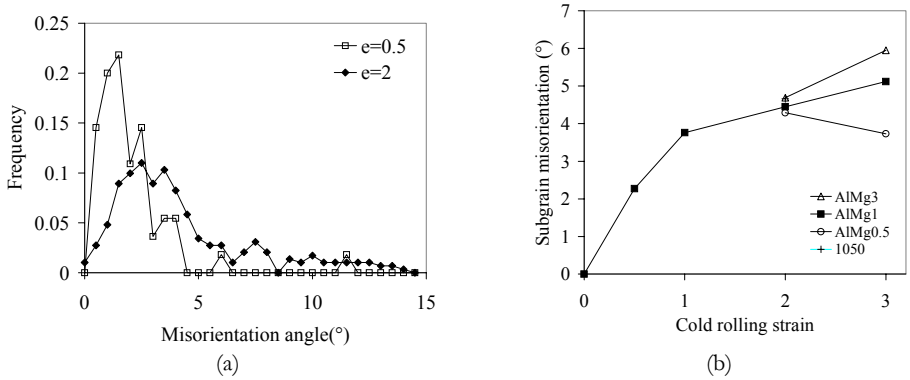

Figure 4.26: Misorientation results from TEM. (a) Frequency distribution of misorientations of 0°-15° for AlMg1, here shown for ε=0.5 and 2. (b) Average misorientations plotted against cold rolling strain for the AlMgX alloys and AA1050.

4.4.4 About substructure measurements

In this work the evolution in substructure during cold rolling was investigated using FE-SEM/EBSD and TEM. Generally, in the literature TEM is considered as the only available tool for the characterisation of cold rolled materials because of its high spatial and angular resolution. In the past years, however, high-resolution EBSD has started pushing the resolution limits of SEMs towards the resolution of TEM. The current high-performance FE-SEMs have a theoretical resolution of about 1 nm. For EBSD applications, such as those in the present work, a spatial resolution of some 25-50 nm is more realistic because of the need for a relatively high beam current, large working distance and the fact that the specimen is tilted 70°. The measurements of the subgrain size in fig. 4.24 are in agreement with other reported values, which demonstrates that the spatial resolution is sufficient.

An interesting qualitative observation is that the deformation structures described by the Risø-group based on TEM work, see fig. 2.5, are detected in the present materials using high-resolution EBSD, fig. 4.16-fig. 4.17. Microbands, cell blocks and lamellae are easily seen from theses EBSD maps.

Distributions of misorientations measured by TEM and FE-SEM/ EBSD in AlMg1, ε=2, are compared in fig. 4.27. 291 measurements were performed in the TEM, while several thousand boundaries were detected in the SEM. This difference in the number of measurements demonstrates the advantage of FE-SEM over TEM on the statistical validity of the data. The inhomogeneity of the structure may alone explain some of the

differences between the results, as it is very time consuming to map a representative area in TEM.

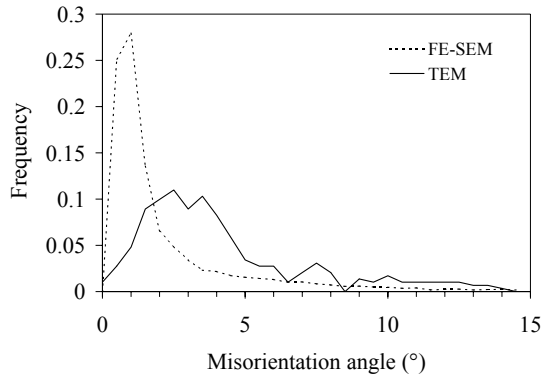

Figure 4.27: Frequency distributions of subgrain misorientations in AlMg1, ε=2, measured with TEM and FE-SEM (EBSD).

The φ-results from TEM are valid down towards 0°, while the FE-SEM obviously shows problems with the angular resolution below 1-1.5°. The high number of misorientations between 0.5 and 1.5° is probably due to orientation noise and results in a lower average φ than what is measured using TEM (compare fig. 4.25 (a) and fig. 4.26 (a)). Even after orientation averaging with the VMAP software, a very high peak is seen at 0.5 and 1°. On the other hand, since all the EBSD maps used for substructure characterisations are acquired by the same procedure, the results obtained from them are comparable. Therefore, the trends in fig. 4.25 are believed to be realistic, although the misorientation values are probably somewhat too low. All in all, the FE-SEM appears to be a promising tool for mapping of subgrain structures. It still has some limitations regarding the angular resolution, but the ever-increasing performance of new instruments may push these limits down.

4.5 Mechanical properties and work hardening

This section is divided into three parts, where the AlMgX alloys and AA1050 are presented in section 4.5.1, the AA3103 alloy in section 4.5.2 and the AA5xxx alloys in section 4.5.3. The materials were tested in uniaxial tension, and partly in compression, from the O-temper condition and cold rolled condition.

4.5.1 AA1050 and AlMgX alloys

O-temper materials

Tension: Alloys with various concentrations of Mg were tested in uniaxial tension, see fig. 4.28 and table 4.3, where the AlMgX alloys are compared to the Mg-free AA1050. The stress-strain curves are obtained from as-cast and homogenised materials, i.e. coarse-grained materials with grain sizes in the range 68-117 μm, see table 4.1. As expected, both the yield stress, the rate of work hardening and the ultimate tensile strength increase with Mg-additions. It is also evident from the curves of AA1050 and AlMg0.5 that only small additions of Mg reduce the ductility. The flow curves of the three AlMg alloys are partly serrated, indicating a dynamic strain ageing effect that appears to increase with the Mg-concentration.

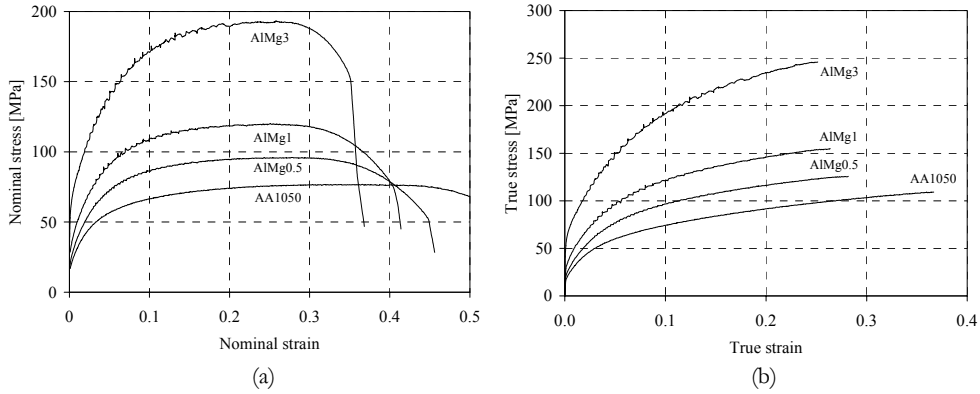

Figure 4.28: Stress-strain curves obtained from uniaxial tension of the AlMg alloys and the AA1050 alloy. (a) Nominal stress and strain. (b) True stress and strain.

A range of grain sizes were obtained for each of the alloys (table 4.2), and stress-strain curves from uniaxial tension of these variants are plotted in fig. 4.29. The effects of decreasing the grain size are seen to be an increase in the yield stress, but only a small increase in the work hardening rate. A slight decrease in ductility is also observed. In AlMg1 and particularly in AlMg3 a reduction of the grain size promotes the formation of Lüders bands, evidenced by a yield point elongation. All the mentioned effects are most prominent when the grain size is reduced to below 15-20 μm, or 1/6 or less of the original grain size.

Table 4.3: Uniaxial tension properties of AA1050 and the AlMgX alloys.

Alloy	$R_{p0.2}$ [MPa]	R_m [MPa]	A_m
AA1050	24.0	76.8	0.44
AlMg0.5	28.0	95.9	0.33
AlMg1	38.3	119.9	0.30
AlMg3	62.1	193.4	0.29

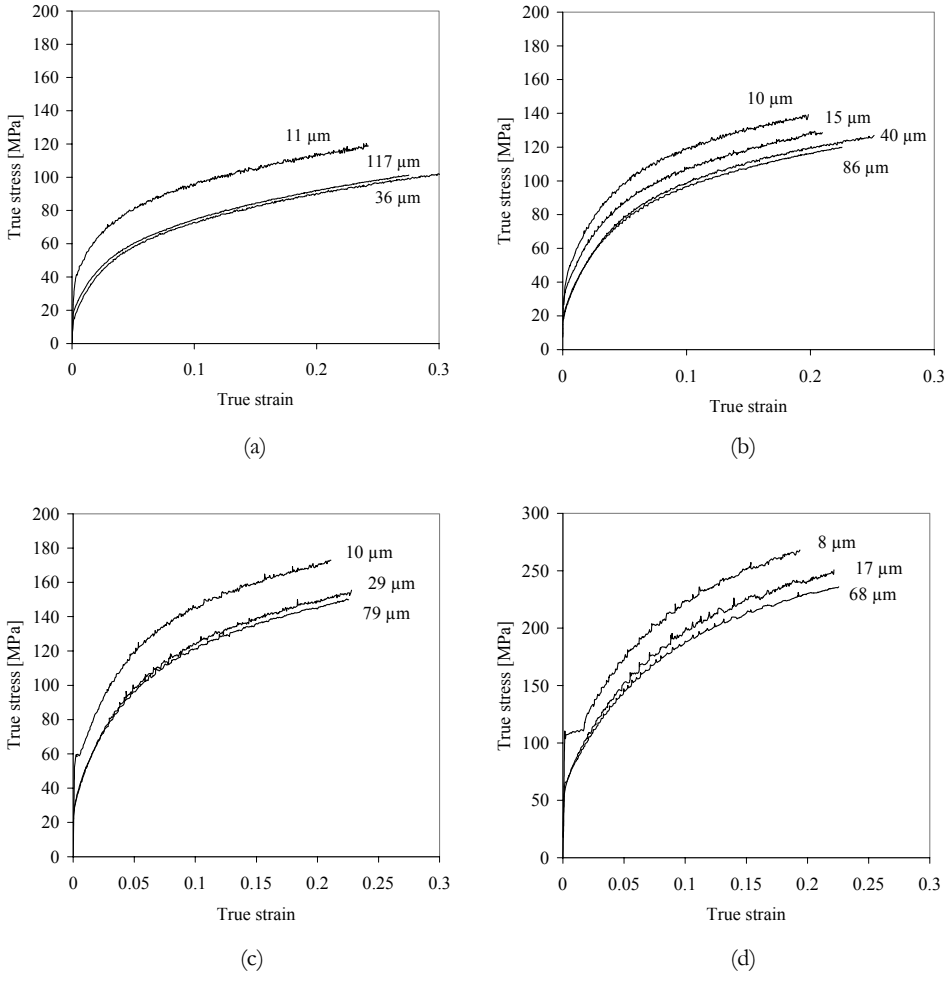

Figure 4.29: Stress-strain curves from uniaxial tension of materials with a range of grain sizes. (a) AA1050. (b) AlMg0.5. (c) AlMg1. (d) AlMg3.

Compression: The coarse-grained alloys were tested in uniaxial compression in the REAP project, and a comparison is made to the tension curves in fig. 4.30. The curves show that the tension and compression results are in good agreement. Therefore, while the tension curves stop at ε=0.25-0.35, the compression results provide continuous flow curves for strains up to ε=0.5-0.8.

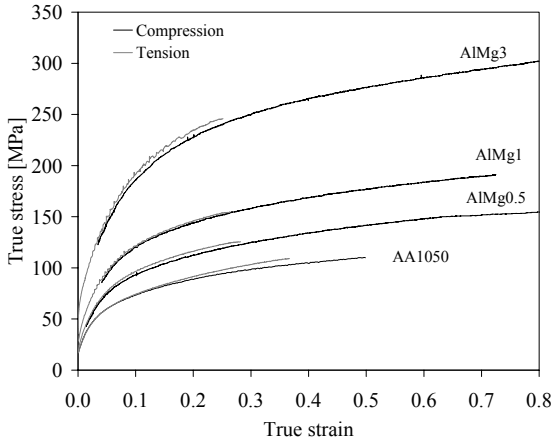

Figure 4.30: Stress-strain curves obtained from uniaxial compression of the AlMg alloys and the AA1050 alloy (results from the REAP project). Results from uniaxial tension shown for comparison.

Work hardening during cold rolling

The coarse- and fine-grained alloys were also tensile tested after various cold rolling reductions. In fig. 4.31 these results (yield stress and ultimate tensile strength) are plotted at the strains they were cold rolled to. The results of the compression and tensile testing are displayed in the same diagrams, so the diagrams give an estimate of the stress-strain behaviour in the strain range ε_{vM}=0-3.5. The stress measured in the cold rolled materials is seen to be somewhat higher than the corresponding stress measured in the compression tests, i.e. at ε=0.5-0.8.

What can be seen from fig. 4.31 (a) is a curved stage II-III with a high but decreasing work hardening rate, followed by a linear stage IV with a low work hardening rate. While the rate of work hardening depends strongly on the amount of Mg at strains up to ε=0.2, the curves are nearly parallel at strains above ε=0.5. Neither the grain size seems to influence the hardening rate of stage IV, fig. 4.31 (b). Another observations is the difference between $\sigma_{0.2}$ and σ_{UTS}. In general this difference is small at the smallest strains and increase towards larger strains. However, the AlMg3 alloy deviates from this trend.

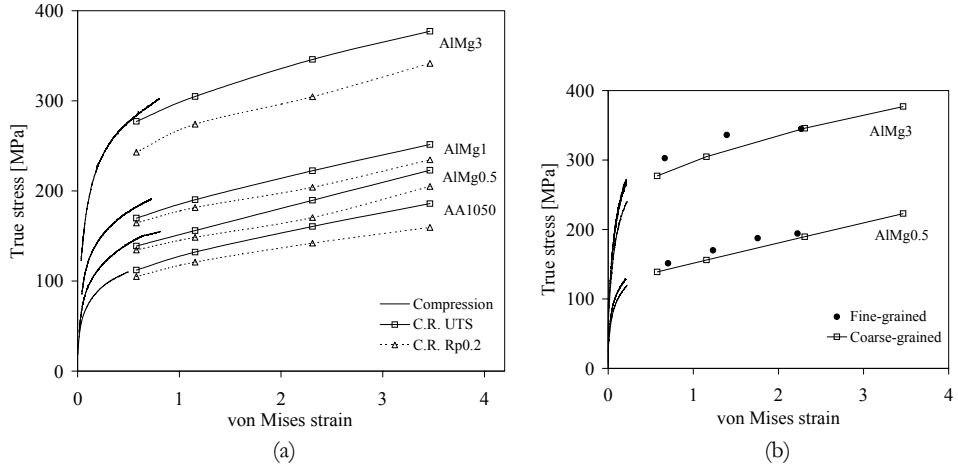

Figure 4.31: Stress-strain behaviour at large strains achieved by cold rolling of the AlMg alloys and the AA1050 alloy. (a) Coarse-grained materials. Both the yield strength and the ultimate tensile strength are plotted. (b) Fine-grained and coarse-grained AlMg0.5 and AlMg3. Only the ultimate tensile strength is plotted here.

For this alloy the difference between $\sigma_{0.2}$ and σ_{UTS} is almost constant for all strains, and the difference is also much larger than for the other alloys.

4.5.2 AA3103

O-temper materials

Four conditions of the AA3103 alloy, having a range of concentrations of Mn in solid solution (see table 3.2) were tested in uniaxial tension, fig. 4.32. Here, they are compared to the Mn-free and almost particle-free alloy AA1050. The stress-strain curves are obtained from the as-cast and homogenised conditions (A, B and C), i.e. coarse-grained materials with a grain size of approximately 65 μm. The homogenisation procedure, giving rise to lower solute levels of Mn, significantly decreases the yield stress and, to a less extent, the work hardening rate. On the other hand, the ductility is seen to increase, especially in the step from the as-cast condition to the homogenised conditions.

A fine-grained variant (D=6 μm) of the condition B was also tested in uniaxial tension, and the stress-strain curve from this is plotted in fig. 4.33 (a) together with the coarse-grained material. The only significant effect of decreasing the grain size seems to be a higher work hardening rate in the strain range 2-10%.

Table 4.4: Mechanical properties of as cast and homogenised variants of AA3103.

Alloy	$R_{p0.2}$ [MPa]	R_m [MPa]	A_m
As cast	58.3	124.1	0.21
Hom A	47.0	109.6	0.30
Hom B	46.0	101.7	0.36
Hom C	40.5	94.1	0.43

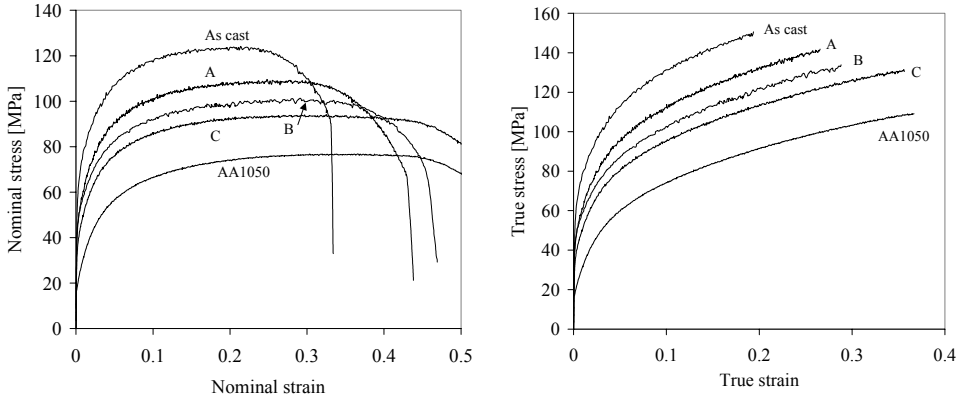

Figure 4.32: Stress-strain curves for the variants of AA3103 with AA1050 added for reference. (a) Nominal stress and strain. (b) True stress and strain.

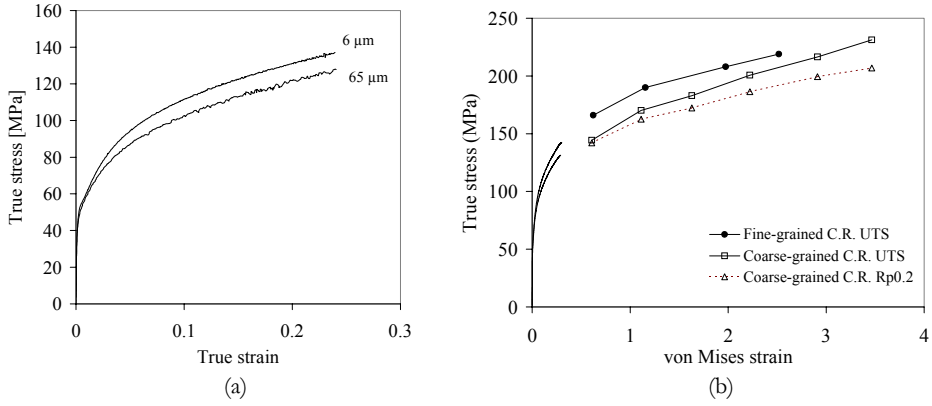

Figure 4.33: (a) Stress-strain curves for the fine-grained and coarse-grained conditions of AA3103-B. (b) Stress-strain behaviour at large strains achieved by cold rolling of the AA3103-B alloy. Both the yield strength and the ultimate tensile strength are plotted for the coarse-grained variant.

Work hardening during cold rolling

The coarse- and fine-grained variants of condition B were also tensile tested after various cold rolling reductions. In fig. 4.33 (b) the yield strength and the ultimate tensile strength of the cold rolled materials are plotted at the strains they were cold rolled to. Results from tensile testing of the O-temper conditions are displayed in the same diagrams, so the diagrams give estimates for the stress-strain behaviour in the strain range ε_{vM}=0-3.5. The results are comparable to the AA1050 and AlMg alloys in the previous subsection.

4.5.3 AA5xxx alloys

The following results were provided by Hydro Aluminium Deutschland, a partner in the VIRFORM project.

O-temper materials

Two commercial alloys from the AA5xxx system were tested in uniaxial tension. These were the low-Mg alloy AA5005 and the high-Mg alloy AA5182. The tests were performed on the transfer slab materials, i.e. materials that were break-down hot rolled after casting and homogenisation. The results are displayed in fig. 4.34 and in table 4.5. Both the yield stress and the rate of work hardening are significantly higher in the AA5182 alloy than in AA5005. This is in agreement with the properties of the AlMgX alloys in section 4.5.1. The total elongation is seen to be almost similar for the two alloys, but necking starts a little earlier in AA5005 than in AA5182. The high-Mg alloy also shows a yield point elongation (cf. fine-grained AlMg1 and AlMg3) and a serrated flow curve, indicating a dynamic strain ageing effect.

Table 4.5: Mechanical properties of AA5005 and AA5182 transfer slab materials.

Alloy	$R_{p0.2}$ [MPa]	R_m [MPa]	A_m
AA5005	54	138.8	0.22
AA5182	107	265.3	0.25

Work hardening during cold rolling

These alloys were also tensile tested after various cold rolling steps. In fig. 4.35 these results (yield stress and ultimate tensile strength) are plotted at the strains they were cold rolled to. The flow curves of the transfer gauge materials are displayed in the same diagrams, and so this diagram gives an estimate of the stress-strain behaviour in the strain range ε_{vM}=0-4.6. The results are comparable to the AlMg model alloys in section 4.5.1

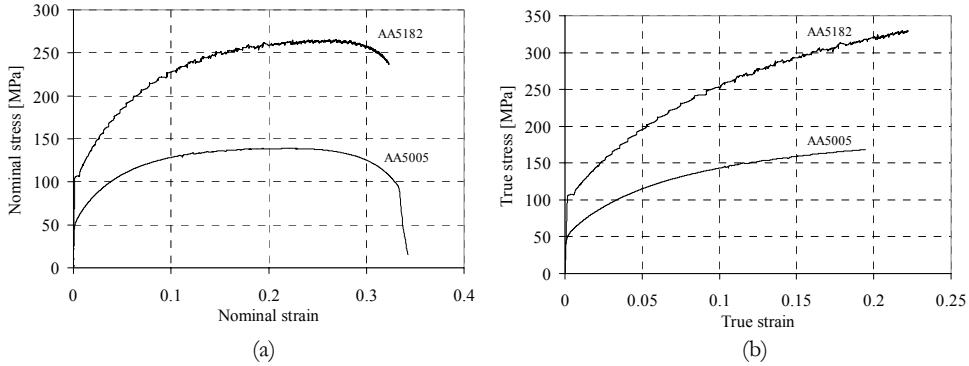

Figure 4.34: Stress-strain curves obtained from uniaxial tension of the transfer slab gauges of AA5005 and AA5182. (a) Nominal stress and strain. (b) True stress and strain. Courtesy of O.Engler.

and the AA3103 alloy in section 4.5.2. Only one major deviation is visible: For AA5182 the difference between the yield stress and the ultimate tensile strength is large at small strains and retards towards larger strains. This is the opposite of what is observed in the low-Mg alloys and AA3103, but consistent with the behaviour of the AlMg3 alloy.

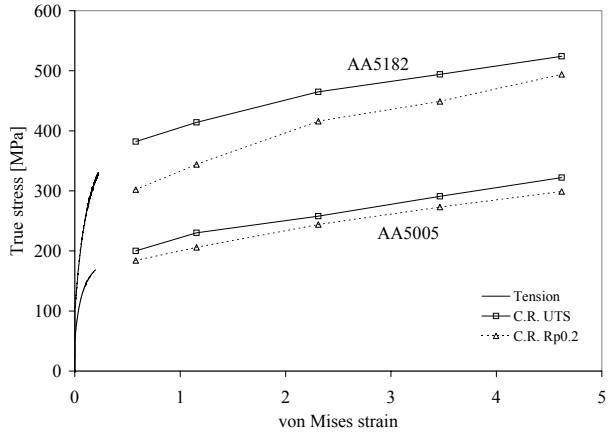

Figure 4.35: Stress-strain behaviour at large strains achieved by cold rolling of the AA5xxx alloys. Both the yield strength and the ultimate tensile strength are plotted. Courtesy of O.Engler.

5. Discussion

In the previous section the microstructure, texture and mechanical properties of a number of aluminium alloys are described. In the present section, these observations are further analysed and correlated to each other. The work hardening model presented in section 2.5.3 is applied to the different alloys in order to verify and improve the model, but also to help explaining the observed results.

Mechanical properties: A rough analysis of the alloying effects on the mechanical properties is given in fig. 5.1. This diagram shows the ultimate tensile strength, R_m, of all the alloys investigated in this work. Both the O-temper and the 87% cold rolled (ε=2) materials are shown with the strength as a function of the total alloying addition (in wt%). The ultimate tensile strength is generally seen to follow a linear relationship in just the same manner as for the alloys in fig. 2.1. The H18 temper in fig. 2.1 corresponds to approximately 75% reduction, while the cold rolled materials plotted in fig. 5.1 were subjected to 87% reduction. This explains the small difference in strength of the cold worked alloys.

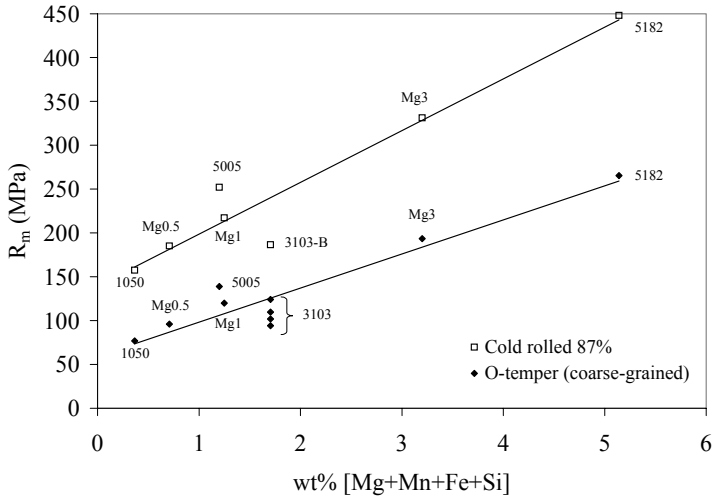

Figure 5.1: Ultimate tensile strength (R_m) plotted as a function of the total alloying content (wt%).

There are however, some notable deviations from the linear approximation. The AA3103 alloy was processed in different ways in order to alter the amount of Mn in solid solution. This resulted in variations in the mechanical properties, despite the fact that the

total amount of alloying elements is constant. Also the AA5005 alloy lies a bit off the trendlines. Therefore, a further analysis of the solute and particle effects is given in the following sections 5.1 and 5.2.1. The materials in fig. 5.1 are all coarse-grained, and a discussion of grain size effects is given in section 5.2.2.

Texture: The evolution of texture during large strain cold rolling is studied in this work. Generally, the texture results presented in section 4.2 are in agreement with observations from the literature, see review in section 2.2.6. Adding 3% Mg to AA1050 promotes the formation of the B-component at high strain (cf. fig. 2.13). Adding about 5% Mg, as in AA5182, results in a stronger B-component due to shear banding (Lücke and Engler 1990, Koizumi et al. 2000), but a weakening of C and S, giving a flat β-fibre (fig. 2.15). Reducing the grain size gives a much more rapid development of the rolling texture, indicating more homogeneous slip in a fine-grained material (fig. 2.14). The AA5005 alloy has a strong initial cube texture where the grains have to undergo large rotations in order to obtain β-fibre orientations. Therefore, this alloy shows a slow rolling texture evolution and a β-fibre different from the other. Additionally, Sjølstad et al. (2002) found that the texture evolution in the AA3103 alloy (condition A, B C) developed a rolling texture very similar to that of AA1050. This is in accordance with Lücke and Engler (1990) and suggests that the deformation zones around the particles are relatively small.

Microstructure: All the microstructural investigations, from light optical microscopy to SEM and TEM, demonstrate the inhomogeneity of the large strain deformation structure, both on the grain scale and the subgrain scale. Qualitatively spoken, the substructure observed in this work corresponds to the picture given by the Risø-group, section 2.2.2. At moderate strains, ε=0.5-1, the original grain shape is still detectable, although elongated in the rolling direction. Inside the grains a substructure has developed, which in some grains is in accordance with fig. 2.4 and fig. 2.5 (a, b). In other grains the substructure is more diffuse. This difference is ascribed to the grain orientations and variations in subdivision within grains (e.g. grain centre vs grain vicinity). Several authors have studied the correlation between grain orientation and subdivision, e.g. Driver et al. (1994) and Delannay et al. (2001), but no great effort is done in this work to study such effects.

The microbanded structure seen in AlMg3 cold rolled to ε=0.5 and ε=1, fig. 4.16, appears more seldom in AA1050 and AlMg1. At larger strains, shear bands are more frequent in the high-Mg alloys. These observations are in agreement with the work of Korbel et al. (1986), who found that both crystallographic microbands and non-

crystallographic shear bands were formed at lower strains in AlMg4.8 than in pure Al. The microbands were formed in a tangled dislocation structure, which in later works has been denoted Taylor lattice. Korbel and co-workers observed that the microbands eventually crossed grain boundaries and organised into shear bands. A further discussion of these and other microstructural features are given in relation to the modelling of stage IV in section 5.3.2.

5.1 Solute effects

In the following discussion of solute effects, it is distinguished between binary and commercial alloys, regarding the purity of the alloys:

- Binary high-purity alloys, impurity level <0.05 wt%
- Commercial alloys, impurity levels 0.2-0.7 wt%

where the impurities basically are Fe, Si and Cu. The first group covers the classical results on AlMg alloys obtained by Sherby et al. (1951) and some other references as well. All the materials shown in fig. 5.1, i.e. AA1050, the AlMgX alloys, the AA5xxx alloys and the AA3103 alloys belong to the second group.

5.1.1 Stage II-III

Stage II of work hardening is often referred to as a linear stage of high rate, followed by a stage III of decreasing rate. In most polycrystalline alloys a linear part of the stress-strain curve is difficult to detect, and a transition between stage II and III is so smooth and diffuse that any separation of the two stages is impossible. In this subsection stage II and III are treated as one "stage", characterised by a stress-strain curve of high, but decreasing rate.

Binary high-purity AlMg alloys

The data from Sherby et al. (1951) in fig. 2.16 (b) shows the effect of Mg additions to high-purity Al on the room temperature stress-strain behaviour. The flow stress at various strain levels from that diagram is plotted against the Mg-content in fig. 5.2. The flow stress of the pure metal ($\sigma_{99.99}$) is subtracted from the alloy data, and the data are fitted to a power law relation of the type:

$$\sigma = \sigma_{99.99} + Kc^{n} \tag{5.1}$$

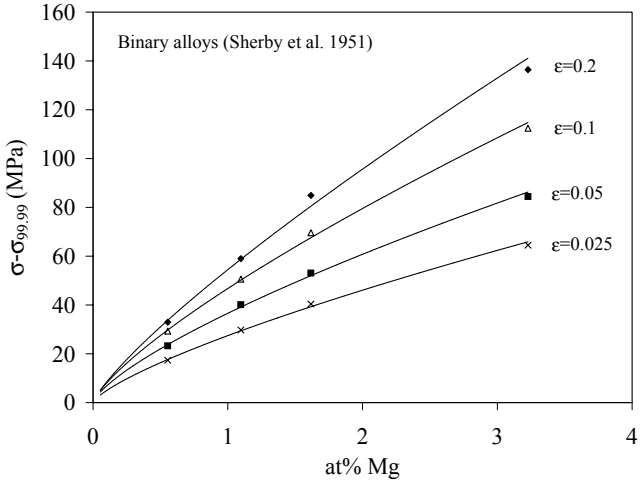

Figure 5.2: Flow stress of binary AlMg alloys with the flow stress of $Al_{99.99}$ subtracted. Variation with Mg content. (Sherby et al. 1951)

where c is the alloying concentration in at% and the values for $\sigma_{99.99}$, n and K given in table 5.1. It is seen that while the hardening coefficient, K, increases with strain, the hardening exponent, n, is close to 0.75 irrespective of strain. This gives a general relationship for the solute dependence in the binary alloys:

$$\sigma = \sigma_{99.99} + Kc^{3/4} \tag{5.2}$$

which deviates slightly from eq. (2.9), given by Mitchell (2001).

Elevated temperature: Sherby and co-workers also tested these alloys at elevated temperatures. Above 200°C the strength of the alloys decreased rapidly with temperature, but the solid solution hardening potential was more or less contained. At 277°C eq. (5.1) turns into:

$$\sigma = \sigma_{99.99} + 28 \cdot c^{0.7} \tag{5.3}$$

i.e. the n-value has become a little smaller than at room temperature. K=28 MPa/at%, is almost invariant of strain at this temperature. At an even higher temperature, 377°C, the trend continues with lower values of n and K:

$$\sigma = \sigma_{99.99} + 12 \cdot c^{0.65} \tag{5.4}$$

Table 5.1: Values of the parameters in eq. (5.1) at various strain levels of binary AlMg alloys, deduced from fig. 5.2.

Strain	$\sigma_{99.99}$ (MPa)	K (MPa/at%)	n
0.025	25.3	27.4	0.75
0.05	34.7	36.6	0.73
0.1	45.5	46.7	0.77
0.2	58.6	54.5	0.81

Commercial AlMg alloys

Based on the stress-strain curves from uniaxial tension of AA1050 and the AlMgX alloys in section 4.5, the contribution to strength from Mg-atoms in solid solution is estimated. AA1050 has, except for the Mg, an almost similar chemical composition as the AlMgX alloys (table 3.1), and can therefore be regarded as a Mg-free reference material. The alloys are processed in the same way and have random initial textures. They are also assumed to contain similar second-phase particle structures. The grain sizes are somewhat different, but since they all are in a range where grain size effects are small (see section 5.2.2), this effect is neglected. Also AA5182 has an almost random texture and a grain size comparable to the alloys above. The Fe and Si content is similar as well, but with a Mn content of 0.27 wt% this alloy is thought to behave differently from the AlMgX alloys. It is seen below however, that all these alloys are comparable. AA5005 is discussed individually below, and is kept out of the following analysis.

In fig. 5.3 the stress at various strain levels are plotted against the concentration of Mg (at%). The flow stress of the AA1050 alloy ($Al_{99.6}$) is subtracted. The results are fitted to a similar relationship as eq. (5.1), and the values of $\sigma_{99.6}$, K and n are given in table 5.2. It

Table 5.2: Values of the parameters in eq. (5.1) at various strain levels of commercial AlMg alloys, deduced from fig. 5.3.

Strain	$\sigma_{99.6}$ (MPa)	K (MPa/at%)	n
0.002	20	11.3	1.22
0.025	47	21.8	0.98
0.05	60	30.6	0.92
0.1	74	40.9	0.92
0.2	92	46.0	0.99

is interesting to see that the flow stress is almost linearly dependent on the concentration of Mg, as *n* is close to 1, higher than for the binary alloys above. It is here assumed that all the Mg is in solid solution, i.e. that the primary particles contain no Mg. This is believed to be a reasonable assumption, supported by a work of Lloyd (1980b), where the particles in the commercial alloys AA5052, 5154 and 5083 contain Fe, Mn and Cr in addition to Al, but no Mg.

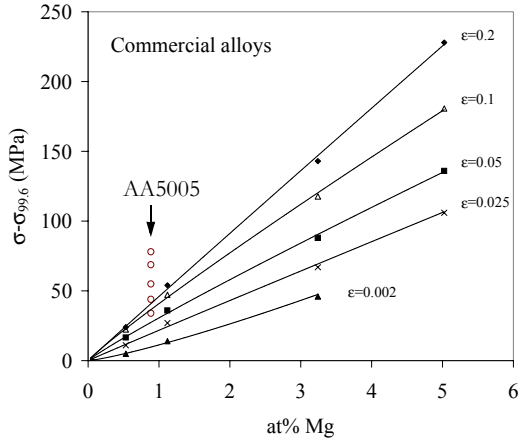

Figure 5.3: Flow stress at various strain levels as a function of the amount of Mg fitted to the power law in eq. (5.1). AA1050, AlMgX alloys and AA5182. AA5005 is also shown, but is not included in the curve fitting. The flow stress of AA1050 ($\sigma_{99.6}$) is subtracted.

Yield strength: Above, a power law relationship was used to fit the concentration dependence of the flow stress. In the literature however, linear relationships are frequently reported. Hence, if a *linear* fitting of the yield strength ($\sigma_{0.2\%}$) of the commercial alloys is performed instead, a slightly different *K*-value as compared to table 5.2 is given:

$$\sigma_{0.2\%} = 20 + 14.5 \cdot c \tag{5.5}$$

In the literature a range of *n*-values is found, varying between 0.5 and 1. However, there is a tendency that pure, idealised solid solutions exhibit *n*-values in the lower part of this spectrum, 0.5-0.65 (Fleischer and Hibbard 1963, Haasen 1996). Commercial AlMg alloys are reported to follow a trend like eq. (5.5), i.e. with n=1. Values of *K* between 14.5 and 17.3 MPa/at% have been reported for the yield strength (Metals Handbook 1990, Burger et al. 1995). These observations are in very good accordance with eq. (5.5). Based on this,

it is suggested that by increasing the impurity level in AlMg alloys, the hardening exponent, *n*, increases from 0.5 in extremely pure alloys to about 1 in commercial alloys. The reason for this is not clear, but may for example relate to the strong effect of impurities (see below), and perhaps a combined hardening from Mg with Fe/Si.

AA5005: The AA5005 alloy is worth an extra comment. As compared to its content of alloying elements (0.8 wt% Mg), this alloy has a relatively high strength that corresponds to a Mg content of about 2 wt%, see fig. 5.1 and fig. 5.3 . An inspection of its flow curve in comparison with AlMg1, fig. 5.4, shows a high yield strength, whereafter the subsequent work hardening does not differ that much from AlMg1. In section 4.1 it was shown that AA5005 has a large grain size and a strong cube texture, but none of these effects are expected to raise the strength of the alloy. However, the stress-strain behaviour is indicative of a particle contribution to the strength (to be discussed further in section 5.2). Also AA5182 was break-down hot rolled, and some precipitation should be expected here as well. But since this alloy gives very small changes to the trendlines in fig. 5.3 and the numbers in table 5.2, any contribution from precipitates is neglected in AA5182.

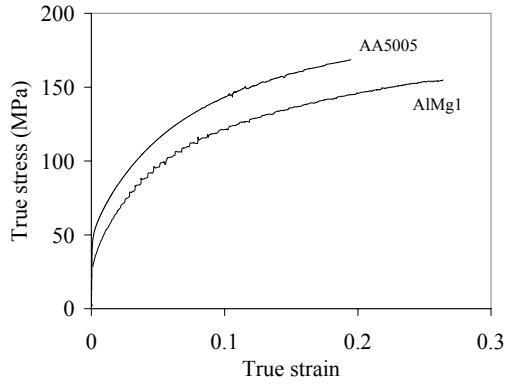

Figure 5.4: Comparison of the stress-strain curves for AA5005 and AlMg1 showing a high initial strength of AA5005.

Elevated temperature: The AA1050 and AlMgX alloys were tested in torsion at elevated temperatures by Nes et al. (2001). Different strain rates and temperatures were used (typically 350-550°C), and the peak flow stress at a selected Zener-Hollomon parameter (ln Z=25) gives a concentration dependence as:

$$\sigma = 20 + 10.4 \cdot c \qquad (5.6)$$

where $\sigma_{99.6}$ is the peak flow stress of AA1050. This linear relationship is approximately *Z*-invariant in the hot-deformation regime. Eq. (5.6) is fairly close to the yield strength at room temperature, eq. (5.5), and shows that the solid solution hardening effect is preserved at elevated temperatures, with n=1. In the binary alloys above it is seen that the n-value decreases with increasing temperature in the binary alloys (eq. (5.3) and eq. (5.4)), but this is not seen in the commercial alloys.

Binary high-purity AlMn alloys

Although AlMn alloys generally are considered as particle containing alloys, a binary high-purity AlMn alloy will be single-phased, i.e. Mn is retained in solid solution, see also section 5.1.2. Mahon and Marshall (1996) investigated the effect of small Mn-additions in pure aluminium with up to 0.1 wt%, i.e. 0.05 at% Mn. With reference to eq. (5.1) the results reveal a nearly linear concentration dependence of the ultimate tensile strength (n=0.93), but a more parabolic dependence of the yield strength, see table 5.3. A comparison of the values of *K* for AlMn in table 5.3 and AlMg in table 5.1 reveals a great different in the strengthening potential of Mn and Mg-atoms in solid solution. Note that the numbers in table 5.3 are based on a very few measurements and a low solute content (0-0.05 at%).

Table 5.3: Values of the parameters in eq. (5.1) at various strain levels of binary AlMn alloys in the range 0-0.05 at% Mn(ss). Based on the results of Mahon and Marshall (1996).

Strain	**$\sigma_{99.99}$ (MPa)**	**K (MPa/at%)**	**n**
0.002	13	48.9	0.59
Uniform strain	34	308	0.93

Table 5.4: Values of the parameters in eq. (5.1) at various strain levels of the commercial AlMn alloys, deduced from fig. 5.5. The hardening exponent, n, is close to unity.

Strain	**$\sigma_{99.6}$ (MPa)**	**K (MPa/at%)**
0.002	23.7	94.7
0.025	48.1	126.3
0.05	60.7	134.5
0.1	74.6	145.6
0.2	92.3	148.5

Commercial AlMn alloys

The strength of a commercial AlMn alloy, as the AA3103 alloy in this work, originates from a combined effect of several factors, e.g. Mn in solid solution, dispersoids and primary particles. Isolating one of these contributions is not easy, as a thermomechanical treatment will change the distribution of Mn-atoms in several ways. The homogenisation process of the present AA3103 alloy resulted in four different solute levels, but also changes in the particle size and volume fraction. However, as will be discussed in the later section 5.2.1, the variations in particle structure is relatively small and consequently the particle contribution is equal for these conditions. Thus, the solute content is considered as the major difference between the three homogenised alloys A, B and C. The as-cast condition, on the other hand, must be treated carefully because of its particle structure differing from the homogenised conditions.

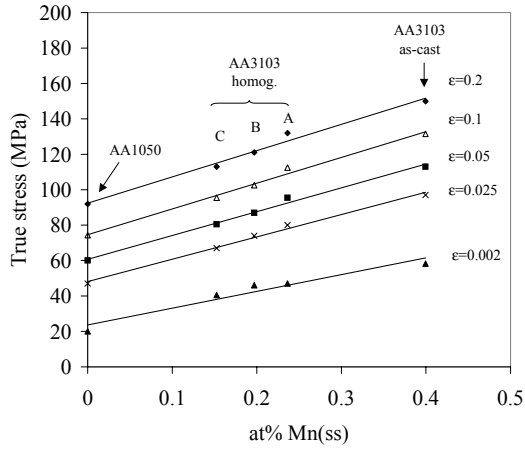

Figure 5.5: True stress as a function of at% Mn(ss) at various strain levels for the AA1050 and AA3103 alloys. The results of the homogenised AA3103 alloys are fitted to a linear relation.

The true stress at various strain levels is plotted for the four conditions of AA3103 along with AA1050 in fig. 5.5. The results are well fitted by linear trendlines, and the values of the parameters in eq. (5.1), assuming n=1, are given in table 5.4. It is seen that condition A is systematically a little above the fitted line, without having any explanation for that. It should be pointed out that in comparison to AA1050, the AA3103 alloys contain a lot more particles, but they also have higher solute levels. Thus, AA1050 is not exactly applicable as a solute-free reference alloy for the AlMn-alloys. Still, it is apparent from fig. 5.5 that AA1050 may serve as a close-to-zero solute alloy when discussing the

Mn(ss)-contribution to the strength. This is supported by the results obtained by Forbord (1999), which in fig. 5.6 are compared to the results from the present alloys. The stress at ε=0.2 of AA1050, AA3003 and two variants of AA3207 is very close to the present observations on AA1050 and AA3103.

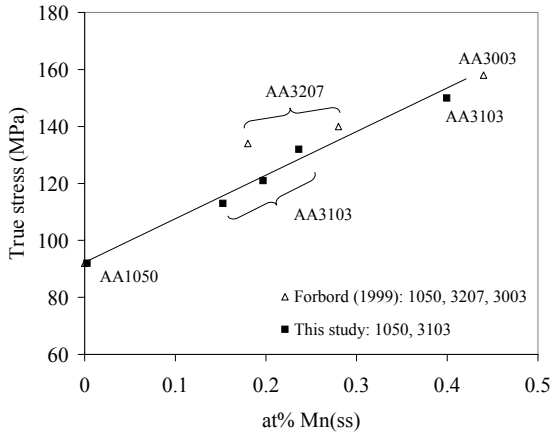

Figure 5.6: True stress as a function of at% Mn(ss) at a strain of ε=0.2 for the AA1050 and AA3103 alloys in this work compared to the results of Forbord (1999) on AA1050, AA3207 and AA3003. The low-solute AA3207 is a precipitated alloy, which explains the higher strength of this (see also fig. 5.16). Note that the strength of AA1050 in the two works is the same.

The hardening coefficient, *K*, of the commercial AlMn alloys, table 5.4, is seen to be considerably larger than for the commercial AlMg alloys in table 5.2. Another important difference is that while the *K*-parameter for the AlMg alloys varied strongly with strain, this variation is much less for the AlMn alloys. These observations may suggest that the relative solid solution hardening effect of Mn is larger than Mg, but that Mn has a lower work hardening potential. If this is true, the Mg and Mn atoms must have highly different properties in the Al lattice. Two main strengthening mechanisms of solute atoms were described in section 2.3.1: Size misfit and modulus misfit. Table 5.5 shows that Mg has a larger atomic size misfit to the Al lattice compared to Mn. The Mn-atoms are in fact smaller than the Al-atoms, and according to eq. (2.5) the interaction force arising between dislocations and Mn-atoms should be considerably smaller than the interaction with Mg-atoms. Thus, another effect of the Mn-atoms must be present that explains the strong hardening of Mn(ss). The modulus misfit, relating to the strength of the atoms, may be different, as the Mn-atoms are denser (heavier and smaller) than the Mg-atoms. But it is unrealistic that this effect can be so large.

Table 5.5: Atomic radii of aluminium and various alloying elements (Aylward and Findlay 1974). Relative deviation from aluminium is shown.

Element	Atomic radius (nm)	Deviation from Al
Al	0.143	-
Mg	0.160	+11.9 %
Mn	0.137	-4.4 %
Fe	0.124	-13.3 %
Si	0.118[a]	-17.4 %

a. Diamond crystal structure

A more plausible explanation may lie in a clustering effect. In that case the solute atoms (Mn, Fe, Si) cluster together during quenching from the homogenisation temperature. The clusters will constitute harder spots in the alloy than the discrete solute atoms do. Haasen (1996) mentions the non-random distribution of solutes that often occurs in alloys, and Sæter (1997) and Hagström (2003) have found indications of solute clusters as a preliminary stage for dispersoid formation. The clustering of vacancies and solutes at the beginning of precipitation in AlZnMg alloys is frequently reported. However, very little attention has been paid to this phenomenon in AlMn alloys.

An observation that may support such a clustering theory is the high-temperature properties of the same AA3103 alloys (A, B and C) as discussed above. The alloys were tested in torsion under various combinations of temperature and strain rate (Sjølstad 2001). The peak flow stress at ln Z=25 is plotted in fig. 5.7 along with AA1050 from Nes et al. (2001). It is clearly seen that the strength difference between the AA3103 alloys and AA1050 at room temperature (fig. 5.5) is lost. A hardening coefficient of K=17.6 is now obtained, a much smaller value than those given in table 5.4. The reason for this loss of hardening is believed to be that the solute clusters dissolve at higher temperatures due to increased diffusivity of the solute atoms. The K-value is more of the order of the AlMg alloys, suggesting that the pure solution hardening effect is nearly similar for Mn-atoms and Mg-atoms. A similar observation was made by Shi et al. (1997), who found a flow stress difference of only 7 MPa between AA1050 and AA3103 in hot plane strain compression. According to Ekström (2003) a dispersoid containing AA3103 alloy with 0.1 wt% Mn(ss) subjected to brazing (5 min. at 600°C) loses some of its strength because of dissolution of dispersoids, even though the solute level increases to 0.7 wt%. This indicates that the solute effect of Mn is relatively small.

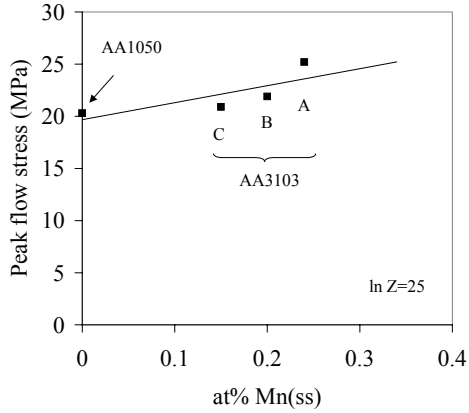

Figure 5.7: Peak flow stress of the homogenised AA3103 alloys and AA1050 tested in torsion at elevated temperatures (here: ln Z=25). (Nes et al. (2001) and Sjølstad (2001)).

Other alloying elements

Mg and Mn are not the only elements that contribute to the solution hardening. Elements like Si and Fe, which are present in all the alloys investigated in this work, are known to influence the strength. Since Si and Fe readily combine into second phase particles, it is often assumed that neglecting other elements than Mg and Mn will not result in any significant errors. Still, despite its low solubility, Fe is one of the most effective solution hardening elements in Al, cf. the large atomic misfit in table 5.5. According to Mahon and Marshall (1996) an addition of only 0.02 wt% Fe(ss) increases the tensile strength of high-purity Al by 20 MPa. In the same work Si and Mn are shown to have somewhat lower hardening potentials, but much higher than the reported values for Mg. Mahon and Marshall ascribes the hardening to a solid solution effect. However, as discussed above, there is a reason to believe that the strong effects of Fe and Si are related to the clustering of solute atoms.

The effect of impurities on the mechanical strength of pure aluminium is illustrated in fig. 5.8, where impurity levels up to 0.4 wt%, as in AA1050, are shown (ASM 1993). An increase in R_m of 25-30 MPa from pure Al to 0.4 wt% impurities is seen. Fig. 5.9 shows a comparison between the commercial and binary AlMg alloys discussed above. A surprisingly large effect of small impurity levels is seen, and the stress-strain curve of AA1050 actually coincides with the binary AlMg0.55 alloy. The difference between AA1050 ($Al_{99.6}$) and the $Al_{99.99}$ is about 30-35 MPa and is caused by small amounts of Fe

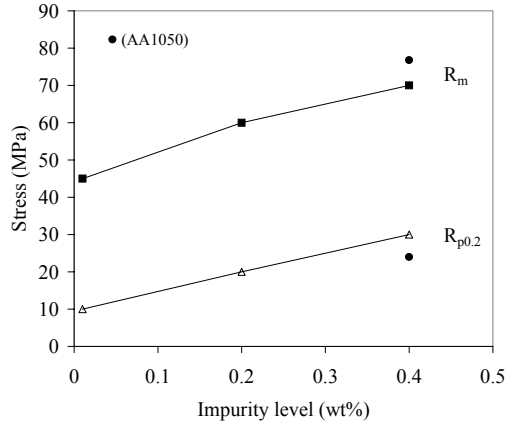

Figure 5.8: Effect of impurities on the yield strength and the ultimate tensile strength (ASM 1993). 0.4 wt% impurities corresponds to AA1050 ($Al_{99.6}$), and the results from this alloy are added to the figure.

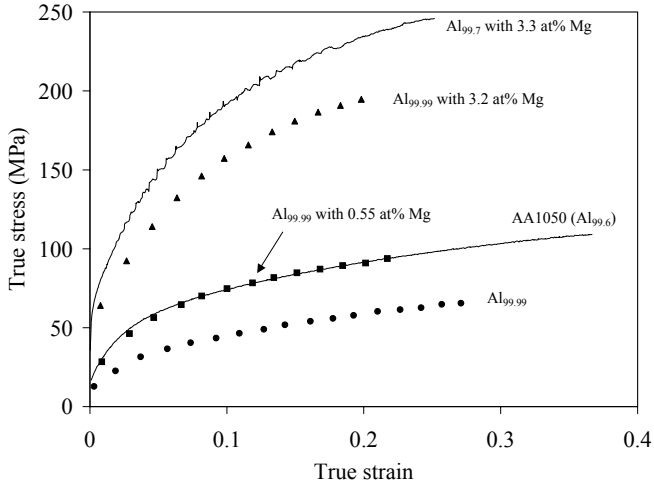

Figure 5.9: Effect of small impurity levels on the stress-strain curves. Binary alloy data (symbols) from Sherby et al. (1951) are compared to commercial alloys (full lines) investigated in this work.

and Si in solid solution, or more likely as solute clusters. As shown in fig. 5.9 the same effect appears for the commercial and the binary AlMg3 alloys.

5.1.2 Stage IV

Stage IV of work hardening is characterised by a linear stress-strain curve with a relatively low θ_{IV}. In this section the results from cold rolled materials presented in section 4.5 are

further discussed. First, however, some pure and binary alloys from the literature are mentioned.

Binary high-purity alloys

In a work by Guyot and Raynaud (1991) high-purity aluminium and binary AlMg3 and AlMg5 alloys (wt%) were cold rolled to large strains and tensile tested. In fig. 5.10 their reported values of the yield strength ($R_{p0.2}$) are plotted together with AA1050 and the commercial AlMg3 alloy investigated in the present work. Guyot and Raynaud observed an increase in the work hardening rate with the introduction of Mg. The high-purity aluminium is nearly in a steady-state condition, with a work hardening rate of only θ_{IV}=1.5 MPa. This is in contrast to AA1050, which has a θ_{IV}=19 MPa (when $R_{p0.2}$ is considered). The commercial and binary AlMg alloys have work hardening rates of the same order, although the commercial ones seem to harden a little more.

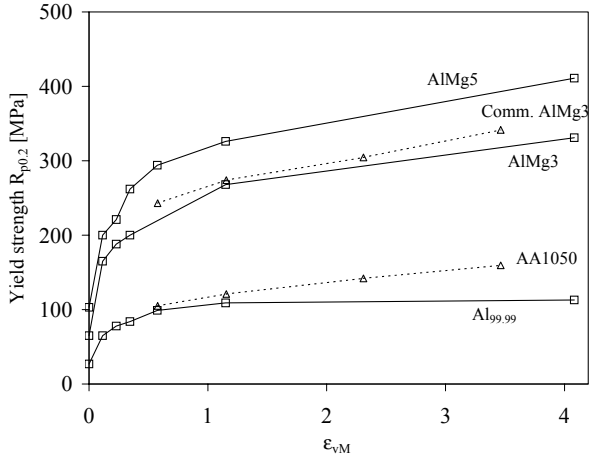

Figure 5.10: Yield strength ($R_{p0.2}$) after cold rolling of pure aluminium and binary AlMg3 and AlMg5 alloys. For comparison, some of the commercial alloys investigated in the present work are shown.

Fig. 5.10 illustrates that only a small amount of impurities raises the stage IV work hardening rate. The fact that high-purity aluminium is close to stress saturation indicates extensive dynamic recovery of subgrains (i.e. subgrain growth) at these high strain levels. The 0.4 wt% of impurities in AA1050 is obviously sufficient to prevent such subgrain growth.

A high-purity aluminium ($Al_{99.99}$), a binary high-purity AlMn1 alloy and a commercially pure Al were cold rolled and tensile tested by Nes et al. (1982). In an alloy containing Mn,

but no other elements, the Mn is supposed to be in complete solid solution. Hence, no particles are present here. In fig. 5.11 the ultimate tensile strength (σ_{UTS}) is plotted (note that in fig. 5.10 $R_{p0.2}$ was plotted). It is seen that the Mn in solution creates a considerable work hardening, as compared to the pure Al. As in fig. 5.10 the $Al_{99.99}$ has a relatively low work hardening rate, most likely due to little resistance against dynamic recovery of subgrains.

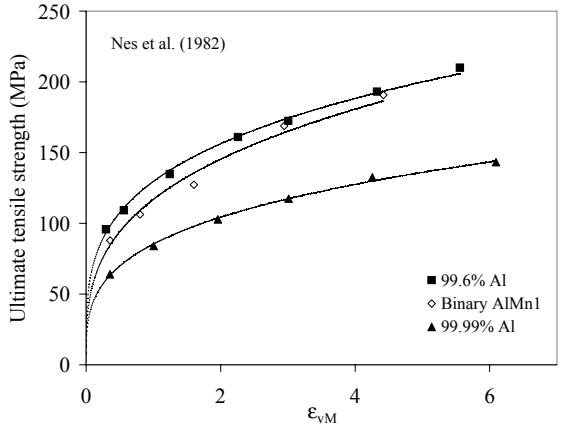

Figure 5.11: High-purity aluminium, binary AlMn1 and commercially pure aluminium (AA1050) cold rolled to large strains and tensile tested (σ_{UTS} plotted). Data from Nes et al. (1982).

Perhaps more interesting is the observation that the commercially pure Al ($Al_{99.6}$ or AA1050) has a slightly higher strength than the AlMn alloy. This implies that the 0.05-0.1 at% of elements in solid solution in AA1050 (Fe and Si) have a stronger effect than the about 0.5 at% of Mn(ss) in the binary AlMn alloy. This stands in contrast to the effect of Mn in the *commercial* AlMn alloy, AA3103, in fig. 5.5. The effects of impurities and solute clusters on the stage II-III behaviour were discussed in section 5.1.1, and an additional suggestion based on fig. 5.11 is that in order to create the strong solute clusters, Mn requires the presence of Fe or Si.

Commercial alloys

From the experiments on cold rolled materials presented in section 4.5 a linear stage IV is seen (AA1050 and AlMgX in fig. 4.31, AA3103 in fig. 4.33 (b) and AA5xxx in fig. 4.35). The hardening rates are relatively low and appear to be similar to the binary alloys shown above. As the diagrams are based on tension tests/ compression tests on O-temper materials and tension tests on cold rolled materials, the transition from stage III to stage

IV is discontinuous and not completely unified. This is also illustrated in fig. 5.12, showing the work hardening rate through stage II, III and IV of AA1050, AlMg1, AlMg3 and AA5182. The work hardening rate is normally given as $\theta = d\tau/d\gamma = M^{-2}d\sigma/d\varepsilon$, while in fig. 5.12 it is given as $d\sigma/d\varepsilon = M^2\theta$, where the Taylor factor is assumed to be $M = 3$. The hardening rate increases with Mg content in stage II-III. At the transition into stage IV, the compression tests of AlMg1 and AlMg3 have a higher θ than the tension tests on the cold rolled materials, a discrepancy that may be caused by the change of strain path and some static recovery.

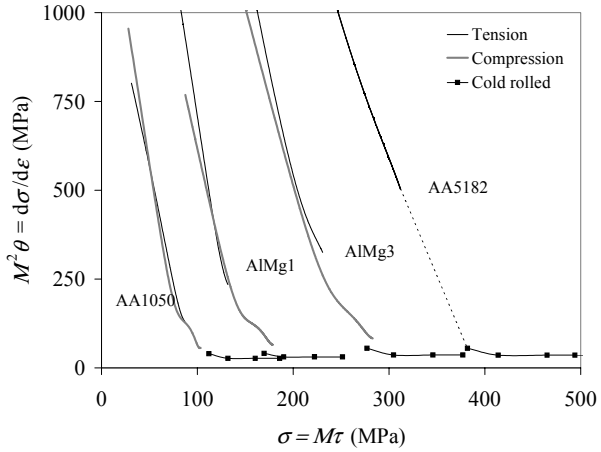

Figure 5.12: Work hardening rate ($M^2\theta$) of AA1050, AlMg1, AlMg3 and AA5182 in stage II-IV obtained from tension tests and compression tests.

Even though the alloys have widely different strengths and work hardening rates up to the point where stage IV begins, they have almost equal θ_{IV}. In fig. 5.13 (a) the stage IV work hardening rate is estimated for the alloys AA1050, AlMgX, AA5005 and AA5182. Here, only the ultimate tensile strength results (σ_{UTS}) are used, and the stage IV is limited to strains above ε=1 where the curves are close to linearity. The $M^2\theta_{IV}$ parameter is here plotted against the concentration of Mg, showing a small increase, mostly from 0 to 0.5 at% Mg. By compensating for the Taylor factor, and normalising with respect to the shear modulus, values of θ_{IV}/G of $0.12\text{-}0.16 \cdot 10^{-3}$ are obtained (assuming $M = 3$). Alberdi (1984), quoted by Gil Sevillano (1993), has reported results for pure aluminium tested in torsion, as in fig. 2.23 (b), with $\theta_{IV}/G = 0.25 \cdot 10^{-3}$ at room temperature.

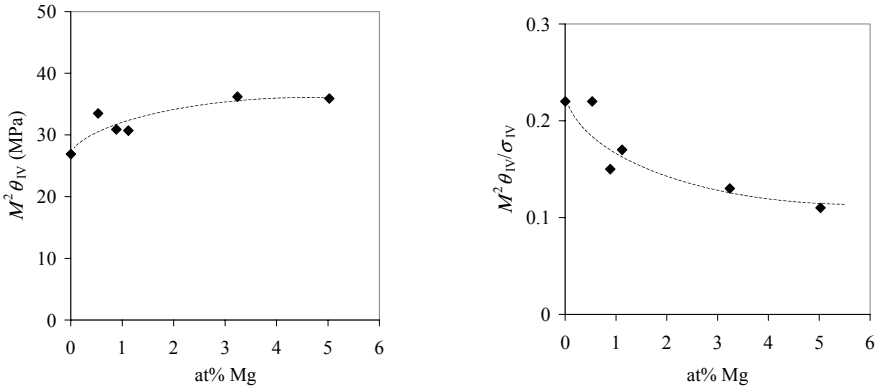

Figure 5.13: (a) $M^2\theta_{IV}$ ($\varepsilon > 1$) as a function of the amount of Mg in the alloy. (b) The ratio between $M^2\theta_{IV}$ and σ_{IV}, i.e. a in eq. (2.10) times M, as a function of the amount of Mg in the alloy.

The increase in θ_{IV} with concentration is small as compared to the increase in σ_{IV}, defined as the stress at $\varepsilon = 1$. The Mg-dependence of this stage IV initiation stress follows eq. (5.1) just as in fig. 5.3, now with $K = 54$ MPa/at%. It is interesting to note that while the work hardening rate is strongly solute dependent prior to stage IV, this is no longer the case beyond stage III. This is illustrated by fig. 5.13 (b), where the ratio between $M^2\theta_{IV}$ and σ_{IV} is plotted. The ratio is the scaling factor a in eq. (2.10) times M, giving values of a ranging between 0.037 and 0.073. The non-constant a shows that eq. (2.10) is not obeyed for the investigated alloys at room temperature. This is further discussed in section 5.3.2. The experiments by Alberdi on pure aluminium at various temperatures mentioned above gave a constant a-value around 0.1.

Some reported experiments indicate that θ_{IV} increases also with alloying. Rollett et al. (1987) investigated the effect of Mg, Mn and Cu on the stress-strain behaviour in torsion up to large strains and found a constant a-value of 0.05. Hughes and Nix (1989) explored the effect of adding large amounts of Co to Ni, which significantly reduced the stacking fault energy and raised the flow stress of the alloy. However, in better agreement with the above results on AlMg alloys, the additions had no visible effect on the stage IV work hardening rate.

The AA3103-B alloy, with 0.20 at% Mn(ss), was cold rolled to large strains and tensile tested, see fig. 4.33 (b). As can be seen from table 5.6, the stage IV work hardening rate of this alloy is of the same order as AA1050 and the AlMg alloys in fig. 5.12.

Table 5.6: Stage IV work hardening rate of AA3103-B compared to AA1050.

Alloy	$M^2\theta_{IV}$ **(MPa)**
AA1050	27
AA3103-B	30

5.1.3 About measuring stage IV

The stage IV work hardening rate is not a straight-forward property to measure. Compression tests, like upsetting and PSC testing, are generally limited to deformations up to ε=1, about where stage IV normally begins. Torsion testing gives a deformation mode that is very different from plane strain, and is also difficult to perform on sheet materials. In the indirect method used in this work, the materials are cold rolled and subsequently tensile tested along the rolling direction. A two-step procedure like this leads to a change in deformation mode and strain rate, and also a relief/ reloading process that can not be neglected.

In the stage IV stress-strain curves, fig. 4.31, fig. 4.33 (b) and fig. 4.35, there are differences between the yield strength and the tensile strength of the cold rolled materials. This difference occurs despite the fact that after cold rolling the materials are actually in a stage IV condition, and ideally they should not display any yield point. The thing is however, that immediately after a step of cold rolling the deformation structure will start to recover. The major recovery process that is expected to occur statically at room temperature is the annihilation of dislocations in the Frank network, while the subgrain structure is believed to remain more or less unchanged. When the material is reloaded, the dislocation configuration has to be restored before stage IV is reached again. This requires an additional plastic deformation.

The alloys behave differently, and in fig. 5.14 this restoration of the dislocation structure is represented by the difference between R_m and $R_{p0.2}$, i.e. the work hardening occurring upon reloading. At a given strain, the high-Mg alloys obviously recover more than AA1050, indicating a higher dislocation density that may recover. This demonstrates the need of a stabilising treatment of industrial high-Mg alloys (H38-temper). Besides the static recovery, which is influenced by strain and solute level, the strain path change, as well as dynamic strain ageing, may contribute to the effects shown in fig. 5.14. This is indeed a complex and many-faceted problem and is not further discussed here.

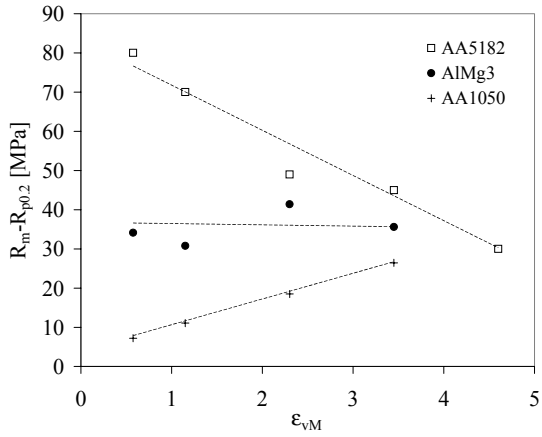

Figure 5.14: Difference between the tensile strength and the yield strength after cold rolling for three selected alloys spanning a range of Mg concentrations.

5.2 Particle and grain size effects

Particles and grain boundaries are features in the microstructure that give rise to more or less similar effects on the stress-strain behaviour. They serve as obstacles limiting the mobility of dislocations, and are essentially treated in the same way by the work hardening model, see section 5.3.3.

5.2.1 Particles

AA3103: After casting the AA3103 alloy was homogenised by three different procedures, see table 3.2. Including the as-cast alloy, this resulted in four conditions of the alloy with variable contents of manganese in solid solution, ranging from 0.15 at% Mn(ss) in AA3103-C to 0.40 at% Mn(ss) in the as-cast alloy. In the as-cast state such alloys contain a dendritic structure with segregation of alloying elements, as well as Fe-rich plate-like primary particles. During homogenisation the concentration gradients across the dendrites are smoothed out and the particles spherodised. New dispersoids will be precipitated, but during further heat-treatment they dissolve too, and the Mn diffuses to the Fe-rich primary particles. The latter phenomenon leads to a decreasing content of Mn in solid solution and an increasing volume fraction of primary particles (Dons 2002).

Based on this and a work by Sjølstad (2003) it is assumed that the three homogenised conditions (A, B and C) contain no small dispersoids but a considerable fraction of

Table 5.7: Estimated volume fractions and average radii of primary particles in the various conditions of AA3103. From Sjølstad (2003).

Alloy	f	r (μm)
AA3103 as cast	0.018	-
AA3103-A	0.045	0.5
AA3103-B	0.046	0.5
AA3103-C	0.048	0.5

primary particles that contribute to the strength as hard non-shearable particles. Among the homogenised conditions, Sjølstad observed no coarsening but a slightly increased volume fraction of the particles, see table 5.7, probably because the volume of Mn-atoms diffusing to one particle is very small compared to the volume of the particle. The as-cast condition is somewhat different, containing dendrites and platelike primary particles. The stress-strain behaviour of these conditions of AA3103 is shown in fig. 4.32.

As we saw in section 5.1.1, elements in solid solution result in an increase in both the yield strength and the rate of work hardening. For the case of Mn containing alloys most of this strengthening was ascribed to a solute clustering effect. Second phase particles contribute to the strength by a general lift of the curves. In fig. 5.15 (a) the AA3103 alloy with the lowest solute level (condition C, 0.15 at%) is compared to AA1050 and the AlMg1 alloy. The solute level in AA3103-C is just a little higher than in AA1050, which is estimated to be around 0.05-0.1 at%, and the flow curves are almost parallel. The difference between them varies from 20 MPa in the first 5% of straining to 22 MPa at ε=0.3. The particles in the AA3103-C alloy are responsible for a constant strength contribution, but 20 MPa is an unreasonably large value, see also section 5.3.3. Therefore, a cluster effect appears as a plausible explanation for a major part of the difference between AA1050 and AA3103. It may be seen from fig. 5.5 that the clusters give a contribution that is close to additive, as the slope of the curves for AlMn alloys are more strain invariant than the curves for AlMg alloys in fig. 5.3.

Extending this discussion to stage IV, it was shown in table 5.6 that AA1050 and AA3103-B have nearly the same work hardening rate. A comparison of fig. 4.31 (a) and fig. 4.33 (b) shows that the difference in ultimate tensile strength in stage IV between these two alloys is approximately 40-50 MPa. However, the AA3103-B alloy has a somewhat higher solute level, and thereby a higher strength in stage II-III.

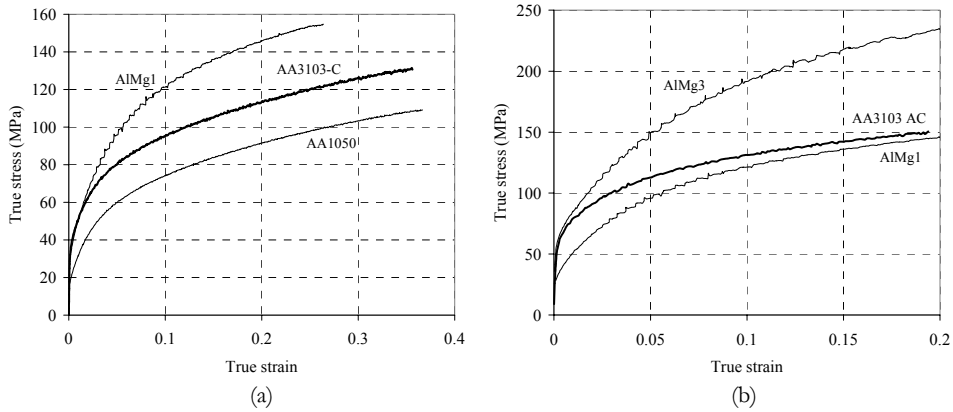

Figure 5.15: Flow curves illustrating the effect of particles on the stress-strain behaviour. (a) AA3103-C compared to AA1050 and AlMg1. (b) AA3103 as-cast compared to AlMg1 and AlMg3.

A comparison of AA3103-C and AlMg1 in fig. 5.15 (a) clearly demonstrates the effect of particles on the initial hardening and curvature in stage II. This is also evidenced by the curves in fig. 5.15 (b), where the particle-containing as-cast AA3103 exhibits a yield strength of the same order as AlMg3. As deformation proceeds, it hardens much less than the Mg containing alloys and approaches the flow curve of AlMg1 at higher strains. This is in accordance with the analysis by Suni et al. (1994) in fig. 2.21. The solutes and particles in combination create a high yield strength. The work hardening potential of the particles is, however, comparatively low. This implies that the size of the deformation zones around the particles is small, so that the fraction of the material volume that work hardens in the deformation zone is negligible. Texture measurements of the cold rolled AA3103 alloys (Sjølstad et al. 2002) support this view, as the rolling texture develops in the same manner as in AA1050.

An interesting observation was made by Forbord (1999). A strip cast AA3207 alloy was processed into two variants by rolling and heat-treatments: One variant containing precipitates (small dispersoids, r=0.1 μm) and a low solute content (0.18 at% Mn), and one variant with a higher solute content (0.28 at%) but no precipitates. The stress-strain curves are shown in fig. 5.16 together with AA1050. The precipitate containing alloy shows a rapid initial hardening, but a lower work hardening rate than the precipitate free alloy above 3% strain. Note that the curves for AA1050 and the alloy with precipitates are almost parallel. This is consistent with the results discussed above (fig. 5.15),

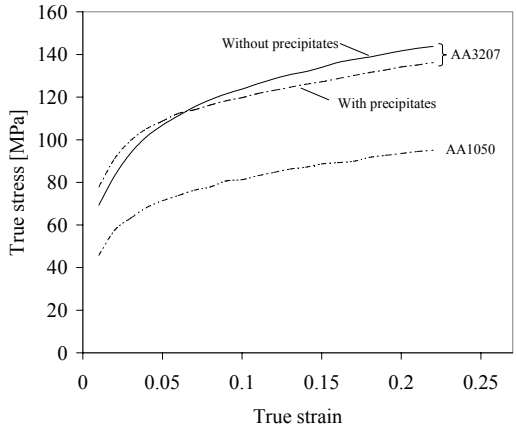

Figure 5.16: Effects of precipitates and solute content in an AA3207 alloy. The precipitate-containing alloy has 0.18 at% Mn(ss), while the non-precipitate containing alloy has 0.28 at% Mn(ss), see also fig. 5.6. AA1050 is added for comparison. Data from Forbord (1999).

indicating that small dispersoids and large primary particles have similar effects on the stress-strain behaviour.

AA5005: In section 5.1.1 and fig. 5.4 the stress-strain behaviour of AA5005 was seen to deviate from that of AlMg1. The high strength at low strain was ascribed to a particle effect, just as in fig. 5.15 (b). The presence of particles seems a bit strange, since the chemical composition is not that different between these two alloys (for example, none of them contain Mn). On the other hand, AA5005 was processed in another way than AlMg1. According to the manufacturer of the alloy (CORUS 2001) the break-down hot rolling resulted in a break-up of the constituent particles and a precipitation of Mg_2Si. These reactions give a reasonable explanation for the higher strength of this alloy.

5.2.2 Grain size

The effects on the stress-strain behaviour of altering the grain size in the present alloys are given in fig. 4.29 and fig. 4.33. In general, a reduction of the grain size results in an increase in both the yield strength and the work hardening rate. This is illustrated in fig. 5.17 where the yield strength at 0.5% strain, $R_{p0.5}$, is plotted against $D^{-1/2}$ according to the Hall-Petch relationship:

$$\sigma_0 = \sigma_i + k \cdot \frac{1}{\sqrt{D}} \tag{5.7}$$

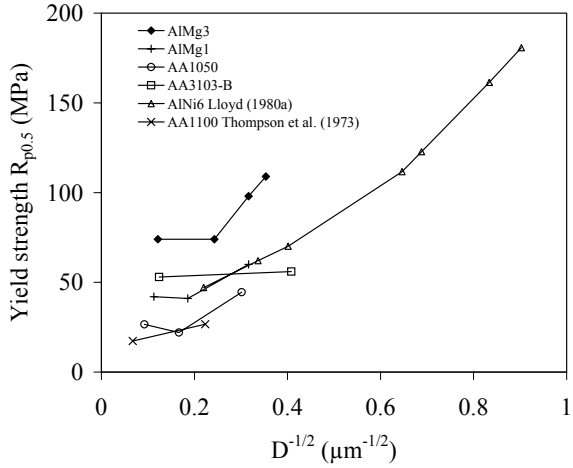

Figure 5.17: Hall-Petch plot illustrating grain size effects on the yield strength at 0.5% strain.

Results by Lloyd (1980a) on an AlNi6 alloy (fig. 2.18 (b)) and Thompson et al. (1973) on AA1100 are here compared to the results from the present work. The strengthening factor k in eq. (5.7) represents the slope of the curves, which for AA1100 is 0.06 MPa $\cdot m^{1/2}$, increasing to 0.15 MPa $\cdot m^{1/2}$ in AlMg3. The gradient generally increases with the Mg content, but this is caused by the yield point phenomenon occurring under the combination of small grains and high solute level (see section 5.2 and fig. 5.18). As Lloyd pointed out, alloys exhibiting a yield point elongation follow a 1/D relationship. This diagram and the stress-strain curves in section 4.5 show that there is no effect at grain sizes above 25 μm (<0.2 in fig. 5.17) for the AlMg alloys and AA1050. At smaller grain sizes the effect is significant.

The AA3103-B alloy behaves in a different way. A reduction in the grain size by an order of magnitude has almost no effect on the yield strength (k=0.01 MPa $\cdot m^{1/2}$). At larger strains however, the difference between the coarse-grained and the fine-grained alloy is significant, see fig. 4.33. This may be a result of the large strength contribution from particles at small strains which overshadows the grain size effect (fig. 5.15). On the other hand, the results from Lloyd on very fine-grained AlNi6 alloys containing a large fraction of particles show a strong grain size dependence also on the yield strength (see fig. 2.18 (b)).

It is worth mentioning that the coarse-grained and fine-grained samples had different deformation and temperature histories. The fine-grained alloys were processed by heavy

cold rolling and annealing which would cause changes in the texture and particle structure. But as described in section 4.1, the texture changes due to the thermomechanical processing were quite small, with only tendencies of cube texture in the fine-grained variants. It was also mentioned in section 3.4 that the electrical conductivity remained unchanged during recrystallisation of the AA3103 alloy, and hence no precipitation of dispersoids was assumed to occur.

Moving into stage IV, fine-grained variants of AlMg0.5, AlMg3 and AA3103-B were cold rolled and tensile tested, see fig. 4.31 and fig. 4.33 (b). It appears that a reduction of the grain size has no effect on the work hardening rate in stage IV. The curves are just lifted up to higher strength, a contribution that originates from earlier stages of work hardening.

5.3 Application of the work hardening model

In this section the work hardening model presented in section 2.5.3 is applied to the alloys above. Effects of solid solution, solute clusters, particles, grain size and microstructure are discussed in terms of the model. Some demonstrations of the prediction power of the model are also given.

5.3.1 Solute effects in stage II-III

Solid solution hardening in stage II-III is covered by the model in several ways:

- Solutes affect the friction stress, or the thermal component τ_t in eq. (2.20) through the activation volume, V_t, and the activation energy, U_t.
- Solutes affect the storage rate of dislocations by reducing the slip length L through the statistical storage parameter C, given in eq. (2.29) and eq. (2.30).
- Moving into stage III, the solutes will affect the dynamic recovery, mainly through the activation volumes V_ρ and V_δ in eq. (2.38) and eq. (2.39).

(i) The thermal component: The thermal component τ_t is of major importance only at small strains, i.e. when the density of mobile dislocations ρ_m is low. At larger strains, τ_t gradually diminishes as the contribution from the substructure, $\hat{\tau}_a$, starts to dominate. This is illustrated schematically in fig. 5.18, where the thermal and athermal components are separated. The total flow stress τ will take the form as shown. Consider a material with a low ρ_m, due either to a small grain size (AlMg3 in fig. 4.29 (d)) or a high solute

content (AA5182 in fig. 4.34). The broken lines indicate such a case where ρ_m is low, i.e. τ_i is large. This gives a high yield point (1) and a minimum in the total stress. This is an unstable situation and the material may take two different strain levels, (1) and (2), where the Lüders bands will take the highest strain. The flow stress will therefore stay at this level while the bands propagate until all the material volume has reached the highest strain. This is the phenomenon that causes the yield point elongation.

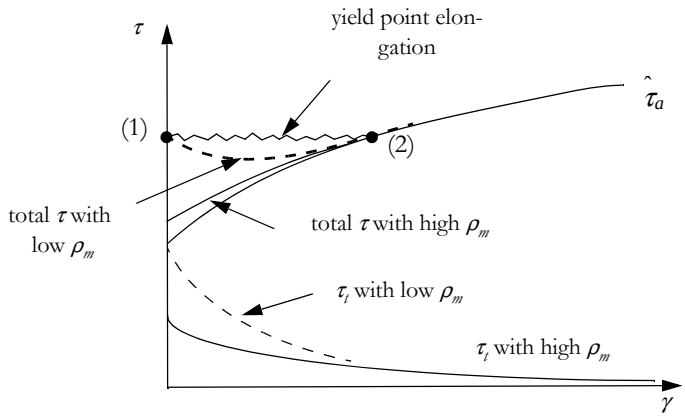

Figure 5.18: Schematic illustration of the effects of the thermal (τ_i) and the athermal ($\hat{\tau}_a$) components on the flow stress at very small strains. A yield point elongation is shown.

(ii) The statistical storage parameter *C*: In the simplest case of a pure single crystal with a linear stage II, the constant *C* is given by:

$$C = \frac{\alpha_1 G}{\theta_{II}} \tag{5.8}$$

where α_1 is a constant of order 0.3. The parameter reflects the probability for a dislocation to be stored and determines the stage II work hardening rate. It decreases as the concentration of solute atoms increases, giving a shorter slip length according to eq. (2.29). The solute dependence of the *C*-parameter is extracted from fig. 2.16 (a), i.e. binary AlMg alloys tested at 78K (Sherby et al. 1951). This is plotted as a function of the Mg-content in fig. 5.19 (a), showing a linear decrease with at% Mg. At higher temperatures a linear stage II is difficult to detect in polycrystals. However, it is apparent from the stress-strain curves of AA1050 and the AlMgX alloys in fig. 4.28 that θ_{II} increases with Mg-content, and hence *C* must decrease. In fig. 5.19 also the *C*-parameters

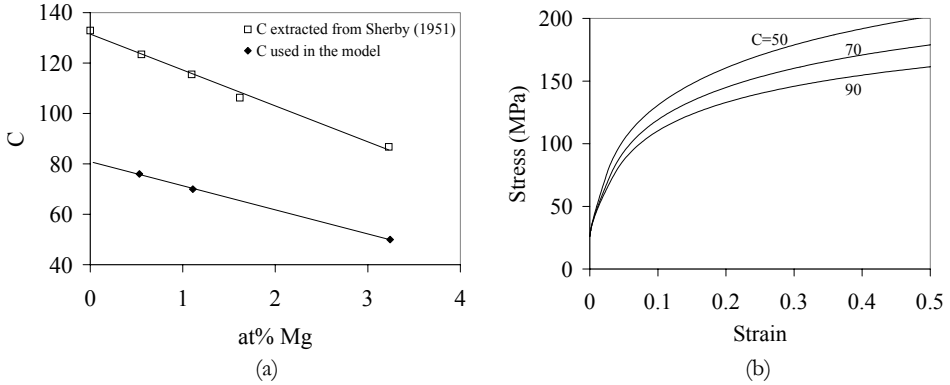

Figure 5.19: (a) Variation in the C-parameter as a function of at% Mg, extracted from data on binary AlMg alloys tested at 78K by Sherby et al. (1951) and values used in the work hardening model. (b) Modelled stress-strain curves using different values of *C*.

used in the model for the AlMgX alloys at room temperature are shown. Due to the higher temperature these values of *C* are smaller than the values obtained at 78K, i.e. the storage rate is lower. Yet, they follow the same trend with the Mg content as the low temperature results from Sherby and co-workers. In fig. 5.19 (b) it is shown that the effect on the model curves of reducing *C* is an increase in work hardening rate in stage II and III.

(iii) Dynamic recovery: The transition from stage II to III is associated with the occurrence of dynamic recovery, which is presented in section 2.5.3. The solute effects are mainly contained within the activation volumes V_ρ and V_δ. In AlMg alloys the rate-controlling reaction in dynamic network growth is expected to be cross-slip. Then, $V_\rho \propto \xi_\rho b^3 c^{-e}$, in contrast to $V_\rho \propto \xi_\rho b^3$ in pure metals. The solute concentration c is powered by a constant e, which is found to be around 0.55 (Marthinsen and Nes 2001). Similarly, $V_\delta \propto \xi_\delta b^3 c^{-e}$ in solid solution alloys, but $V_\delta \propto b^3$ in pure metals.

Modelled stress-strain curves in stage II-III

The stress-strain curves from uniaxial tension of the commercial AlMgX alloys (fig. 4.28) are simulated by the work hardening model in fig. 5.20. The effect of Mg is captured quite nicely by an increase of yield stress and work hardening rate due to solute atoms. Basically, the thermal component is responsible for the increase in initial strength (see fig. 5.18) while the variation in *C* given in fig. 5.19 results in a higher θ. A grain size of 60 μm and a volume fraction of particles f=0.015 with average radius r=0.5 μm, are used in the calculations, giving an effective slip length of L_{eff}=20 μm. A strain rate of 0.001 s^{-1}

and an average Taylor factor of 3 are also used. A statistical distribution of the subgrain size is here used in order to obtain a gradual transition between stage II and III.

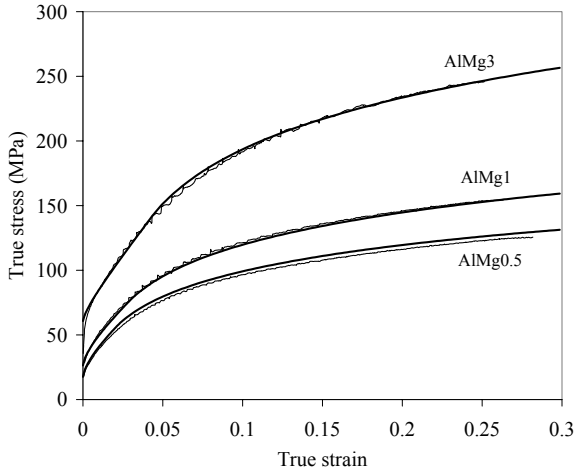

Figure 5.20: Modelled stress-strain curves (bold, smooth curves) compared to the experimental tension test results (thin, serrated curves) for the AlMgX alloys.

5.3.2 Solute effects in stage IV

In the work hardening model, stage IV is associated with a refinement of the substructure. The subgrain size is reduced slowly, while the dislocation density within the subgrains and the boundary misorientation remain approximately constant.

The hardening rate is often seen to scale with the stress at the transition into stage IV, as given by eq. (2.10), which is valid for temperature changes. Generally, solute effects appear to be analogous to temperature effects in stage II-III. This can for example be seen by inspecting the stress-strain curves of pure Al and AlMg alloys at -195°C and 20° in fig. 2.16, where both temperature and solute effects on the stage II-III behaviour are shown (Sherby et al. 1951). For the alloys investigated in this work, see fig. 5.12, which in stage II-III corresponds to fig. 2.23 (b). The modelling curves in fig. 2.30, showing solute effects on the stress-strain behaviour, display an increasing work hardening rate with the Mg content. However, in section 5.1.2 it was seen that the experimentally observed θ_{IV} is almost invariant of the alloy composition. The ratio between θ_{IV} and σ_{IV} shown in fig. 5.13 (b) demonstrates that these materials do not obey the relation given in eq. (2.10).

The disagreement between the model predictions and the experiments concerning θ_{IV} are believed to be related to the nature of the microstructure evolution, and more specifically to the storage and dynamic recovery of dislocations. Even though much progress has been done on the evolution of deformation structures during rolling (section 2.2), the current knowledge is not complete. Moreover, the model uses a simplified description of the microstructure. Therefore, an attempt has been made to explore some microstructural effects. In the following the low work hardening rate of high-Mg alloys is discussed in terms of:

- the way the dislocations are stored in the subgrain interior or by forming new boundaries (parameter q_c)
- the evolution in subgrain misorientation (φ_{IV})
- break-up of grains by new high-angle grain boundaries
- shear banding

As illustrated in fig. 2.27 the dislocations are stored either in the subgrain interior, by creating new boundaries or by increasing the misorientation of already existing boundaries. This "book-keeping" is analysed statistically (Nes 1998), but in the following it is shown that the storage pattern may be slightly altered, giving rise to a different work hardening behaviour.

The q_c-parameter

The q_c-parameter given in eq. (2.33) determines the mutual storage of dislocations in the subgrain interior and the boundaries in stage II. This storage pattern will be more or less conserved into stage IV and affects the hardening rate. From the TEM micrographs of AA1050 and AlMgX at ε=2 in fig. 4.22 it is apparent that the distribution of dislocations varies considerably with solute content. The dislocation density inside the subgrains increases from AA1050 to AlMg3, an observation in accordance with previous reports on non-cell forming alloys, see section 2.2.3.

It is therefore suggested that q_c should increase with the solute content as ρ_i increases with the concentration of Mg. This will give a reduction of the work hardening rate in stage IV because some of the dislocations are stored in the subgrain interior instead of in new sub-boundaries (Ryen et al. 2001). In fig. 5.21 (a) estimated (tuned) values of q_c used in the model are shown for the Mg concentrations of the present alloys. The effect

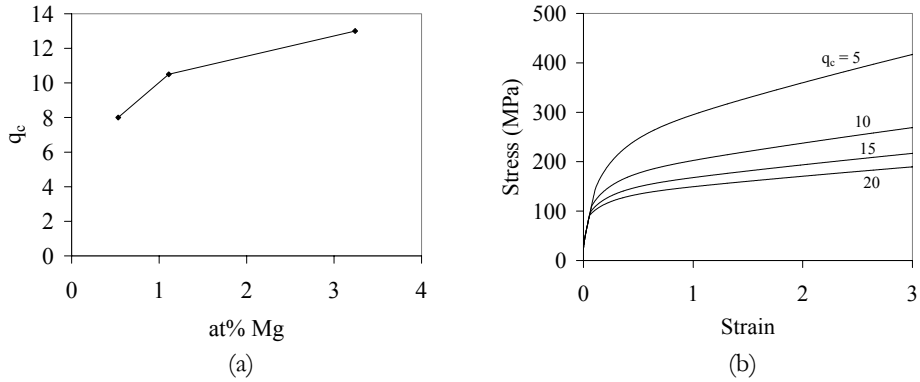

Figure 5.21: (a) Estimated values for q_c as a function of the Mg content. (b) Effect of different q_c-values on the modelled stress-strain behaviour.

on the stress-strain behaviour as predicted by the model is shown in fig. 5.21 (b), where an increased q_c lowers the stage IV work hardening rate.

Subgrain misorientation

One assumption in the work hardening model is that the subgrain misorientation remains constant in stage IV (ε>1). If, however, the misorientation increases during stage IV, this implies a change of the storage pattern for the dislocations. As the dislocation density inside the subgrains (ρ_i) has saturated at this strain level, the dislocations created during subsequent deformation must be stored in either old or new boundaries. The formation of new boundaries gives a strengthening through a smaller δ, while the increase in the misorientation does not contribute to the strength. So if a larger fraction of the dislocations are stored in old boundaries, a lower hardening rate in stage IV becomes the consequence (see also Holmedal et al. 2002a and Holmedal et al. 2002b). This is controlled by the scaling parameter S_{IV}, and θ_{IV} is in the model given as:

$$\theta_{\mathrm{IV}} = \alpha_2 Gb \frac{2\rho_i C S_{\mathrm{IV}}}{\kappa\varphi_{\mathrm{IV}} \sqrt{\rho_i + \frac{\kappa\varphi_{\mathrm{IV}}}{b\delta}}} \tag{5.9}$$

where the parameters are explained in section 2.5.3. The equation shows that the work hardening rate is reduced if the subgrain misorientation is allowed to increase beyond φ_{IV}. An experimental observation that confirms the existence of work softening is provided by a work of Lloyd and Kenny (1980). They found that aluminium containing nickel work softened at large strains, an effect that may be explained by an increase in

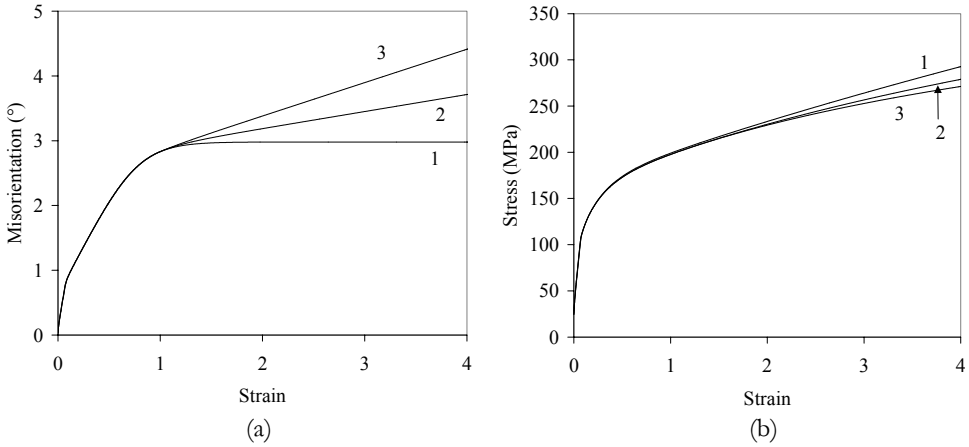

Figure 5.22: (a) Three different cases of sub-boundary misorientation evolution in stage IV and (b) corresponding stress-strain curves (generic case).

misorientation (Holmedal et al. 2002a). The effect of φ in stage IV is illustrated schematically in fig. 5.22 with three different cases of misorientation evolution for a generic AlMg1 alloy. Case 1, where φ saturates at 3° gives the highest stress in the model results. In case 2 and 3 the increasing misorientation results in somewhat lower strengths. However, the effect is small, as an increase in misorientation of 1° at ε=3 gives a reduction in strength of only 10 MPa.

In the present work the evolution in misorientation with cold rolling is measured in AA1050, AlMg1 and AlMg3. TEM and high resolution EBSD are used and the results are given in section 4.4.3. The measurements show that the misorientation increases slowly during stage IV, but no evidence for any solute concentration effect is observed. This only partly supports the discussion above, as it can not explain the low hardening rate of the high-Mg alloys.

Grain break-up

The grain break-up during cold rolling is investigated in order to see if there are any effects of the Mg-content. During cold rolling the grains subdivide into smaller volume elements (see sections 2.2.2 and 4.3.2). One aspect of this subdivision is the introduction of new high-angle grain boundaries (HAGBs), and a simple way of quantifying the break-up phenomenon is to measure the amount of newly introduced HAGBs. From the measured separation of HAGBs in fig. 4.15 a break-up factor is calculated, defined as:

$$\text{Break-up factor} = \frac{D_{ND}}{D^*_{ND}} \tag{5.10}$$

where D_{ND} is the theoretical grain size in the normal direction, based on the initial grain size and the assumption of plane strain compression, while D^*_{ND} is the grain size measured in the normal direction.

The variation in grain break-up among the AA1050 and AlMgX alloys is plotted with deformation in fig. 5.23. In coarse-grained materials most of the break-up appears to happen during the early stages of deformation, i.e. $\varepsilon<1$. At further deformation the break-up tends to saturate, giving a grain thickness of about one third to one half of the theoretical thickness in all the alloys. However, no effect of solute content can be seen in this diagram, and it is not possible to relate the low work hardening rate of high-Mg alloys to the grain break-up phenomenon.

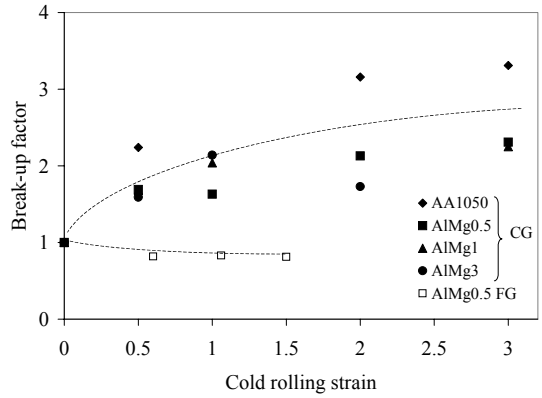

Figure 5.23: Grain break-up, represented by a break-up factor, for coarse-grained AlMgX alloys and AA1050, as well as the fine-grained AlMg0.5.

The picture is quite different for the fine grained alloys. Here the measured grain thickness almost follows the predicted grain thickness, which results in a break-up factor near unity. Such a grain size dependence of the grain break-up has been pointed out by several authors, e.g. Hughes (1995) and Sæter (1997). It is ascribed to a more homogeneous deformation in small grains than in large grains, i.e. there are fewer selected combinations of slip systems within one grain. This is also thought to be the reason for the large break-up in AA1050, which has a higher initial grain size than the AlMg alloys.

Shear banding

As mentioned in section 2.2.5 the formation of shear bands may be associated with a work softening. The theory behind this is that the material volumes within the shear bands are subjected to extensive dynamic recovery, perhaps due to a local temperature increase resulting from the intense shear deformation. The shear bands may therefore accommodate large strains in hard oriented grains, with a corresponding reduction of the work hardening compared to the expected (Korbel et al. 1986, Inagaki et al. 2002).

Shear banding has been studied in the present alloys, see section 4.3.1. A quantification of the phenomenon has not been attempted in this work, but a brief characterisation is performed. This indicates that the amount of shear banding increases with the concentration of Mg, a trend observed by many authors, e.g. Inagaki and Kohara (1997). The discrepancies between the observed work hardening rate in stage IV of AlMg alloys and the model results correspond, at least qualitatively, to the increasing amount of shear bands with Mg-content. This appears as a plausible explanation for the low rate of work hardening in stage IV of the AlMg alloys.

An indirect method to implement the shear banding in the work hardening model can be to ascribe the phenomenon to a different storage mode. If the shear bands "steal" dislocations from the other storage mechanisms described in fig. 2.27, and the recovery rate of dislocations is higher in the bands than elsewhere, a lower net storage rate is expected. Stage IV is related to the decrease of the subgrain size, eq. (2.36), which will be less dominant if the shear bands consume a fraction of the dislocations. The storage pattern is reflected by the S-parameter. If S_{IV} in eq. (5.9) is assumed to be alloy independent, the stage IV work hardening rate will depend only on $\rho_{\mathrm{i}}/\sqrt{\rho}$, which increases with solute concentration. If, however, the S_{IV}-parameter is adjusted so as to account for the shear banding that occurs, a lower θ_{IV} may be predicted. In fig. 5.24 values of S_{IV}/S_{sc} used in the model calculations are shown as a function of the Mg content (S_{sc} is given by eq. (2.34)). The normalised parameter S_{IV}/S_{sc} is assumed to be 1 for a pure metal and decreases upon Mg addition.

It should be pointed out here that effects due to an increase in boundary misorientation or storage of dislocations, for instance in shear bands, are more direct expressions for the effects due to dislocation debris in the Rollett-Kocks model (Rollett et al. 1987, Rollett and Kocks 1994).

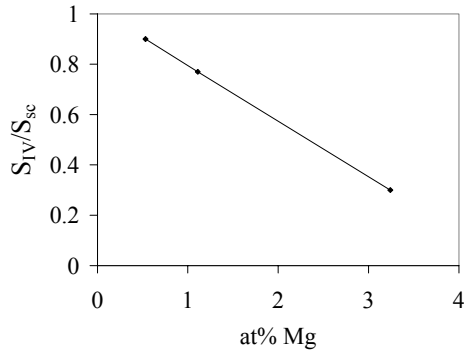

Figure 5.24: Values of S_{IV}/S_{sc} for various Mg concentrations used in the model.

Modelled stress-strain curves in stage IV

The modelling of solute effects in the generic case in fig. 2.30 predicted too high work hardening rates for the high-Mg alloys in stage IV. These discrepancies are in the above discussion suggested to origin from a different storage pattern of dislocations, reflected by q_c and S_{IV}. The estimated values for these parameters as functions of the Mg content, given in fig. 5.21 and fig. 5.24, are used in the model in order to obtain a better representation of stage IV. The values of C in fig. 5.19 are also taken into account, and C and q_c are mutually "balanced" in order to obtain the correct work hardening rates in all stages. The misorientation evolution case 1 in fig. 5.22 (a) is used. Fig. 5.25 shows the modelled stress-strain curves up to large strains for AlMg0.5, AlMg1 and AlMg3.

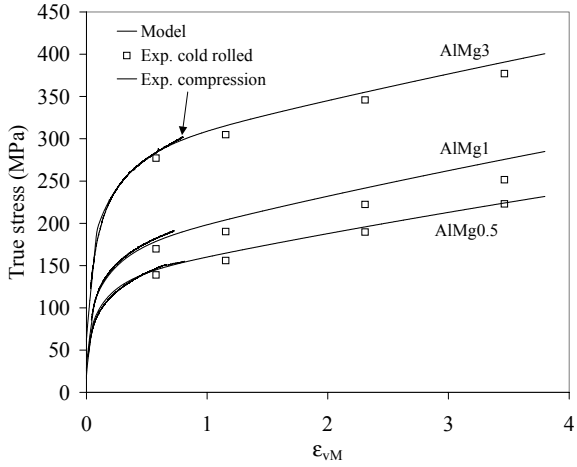

Figure 5.25: Modelled stress-strain curves up to large strains with corrections for the effect of Mg content on C, q_c and S_{IV}.

Experimental results from compression tests on O-temper materials and tensile tests on cold rolled materials are displayed for comparison, and it is seen that a good agreement is obtained. Almost correct work hardening rates in stage IV are achieved, in contrast to fig. 2.30.

5.3.3 Particle and grain size effects

The effects of grain boundaries and non-shearable particles on the work hardening behaviour are of two kinds:

- A direct effect on the flow stress (τ_p and $1/D$ in eq. (2.22))
- An indirect effect through the slip length in eq. (2.30) and eq. (2.31) influencing the athermal storage of dislocations

The Orowan bypass stress, τ_p, given by eq. (2.23) will give a constant contribution to the flow stress. The large initial hardening seen in AA3103-C in fig. 5.15 (a) however, may relate to limitations on the slip length from the particles. It was discussed in section 5.2.1 that the difference between AA1050 and AA3103-C in fig. 5.15 (a) was related to both a particle effect and a clustering effect. Estimated values of r and f_r were given in table 5.7 and are used as input to eq. (2.23) and eq. (2.24), where A=1 is assumed, the Orowan contribution ($\sigma_p = M \cdot \tau_p$) is calculated to be around 10 MPa. The constant A is in a recent work estimated to only be around 0.3 in an alloy containing dispersoids (Nes et al. 2001). Additionally, according to Dons (2003) a more realistic value of the volume fraction of particles is around f=0.03. Therefore, it is more likely that σ_p is of the order 4 MPa.

The rest of the 20 MPa difference between these alloys must originate from a slip length effect and a solute cluster contribution. As seen from eq. (2.30) and eq. (2.31) the slip length is determined by the substructure (L_ρ), particles (L_p) and grain size (L_D), given by:

$$L_\rho = \frac{C}{\sqrt{\rho}}\ ,\ L_p = \frac{r}{2f_r} \text{ and } L_D = D \tag{5.11}$$

An analysis of the different terms in eq. (5.11) suggests that out of these the particles give the strongest slip length restriction (L_p=8.3 μm) in AA3103-C. This is considerably smaller than the slip length due to dislocations and the grain size, estimated to L_ρ=12 μm and L_D=65 μm, respectively. Using eq. (2.30) this means that the effective slip length is reduced from about 11 μm to 7 μm by introducing particles. As seen from fig. 2.30 (a) this corresponds to quite a significant increase of the flow stress, and an estimate based

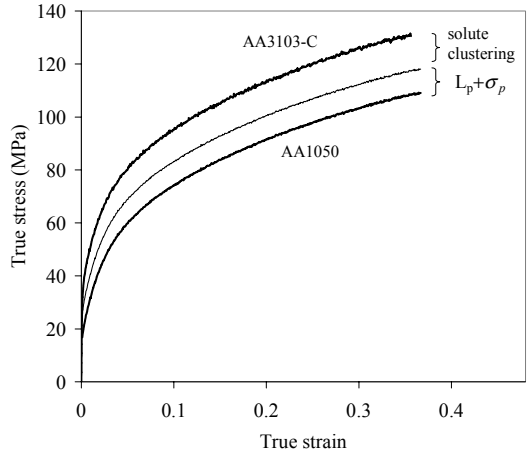

Figure 5.26: Curves showing an estimate of the Orowan contribution added to AA1050. Slip length and solute effects explain the remaining difference up to AA3103-C.

on this figure gives a stress contribution due to the slip length of about 5 MPa. In fig. 5.26 the estimated contribution of direct and indirect particle effects is added to the AA1050 curve, leaving a considerable gap to the AA3103-C curve, a difference that is ascribed to a solute clustering effect.

The grain size effects are analysed in a similar way. From eq. (2.22) it can be seen that the direct grain size effect on the flow stress is:

$$\sigma_D = \alpha_2 MGb \cdot \frac{1}{D} \tag{5.12}$$

for a material without subgrains. By reducing the grain size from 79 to 10 μm, as in AlMg1, eq. (5.12) predicts a direct strength contribution of 4 MPa. In fig. 5.27 (a), these 4 MPa are added to the coarse-grained AlMg1. Similarly, a contribution of 7 MPa in AA3103-B are added to the coarse-grained curve in fig. 5.27 (b). What is interesting here is that the direct grain size contribution given by eq. (5.12) is much too small to account for the real grain size effect in AlMg1, but sufficient in the AA3103-B alloy. This can be understood in terms of the slip length restrictions. At grain sizes around 5-10 μm L_D becomes of the same order as L_ρ, and will therefore contribute significantly to the strength. In AA3103-B however, L_D is still larger than the slip length L_p due to particles. Thus, in this alloy the grain size does not contribute as much to the strength as in AlMg1. In the particle-free AlMg1 the effective slip length, L_{eff}, is given solely by L_ρ and L_D,

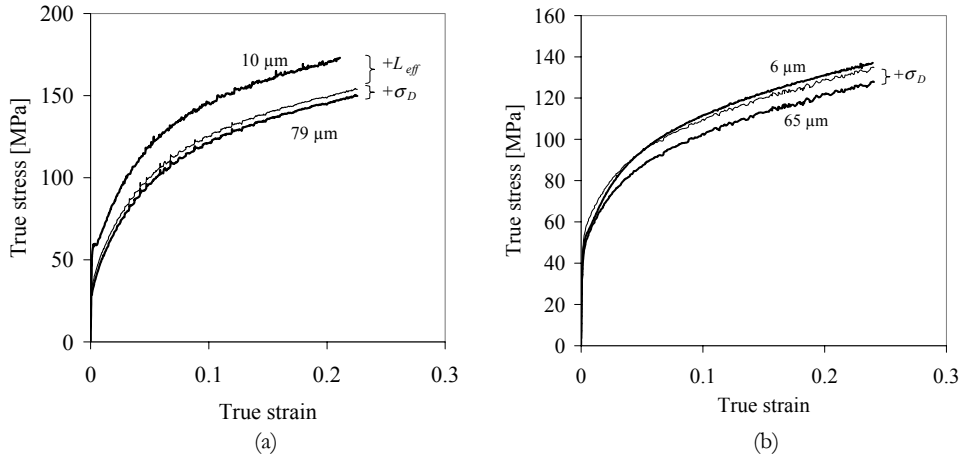

Figure 5.27: Direct grain size effect (σ_D) added to the coarse-grained curves for (a) AlMg1 and (b) AA3103-B. Experimental curves for fine-grained materials shown for comparison.

giving rise to a large part of the grain size hardening in fig. 5.27 (a). Whether the grain size influences the storage of dislocations, and hence L_ρ, is not clear from the investigations done in this work.

5.4 Suggestions for further work

Shear banding is believed to have a strong influence on the work hardening of AlMg alloys. However, in order to incorporate the phenomenon in the model, a good quantitative description of the amount of shear bands is necessary. In section 4.3.1 it was distinguished between two types of shear bands, characterised by their appearance in the light optical microscope. This distinction needs to be explored in more detail, and the works by Inagaki and co-workers (e.g. Inagaki and Kohara 1997) are recommended in this context. How the shear bands really affect the mechanical properties is not fully understood, but may be explained in terms of the microstructure. The increasing performance of FE-SEM and EBSD analysis methods may help improving the understanding of shear bands. A more detailed characterisation of the shear banding phenomenon, with emphasis on quantification, should therefore be of great value for the present model.

Even though the present EBSD analyses cover much larger areas than what is possible in TEM, there is always a need for more detailed and comprehensive experiments. It is

well known that the substructure evolution depends on the grain orientation. Therefore, an effort should be done in order to examine grains of a representative selection of orientations.

A better quantitative description of the effect if Mg content on the dislocation density (ρ_i) should be attempted in order to obtain more correct estimates for the q_c-parameter. Detailed TEM investigations are then required.

Solute clustering of Mn, Fe and Si is discussed in section 5.1.1. The phenomenon is barely mentioned in the literature, and advanced high-resolution TEM investigations or other high-resolution techniques are probably required in order to confirm the existence of clusters. Indirect methods may also be used for studying the phenomenon.

Recently, a statistical distribution of subgrain sizes has been included in order to avoid a sudden change of gradient between stage II and III in the modelled results. This procedure needs further development, and work is in progress (Holmedal and Nes 2003).

A model for dynamic strain ageing (DSA) that accounts for the negative strain rate sensitivity is currently being implemented in the work hardening model. This work is in progress (Holmedal and Nes 2003) and is not included in the present thesis.

6. Conclusions

In part A of this thesis, materials belonging to the AA1xxx, AA3xxx and AA5xxx alloy systems are investigated. Industrial alloys, as well as commercial grades of AlMg alloys, are compared to high-purity aluminium and binary alloys. The most important results from experiments and modelling are summarised in the following.

1. The overall strength increases with alloying and plastic deformation because of solution hardening, particle hardening and work hardening.

2. Magnesium in solid solution gives a simple concentration dependence of the strength at a given strain: $\sigma = \sigma_{pure} + Kc^{n}$, where K increases with strain due to work hardening, and $n \approx 3/4$ for binary alloys and $n \approx 1$ for commercial alloys at room temperature. The difference in n is ascribed to an effect of impurity elements.

3. Manganese in solid solution is, in combination with iron and silicon atoms, believed to create solute clusters at room temperature that dissolve at higher temperatures. Compared to the small amounts of these elements in solution, the clusters result in a considerable increase of the strength of the alloys. The pure solid solution hardening of Mn however, is of the same order as that of magnesium.

4. Impurities, such as iron and silicon, significantly increase the strength. This is ascribed to a solute clustering effect of these elements.

5. Solute effects of magnesium on the stage II-III behaviour are successfully modelled using the present work hardening model. Different rates of storage and dynamic recovery of dislocations with solute atoms present are accounted for by the model.

6. Non-shearable particles in AA3103 and AA5005 give a high initial strength, but a negligible contribution to the work hardening. Stage II is then characterised by a more curved stress-strain behaviour.

7. A reduction of the grain size below 25 μm increases the yield strength. An exception is AA3103, where the particle contribution overshadows the grain size effect.

8. The strength contribution from particles and reduced grain size is a combination of direct effects from the particles and grain boundaries, and indirect effects from slip length restrictions. In fine-grained AA3103 however, the particles dominate the

effective slip length, and the direct grain size effect explains all the grain size hardening.

9. Small grain sizes and high solute contents, particularly in combination, promote yield point elongation (Lüdering) in O-temper materials due to the lack of mobile dislocations.

10. During cold rolling to strains above ε=0.5-1 the materials turn into a stage IV of linear work hardening rate. β-fibre rolling textures evolve, the substructure is refined and the subgrain misorientation increases with strain. The effects of magnesium additions are a reduced subgrain size, a higher dislocation density inside the subgrains and more frequent shear banding. The rolling texture is also influenced by the magnesium content, and reducing the grain size gives a faster development of the β-fibre with strain.

11. The substructure is characterised using TEM and high-resolution EBSD in an FE-SEM. The latter technique gives a far better statistical basis for quantitative analyses than TEM, and the spatial resolution appears to be sufficient for providing reasonable values for the subgrain size. The angular resolution is not good enough, but at least trends in the misorientation evolution with strain are possible to measure.

12. The work hardening rate in stage IV is almost invariant of the alloying content, even though the flow stress at the beginning of stage IV increases strongly with alloying.

13. The unexpectedly low work hardening rate in stage IV of high-Mg alloys is believed to result from a different storage pattern of dislocations in subgrain interior and boundaries, but also from an increased shear band formation. These effects are included in the model and give reasonable predictions of the work hardening in stage IV.

PART B: EXTRUDED MATERIALS

7. Materials and experiments

7.1 Materials

Four industrial extrusion alloys were investigated in this part, table 7.1.

Table 7.1: Chemical composition of the investigated extrusion alloys.

Alloy	wt% Mg	wt% Si	wt% Zn	wt% Mn	wt% Zr	wt% Fe	wt% Cu
AA6063[a]	0.46	0.44	-	0.03	-	0.19	0.006
AA6082[b]	0.67	1.04	-	0.54	-	0.20	0.003
AA7030[c]	0.85	0.05	5.63	0.01	0.001	0.12	0.006
AA7108[c]	0.74	0.05	4.94	0.03	0.145	0.14	0.005

a. Pettersen and Furu (2001a)
b. Pettersen and Furu (2001b)
c. Furu (2001)

- AA6063: A low strength precipitation hardening alloy from the Al-Mg-Si-system.
- AA6082: A relatively high strength precipitation hardening alloy from the Al-Mg-Si-system containing Mn-dispersoids that prevent recrystallisation and grain growth.
- AA7030: A high strength precipitation hardening alloy from the Al-Zn-Mg-system.
- AA7108: A high strength precipitation hardening alloy from the Al-Zn-Mg-system containing Zr-dispersoids that prevent recrystallisation and grain growth.

The materials were DC-cast and homogenised (see fig. 7.1) by Hydro Aluminium, Sunndal. Billets with diameter 203 mm were extruded, by a reduction ratio of 53 and a ram speed of about 15 mm/sec, into flat profiles of thickness 3 mm and width 205 mm by Hydro Aluminium Profiler, Raufoss (fig. 7.1). After the outlet of the die the 6xxx-alloys were cooled with maximum spray-cooling, followed by forced air-cooling. The 7xxx-alloys were cooled by forced air-cooling only.

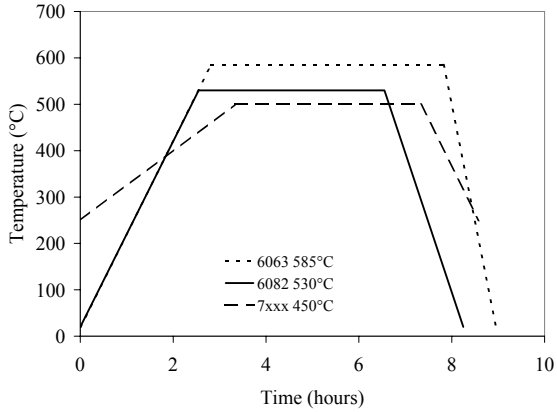

Figure 7.1: Approximate homogenisation treatments of the billets before extrusion.

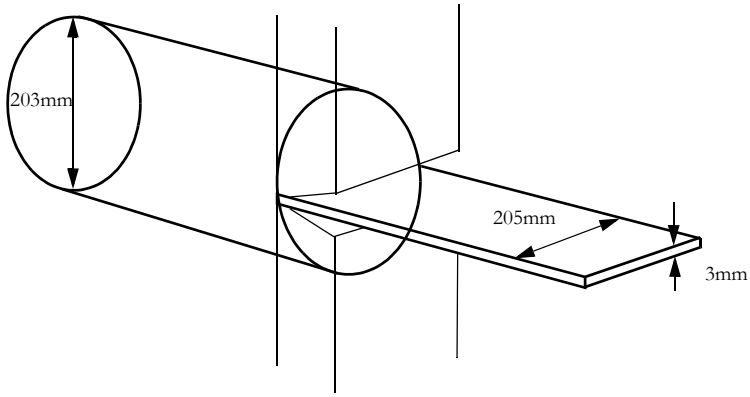

Figure 7.2: Sketch of the extrusion of the billet to the flat profile.

7.2 Solution heat treatment and natural ageing

Before tensile testing the specimens were solutionised in salt bath for 30 minutes followed by water quenching. 530°C was applied to the 6xxx-alloys (Pedersen 2001), while the 7xxx-alloys were heat treated at 480°C in accordance with Søreng (1997) and Fjeldly (1999). The subsequent natural ageing behaviour, i.e. ageing at room temperature, was explored by measuring the Vickers hardness after various storage times after water quenching. 5 kg load was used together with a short loading time of 5 seconds in order to obtain as instantaneous measurements as possible. The ageing behaviour is seen in fig. 7.3.

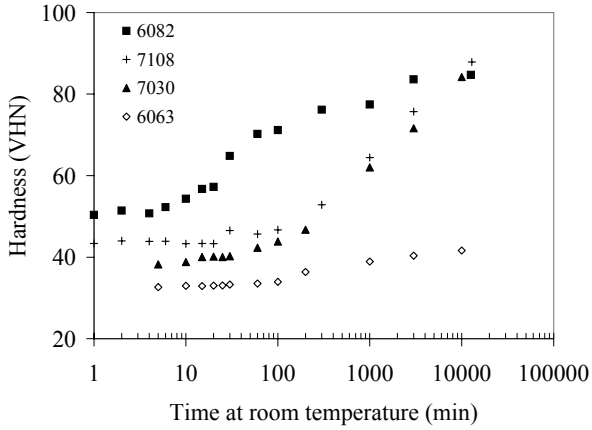

Figure 7.3: Ageing behaviour of the extruded alloys at room temperature.

7.3 Tensile testing

All mechanical testing was performed in the W-temper, i.e. in the solution heat treated condition as described in section 7.2. To avoid any effects from natural ageing on the test results, it was decided that the tests should be started after maximum 3 minutes at room temperature, cf. fig. 7.3. The material condition may therefore be denoted W3. This was especially important with the AA6082-alloy, in which the precipitation seemed to start already after four minutes. With the applied strain rate the tests were accomplished within maximum one minute. The specimens were stored in liquid nitrogen after solutionising and rapidly tempered in water to room temperature before testing.

The tensile specimens were cut from the extruded profiles in eight different directions with respect to the extrusion direction:

0°(ED) 15° 30° 45° 55° 60° 75° 90° (TD)

The tests were performed in an MTS 880 servo-hydraulic testing machine at a constant ramp rate corresponding to an initial strain rate of $0.008s^{-1}$. Longitudinal and transverse extensiometers were used. The specimens had a width of 12.7 mm and a parallel length of 65 mm. The test directions, strain rate and specimen dimensions were chosen in accordance with the experiments of Fjeldly and Roven (2000).

Additionally, to study the effect from the layers of the microstructure, tensile specimens thinned from both profile surfaces were tested. These tests were performed on the 0°,

45° and 90°-directions of the AA6063 and AA7030 alloys. The mid 1.5 mm, i.e. from s=0.5 to s=0.5, of the profiles were tested.

7.4 Global texture

In order to examine the texture gradients through the profile thickness, specimens from the profiles were ground to the desired positions from where the global texture was measured, fig. 7.4. The positions are given by s-values, where s=0 represents the mid-thickness and s=1 the profile surface. For more details about specimen preparation and texture measurements, see section 3.6.

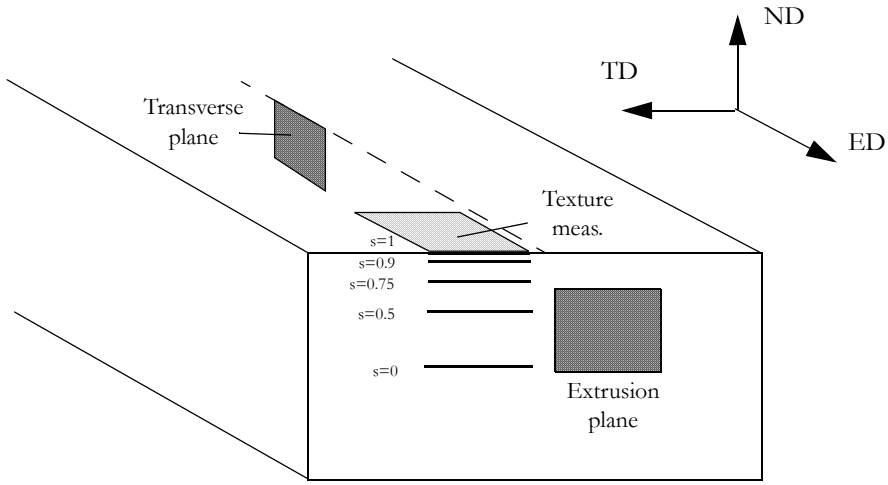

Figure 7.4: Sketch showing the transverse plane and the extrusion plane, as well as the positions for measurements of global texture in the extruded profiles.

7.5 Microscopy

Light optical microscopy and scanning electron microscopy were applied to these alloys in order to examine the grain and subgrain structure, as well as the microtexture in as-extruded condition and after tensile deformation. The materials were investigated on the longitudinal transverse plane, i.e. the plane containing the extrusion direction and the normal direction, but in some cases also on the extrusion plane, see fig. 7.4. See section 3.7 for details about the experimental techniques of OM and EBSD.

8. Experimental results

The main objective of this section is to present some observations that may provide a better understanding of why the mechanical properties and formability of extruded profiles vary as they do. The formability can be defined in terms of several properties, such as yield stress, rate of work hardening, uniform strain and plastic strain ratio. These results are presented in section 8.2. But first a detailed characterisation of the initial microstructure and texture is given (section 8.1). This is necessary in order to be able to explain the mechanical properties and the anisotropy, but also for modelling purposes. In addition, an investigation of the development of the microstructure and texture during tensile testing is presented in section 8.3.

8.1 Characterisation of as-extruded materials

The microstructure of the extruded profiles is examined through their cross-section using EBSD. Two of the alloys, AA6063 and AA7030, recrystallised subsequent to the extrusion process. The other alloys, AA6082 and AA7108, kept their fibrous deformation structure from extrusion, except for the surface layers that recrystallised down to depths of about 150 μm on each side.

The global texture is measured by X-ray diffraction in several positions parallel to the normal plane from the centre to the surface of the profiles (s=0-1). In the following text, only selected sections of the calculated ODFs from the positions s=0 and s=0.75 are presented. The texture gradients through the profiles, as well as cube-fibre and β-fibre density plots at different positions in the profiles are shown.

Common for all the alloys is the extremely strong textures. Intensities up to 120x random are observed. The two recrystallised alloys contain typical recrystallisation textures, i.e. cube, rotated cube and Goss textures. The non-recrystallised alloys both have a rolling-type texture, i.e. a β-fibre. Some texture gradients are observed through the profiles. However, the AA7xxx alloys are generally more uniform through the thickness than the AA6xxx alloys, with respect to both microstructure and texture.

8.1.1 AA6063

Fig. 8.1 (a) shows the grain structure of AA6063 between the two surfaces of the profile (s=1-1). The alloy appears to be completely recrystallised, but there are large variations

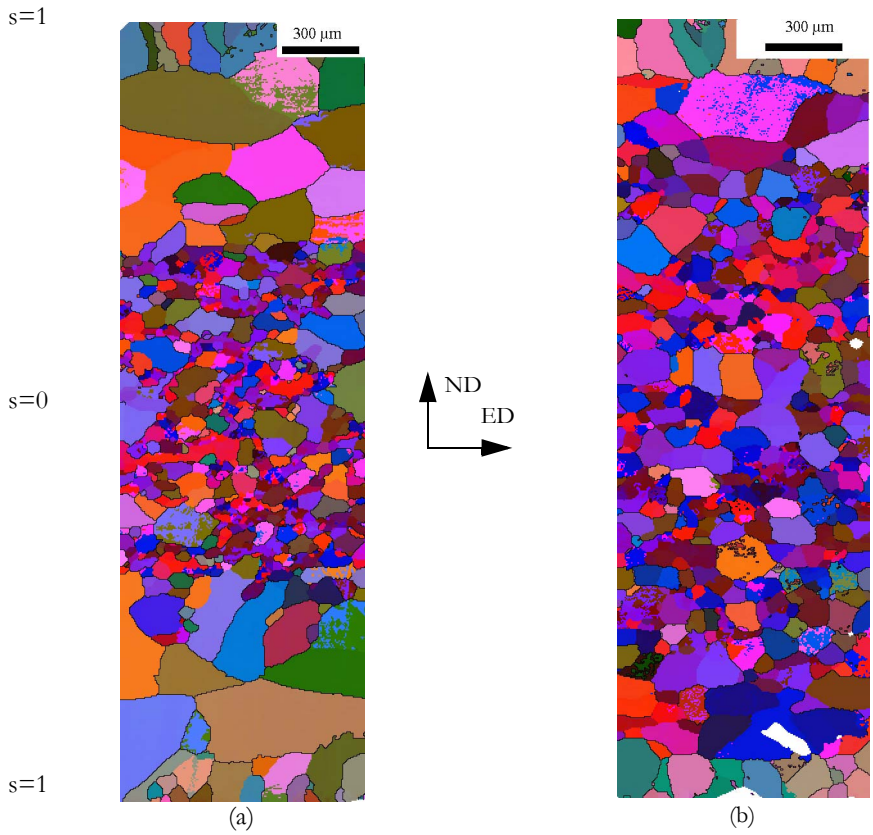

Figure 8.1: EBSD-maps of (a) AA6063 and (b) AA7030, both as-extruded, taken between the two profile surfaces with a step size of 5 µm. High-angle boundaries >15° are shown.

in the grain structure. The structure can be divided into three layers and the grain size of each layer is listed in table 8.1:

1. In the middle of the profile (around s=0) there is a mixture of small and large grains. Many of these grains are separated by boundaries of rather low misorientations. The lower limit for the definition of high-angle grain boundaries is set to 15° and some misorientations are smaller than that, even though the structure looks like a recrystallised grain structure and not a subgrain structure. In AA6063 this layer constitutes 45 % of the cross-section (s=0-0.45).

2. Between the mid-layer and the surface layer there is a region consisting of some very large grains, up to 1 mm in the longest direction.

3. At the surface the grains are columnar with a moderate grain size.

Table 8.1: Grain size measured by the linear intercept method, average of ED and ND. 15° is used as the lowest misorientation.

Alloy	Layer 1 (middle)	Layer 2	Layer 3 (surface)
AA6063	75	157	117
AA7030	96	167	92

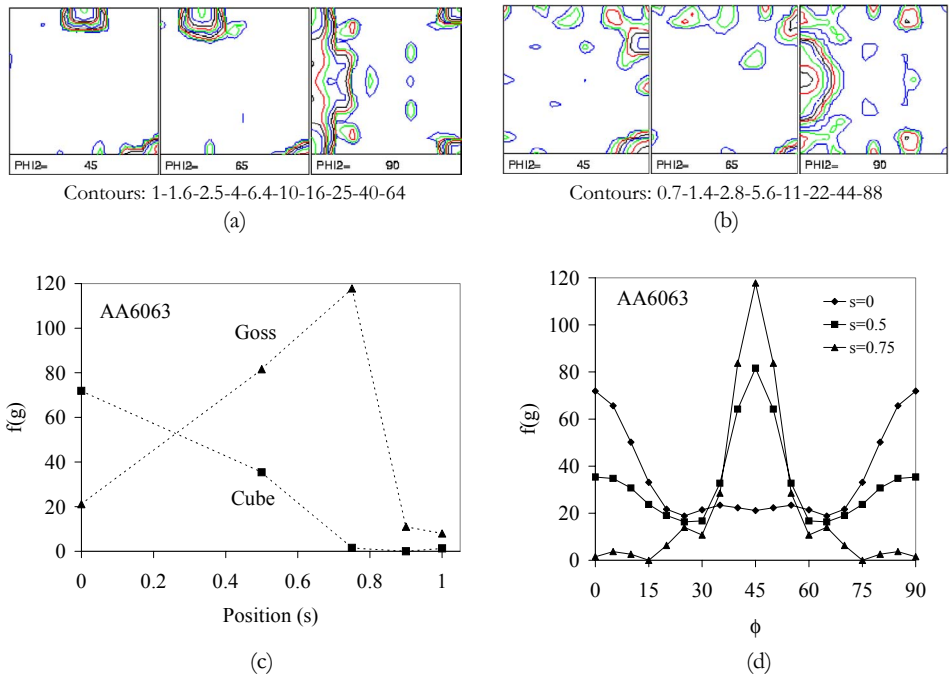

Figure 8.2: Results from the global texture measurements of AA6063. (a) ODF sections from s=0. (b) ODF sections from s=0.75. (c) Texture gradient from s=0 to s=1. (d) Cube-fibre density plots in various positions.

The alloy has an ED-rotated cube texture ((100)-fibre) which is dominated by the cube orientation in layer 1 and by the Goss orientation in layer 2, i.e. around s=0.5-0.75 (see fig. 8.2). In the surface layer the texture is weak.

From the EBSD maps the texture is studied in more detail. Grains within 15° deviation from the cube orientation, the Goss orientation and the (100)-fibre orientations are detected and shown in fig. 8.3. The area fractions and the grain size of each texture component are listed in table 8.2. These numbers show that 2/3 of the material belong to the (100)-fibre, in which the cube and Goss are rather evenly distributed. It is observed

that the small grains and the large grains in layer 1 belong to cube and Goss, respectively. Furthermore, some of the grains in layer 2 have a near Goss orientation. These observations correspond to the measured global textures in fig. 8.2.

Table 8.2: Texture components in AA6063: Area fraction and grain size. Texture components were defined within 15° from the ideal orientation and HAGB >15°.

Texture component	Area fraction	Grain size||ED	Grain size||ND
All grains	100	80.5	93.0
Cube (15°)	21.6	65.0	53.5
Goss (15°)	26.2	110.2	106.3
(100)-fibre (15°)	65.5	81.6	87.9

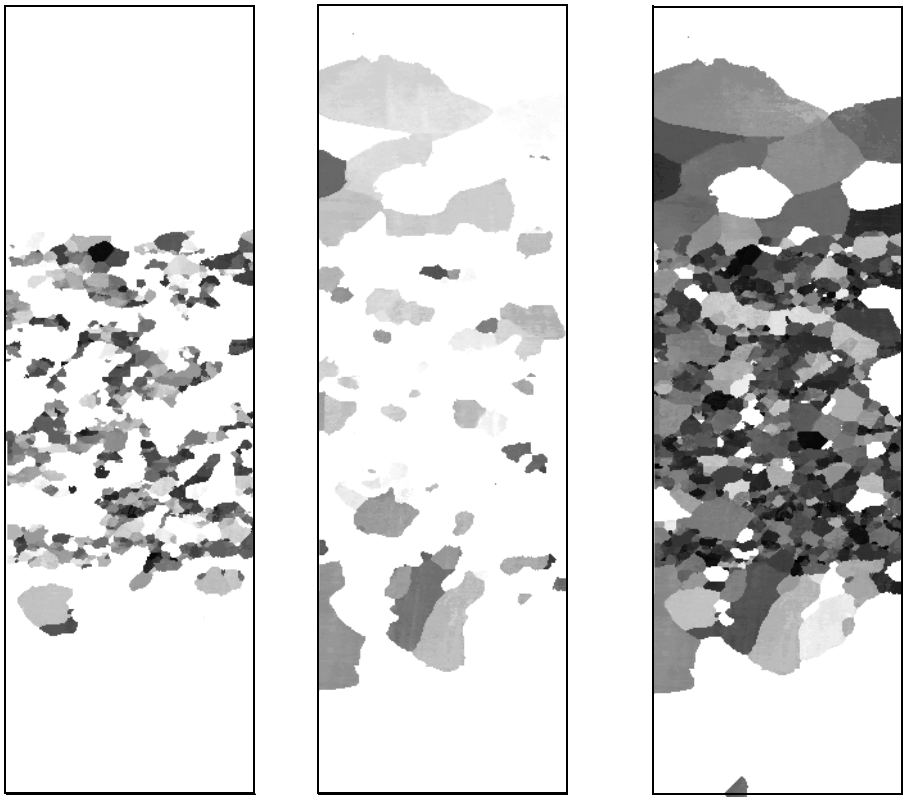

Figure 8.3: EBSD-maps of AA6063 with grains lying within 15° from (a) cube orientation, (b) Goss orientation and (c) the (100)-fibre.

8.1.2 AA7030

As fig. 8.1 shows, the grain structure of the AA7030 alloy has much in common with AA6063, section 8.1.1. However, the mid-layer (1) occupies a larger part of the section, about 70%. Also the texture is comparable in these two alloys, with a strong cube and ED-rotated cube texture, fig. 8.4. In AA7030 the strong Goss intensity observed in AA6063 is missing, and there is almost no texture gradient through the thickness, except for the surface layer.

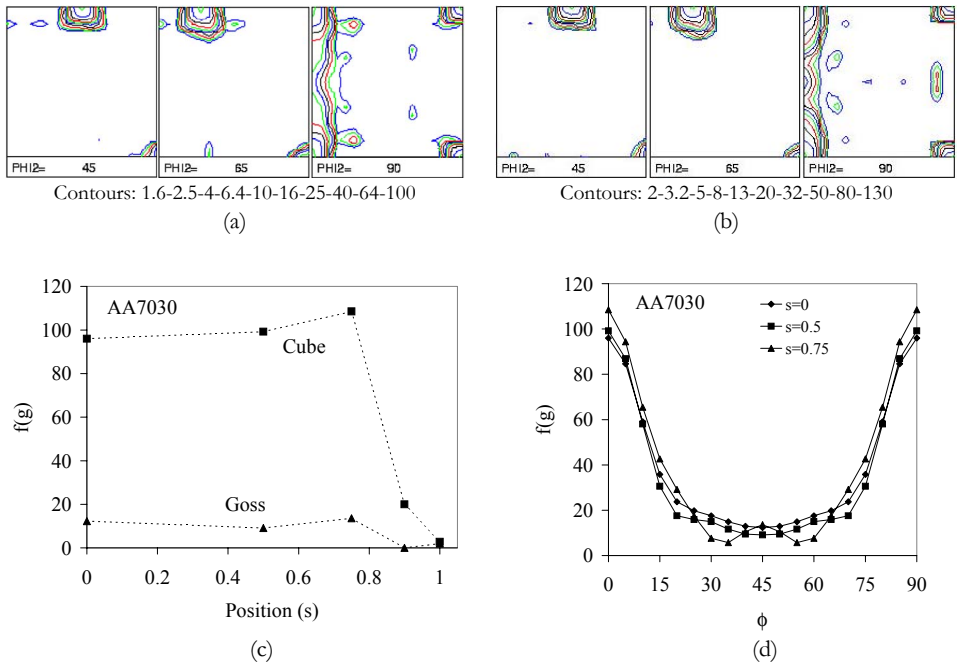

Figure 8.4: Results from the global texture measurements of AA7030. (a) ODF sections from s=0. (b) ODF sections from s=0.75. (c) Texture gradient from s=0 to s=1. (d) Cube-fibre density plots in various positions.

An in-depth analysis of the microtexture is performed in the same way as for AA6063. EBSD maps showing cube grains, Goss grains and (100)-fibre grains are shown in fig. 8.5. The measurements are given in table 8.3, which shows that more than 80% of the grains lie on the (100)-fibre, and more than 50% of these grains are close to the cube orientation. Only a small fraction of Goss grains are observed. In contrast to AA6063, the cube grains are larger than the Goss grains. This is caused by the fact that many of the large grains in layer 2 have cube orientation. In layer 1 the small grains generally have cube orientation, while the larger grains have Goss orientation, as for AA6063.

Table 8.3: Texture components in AA7030: Area fraction and grain size. Texture components were defined within 15° from the ideal orientation and HAGB >15°.

Texture component	Area fraction	Grain size||ED	Grain size||ND
All grains	100	85.7	73.7
Cube (15°)	48.0	102.3	83.8
Goss (15°)	7.8	53.8	42.7
(100)-fibre (15°)	81.3	105.1	88.3

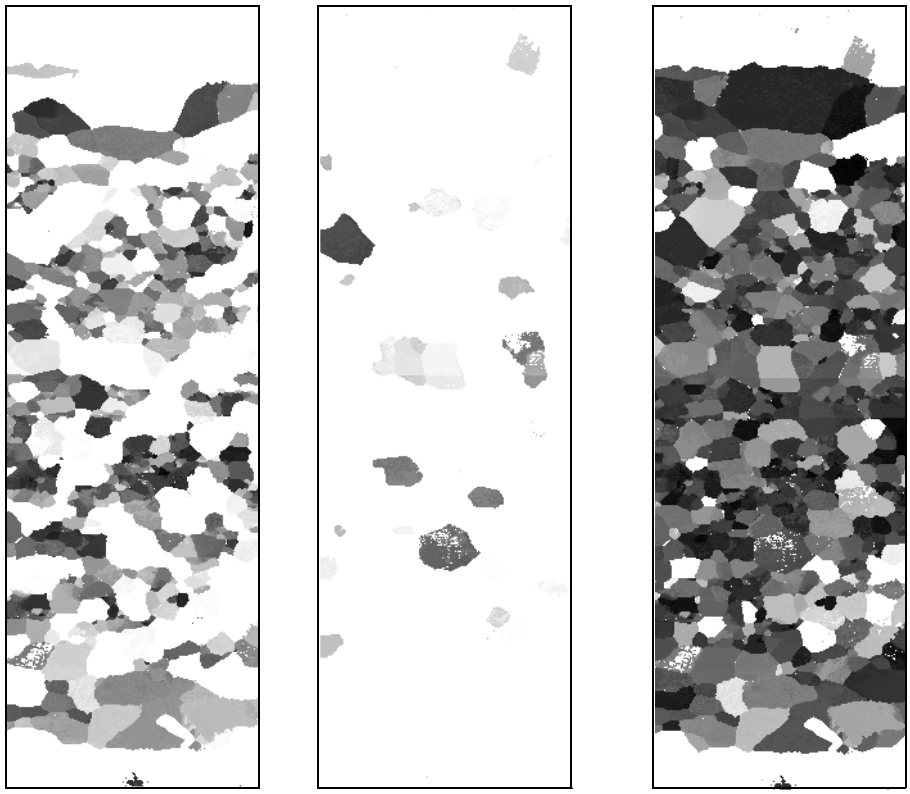

Figure 8.5: EBSD-maps of AA7030 with grains lying within 15° from (a) cube orientation, (b) Goss orientation and (c) the (100)-fibre.

8.1.3 AA6082

The grain structure of the fibrous alloy AA6082 is shown in fig. 8.6 (a) between s=0 and s=1. The cross-section is dominated by a deformation structure with flat, elongated grains, but also with some smaller grains. Between s=0 and s=0.5 there are grains, or

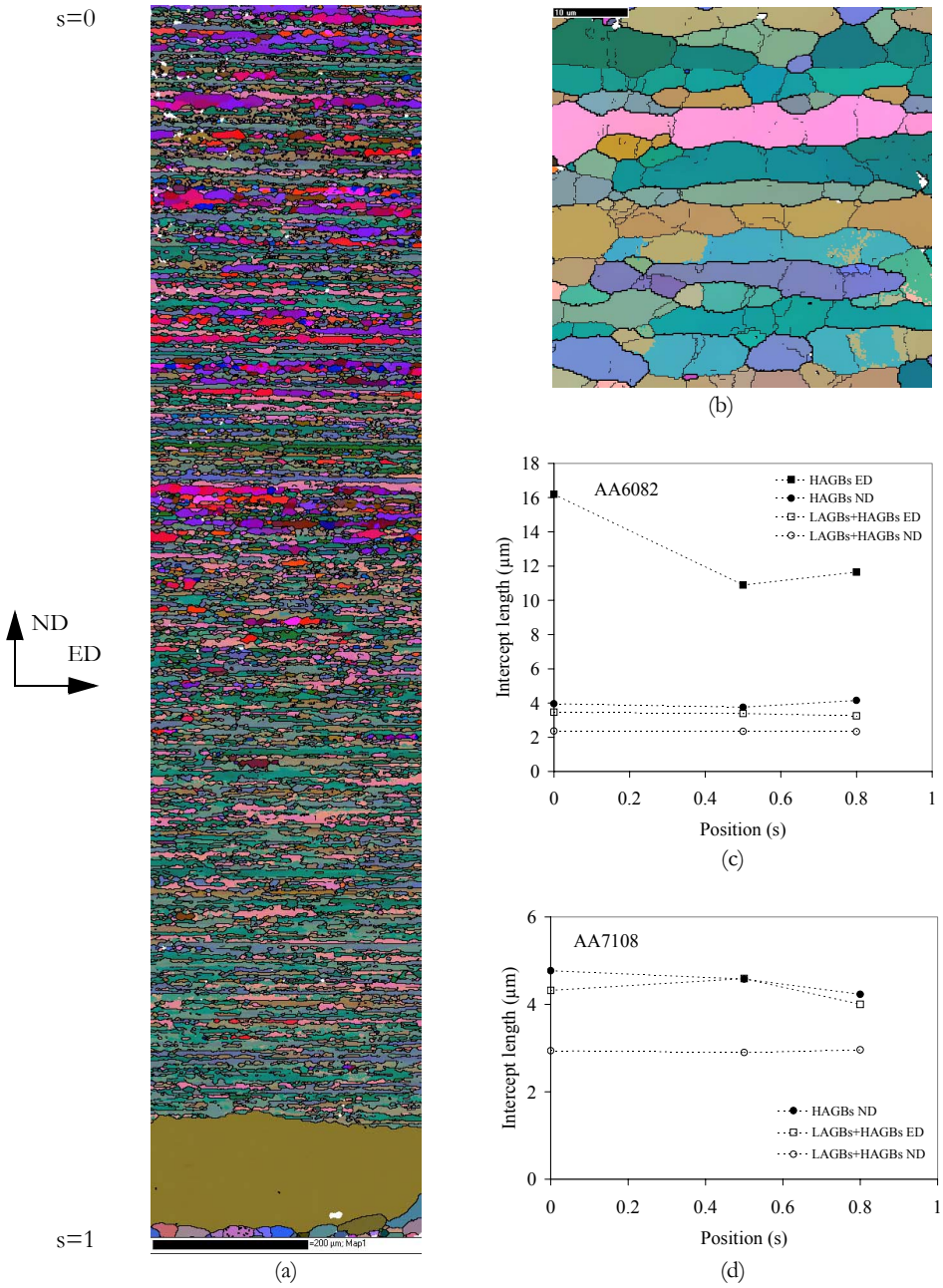

Figure 8.6: (a) EBSD-map of AA6082 as-extruded taken between s=0 (top) and s=1 (bottom). Step size: 1 µm. Grain boundaries: >15°. (b) EBSD-map of the subgrain structure in AA6082, s=0. Step size: 0.2 µm. Grain boundaries: Bold >15°, thin >1°. (c,d) Distance between HAGBs (>15°) and LAGBs + HAGBs (i.e. all boundaries >0.5°), along the extrusion direction and the normal direction. AA6082 and AA7108, respectively.

bands of grains, that are somewhat coarser than the other. Near the surfaces the material is recrystallised, with small columnar grains at the surface and some very large grains inside of them. The recrystallised layer extends to a depth of approximately 150 μm, or s=0.9.

Increasing the magnification and EBSD resolution, the deformed grains are seen to be divided into subgrains as shown in fig. 8.6 (b). The distances between HAGBs and LAGBs are measured using the linear intercept method along both the extrusion direction and the normal direction, and plotted in fig. 8.6 (c). On average, the grains seem to be divided into two subgrains in the normal direction, and into several subgrains in the extrusion direction. Especially in the middle of the profile, the HAGB spacing parallel to ED is large. The subgrain size is almost constant through the cross-section, with an aspect ratio of about 1.5.

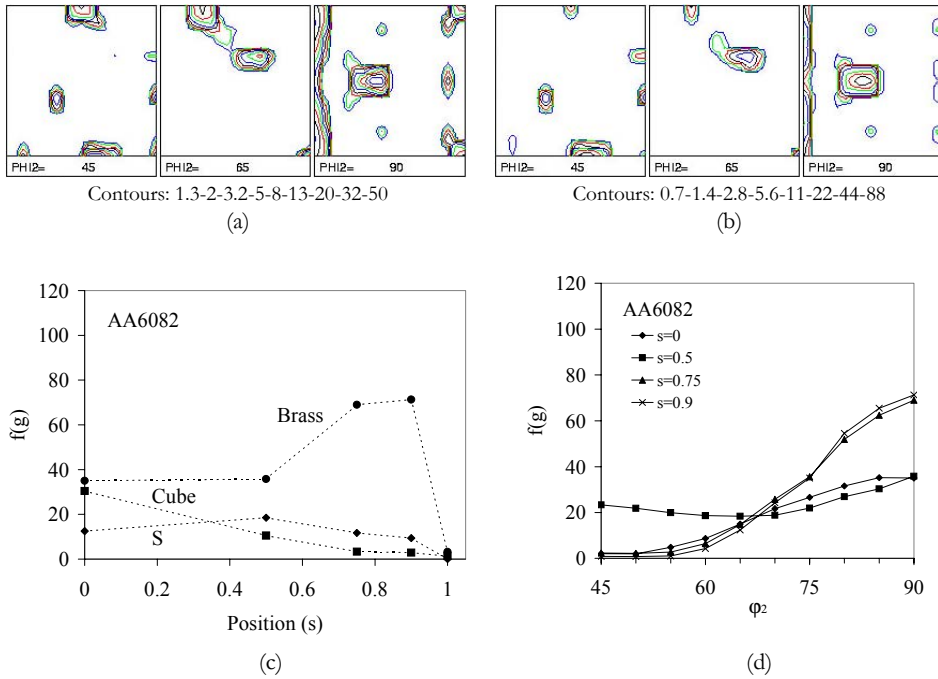

Figure 8.7: Results from the global texture measurements of AA6082. (a) ODF sections from s=0. (b) ODF sections from s=0.75. (c) Texture gradient from s=0 to s=1. (d) β-fibre density plots in various positions.

The AA6082 alloy has a well-defined fcc rolling-type texture, i.e. a β-fibre ranging from the C-orientation through the S-orientation to the B-orientation. In this alloy the β-fibre is strongly dominated by the B-component, while the C-component is almost absent.

Especially between s=0.7 and s=0.9 the B-component is very strong. There is also a fraction of cube-grains, particularly evident in the middle of the profile. Outside s=0.9, i.e. in the recrystallised layer, the texture is weak with only incidental recrystallisation texture components.

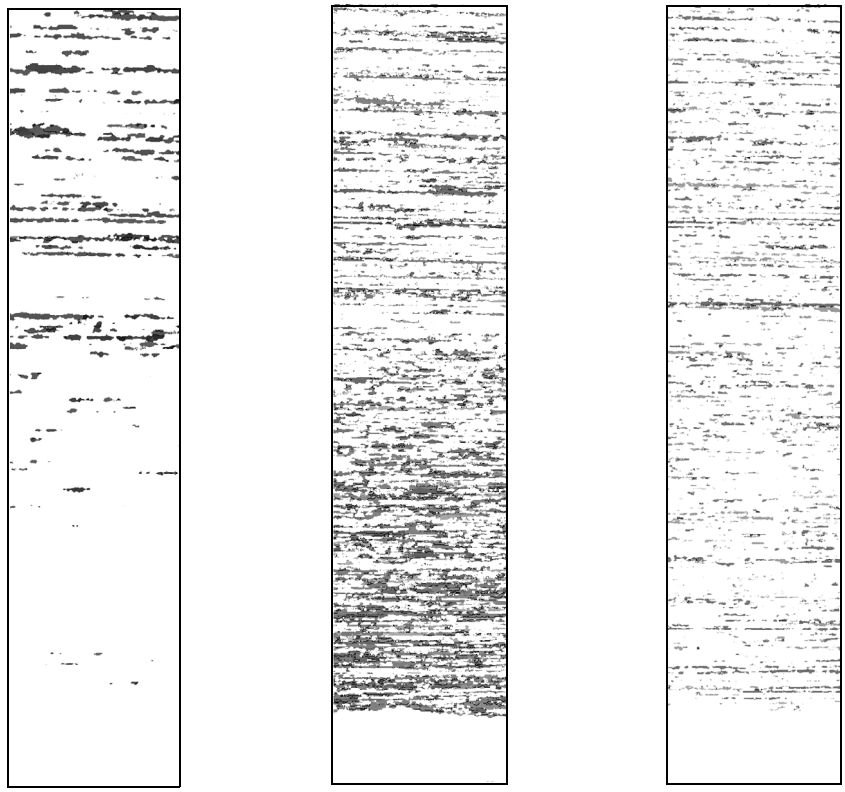

Figure 8.8: EBSD-maps of AA6082 with grains lying within (a) 15° from cube orientation (b) 10° from brass orientation and (c) 10° from S orientation.

In fig. 8.8 the cube grains, brass grains and S-grains in this alloy are shaded. Equivalent orientations of brass and S are included. The area fraction and grain size of each texture component are listed in table 8.4. The first thing to notice is that the coarse grains or bands mentioned above have cube orientation. As these grains appear to be most frequent in the middle of the profile, this corresponds to the observation of higher cube intensity at s=0, fig. 8.7 (c). Secondly, the density of brass grains is highest between s=0.5 and 0.9, cf. the high brass intensities at these positions in (c,d). The S-grains are evenly

distributed through the profile. The higher amount of copper orientation in s=0.5 in AA6082 is not confirmed by the EBSD analysis.

Table 8.4: Texture components in AA6082: Area fraction and grain size. An orientation spread of 15° was used for the cube orientation, while 10° was used for the rolling texture components.

Texture component	Area fraction	Grain size||ED	Grain size||ND
Cube (15°)	8.2 %	13.3 μm	6.8 μm
Brass (10°)	34.2 %	7.6 μm	4.4 μm
S (10°)	13.2 %	6.5 μm	3.6 μm

8.1.4 AA7108

The AA7108 alloy is not studied to the same detail as AA6082. However, a brief investigation is performed, indicating a strong similarity to AA6082 with respect to microstructure and texture. Thus, the interpretations in section 8.1.3 is generally valid also for this alloy. A fairly uniform subgrain size across the profile, and approximately two subgrains across one grain are observed, see fig. 8.6 (d). The subgrain size is somewhat larger in AA7108 than in AA6082. The number of HAGBs in ED was too small to be measured.

The texture is dominated by a strong β-fibre with preference on the B-side, see fig. 8.9 compared to fig. 8.7. The two alloys are somewhat different in that the density of B-grains is higher in AA7108, while the density of cube-grains in the middle of the profile is smaller as compared to AA6082.

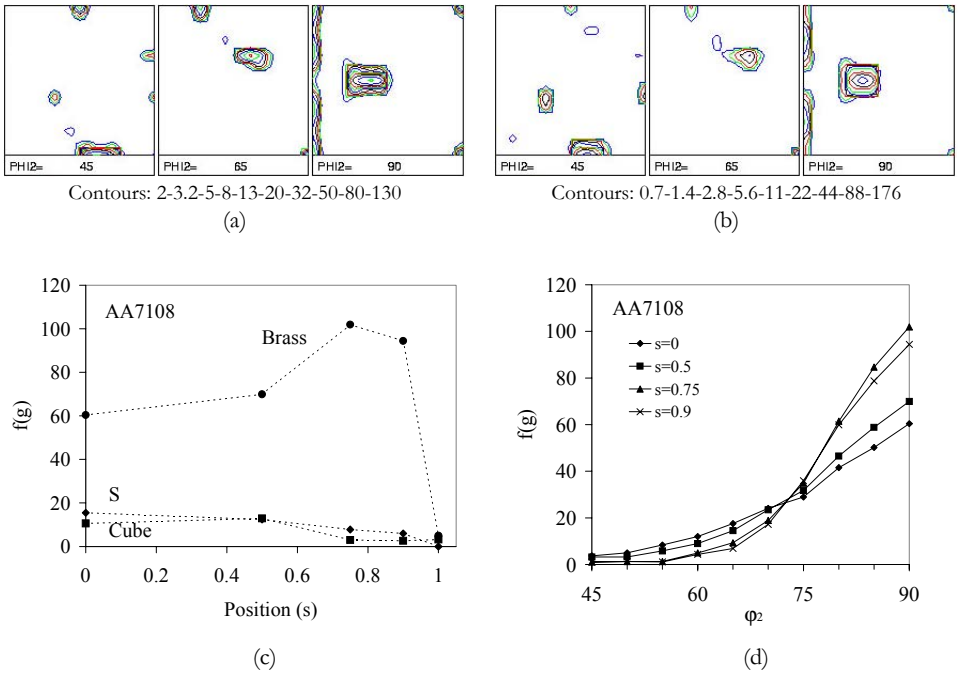

Figure 8.9: Results from the global texture measurements of AA7108. (a) ODF sections from s=0. (b) ODF sections from s=0.75. (c) Texture gradient from s=0 to s=1. (d) β-fibre density plots in various positions.

8.2 Mechanical properties and anisotropy

In this section, results from the tensile tests are presented for each of the investigated alloys, AA6063, AA7030, AA6082 and AA7108 in the solution heat-treated condition (W). Nominal stress-strain curves are presented, showing the serrated flow appearance of the materials. Three to five parallels from each direction were tested and the stress at various strain levels were collected. Since there were some spread in the results, the stress-strain curves were averaged and plotted as smooth σ–ε curves (section 8.2.1). The yield stress, $\sigma_{0.2}$ or $R_{p0.2}$, and the stress at 10% plastic strain, σ_{10}, are read from the stress-strain curves and plotted as functions of the test direction. Also the work hardening rate is calculated by fitting the true stress-strain curves to a forth-order polynomial. The ductility in terms of uniform strain (ε_u) and fracture strain (ε_f) is presented in section 8.2.2. In section 8.2.3 the plastic strain ratio, or the r-value, is calculated on the basis of measured longitudinal and transverse strain.

8.2.1 Yield strength and work hardening

AA6063

The mechanical anisotropy of AA6063 in terms of strength is shown in fig. 8.10. Representative curves for the nominal stress-strain behaviour are given in fig. 8.10 (a), and the average true stress-strain curves for all the test directions in fig. 8.10 (b). Fig. 8.10 (c) shows the rate of work hardening for some directions. The true stress at the yield point, $\sigma_{0.2}$, and at 10% plastic strain, σ_{10}, with respect to the test direction are plotted in fig. 8.10 (d) showing the strength anisotropy. Some of tensile properties are also listed in table 8.5. It is seen that the strongest directions are around 60° while the minimum strength is in the 15-45° and 90°-directions. The strength of the 0°-direction is between

Table 8.5: Tensile properties in selected test directions of AA6063: Yield strength, ultimate tensile strength, uniform strain, fracture strain and r-value.

Direction	$R_{p0.2}$	R_m	A_m	A_f	r-value
0°	43.3	113	0.16	0.20	0.55
30°	36.9	117	0.30	0.33	0.29
45°	37.3	121	0.30	-	0.40
60°	49.6	139	0.27	0.31	0.72
90°	32.7	115	0.28	0.35	1.81

those. The anisotropy in the flow stress is quite similar at both 0.2 and 10% plastic strain. An interesting observation is the stress-strain behaviour of the 0° direction which is distinct from the other. This direction shows a rapid hardening up to 5% strain, but flattens out to a low hardening rate beyond that. Large variations in the work hardening rate with the test direction are observed.

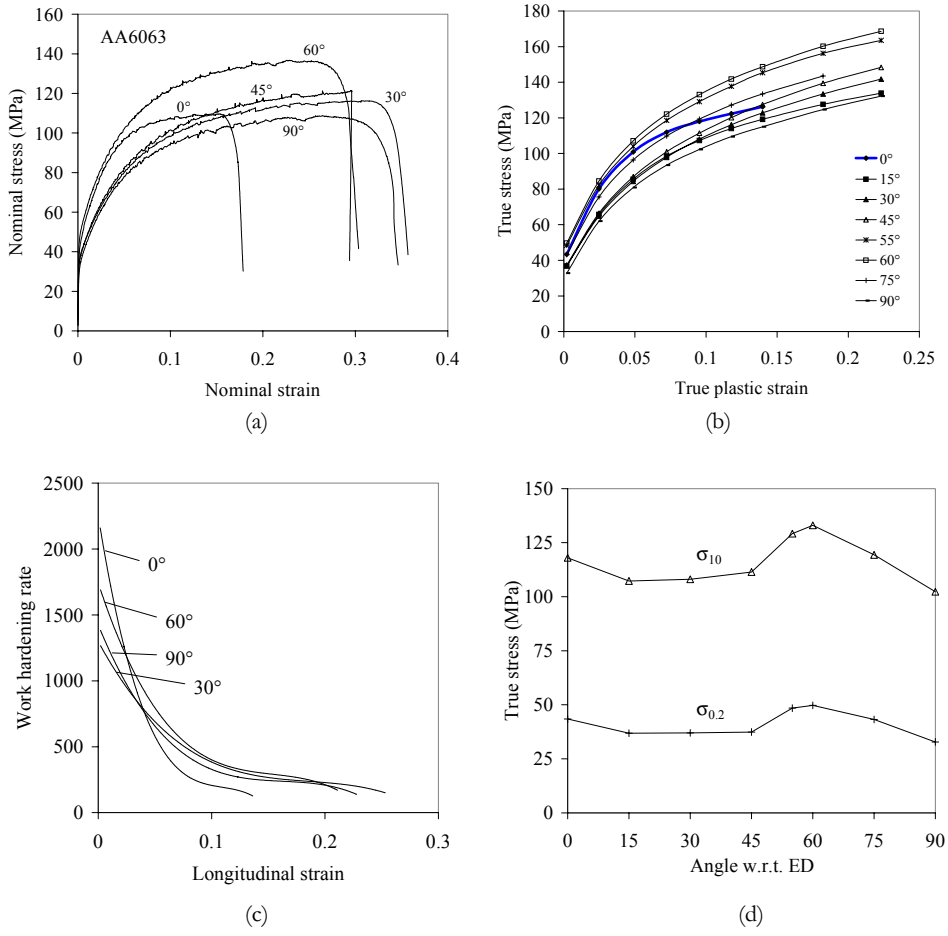

Figure 8.10: Stress-strain behaviour of AA6063: (a) Nominal stress-strain curves for 0, 30, 45, 60 and 90°. (b) True stress-strain curves for all test directions. 0°-direction emphasised with blue colour. (c) Work hardening rate ($d\sigma/d\varepsilon$) in 0, 30, 60 and 90°. (d) Yield stress ($\sigma_{0.2}$) and true stress at 10% plastic strain (σ_{10}).

AA7030

The mechanical anisotropy of AA7030 in terms of strength is shown in fig. 8.11. Representative curves for the nominal stress-strain behaviour are given in fig. 8.11 (a), and the average true stress-strain curves for all the test directions in fig. 8.11 (b). Fig. 8.11 (c) shows the rate of work hardening for some directions. The true stress at the yield point, $\sigma_{0.2}$, and at 10% plastic strain, σ_{10}, with respect to the test direction are plotted in fig. 8.11 (d) showing the strength anisotropy. Some of tensile properties are also listed in table 8.6. This alloy is more isotropic with respect to the flow stress than AA6063. Furthermore, the relative anisotropy of the flow stress is a little larger at 0.2 than at 10% plastic strain. The 0° direction is the strongest, the directions between 15° and 45° are weak, and 60-90° have intermediate high strengths. The same odd shape of the 0°-curve seen in AA6063 is observed in this alloy. Large variations in the work hardening rate with the test direction are observed.

Table 8.6: Tensile properties in selected test directions of AA7030: Yield strength, ultimate tensile strength, uniform strain, fracture strain and r-value.

Direction	$R_{p0.2}$	R_m	A_m	A_f	r-value
0°	56.2	140	0.13	-	0.52
45°	38.4	138	0.32	0.36	0.18
90°	42.8	132	0.24	0.30	2.03

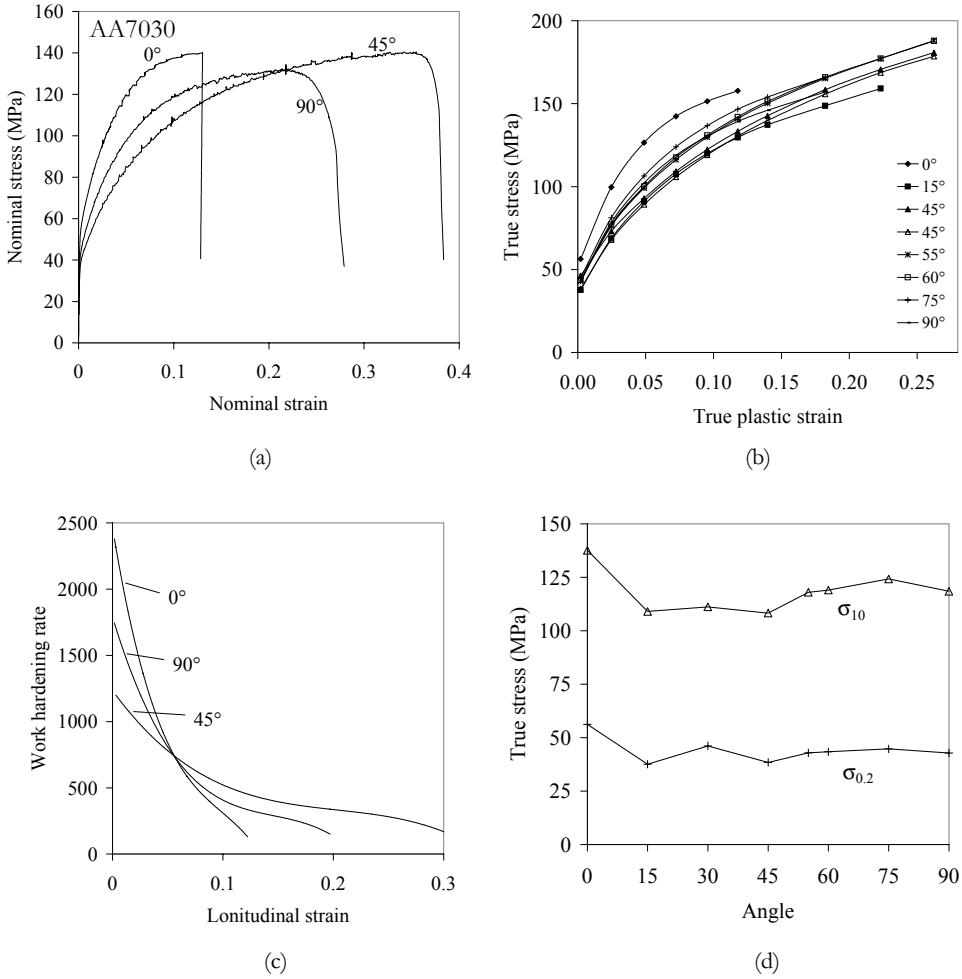

Figure 8.11: Stress-strain behaviour of AA7030: (a) Nominal stress-strain curves for 0, 45 and 90°. (b) True stress-strain curves for all test directions. (c) Work hardening rate ($d\sigma/d\varepsilon$) in 0, 45 and 90°. (d) Yield stress ($\sigma_{0.2}$) and true stress at 10% plastic strain (σ_{10}).

AA6082

The mechanical anisotropy of AA6082 in terms of strength is shown in fig. 8.12. Representative curves for the nominal stress-strain behaviour are given in fig. 8.12 (a), and the average true stress-strain curves for all the test directions in fig. 8.12 (b). Fig. 8.12 (c) shows the rate of work hardening for some directions. The true stress at the yield point, $\sigma_{0.2}$, and at 10% plastic strain, σ_{10}, with respect to the test direction are plotted in fig. 8.12 (d) showing the strength anisotropy. Some of tensile properties are also listed in table 8.7. The shapes of the anisotropy curves (fig. 8.12 (d)) at 0.2 and 10% plastic strain correspond to each other, even though the variations in $\sigma_{0.2}$ are relatively small. The directions around 90° are the strongest, with the 0°-direction a little softer. The 45-55°-directions are the weakest. The work hardening rate is almost equal in all directions, but somewhat lower around 45° than in the other directions.

Table 8.7: Tensile properties in selected test directions of AA6082: Yield strength, ultimate tensile strength, uniform strain, fracture strain and r-value.

Direction	$R_{p0.2}$	R_m	A_m	A_f	r-value
0°	78.3	206	0.17	-	0.41
45°	71	183	0.26	0.30	1.47
90°	90.5	220	0.23	0.26	1.05

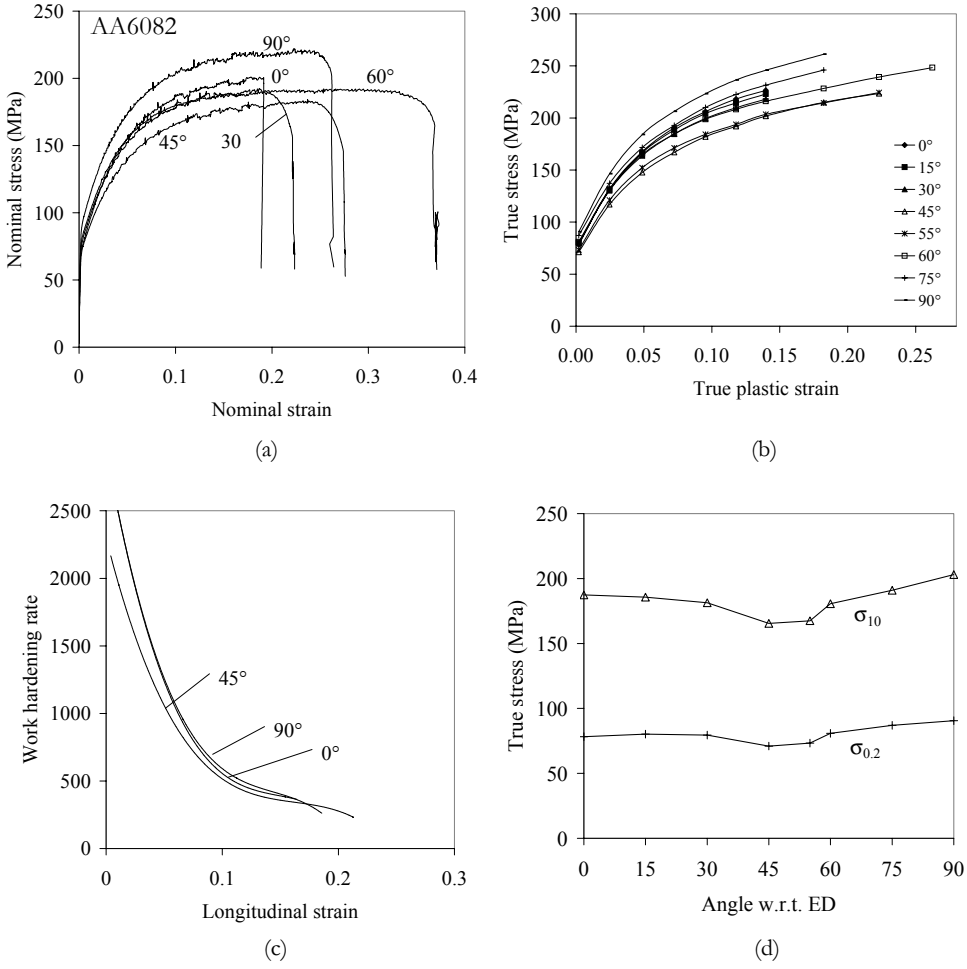

Figure 8.12: Stress-strain behaviour of AA6082: (a) Nominal stress-strain curves for 0, 30, 45, 60 and 90°. (b) True stress-strain curves for all test directions. (c) Work hardening rate ($d\sigma/d\varepsilon$) in 0, 45 and 90°. (d) Yield stress ($\sigma_{0.2}$) and true stress at 10% plastic strain (σ_{10}).

AA7108

The mechanical anisotropy of AA7108 in terms of strength is shown in fig. 8.13. Representative curves for the nominal stress-strain behaviour are given in fig. 8.13 (a), and the average true stress-strain curves for all the test directions in fig. 8.13 (b). Fig. 8.13 (c) shows the rate of work hardening for some directions. The true stress at the yield point, $\sigma_{0.2}$, and at 10% plastic strain, σ_{10}, with respect to the test direction are plotted in fig. 8.13 (d) showing the strength anisotropy. Some of tensile properties are also listed in table 8.8. The anisotropic behaviour of this alloy is very much similar to that of AA6082, with the 90° and 45° directions as the strongest and weakest, respectively. The relative anisotropy is, however, higher than in AA6082, i.e. with more scattered properties. Note the significant difference in strength between 30° and 45°. The differences in work hardening rate are somewhat larger in this alloy.

Table 8.8: Tensile properties in selected test directions of AA7108: Yield strength, ultimate tensile strength, uniform strain, fracture strain and r-value.

Direction	$R_{p0.2}$	R_m	A_m	A_f	r-value
0°	69.4	167	0.14	-	0.28
45°	60.6	143	0.32	0.38	2.37
90°	76.4	187	0.23	0.30	1.12

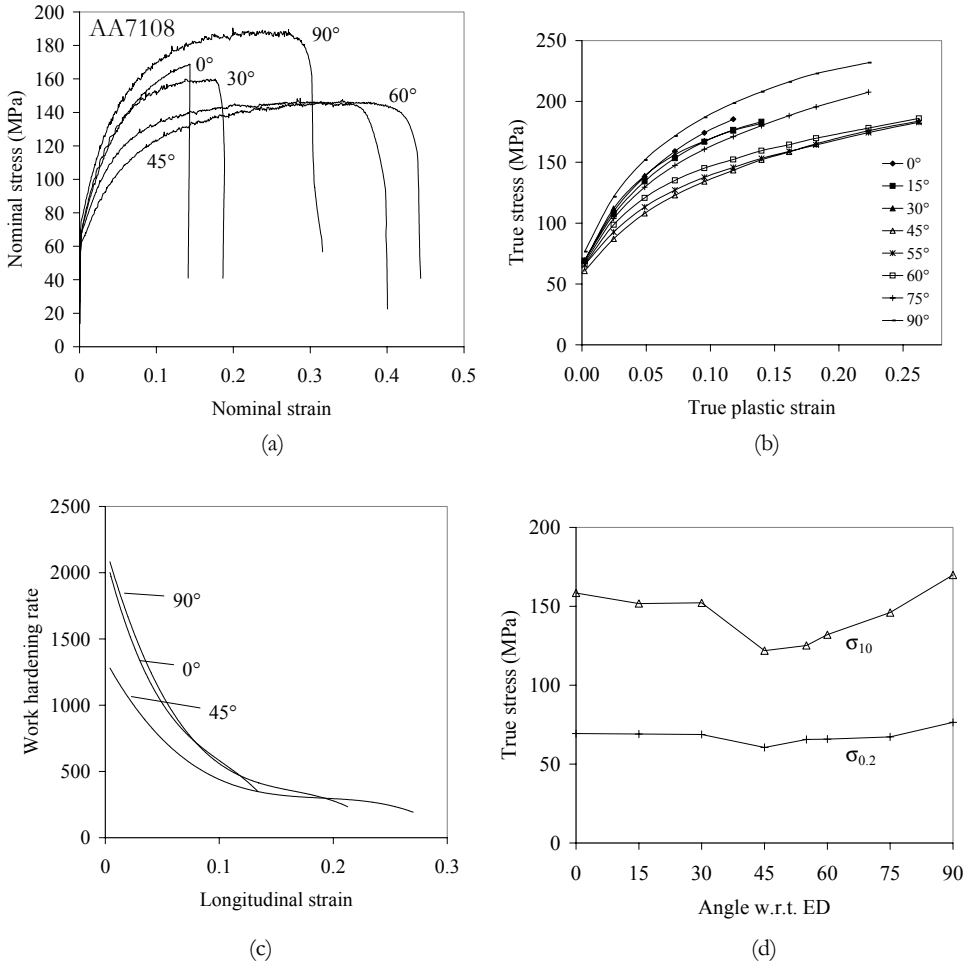

Figure 8.13: Stress-strain behaviour of AA7108: (a) Nominal stress-strain curves for 0, 30, 45, 60 and 90°. (b) True stress-strain curves for all test directions. (c) Work hardening rate ($d\sigma/d\varepsilon$) in 0, 45 and 90°. (d) Yield stress ($\sigma_{0.2}$) and true stress at 10% plastic strain (σ_{10}).

8.2.2 Ductility

The uniform strain, i.e. the strain at the onset of necking, is read from each flow curve and averaged. Also the fracture strain is collected from each sample, except for the specimens where the fracture took place outside of the extensiometer. This was in fact a big problem with a number of the tests, and therefore some of the values of fracture strain are based on just one or two measurements. The nominal strain values are plotted in fig. 8.14 and some numbers given in table 8.5-table 8.8.

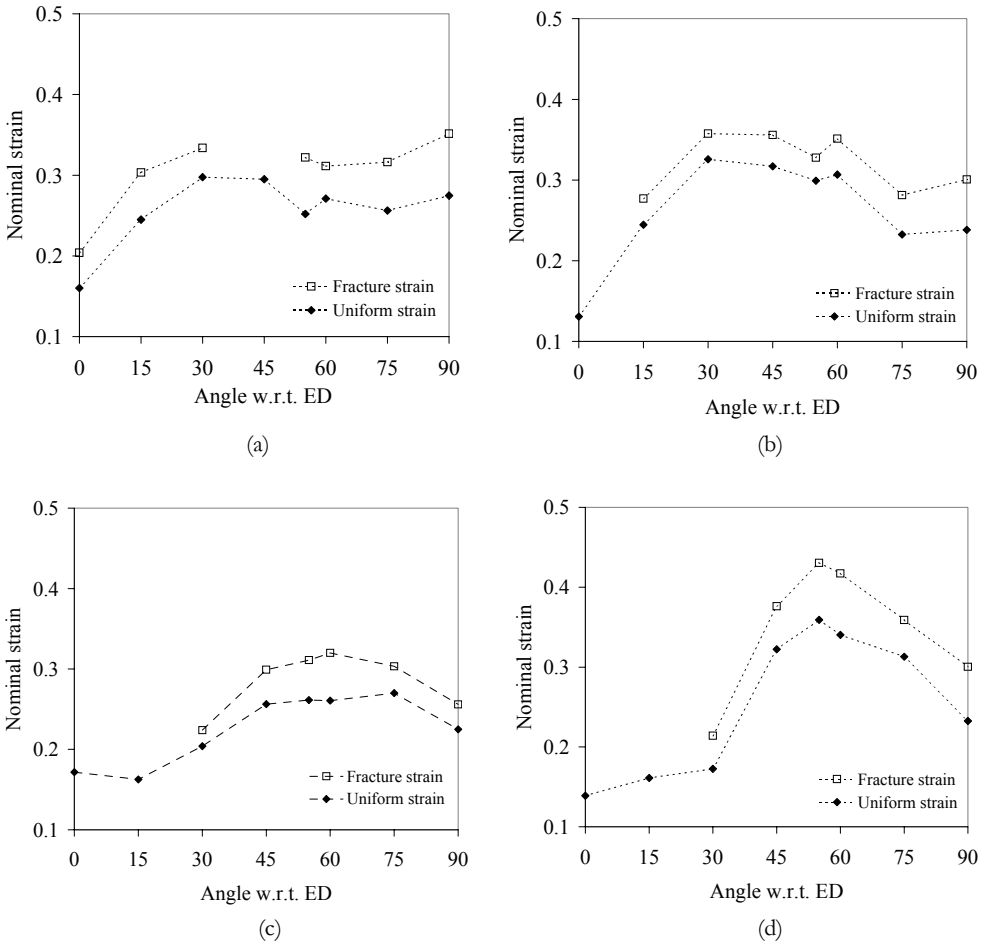

Figure 8.14: Nominal uniform strain and fracture strain of (a) AA6063, (b) AA7030, (c) 6082 and (d) AA7108.

The general trend is that the 0°-direction has a low ductility in all the investigated alloys (uniform strain: 13-17%). In the fibrous alloys (AA6082 and AA7108) also the directions

in a 30° range around the extrusion direction fail at low strains. These alloys are most ductile between the 45 and 75°-directions, while the recrystallised alloys (AA6063 and AA7030) are most ductile between 30° and 60°. Another general observation is that the AA7xxx alloys have higher ductility than the AA6xxx alloys.

8.2.3 Plastic strain ratio (r-value)

An average plastic strain ratio between the transverse and thickness strain (r-value) is estimated up to 5% longitudinal strain. The variation in r-value with test direction is shown for all alloys in fig. 8.15, and some numbers are given in table 8.5-table 8.8. The first thing to notice is that the recrystallised and the fibrous alloys have almost opposite behaviour. In the two recrystallised alloys, AA6063 and AA7030, the r-values are well below 1 in the directions between 0 and 60°. The maximum values are at 90°. The fibrous alloys, AA6082 and 7108, have their minima around 0° and 90° and a maximum around 45°. Both the AA7xxx alloys have larger variations in their r-values, i.e. a stronger anisotropy, than the AA6xxx alloys. Common for all the alloys is the low r-value (<0.6) close to the extrusion direction.

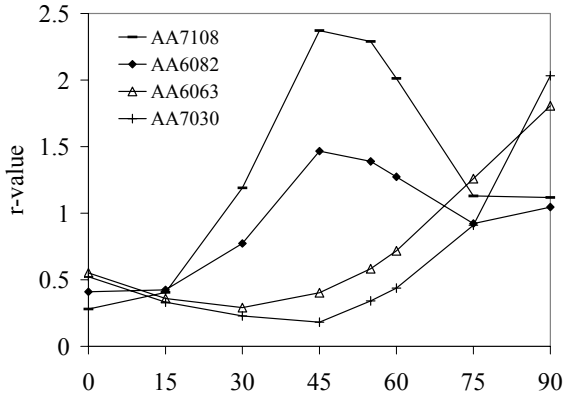

Figure 8.15: r-values for all the investigated alloys.

8.2.4 Thin specimens

Tensile specimens of the recrystallised alloys, AA6063 and AA7030, were thinned to half their thickness from both sides of the profile. These specimens therefore consisted of a more homogeneous microstructure, i.e. layer 1 only. In fig. 8.16 their stress-strain curves are compared to the full thickness specimens presented in section 8.2.1. The first thing to notice is that the flow curves from the thick and thin specimens almost coincide. The

0°-direction in AA6063 is an exception from this, but the discrepancy is relatively small. This shows that the removal of layer 2 and 3 from the specimens does not give any significant changes to the mechanical strength of the alloys. A more prominent effect of reducing the thickness of the specimens is the considerably smaller uniform elongation in the 0°-direction, which occurs in both alloys. A reduced elongation is seen in the other directions as well, except in 90° in AA6063.

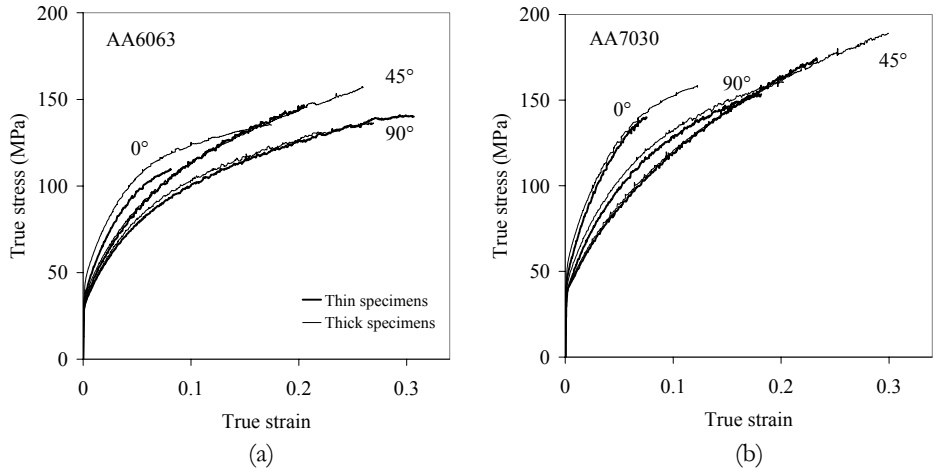

Figure 8.16: Stress-strain curves of thick and thin specimens of (a) AA6063 and (b) AA7030. Thin specimens from the 0°, 45° and 90°-directions were tested.

8.2.5 Correlation of mechanical properties

Some general trends in the experimental observations can be deduced. A rough summary of the directionality of some of the mechanical properties is given in table 8.9, where it is distinguished between recrystallised and non-recrystallised alloys. High strength and high work hardening rate seem to occur in the same directions, e.g. in the 0 and 90°-direction of AA6082 and 7108. The opposite trend is seen in other directions, e.g. in the 45°-direction in AA7030. The high-strength directions appear to have lower ductility, while the ductility is better in the weaker directions. High r-values generally correspond to high ductility and large post- uniform strains (fracture strain-uniform strain), and opposite. An exception from the latter trend is the high ductility in the 30-60° directions of AA6063 and AA7030, despite of the low r-values observed in these directions.

Table 8.9: Summary of the directionality of some mechanical properties for recrystallised alloys and non-recrystallised alloys.

Property	Recrystallised (AA6063 and AA7030)	Non-recrystallised (AA6082 and AA7108)
High strength	around 60° (and 0°)	0 and 90°
Low strength	15-45°	45-60°
High ductility	60-90°	45-75°
Low ductility	0-15°	0-30°
High r-value	60-90°	30-75°
Low r-value	0-60°	0-30° and 75-90°

8.3 Microstructural evolution during tensile testing

One possible way to explain the anisotropy in mechanical properties may be to study the evolution in microstructure and crystallographic texture. This may reveal changes occurring in the material during deformation, leading to different properties. Therefore, some work is done on a microstructural characterisation of the deformed specimens of the AA7030 alloy. Thinned specimens of the AA7030 alloy were solution heat treated and tensile tested in the 0° and 90°-directions. In the 0°-direction the specimens fractured after just 8% strain, while the 90°-specimens were more ductile. In order to compare the developing microstructure in the two directions, a 90°-test was interrupted at 8% strain and another one at 15% strain.

EBSD maps of the microstructure before and after straining are shown in fig. 8.17. Fig. 8.17 (a) shows the initial microstructure, which appears to be equal in both the transverse plane and the extrusion plane (here the transverse plane is shown). In fig. 8.17 (b), after 8% strain in the 0°-direction, a dislocation structure has developed in some grains, while other grains appear to be deformation-free. A vague alignment of the sub-boundaries may be seen, indicating a banded structure. In the specimen strained 8% in the transverse direction, a much more diffuse substructure has evolved, fig. 8.17 (c). The deformation also seems to be more homogeneously distributed among the grains with this test direction, an observation made after 15% strain as well (fig. 8.17 (d)).

A correlation of the deformation structure and the grain orientation reveals that the cube grains in fig. 8.17 (b) contain a low density of dislocation boundaries. In other words,

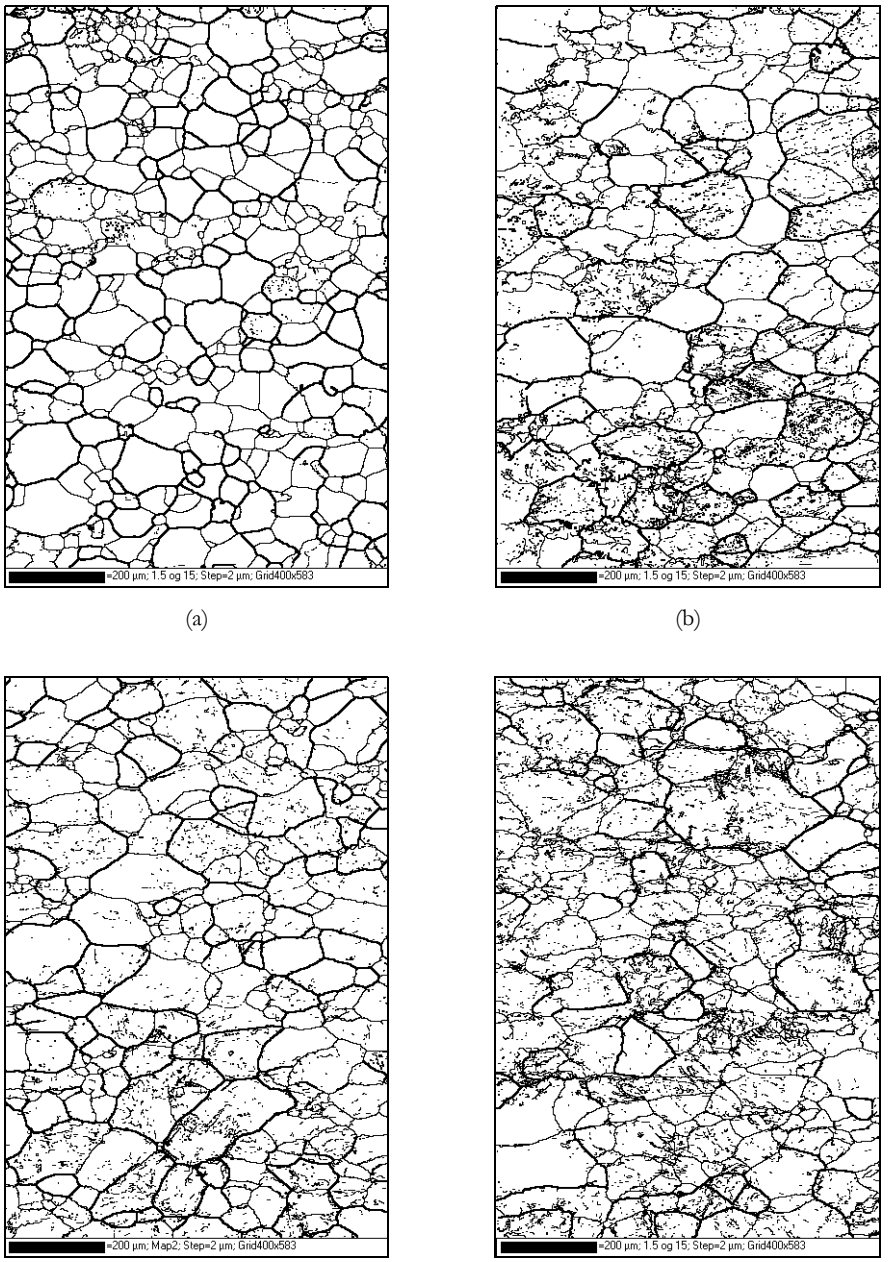

Figure 8.17: Evolution in microstructure during tensile deformation illustrated by EBSD-maps from the side view showing misorientations >15° (bold lines) and 1.5-15° (thin lines). (a) Microstructure before straining, (b) after 8% strain in the 0°-direction, (c) after 8% strain in the 90°-direction, (d) after 15% strain in the 90°-direction.

after straining in the extrusion direction, the grains that exhibit the most distinct substructure are oriented off the cube orientation. Such a relationship is not observed in the specimen tested in the transverse direction.

The texture is measured in the same specimens using the EBSD technique. Both test directions give only small changes in the texture. A small increase of the ED-rotated cube is observed after straining in the 0°-direction, while a small decrease of this component occurs during straining in the 90°-direction.

9. Discussion

The mechanical properties of heat-treatable aluminium alloys, such as AA6xxx and AA7xxx, are determined by a number of factors:

- Solute elements: In the present alloys this concerns Mg, Si and Zn.
- Precipitates: Not relevant in the solution heat treated condition (W).
- Microstructure: Grain size, grain morphology, subgrain size, dislocation structure.
- Crystallographic texture

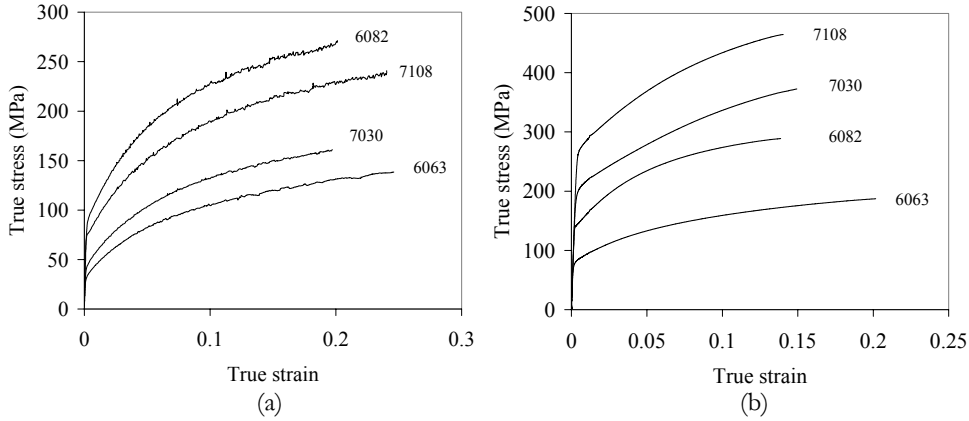

Figure 9.1: True stress-strain curve from the 90°-direction of each alloy. (a) Solution heat treated condition, (b) as-extruded condition (Engler 2002).

A comparison of the alloys investigated in this work is given in fig. 9.1 (a), where the stress-strain curve from the 90°-direction of each alloy is shown. It is evident that AA6063 and AA7030, which are recrystallised, have a significantly lower strength than the non-recrystallised AA6082 and AA7108. This is related to a strengthening contribution from the substructure present in the latter alloys, but also to a difference in texture and Taylor factor, as will be shown later. The difference between the two recrystallised alloys must origin from the higher content of Mg and Zn in AA7030. On the other hand, the low strength of AA7108 as compared to AA6082 must imply that Zn in solid solution has a minor effect, even with concentrations above 5 wt%. The high Si-content in AA6082 is therefore believed to give a strong solution hardening effect, but also some Mn may be present in solution. In fig. 9.1 (b) the same alloys tested in the as-

extruded condition (T1) are shown (Engler 2002). These alloys contain precipitates, and the strength is therefore much higher than in the solutionised condition. Especially the AA7xxx alloys exhibit a strong precipitation hardening that is more than twice the strength of the W-condition.

Solution hardening: A simple test is performed in order to validate eq. (5.1) and the solution hardening given in table 5.2 for the present alloys. An average stress of the direction at a strain of 2.5% is used and divided by the average Taylor factor from fig. 9.3-9.4. This gives a $\tau_{2.5\%}$=28 MPa for AA6063 and 30 MPa for AA7030. Eq. (5.1) can according to table 5.2 be written as:

$$\tau_{2.5\%} = \frac{1}{M}(47 + 21.8 \cdot c) \tag{9.1}$$

for a commercial aluminium alloy, where the Taylor factor for a randomly textured material is M=3. For AA6063 the Mg and Si content in at% is included in c (see eq. (3.1)). This gives a $\tau_{2.5\%}$=22.4 MPa, i.e. 20% lower than the experimental value. This may be explained by a higher strengthening effect from Si (see section 5.1.1). In AA7030 the Mg and Zn contents are included. From the work of Sherby et al. (1951) a solution hardening effect of Zn is estimated to 10MPa/at%, i.e. a considerably lower contribution than the Mg atoms. Therefore, 21.8 $\cdot c$ in eq. (9.1) is replaced by 21.8 $\cdot c_{Mg}$+10 $\cdot c_{Zn}$, giving $\tau_{2.5\%}$=29.5 MPa. This is almost identical to the experimental value.

For the non-recrystallised alloys, also the subgrain size and the grain size must be included through the last term of eq. (2.22). From fig. 8.6 an approximate subgrain size of δ=2.5 μm and a grain size of D=5 μm is used. The resulting $\tau_{2.5\%}$ becomes 36.3 MPa, again significantly lower than the corresponding experimental value of 42.2 MPa. For AA7108, δ=4 μm and a D=6 μm, giving $\tau_{2.5\%}$=35.7 MPa, just slightly higher than the experimental 33.6 MPa. This analysis demonstrates that eq. (2.22) and the discussion in section 5.1.1 are valid also for these materials.

Anisotropy: The solute contribution is normally thought to be independent of the test direction, i.e. it gives no anisotropy. The grain size and the subgrain size will also give variations in properties between the alloys, but negligible anisotropy effects as long as the grains and subgrains are equiaxed. On the other hand, grain morphology, alignment of dislocation walls and grain orientation will give direction dependent properties. This relates mainly to the selection and activation of slip systems in differently oriented grains, and to slip length restrictions from grain boundaries and dislocation walls. In addition,

continuum mechanical effects will play a great role on the stress-strain behaviour, especially on the ductility and r-value.

Based on the microstructure and texture, the alloys investigated in this work may be classified into two groups: Recrystallised and non-recrystallised. The non-recrystallised alloys, AA6082 and AA7108, have a rolling type texture with dominance of Brass (B), which is typical for high temperature plane strain compression (Humphreys and Hatherly 1996). Non-octahedral slip is therefore supposed to be activated during extrusion (Maurice and Driver 1997). In AA6082 a considerable fraction of retained cube bands are present as well. The expected shear texture near the surface has disappeared because of recrystallisation of this layer. The recrystallised alloys, AA6063 and AA7030, have the typical recrystallisation textures cube, ED-rotated cube and Goss. The origin of the cube texture is the growth of highly mobile 40°<111> interfaces between retained cube grains and S-grains from extrusion (Vatne et al. 1996). The Goss grains are believed to grow out of transition bands within grains of B-orientation (Hjelen et al. 1991). The strong Goss texture around s=0.75 in AA6063 seems to correspond to the strong B-texture at the same position in AA6082. In the following subsections the mechanical anisotropy described in section 8.2 is discussed in terms of the texture and microstructure described in sections 8.1 and 8.3.

9.1 Crystal plasticity modelling of anisotropy

As mentioned in the introduction to this section, several factors may contribute to the mechanical anisotropy of metals and alloys. In a case where the texture is assumed to be the major source of anisotropy, a good crystal plasticity model should be able to predict the variations in mechanical properties with the initial texture as the only input. In the following the Taylor model and the Sachs model, briefly presented in section 2.6.2, will be discussed and used to explain the mechanical anisotropy of the alloys.

The Taylor factor gives an indication of how easy it is for a polycrystalline aggregate to activate slip systems. The model suggests that a number of independent slip systems must be active in order to achieve plastic deformation. In the Taylor FC model, five independent active slip systems are required, while three slip systems are necessary in the RC model ("pancake") used here.

9.1.1 Taylor and Sachs analysis based on initial texture

Based on the texture measurements presented in section 8.1 the Taylor model is used to calculate the Taylor factor for tensile testing in various directions of the sheet plane. For this purpose the MTM-FHM software, developed by Van Houtte (2000), is applied with its option to choose between the full constraints model (FC) and the relaxed constraints model (RC). In order to include the texture gradients in the Taylor modelling, the measurement in each position is given a weighting factor. This factor, or actually the volume fraction corresponding to that position, is estimated by an inspection of the microstructure, see table 9.1.

Table 9.1: Volume fraction of the material corresponding to each texture measurement position, used as weighting factors in the Taylor modelling.

Position	AA6063	AA7030	AA6082	AA7108
s=0	45 %	45 %	30 %	30 %
s=0.5	25 %	20 %	30 %	30 %
s=0.75	15 %	20 %	20 %	20 %
s=0.9	10 %	10 %	10 %	10 %
s=1	5 %	5 %	10 %	10 %

A simple Sachs analysis is also performed. The inverse Schmid factor, $1/m$, is calculated for each grain in the EBSD-maps using the HKL software. An average value is then obtained for each test direction.

AA6063 and AA7030

In fig. 9.2 the Taylor factor is calculated for each position through the thickness of the AA6063 profile. An average M-value for the complete cross-section is given as a bold line. It is evident that the texture has some influence on the Taylor factor, which close to the surface is very different from the centre. In the surface layer the texture is quite random compared to the strong ED-rotated cube in the interior of the profile (fig. 8.2), and this has affected the Taylor factor. The texture gradient from s=0 to s=0.75, however, does not seem to give any significant variations in the calculated M, and the average value is actually very close to the value for s=0. The calculations give a high Taylor factor around 45-60°, and a low M in 0° and 90°.

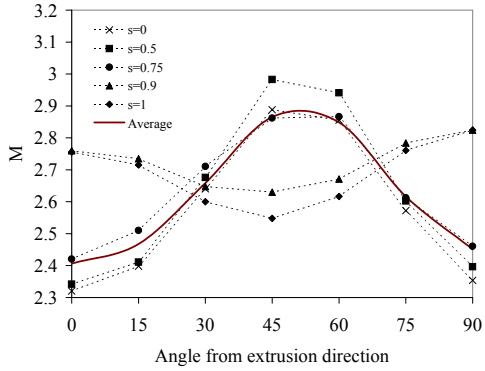

Figure 9.2: Calculated Taylor factor (FC) in various positions and an average curve (AA6063).

Fig. 9.3 (a) shows the Taylor and Sachs calculations of AA6063 in comparison. It is seen that the FC and RC models give relatively similar results, except for some lower amplitudes using RC. The Sachs results are considerably lower, about 10-20% below Taylor FC, but in some way follow the same trend. The Taylor and Sachs calculations of M and $1/m$ of the AA7030 alloy are shown in fig. 9.3 (b) and are directly comparable to AA6063.

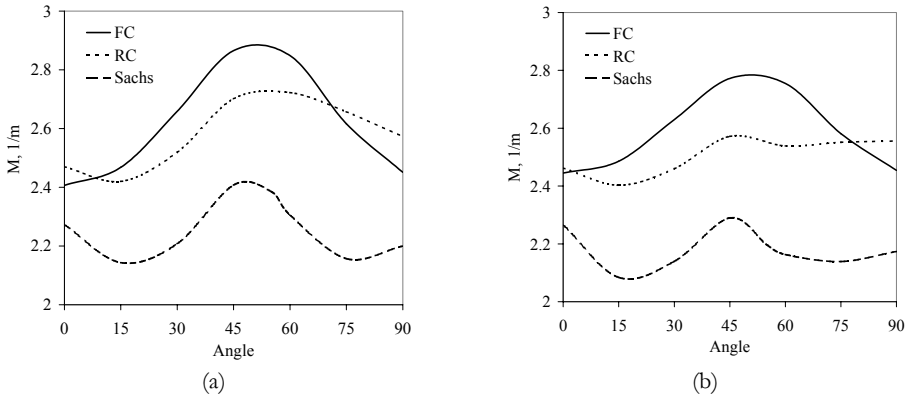

Figure 9.3: Taylor and Sachs modelling of (a) AA6063 and (b) AA7030.

AA6082 and AA7108

The Taylor and Sachs calculations of M and $1/m$ of the AA6082 and AA7108 alloys are shown in fig. 9.4. For each alloy the FC and RC calculations generally correspond to each other. The FC model is seen to predict higher M-values than the RC model, and considerably higher than for the recrystallised alloys above (FC around 3.0-3.2). AA7108

has a distinct minimum at 45°, and in both alloys the 90°-direction is predicted as the strongest. The Sachs calculations give a relatively low $1/m$ value compared to the Taylor model.

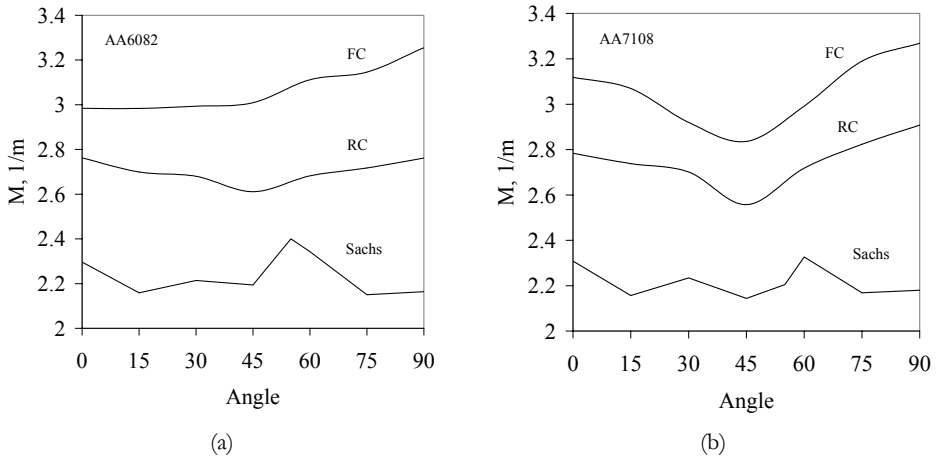

Figure 9.4: Taylor and Sachs modelling of (a) AA6082 and (b) AA7108.

Comparison with experimental results

In fig. 9.5 the average M-values from fig. 9.3 and fig. 9.4 are compared to the experimental results ($\sigma_{0.2}$ and σ_{10}). The yield strength ($\sigma_{0.2}$) displays the ability of the material to withstand plastic deformation. At 10% plastic strain (σ_{10}) a considerable work hardening on the slip planes has occurred, as well as some rotation of the crystals. The ultimate tensile strength is in this context considered as less meaningful, as its magnitude depends strongly on the uniform elongation and is therefore difficult to compare in the various directions. In order to be able to compare the experimental and modelled results, all values are normalised to one of the directions, here either 0° or 90°. These figures illustrate the capability of the Taylor model to predict the mechanical anisotropy based on the texture of the materials.

In general, it is seen that the Taylor model, and particularly the RC model, does not capture the largest amplitudes of the anisotropy. For the recrystallised alloys, AA6063 and AA7030, there appears to be a poor agreement between the experiments and calculations. However, this is partly due to the distinct behaviour of the 0°-direction, and when normalising to 90° instead of 0° as in fig. 9.5 (b), the picture looks better. In such a case the FC model partly predicts reasonable M-values for AA6063, whereas the RC

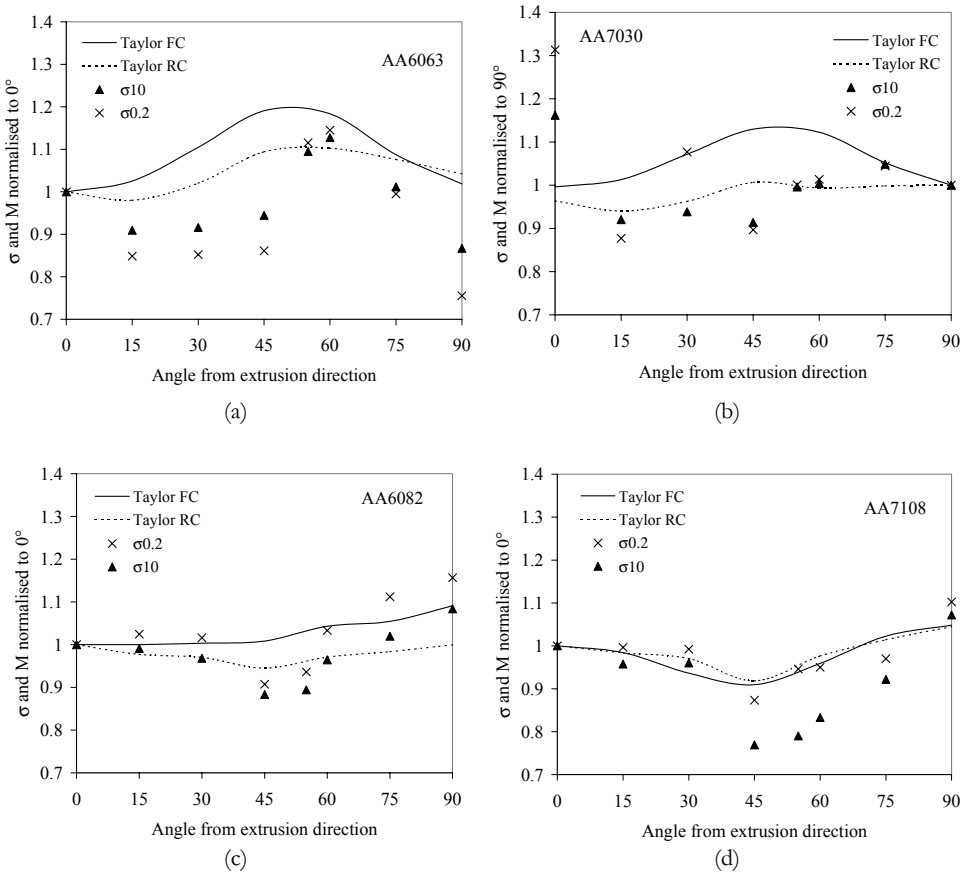

Figure 9.5: Comparison of the observed strength, in terms of yield stress and the stress at 10% plastic strain, and predictions by the Taylor factor, using the Taylor FC and RC models. The results are normalised to the 0°-direction (AA7030 to the 90°-direction).

model seems to fit best to the AA7030 alloy when the 0°-directions are excluded. As seen in fig. 9.3 the absolute values of the FC and RC model are quite similar for these alloys, so in fact the difference between the two models is small for the strong recrystallisation textures seen in AA6063 and AA7030.

The absolute values of the calculated Taylor factors for the non-recrystallised alloys, AA6082 and AA7108, depend more on the choice of model, FC or RC, see fig. 9.4. Compared to the observed strengths of these alloys, the FC model is in good agreement with the yield stress, $\sigma_{0.2}$, but deviates more from the stress at 10% strain (fig. 9.5 (c, d)). In the directions around 45°, too high *M*-values are predicted for the non-recrystallised

alloys. Fewer active slip systems than the five required by Taylor FC are therefore supposed to be active in this direction as compared to 0 and 90°.

Less attention is here paid to the Sachs model, which is generally considered as an unrealistic crystal plasticity model. Although the calculated values for the recrystallised alloys in fig. 9.2 to some extent correspond to the observed anisotropy, this is because of the high strength around the 0°-direction. In other directions the Sachs analysis predicts false values. As mentioned, this model is a lower bound approach, and the absolute values are seen to be much lower than the Taylor calculations, fig. 9.2 and fig. 9.3. Especially in AA6082 and AA7108 the Sachs values are very low.

9.1.2 r-values based on initial texture

The r-values predicted by the Taylor RC model and the experimental r-values are compared in fig. 9.6. This demonstrates that the Taylor RC model is able to predict the r-values very well. The alloys basically have two widely different textures, namely a recrystallisation texture in AA6063 and AA7030, and a rolling-type texture in AA6082 and AA7108. As shown, these textures result in different anisotropy of the r-value, but still the Taylor model captures the variations.

Some overpredictions are seen. In the 90°-direction in AA6063 the strong Goss texture measured at s=0.5-0.75 results in a very high calculated r-value. At 45° in AA7030 the r-values calculated from the surface layer are higher than those from the centre, leading to a higher average r-value here. Finally, around 45° in the non-recrystallised alloys the model results are too high. Except for the latter deviation, the model correctly accounts for the effect of a stronger texture, and hence a more anisotropic r-value, in AA7108 than in AA6082. Perhaps most interesting for the formability of the alloys, however, is the fact that all the low r-values observed are predicted very precisely. Low r-values are associated with pronounced thinning of the profile, and are generally undesired properties in materials that are subjected to sheet forming.

All in all this means that the Taylor RC (pancake) model, which assumes three active slip systems, is able to predict the strain ratio to a very high accuracy. Predictions made by the Taylor FC model (not shown here) result in large overestimates of all the maxima in fig. 9.6, i.e. at 0 and 90° in the recrystallised alloys and at 45° in the fibrous alloys. This behaviour was also observed by Iveland (2000), Fjeldly (1999) and Søreng (1997) on extruded profiles of AA7030 and AA7108 in the W-temper. Iveland pointed out that since also the RC model predicts too high r-values, the calculations should be even more

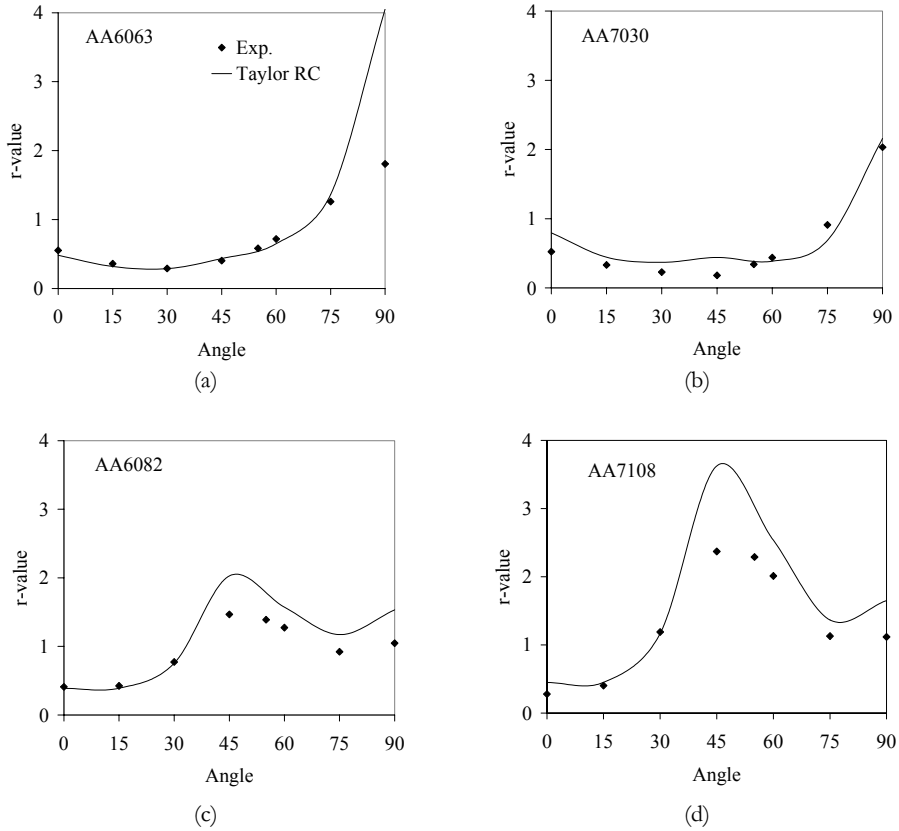

Figure 9.6: Comparison of the observed r-values and predictions by the Taylor RC model.

relaxed than the requirement of three active slip systems in the RC model. On the other hand, in a Sachs analysis by Fjeldly the r-value was generally underpredicted, especially around 45° in AA7108. Based on this it may be suggested that the number of active slip systems during tensile deformation of these alloys is between two and three, at least up to 5% longitudinal strain (the r-values were measured up to that strain). Using Schmids law, Søreng estimated the number of *potentially* active slip systems at 5% strain to be around seven in AA7030 and between four and five in AA7108. This difference between recystallised and non-recystallised alloys are seen also from fig. 9.6, where the RC-model fits the recystallised alloys best and indicates that more slip systems are active in these alloys.

9.1.3 Texture change

The texture was measured in the tensile specimens before and after deformation by the VIRFORM-partners at KUL, Belgium (Li, Van Houtte 2002b). (This was done on materials tested in the T1-condition, i.e. precipitate-containing materials. Some texture measurements performed on materials tested in the W-condition by the present author confirmed the results from KUL, indicating that there were no precipitate effect on the texture evolution during tensile deformation.) The Taylor factor (FC) is calculated from the texture measurements at mid-thickness before and after tensile deformation and plotted in fig. 9.7. The uniform elongation of the different test directions and alloys varied, so the texture after deformation is measured at strains between 0.12 and 0.28.

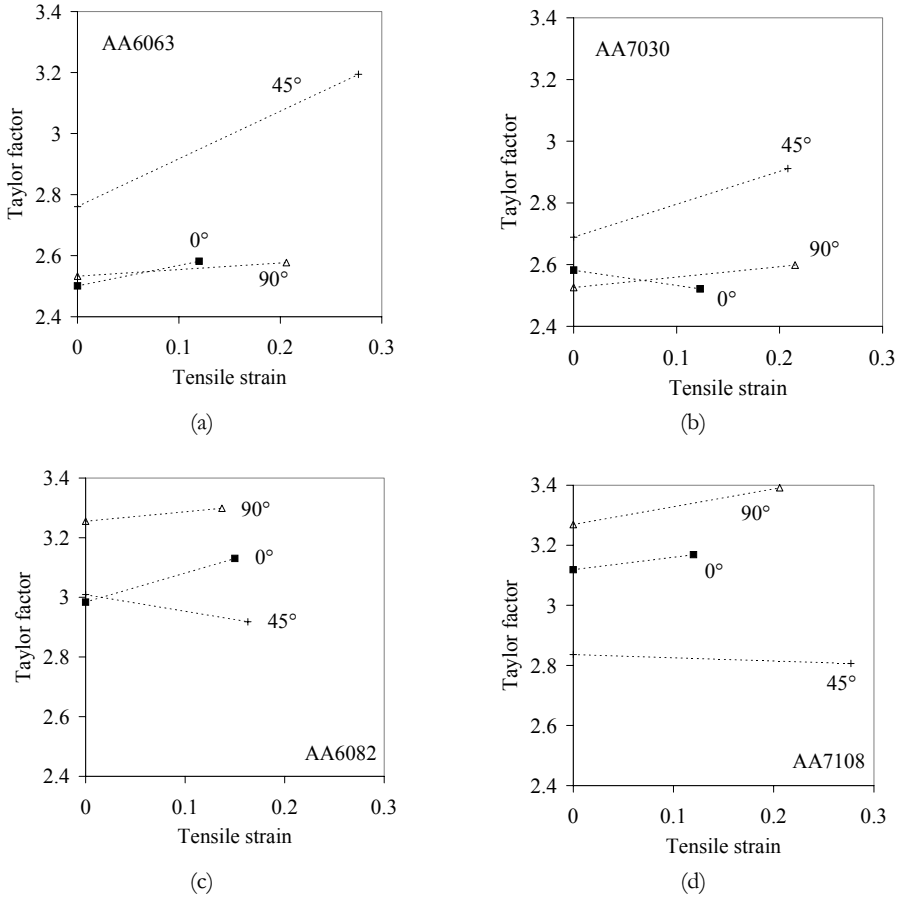

Figure 9.7: Change in Taylor factor (FC) based on texture measurements before and after tensile deformation in the 0°, 45° and 90°-directions. (a) AA6063 (b) AA7030 (c) AA6082 (d) AA7108. Data from Li and van Houtte (2002b).

The most significant changes in the Taylor factor are seen in the 45°-direction of the recrystallised alloys, AA6063 and AA7030, where M increases by 15% and 8%, respectively. In these alloys the 0° and 90°-directions exhibit just minor changes. In AA6082, M increases in 0° and decreases in 45°, while in AA7108 a small increase is observed in 0° and 90°.

The analyses of the Taylor factors in section 9.1.1 are based on the initial textures, i.e. as they are before deformation starts. However, by considering the texture changes, the effect of a change in M may be investigated in relation to the observed strength beyond the yield point. In fig. 9.7 the Taylor factor is shown as $M=M(\varepsilon)$. Only two points are available for each test direction, but a linear relationship is assumed to be realistic. This is supported by a work on a cube textured AA1200 alloy by Bate et al. (2002), where the Taylor factor was calculated at ε=0, ε=0.27 and ε=0.40, giving a linear evolution of M with ε. We can therefore expect that:

$$\tau = \frac{\sigma}{M(0) + a \cdot \varepsilon} \quad \text{and} \quad \gamma = \varepsilon \cdot (M(0) + a \cdot \varepsilon) \tag{9.2}$$

where a is the slope of the dotted lines in fig. 9.7. Hence, the shear stress, τ, and shear strain, γ, may be calculated from the normal stress and strain, σ and ε, and the Taylor factor at a certain strain. This correction for the Taylor factor may then be applied to each stress-strain curve, giving shear stress vs. shear strain where the effect of the texture is eliminated. Ideally, if the texture is responsible for the mechanical anisotropy alone, and assuming the estimates of the Taylor factors are correct, the τ–γ curves should coincide in all test directions. In fig. 9.8 the τ–γ curves are shown for the 0°, 45° and 90° directions of the four alloys.

AA6063 and AA7030

Considering the recrystallised alloys first, fig. 9.8 (a, b), the correction for the M-value has not managed to get the shear stress-shear strain curves in the various directions closer together. In fact, the 45°-curves of the two alloys are now even further away from the other, compared to the σ–ε curves in fig. 8.10-8.11. Even at the onset of plastic flow, where no work hardening or texture change has occurred, the estimated shear stresses are widely different.

Other authors, who have investigated cube textured alloys, have reported equal stress-strain behaviour for the 0° and 90°-directions because the Taylor factor is equal for cube grains tested in these directions (e.g. Lopes et al. 2003, Li and Bate 1991). The present

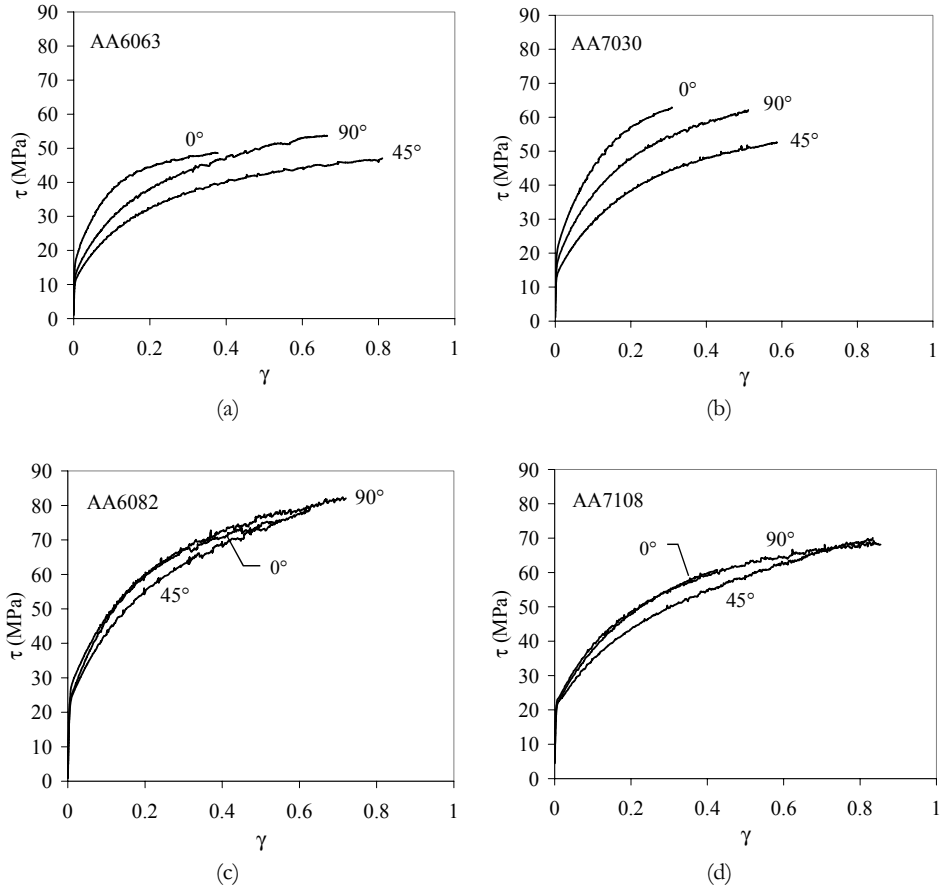

Figure 9.8: Curves showing shear stress vs. shear strain (τ–γ) for three directions of each alloy, estimated by correcting for the Taylor factor calculated before and after tensile deformation.

alloys do, indeed, have a *rotated* cube texture, i.e. a spread of orientations around the extrusion directions (see the cube-fibre plots in fig. 8.2 and fig. 8.4). This may cause a different Taylor factor between 0° and 90°, but it is difficult to believe that this is sufficient to give rise to the large observed differences in strength.

Several possible explanations are therefore considered. First of all, other factors than the texture may cause the anisotropic behaviour. This will be discussed in section 9.2. Secondly, the calculations of the Taylor factors are based on experiments, a theory and a software, and are not necessarily exact values. The textures we are working with here are very strong, up to 100x random or more. It has been argued that the software used for calculations of texture and Taylor factors is unable to handle such strong textures

because of the problem of discretising the ODF when the density peaks are so high (Li and van Houtte 2001). A 5°x5°x5° discretisation is used here, and a finer resolution would therefore be preferable.

AA6082 and AA7108

The Taylor factor correction of the non-recrystallised alloys, AA6082 and AA7108, gives more promising results. In fig. 8.12-8.13 it is seen that the differences between the flow curves in 0°, 45° and 90° are relatively large. After correcting for the Taylor factor the curves almost coincide, see fig. 9.8 (c, d). The three directions are seen to have nearly identical shear stresses at the yield point, i.e. before any work hardening occurs. During deformation the 0° and 90°-directions obtain almost equal τ–γ curves, while the 45°-direction lies a bit below at the intermediate strains. The latter is not surprising as the measured work hardening rates in fig. 8.12-8.13 (c) are similar for 0° and 90°, but lower for 45°.

These results demonstrate that the Taylor FC model is useful for predicting the mechanical anisotropy of materials with a fibrous structure and a strong rolling-type texture. They also indicate that the texture is the main contributor to anisotropy in these alloys. Some deviations arise when a different work hardening behaviour comes into account, as for the 45°-direction. The effect of work hardening is obviously a problem for the Taylor model. This is especially evident in the recrystallised alloys, which have large differences in the work hardening rate. An integration of the work hardening model presented in section 2.5.3 and the Taylor model is in progress (Holmedal et al. 2002a).

9.2 Mechanical properties, microstructure and texture

In the previous section the Taylor model was used to calculate the Taylor factors and r-values based on the texture of the materials. The analyses showed that the RC model is capable of predicting the r-values in all alloys, and that the FC model predicts reasonable Taylor factors for the non-recrystallised alloys, AA6082 and AA7108. The latter result is somewhat surprising since materials with flat, elongated grains often are reported to be better described by the RC approach. The RC model was in fact made for such grain shapes. As to the recrystallised alloys, AA6063 and AA7030, the calculated Taylor factors are in poor agreement with the experiments. As mentioned, one reason for this may be that other factors than the texture affect the directionality of properties. In this section some possible explanations are discussed.

Grains and dislocation structure

The grain morphology is mentioned as a possible source of anisotropy. However, microstructural investigations of the recrystallised alloys show that the grains are equiaxed (fig. 8.17 (a)), also in the transverse direction. Additionally, as seen from fig. 8.16, the stress-strain curves of the AA6063 and AA7030 alloys are unaffected by a removal of the outer layers of the microstructure. So basically the strength and the anisotropy are similar in the various layers through the profile. The grains in layer 2 appear to be somewhat elongated in the extrusion direction, but the effect of this is assumed to be minimal, since the existence of the layer does not influence the strength. Therefore, these effects can be neglected.

After some deformation a clearly visible dislocation structure has been developed. The microstructure after tensile testing of AA7030 in the 0° and 90°-directions is shown in fig. 8.17. After 8% strain a difference in dislocation structure is seen between these test directions. In 0° a tendency of alignment is observed in some grains, whereas in 90° a more evenly distributed dislocation structure is apparent. This picture is consistent with the observations of Søreng (1997) who discovered a rapid development of a microband structure in the 0°-direction during uniaxial tension of an AA7030 alloy. In 90° and 55° such a structure was seen at later stages of deformation. Søreng concluded that in the 0°-direction slip was restricted to just a few slip systems, leading to a clustering of microbands on the {111}-planes. Such microbands are probably identical to the linear dislocation structure observed in fig. 8.17. The concentrated slip activity will give a strong hardening on the active slip systems, and may explain the strong work hardening in the 0°-direction of AA6063 and AA7030.

Fjeldly et al. (2001) found evidence for the formation of Taylor lattices in AA7030 and AA7108 deformed in tension in the W-temper (section 2.2.3). Superimposed on the Taylor lattice narrow parallel slip traces, or microbands, appeared in the <220>-directions. This corresponds to a low number of active slip systems in each grain, as discussed in section 9.1.2. The localised dislocation motion was a result of repeated yielding on the most highly stressed slip systems caused by dynamic strain ageing in these solute containing alloys (section 2.3.3). The microbands developed into coarser slip bands, and finally into shear bands and fracture.

Solid solution

Anisotropic solid solution hardening is an effect that is rarely discussed in the literature, but might be of importance, e.g. on the activation of slip systems. The atoms in solid solution result in the serrated yielding behaviour seen in section 8.2.1, and in order to explore other possible effects of the solutes it would be interesting to compare these alloys to solute-free alloys.

Other partners in the VIRFORM project (Engler 2002) performed tensile tests on the alloys above in both the T1 condition, i.e. as-extruded and stored at room temperature for several months, and the W10 condition, i.e. solutionised for 10 min. at 470°C (AA7xxx) or 530°C (AA6xxx) and tested 10 min. after quenching. An example of the stress-strain behaviour of the T1 and W10 conditions is shown in fig. 9.9 for the AA7030 alloy. The results show no serrated yielding in the materials stored at room temperature for a long time, indicating that most of the elements in solid solution have precipitated and formed particles. The subsequent solution heat treatment makes the serrated flow appear, and the overall strength of the alloy becomes lower as a result of the dissolution of precipitates. The main point is, however, that the anisotropy of strength is more or less unaffected by the solution heat treatment, a result that yielded all these alloys. Hence, unless the precipitates create a directionality of properties that are equal to the directionality the solutes create, which is not very likely, an anisotropic solution hardening effect is therefore regarded as less probable.

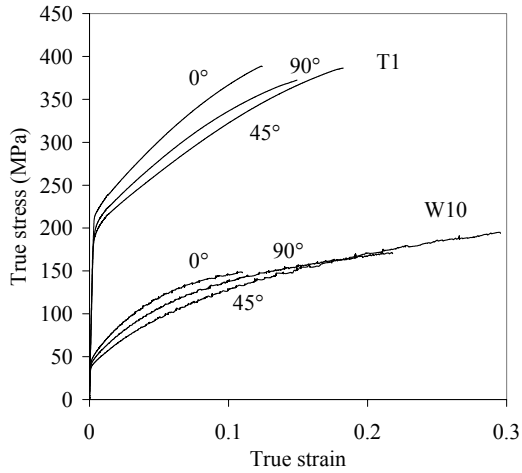

Figure 9.9: Three directions in AA7030, tested in uniaxial tension in the T1 condition and the W10 condition (Engler 2002).

Another observation that speaks against such a phenomenon is that the amount of serrations on the stress-strain curves is independent of test direction, fig. 8.10 (a) and fig. 8.11 (a). This confirms that the solid solution hardening is equal in all directions.

9.3 Suggestions for further work

The way the slip systems are activated is an essential aspect of the anisotropic plasticity. Hence, further analyses of the slip activity are probably required for a deeper understanding of the problem, and a more detailed study of the evolution of the deformation structure in the various test directions should therefore be performed.

In the discussion above the alloy strengths and the Taylor factors are compared by normalising the data to one direction. For a further improvement of the predictability of strength and anisotropy, a combination of the work hardening model in section 2.5.3 and the Taylor model may provide absolute values for the strength at various strain levels.

10. Conclusions

Part B of this thesis considers four industrial extrusion alloys. Two recrystallised alloys, AA6063 and AA7030, and two non-recrystallised alloys, AA6082 and AA7108 extruded into flat 3 mm profiles are investigated. The main objective has been to try to clarify why the mechanical properties vary with the direction of deformation as they do. Tensile testing is performed in the solution heat-treated condition (W), and therefore no effects of precipitation are present. The relationships between microstructure, texture, mechanical anisotropy and formability are searched and the following conclusions can be drawn from the experimental results and the Taylor model calculations:

1. The overall strengths of the alloys are ascribed to the content of Mg, Si and Zn in solid solution and, for the non-recrystallised alloys, the grain and subgrain size. Zn has a relatively small effect in solid solution, as compared to Mg. Si gives a higher strengthening, but this is thought to be related to a solute clustering effect.

2. The extruded profiles exhibit very strong textures, giving rise to variations in the Taylor factor in the profile plane. Consequently, the materials have a strong mechanical anisotropy, up to 20-30% variation in strength within one alloy. The recrystallised alloys have cube, rotated cube and Goss textures, while the non-recrystallised alloys have β-fibre textures with strong Brass components.

3. The extruded profiles have significant microstructural and textural gradients through the thickness, but these give only minor effects on the mechanical properties. Some changes of the texture and Taylor factor occur during tensile testing, especially in the 45°-direction of the cube textured materials.

4. In the non-recrystallised alloys the texture appears to be responsible for most of the strength anisotropy, which is well predicted by the Taylor FC model. The anisotropy of work hardening however, is not captured by the Taylor model.

5. Other sources to anisotropy than the texture are dominating in the recrystallised alloys. One of them is the difference in deformation structure between the various directions, probably related to different activation of slip systems. A substructure consisting of clustered microbands develops in the 0°-direction of AA7030, while the dislocation structure in the 90°-direction is more uniform. More detailed work is needed at this point.

6. The r-value is strongly direction dependent, and in some directions it is very low (<0.2). The Taylor RC model, assuming three active slip systems, predicts the r-values very well for all the alloys. In some cases the model still overpredicts the r-value, and a number of active slip systems in each position between two and three is assumed to be realistic for all alloys and directions.

References

Alberdi Garitaonandia, J.M., PhD thesis, University of Navarra (1984)

Aluminium Standards and Data, Aluminium Association, Inc., Washington D.C. (1986)

Ashby, M.F. in: Kelly, A., Nicholson, R.B. (eds.), Strengthening Methods in Crystals, Elsevier, Amsterdam, p.136 (1971)

Ashby, M.F., Acta Metall., 14, p.679 (1979)

ASM Specialty Handbook, Davies, J.R. (ed.), ASM International (1993)

Aylward, G.H., Findlay, T.J.V., SI chemical data, 2.edition, John Wiley & Sons (1974)

Bate, P., Eardley, E., Humphreys, F.J., unpublished work (2002)

Bay, B., Hansen, N., Hughes, D.A., Kuhlmann-Wilsdorf, D., Acta Met. Mater., 40, p.205 (1992a)

Bay, B., Hansen, N., Kuhlmann-Wilsdorf, D., Mat. Sci. Eng., 158, p.139 (1992b)

Brown, L.M., Ham, R.K. in: Kelly, A., Nicholson, R.B. (eds.), Strengthening Methods in Crystals, Elsevier, Amsterdam, p.12 (1971)

Bunge, H.J., Texture analysis in Material Science, Butterworth & Co, London (1982)

Burger, G.B., Gupta, A.K., Jeffrey, P.W., Lloyd, D.J., Mater. Charact., 35, p.23 (1995)

Carle, D., Blount, G., Materials and Design, 20, p.267 (1999)

Castro-Fernandez, F.R., Sellars, C.M., Whiteman, J.A., Mater. Sci. Tech., 6, p.453 (1990)

CORUS Research Development & Technology Centre, AA5005 Basic Characterisation, VIRFORM-report (2001)

Delannay, L., Mishin, O.V., Juul Jensen, D., Van Houtte, P., Acta Mat., 49, p.2441 (2001)

Dieter, G E., Mechanical Metallurgy, McGraw-Hill, London (1988)

Dillamore, I.L., Roberts, J.G., Busch, A.C., Met. Sci., 13, p.73 (1979)

Dons, A.L., Dr.techn. thesis, NTNU (2002)

Dons, A.L., personal comm. (2003)

Driver, J.H., Juul Jensen, D., Hansen, N., Acta Met. Mater., 42, p.3105 (1994)

Ekström, H.E., personal comm. (2003)

Embury, J.D. in: Kelly, A., Nicholson, R.B. (eds.), Strengthening Methods in Crystals, Elsevier, Amsterdam, p.331 (1971)

Engler, O., VIRFORM Report, Hydro Aluminium Deutschland (2002)

Estrin, Y., Mecking, H., Acta Met., 32, p.57 (1984)

Fjeldly, T.A., Dr.Ing. thesis NTNU (1999)

Fjeldly, A., Roven, H.J., Met. Mat. Trans., 31A, p.669 (2000)

Fjeldly, A., Søreng, A., Roven, H.J., Mat. Sci. Eng., A300, p.165 (2001)

Fleischer, R.L., Hibbard, W.R. in: The Relation Between the Structure and Mechanical Properties of Metals, Her Majesty's Stationary Office, London, p.262 (1963)

Forbord, B., Dr.ing. thesis, NTNU (1999)

Furu, T., Ørsund, R., Nes, E., Acta Met. Mater., 43, p.2209 (1995)

Furu, T., Ørsund, R., Nes, E., Mat. Sci. Eng., A214, p.122 (1996)

Furu, T., AA7108 and AA7030 Basic Characterisation, VIRFORM-report, Hydro Aluminium, Norway (2001)

Gil Sevillano, J., van Houtte, P., Aernoudt, E., Prog. Mat. Sci., 25, p.69 (1980)

Gil Sevillano, J. in: Cahn, R.W. (ed.), Material Science and Technology. A Comprehensive Treatment, vol.6, VCH, Weinheim, p.19 (1993)

Guyot, P., Raynaud, G.M., Acta Met. Mater., 39, p.317 (1991)

Haasen, P. in: Cahn, R.W., Haasen, P. (eds.), Physical Metallurgy, 4th edition, Elsevier Science BV, p.2009 (1996)

Haenle, U., Kalke, S., Lehnert, F., Seethaler, L., Proc. EUROMAT, paper no.71 (2001)

Hagström, J., VIRFAB-report (2003)

Hall, E.O., Proc. Roy. Soc. (London) B64, p.747 (1951)

Hansen, N., Mat. Sci. Tech., 6, p.1039 (1990)

Harren, S.V., Déve, H.E., Asaro, R.J., Acta metall., 36, p.2435 (1988)

Hirsch, J.R., Mat. Sci. Tech., 6, p.1048 (1990)

Hjelen, J., Ørsund, R., Nes, E., Acta Met., 39, p.1377 (1991)

HKL: User manual HKL Channel5, URL: www.hkltechnology.com

Holmedal, B., Ryen, Ø., Van Houtte, P., Nes, E., Aluminium, 78, p.923 (2002a)

Holmedal, B., Abtahi, S., Marthinsen, K., Nes, E., Mat. Sci. Forum, 396-402, p.315 (2002b)

Holmedal, B., Nes, E., unpublished work (2003)

Hopperstad, O.S., Lademo, O.-G., Berstad, T., Pedersen, K., Svinning, T., NorLight Conference, Trondheim, URL: www.sintef.no/units/matek/norlight (2003)

Hughes, D.A., Nix, W.D., Mat. Sci. Eng., A122, p.153 (1989)

Hughes, D.A., Acta Met. Mater., 41, p.1421 (1993)

Hughes, D.A. in: Hansen, N., Juul Jensen, D., Liu, Y.L., Ralph, B. (eds.), Proc. 16th Risø Int. Symp. Mat. Sci., Risø National Laboratory, Roskilde, p.63 (1995)

Hughes, D.A., Hansen, N., Acta Mat., 48, p.2985 (2000)

Humphreys, F.J., Hatherly, M., Recrystallization and related annealing phenomena, Pergamon, Oxford (1996)

Humphreys, F.J., J.Mat.Sci., 36, p.3833 (2001)

Humphreys, F.J., VMAP v8 User manual (2002)

Inagaki, H., Kohara, S., Z.Metallk., 88, p.570 (1997)

Inagaki, H., Koizumi, M., Chang, C.S.T., Duggan, B.J., Mat. Sci. Forum, 396-402, p.587 (2002)

Iveland, T., Dr.ing. thesis, NTNU (2000)

Kocks, U F., J. Eng. Mater. Tech. (ASME-H), 98, p.76 (1976)

Kocks, U F., Mecking, H., Prog. Mat. Sci., 48, p.171 (2003)

Koizumi, M., Kohara, S., Inagaki, H., Z. Metallk., 91, p.88 (2000)

Korbel, A., Embury, J D., Hatherly, M., Martin, P L., Erbsloh, H W., Acta Met., 34, p.1999 (1986)

Lademo, O.-G., Hopperstad, O.S., Malo, K.A., Pedersen, K., J. Mat. Proc. Tech., 125-126, p.84 (2002)

Langford, G., Cohen, M., Trans. Am. Soc. Met., 62, p.623 (1969)

Leffers, T., Scripta Metall., 2, p.447 (1968)

Li, F., Bate, P.S., Acta Metall. Mater., 39, p.2639 (1991)

Li, S., van Houtte, P., VIRFORM Report, Katholieke Universiteit Leuven, Belgium (2001)

Li, S., van Houtte, P., VIRFORM Report D12, Katholieke Universiteit Leuven, Belgium (2002a)

Li, S., van Houtte, P., VIRFORM Report D13, Katholieke Universiteit Leuven, Belgium (2002b)

Liu, Q., Juul Jensen, D., Hansen, N., Acta mater., 46, p.5819 (1998)

Lloyd, D.J., Metal Science, May, p.193 (1980a)

Lloyd, D.J., Met. Trans., 11A, August, p.1287 (1980b)

Lloyd, D.J., Kenny, D., Acta Metall., 28, p.639 (1980)

Lloyd, D.J. in: Sachdev, A.K. Embury, J.D. (eds.), Formability and metallurgical structure, The Metallurgical Society, Inc., p.193 (1986)

Lopes, A.B., Barlat, F., Gracio, J.J., Ferreira Duarte, J.F., Rauch, E.F., Int. J. Plasticity, 19, p.1, (2003)

Lücke, K., Engler, O., Mat. Sci. Tech., 6, p.1113 (1990)

Mahon, G.J., Marshall, G.J., JOM, June, p.39 (1996)

Marciniak, Z., Duncan, J., Mechanics of Sheet Metal Forming (1992)

Marthinsen, K., Nes, E., Mat. Sci. Tech., 17, p.376 (2001)

Maurice, Cl., Driver, J.H., Acta Mater., 45, p.4627 (1997)

Mecking, H., Kocks, U F., Acta Met., 29, p.1865 (1981)

Metals Handbook, ASM International, Tenth Edition, vol. 2, p.37 (1990)

Miller, W.S., Zhuang, L., Bottema, J., Wittebrood, A.J., De Smet, P., Haszler, A., Vieregge, A., Mat. Sci. Eng., A280, p.37 (2000)

Mitchell, T.E. in: Jürgen Buskow, K.H., Cahn, R.W., Flemings, M.C., Ilschner, B., Kramer, E.J., Mahajan, S. (eds.), Encyclopedia of Materials: Science and Technology, Elsevier, Amsterdam, vol.10, p.9827 (2001)

Mughrabi, H., Mater. Sci. Eng., 85, p.15 (1987)

Nes, E., Dons, A.L., Ryum, N. in: Gifkins, R.C. (ed.), Proc. ICSMA 6, Pergamon Press, Oxford (1982)

Nes, E., Prog. Mat. Sci., 41, p.129 (1998)

Nes, E., Marthinsen, K., Rønning, B., J. Mater. Proc. Tech., 117, p.333 (2001)

Nes, E., Marthinsen, K., Mat. Sci. Eng., A322, p.176 (2002)

Nes, E., Marthinsen, K., Brechet, Y., Scripta Mat., 47, p.607 (2002)

Nord-Varhaug, K., Forbord, B., Benestad, J., Pettersen, T., Rønning, B., Bardal, A., Benum, S., Marthinsen, K., Nes, E., Mat. Sci. Forum, 331-337, p.1387 (2000)

Pechiney CRV, AA5182 Basic Characterisation, VIRFORM-report (2001)

Pedersen, K, personal communication (2001)

Petch, N.J., J.Iron Steel Inst., 174, p.25 (1953)

Pettersen, T., Furu, T., AA6063 Basic Characterisation, VIRFORM-report, Hydro Aluminium, Norway (2001a)

Pettersen, T., Furu, T., AA6082 Basic Characterisation, VIRFORM-report, Hydro Aluminium, Norway (2001b)

Raabe, D., Computational Materials Science, Wiley-VCH, Weinheim (1998)

Randle, V., Engler, O., Introduction to Texture Analysis, Gordon and Breach Science Publishers (2000)

Rollett, A.D., Kocks, U.F., Doherty, R.D. in: Sachdev, A.K. Embury, J.D. (eds.), Formability and metallurgical structure, The Metallurgical Society, AIME, p.211 (1987)

Rollett, A.D., Kocks, U.F., Solid State Phenomena, 35-36, p.1, (1994)

Roters, F., Raabe, D., Gottstein, G., Acta Mater., 48, p.4181 (2000)

Ryen, Ø., Laukli, H.I., Holmedal, B., Marthinsen, K., Nes, E., Proc. EUROMAT (2001)

Sachs, G., Z. Verein Deut. Ing., 72, p.734 (1928)

Schmid, E., Proc. Int. Conf. Appl. Mech., Delft, 342 (1924)

Schuh, F., von Heimendahl, M., Z. Metallk., 65, p.346 (1974)

Sherby, O.D., Anderson, R.A., Dorn, J.E., Journal of Metals, August, p.643 (1951)

Shi, H., McLaren, A.J., Sellars, C.M., Shahani, R., Bolingbroke, R., Mat. Sci. Tech., 25, p.61 (1997)

Sjølstad, K., unpublished work (2001)

Sjølstad, K., Engler, O., Tangen, S., Marthinsen, K., Nes, E., Mat. Sci. Forum, 396-402, p.463 (2002)

Sjølstad, K., Dr.ing. thesis, NTNU (2003)

Suni, J.P., Shuey, R.T., Doherty, R.D. in: Sanders, T.H., Starke, E.A. (eds), Proc. ICAA-4, p.521 (1994)

Sæter, J.A., Dr.ing. thesis, NTNU (1997)

Søreng, A., Dr.ing. thesis, NTNU (1997)

Taylor, G.I., J. Inst. Mater., 62, p.307 (1938)

Thompson, A.W., Baskes, M.I., Philos. Mag., 28, p.301 (1973)

Thompson, A.W., Baskes, M.I., Flanagan, W.F., Acta Metall., 21, p.1017 (1973)

Van Houtte, P., Textures and Microstructures, 8-9. p.313 (1988)

Van Houtte, P., The "MTM-FHM" software system, version 2, manual, Katholieke Universiteit Leuven, Belgium (2000)

Vatne, H.E., Furu, T., Ørsund, R., Nes, E., Acta Mater., 44, p.4463 (1996)

Verhoeven, J.D., Fundamentals of Physical Metallurgy, John Wiley & Sons, New York (1975)

Williams, D B. Carter, B C., Transmission Electron Microscopy (part II), Plenum Press, New York (1996)

Appendix

Table A-1: Specimen dimensions [mm] for tensile testing.

Alloy		Cross section	Thick-ness	Width	Dia-meter	Length
AA1050 and AlMgX	As-cast	Round	-	-	6	30
	ε=0.5	Round	-	-	6	30
	ε=1	Round	-	-	6	30
	ε=2	Flat	3.4	6	-	30
	ε=3	Flat	1.2	6	-	30
	Fine-grained	Flat	3-4	12.7	-	65
AA3103	As-cast/ hom. A, B, C	Round	-	-	5	30
	B: Cold rolled	Flat	1.5-7.6	12.7	-	65
	B: Fine-grained	Flat	4.3	12.7	-	65
	B: Fine-grained+c.r.	Flat	0.5-2.5	12.7	-	65
	AA6xxx, AA7xxx	Flat	3	12.7	-	65
	AA5xxx[a]	Flat	0.5-23	7.8-40		25-95

a. O.Engler

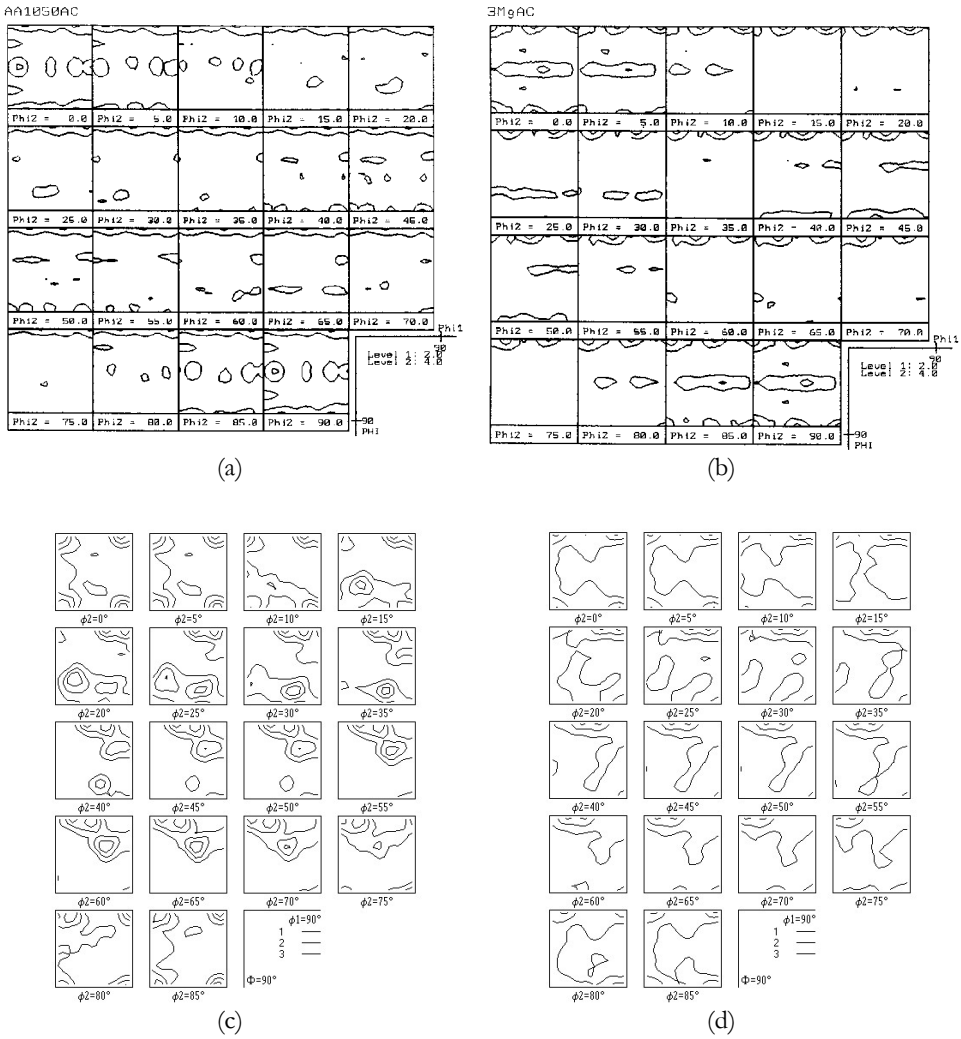

Figure A-1: ODFs of as-cast and fine-grained alloys.(a) AA1050 as-cast, (b) AlMg3 as-cast, (c) AlMg0.5 fine-grained, (d) AlMg3 fine-grained. Fig. a and b are from X-ray diffraction, fig. c and d from EBSD.

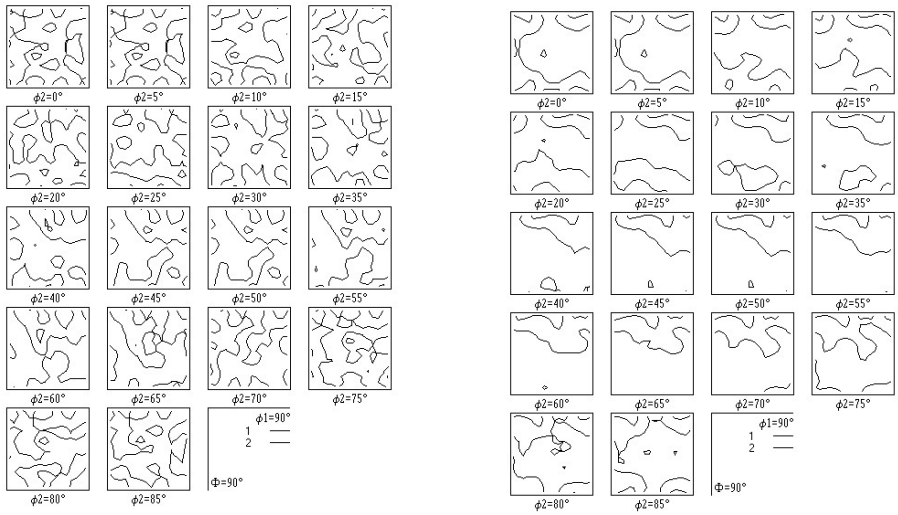

(a) (b)

Figure A-2: ODFs of as-cast and fine-grained AA3103.(a) As-cast, (b) fine-grained. Texture measured by EBSD.

Table A-1: Presence of shear bands (SB) after cold rolling of various alloys.

Alloy	**ε=0.5**	**ε=1**	**ε=2**	**ε=3**	**ε=4**
AA1050	no SB	no SB	no SB	no SB	-
AlMg0.5	no SB	no SB	no SB	**SB**	-
AlMg1	no SB	no SB	**SB**	**SB**	-
AlMg3	no SB	no SB	**SB**	**SB**	-
AA5005	no SB	no SB	**SB**	**SB**	**SB**
AA5182	no SB	**SB**	**SB**	**SB**	**SB**
AA3103-B	no SB	no SB	no SB	no SB	-
AA3103-B FG	no SB	no SB	no SB	-	-

Table A-2: Summary of EBSD substructure analyses (step size 0.05 μm).

Alloy	ε	# maps	Average indexing fraction (%)
AA1050	0.5	5	98
	1	4	89
	2	4	89
	3	2	86
AlMg1	0.5	3	95
	1	6	93
	2	5	76
	3	5	76
AlMg3	0.5	6	90
	1	4	90
	2	4	72

Table A-3: Average misorientation and number of boundaries measured in TEM.

Alloy	ε	φ (°)	# boundaries
AA1050	2	4.66	294
AlMg0.5	2	4.29	120
	3	3.73	69
AlMg1	0.5	2.27	55
	1	3.76	76
	2	4.45	291
	3	5.12	84
AlMg3	2	4.69	62
	3	5.95	40